InAs Avalanche Photodiodes

Silvia Butera

Submitted for the Degree of Doctor of Philosophy

Heriot-Watt University

School of Engineering and Physical Sciences

April 2015

Abstract

The ability to efficiently detect low-level light in the infrared above wavelengths of 1.7 μm is becoming increasingly important for many applications such as gas sensing, defence/geoscience ranging and clinical thermography. The III-V narrow gap semiconductor InAs, with a bandgap of 0.36 eV, is well known for its use as a conventional photodiode. The aim of this thesis was to design, build and test InAs devices for use as reverse biased avalanche photodiodes. In order to fabricate a low-noise detector, a passivation study was conducted. For the first time we report the achievement of high quality single crystal II-VI passivation layers on InAs mesa structures. Pre-growth surface oxide removal processes were developed to improve surface morphology of II-VI layers grown on InAs samples. ZnSe and ZnTe successfully terminate the InAs mesa devices preventing atmospheric oxidation. Low surface leakage currents are observed at low reverse bias and at room temperature for both materials. LIDAR at wavelengths greater than 2 μm was studied using these InAs mesa photodiodes, showing potential to take advantage of the low solar background at these wavelengths. For the first time, laboratory based LIDAR experiments, with ranges of around 0.5 metre stand-off distance, were performed with InAs n-i-p edge illuminated mesa photodiodes, used in linear multiplication mode. Time-of-flight measurements were demonstrated at wavelengths from 1.3 μm to 2.365 μm. A 6 mm ranging error was observed in these short range measurements.

Acknowledgments

In this section I would like to thank all the people that supported me and helped me during these PhD years.

Firstly, I would like to thank my supervisor Prof. Gerald Buller for his guidance, for his support, and for all the input he gave in this project. Thanks also go to my second supervisor Dr Kevin Prior for letting me actively collaborate with his group in the growth of II-VI compounds, and for discussion on II-VI compounds. My gratitude also goes to Prof. Carl Pidgeon for all the things he taught me about science but also about English grammar.

Thanks to Dr Ryan Warburton, the Wee Boss, for his assistance, support, for his patience, and for always managing to make me smile, even when it was the last thing I wanted. My gratitude also go to Dr Peter Vines for all his assistance through the work performed in this thesis and for all the time he has given to this work. Thanks also go to Dr Richard Moug for all his effort in the growth of the II-VI layers and for his support in developing this original idea of II-VI as a possible passivation layer for InAs photodiodes.

Thanks to all the Photon Counting group, in particular to Dr Aongus McCarthy for lending me some optical components that helped me in my experiments and for all his precious advice; to Dr Robert Collins for his help every time I needed it. My gratitude goes also to Giuseppe for sharing the lab with me, PJ and of course Ross for all the interesting chat we had and for all the laughs that made even the endless days more acceptable.

Thanks also go to various collaborators with whom I have worked. I thank Prof. Chee Hing Tan and the rest of the group at the Centre for III-V technologies at the University of Sheffield for providing the InAs samples, in particular Dr. Ian Sandall for processing the mesa samples analysed in this thesis; Prof. Maria Tamargo and her group for helping us with the Te compounds and inviting me to the City College of New York, in particular Vasilios Deligiannakis for the help during the growth of the New York samples analysed in this thesis; and Prof. Robert Hadfield and the Quantum Sensors group for bothering him even in Glasgow to use his wire bonding machine, in particular Dr. Alessandro Casaburi for resolving any technical problem during the bonding

process.

Thanks go to Jonathan Morton and Neil Ross for teaching me the ellipsometry and SEM techniques, respectively; and to Loraine Markland for removing the worries of the bureaucracy letting me focus on my project.

I would like also to thank Helia Photonics Ltd. for the SiN and Al_2O_3 coating and for the help in the filter transmission measurements.

My gratitude also goes to my officemates, Dr Tuminse Dada, Dr Akhil Rajan and Dr Chaitanya Joshi without whom my working days could be very sad and stressful. I will always remember our long coffee breaks with the " delicious" ginger coffee made just for us by Joshi. A special thanks go to my friend Joshi for being part of my life in Edinburgh; you had an important role in my PhD but also outside the university, I don't know if I could have done a lot of things without your support and it was a shame you went away so early, I missed you a lot.

I would like to thank also my first family in Edinburgh: Massimo and Laura. We had a lot of fun all together in that small house. I will always remember that period as a one of the most exciting periods of my life, every problem we took with a laugh or a dance on the table.

Thanks to my friends Federica, Elisea, Luisa, Giovanna and Enrico who, although far, always gave me friendship and support.

I thank my parents for always believing in me, for comforting and pushing me when I needed it, allowing me to reach the end of this PhD. My mum for coming to Edinburgh often and bringing with her a bit of the home I left in Sicily that I always miss. Thanks go also to my lovely brother for his advice and support on which I could count every time I needed it.

Finally, but not less importantly, I would like to thank Nathan for always being next to me in sad or happy moments, to comfort me, to believe in me, or to make me laugh. During my PhD I had the possibility to learn a lot of new and interesting topics, to meet and collaborate with very nice people, but the most important thing I got from it is that it allowed me to be on your way where I always will want to be.

ACADEMIC REGISTRY
Research Thesis Submission

Name*:*			
School/PGI:			
Version: *(i.e. First, Resubmission, Final)*		Degree Sought (Award **and** Subject area)	

Declaration

In accordance with the appropriate regulations I hereby submit my thesis and I declare that:

1) the thesis embodies the results of my own work and has been composed by myself
2) where appropriate, I have made acknowledgement of the work of others and have made reference to work carried out in collaboration with other persons
3) the thesis is the correct version of the thesis for submission and is the same version as any electronic versions submitted*.
4) my thesis for the award referred to, deposited in the Heriot-Watt University Library, should be made available for loan or photocopying and be available via the Institutional Repository, subject to such conditions as the Librarian may require
5) I understand that as a student of the University I am required to abide by the Regulations of the University and to conform to its discipline.

* *Please note that it is the responsibility of the candidate to ensure that the correct version of the thesis is submitted.*

Signature of Candidate*:*		Date:	

Submission

Submitted By *(name in capitals):*	
Signature of Individual Submitting:	
Date Submitted:	

For Completion in the Student Service Centre (SSC)

Received in the SSC by *(name in capitals):*			
Method of Submission *(Handed in to SSC; posted through internal/external mail):*			
*E-thesis Submitted (**mandatory for final theses)***			
Signature:		Date:	

Contents

Chapter One – Introduction	1
1.1 Light and its properties: historical overview	1
1.2 Detection of infrared radiation and emerging infrared applications	2
1.2.1 Laser Ranging	3
1.2.1.1 Three-dimensional imaging using Time of flight laser ranging	5
1.2.1.2 Gas sensing with LIDAR	8
1.2.2 Thermometry	11
1.2.2.1 Thermography for human diagnostic techniques	12
1.2.2.2 Rocket plume detection	13
1.2.2.3 Industry manufacturing and civil monitoring using thermometry	14
1.3 Detection system overview	15
1.3.1 Single photon detection and the Time-Correlated Single-photon Counting technique	16
1.3.2 Single photon key figures of merit	18
1.3.3 Single photon detectors	19
1.3.3.1 Photomultiplier Tube	19
1.3.3.2 Microchannel plates	22
1.3.3.3 Quantum dot based detectors	23
1.3.3.4 Superconducting detectors	25
1.3.3.5 Avalanche Photodiodes	30
1.4 Conclusion	30
1.5 Thesis overview and motivation	31
1.6 References	33
Chapter Two – Avalanche Photodiodes in the Near and Mid-infrared	41
2.1 p-n and p-i-n junctions	41
2.2 Avalanche photodiodes (APDs)	42
2.3 Single-photon Avalanche photodiodes	45
2.4 APD and SPAD design	47
2.5 Material choice in APDs and SPADs	48

2.5.1 Ge photodiodes 48
2.5.2 InGaAs and InGaAs/InP avalanche photodiodes 51
2.5.3 Mid-IR range photodiodes 55
2.5.3.1 Type II superlattice photodiodes 55
2.5.3.2 HgCdTe photodiodes 59
2.5.3.3 InSb photodiodes 61
2.6 Conclusions 63
2.7 References 65

Chapter Three – InAs Avalanche Photodiodes 70
3.1 InAs crystal and band structures 70
3.2 InAs Avalanche Photodiodes multiplication 72
3.3 InAs Avalanche Photodiodes excess noise 76
3.4 InAs ionisation coefficients and avalanche breakdown 78
3.5 High frequency behaviour of InAs avalanche photodiodes 83
3.6 Conclusions 84
3.7 References 86

Chapter Four – InAs photodiodes: post growth processes, mask set design and preliminary passivation results. 89
4.1 Introduction 89
4.2 Growth and post-growth processing: etching processes, passivation coating and device packaging 89
4.3 New mask design for InAs detector 94
4.4 Conclusions 105
4.5 References 107

Chapter Five – ZnSe, CdSe, CdMgSe and ZnTe as alternative passivation layers for InAs photodiodes 108
5.1 Introduction 108
5.2 Relevance to other work on II-VI layers for InAs diode passivation 109
5.3 Characterisation techniques 112
5.3.1 X-ray Diffraction 112
5.3.2 RHEED Oscillation technique 114

5.3.3 Ellipsometry spectroscopy 117
5.3.4 Photoluminescence Spectroscopy 119
5.3.5 Atomic Force Microscopy 120
5.3.6 Optical and Electron Microscopies 124
5.4 Growth of II-VI compounds on InAs conducted at Heriot-Watt University 125
5.4.1 Growth of ZnSe on InAs 127
5.4.1.1 ZnSe growth on heat cleaned InAs samples 128
5.4.1.2 ZnSe growth on chemically cleaned InAs samples 130
5.4.2 Growth of CdSe on InAs 140
5.4.2.1 CdSe growth on heat cleaned InAs samples 140
5.4.2.2 CdSe growth on chemically cleaned InAs samples 143
5.4.3 Growth of CdMgSe on InAs 149
5.4.3.1 CdMgSe growth on heat cleaned InAs samples 150
5.4.3.2 CdMgSe growth on chemically cleaned InAs samples 155
5.5 Growth of II-VI compounds on InAs conducted at the City College of New York. 160
5.5.1 Growth of ZnTe on InAs 162
5.5.1.1 ZnTe growth on heat cleaned InAs samples 162
5.5.2 Growth of ZnSe on InAs 170
5.5.2.1 ZnSe growth on heat cleaned mesa InAs samples 170
5.5.3 Growth of ZnSeTe on InAs 173
5.5.3.1 ZnSeTe growth on heat cleaned InAs samples 174
5.6 Conclusions 175
5.7 References 178

Chapter Six – Time of flight ranging using InAs photodiodes 182
6.1 Introduction 182
6.2 Samples 182
6.3 Characterisation of p-i-n and n-i-p photodiodes 187
6.3.1 Dark current IV curves 187
6.3.1.1 Measurements at room temperature 187
6.3.1.2 Measurements at lower temperature 188
6.3.2 Photocurrent measurements with reverse biased InAs photodiodes 190
6.3.2.1 Experimental set up 190

6.3.2.2 Avalanche multiplication in p-i-n structure 194
6.3.2.3 Avalanche multiplication in n-i-p structure 203
6.3.2.4 Timing of the InAs device output pulse as a function of laser spot position 206
6.3.2.5 Study of the InAs device output pulse as a function of laser power and reverse bias 210
6.4 Ranging experiments using n-i-p photodiodes 213
6.4.1 Experimental set up 213
6.4.2 Ranging measurements 215
6.4.3 Measuring the speed of light 222
6.5 Conclusions 224
6.6 References 226

Chapter Seven – Conclusions and future work 227
7.1 Conclusions 227
7.2 Future work 230
7.3 References 232

Glossary of acronyms alphabetically

ADC	Analogue to Digital Converter
AFM	Atomic force microscopy
AOTF	Acousto-optic Tunable Filter technology
APD	Avalanche Photodiode
ARC	Anti-reflection Coating
BCB	B-stage Bisbenzocyclobutene
CCD	Charge coupled device
CFD	Constant Fraction Discriminator
DCR	Dark Count Rate
DIAL	Differential Absortion LIDAR
FCC	Face Centred Cubic
FET	Field Effect Transistor
FWHM	Full width at half maximum
GR	Guard Ring
IR	Infrared
LIA	Lock In Amplifier
LIDAR	Laser Imaging detection and Ranging
LWIR	Long Wave Infrared range
MBE	Molecular Beam Epitaxy
MCP	Microchannel Plate
MOCVD	Metalorganic Vapour Phase Epitaxy
MWIR	Mid Wave Infrared range
NEP	Noise Equivalent Power
NWIR	Near Wave Infrared range
PECVD	Plasma-enhanced chemical vapor deposition
PL	Photoluminescence
PMT	Photomultiplier Tube
QD	Quantum Dot
RHEED	Reflection High Energy Electron Diffraction
SACM	Separate Absorption, Charge and Multiplication
SAM	Separate Absorption Multiplication
SEM	Scanning Electron Microscope
SL	Superlattice

SNSPD	Superconductive Nanowire Single Photon Detector
SPAD	Single Photon Avalanche Diode
SPDE	Single Photon Detection Efficiency
TAC	Time to Amplitude Converter
TCSPC	Time Correlated Single Photon Counting
TE	Thermo electrically cooling
TEM	Transmission Electron Microscopy
TES	Transistor Edge Sensor
TLM	Transmission line method
TOF	Time of flight
UV	Ultraviolet
XRD	X-ray diffraction

List of Publications

The work carried out in this thesis resulted in the following publications.

Papers published in peer reviewed Journals

• **S. Butera**, R.T. Moug, P. Vines, G.S. Buller, and K.A. Prior. (2014). Direct growth of ZnSe and CdSe on (100) InAs substrates. *Physica status solidi (c).*

• R.T. Moug, **S. Butera**, P. Vines, I. Sandall, C.H. Tan, M. Tamargo, G.S. Buller, and K.A. Prior. MBE growth and characterization of II-VI compounds for InAs device passivation. *In Preparation.*

• R.T. Moug, **S. Butera**, P. Vines, R.E. Warburton, G.S. Buller, and K.A. Prior. Optical and structural properties of MBE grown CdMgSe on InAs. *In Preparation.*

• **S. Butera**, P. Vines, I. Sandall, C.H. Tan, and G.S. Buller. LIDAR ranging experiment with wavelengths up to 2.4 μm using InAs APD in linear mode operation. *In Preparation.*

Peer reviewed Conference papers

• **S. Butera**, P. Vines, R.T. Moug, K.A. Prior, and G.S. Buller. Passivation of low noise InAs avalanche photodiodes using II-VI molecular beam epitaxy overgrowth.18th International Conference on Molecular Beam Epitaxy, September 2014, Flagstaff, Arizona

• **S. Butera**, P. Vines, R.T. Moug, K.A. Prior, I. Sandall, C.H. Tan, and G.S Buller. Passivated InAs mesa photodiodes for infrared detection. Photon14, September 2014, London, UK.

• R.T. Moug, **S. Butera**, P. Vines, G.S. Buller, and K.A. Prior. Direct Growth of ZnSe and CdSe on (100) InAs substrates. 16th International Conference on II-VI Compound and Related Materials. September 2013, Nagahama, Japan.

• **S. Butera**, R.E. Warburton, P. Vines, I. Sandall, P.J. Ker, C.H. Tan, and G.S. Buller. Towards Single Photon Avalanche Diode detectors using narrow bandgap InAs. Photon12, September 2012, Durham, UK.

Chapter One

1. Introduction

1.1 Light and its properties: historical overview

The nature of light has been the subject of critical discussion for thousands of years. In 1801 Thomas Young used an interference experiment to demonstrate the wave nature of light and measured its wavelength [1]. Further evidence for its wave-like behaviour are the reflection, refraction, and diffraction phenomena. As an electromagnetic wave, the light is characterized by amplitude and frequency, with a velocity *c* in vacuum. Figure 1.1 shows the electromagnetic spectrum from γ-rays to long wavelength radio waves, with the visible region from 400 (blue) to 700 (red) nm.

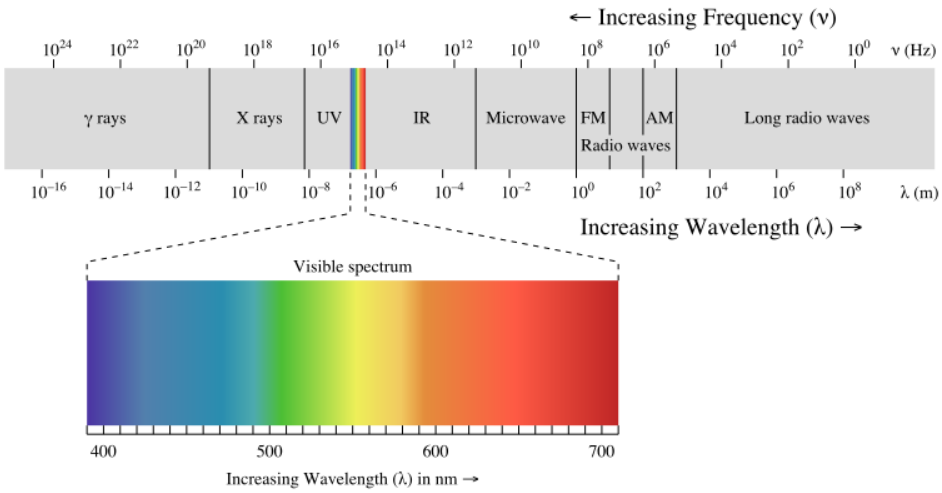

Figure 1.1 *Schematic of the electromagnetic spectrum. Figure taken from [2].*

Albert Einstein, in 1905 [3], stated that, in particular circumstances, the light behaves as if its energy is concentrated in localized particles, called photons. The energy of every photon is given by

$$E = h\nu = \frac{hc}{\lambda} \tag{1.1}$$

where *h* is Planck's constant, ν, λ and *c* are frequency, wavelength and speed of light respectively.

The idea that the light ray can be described as a beam of particles appeared initially to be at odds with the evidence of wave propagation, so at first it was treated with caution. While in the wave theory the energy is spread throughout the wave, in the photon theory it is concentrated in a particle. In 1916, Millikan tried to verify Einstein's equation experimentally, studying the photoelectric effect. Even if his results confirmed Einstein's predictions, he was suspicious about this particle theory and concluded his studies saying, "…it seems at the present to be wholly untenable" [4]. A few years later Compton [5], obtained further experimental evidence of this particle-like behaviour of light, studying what would be called the Compton effect. He analysed the interaction of an X-ray beam with a graphite target and observed a wavelength shift in the beam. The Compton shift can be easily explained if the light is thought of as photons: during the interaction the photons transfer part of their energy to the electrons in the target resulting in a scattered beam with lower energy, and so a longer wavelength, with respect to the original light beam.

For many years, scientists tried to prove that light behaved either as a particle or wave. The experimental evidence was that the light could be a beam of particles or a wave depending on the experiment performed.

Only in the 20th century, wave-particle duality became accepted as a description of light, where light phenomena can only fully be described by considering both the photon description and wave propagation [6]. Nowadays the detection of light and in particular the detection of single photons remains a fascinating area for research and applications.

1.2 Detection of infrared radiation and emerging infrared applications

The ability to efficiently detect light in photon-starved regimes is becoming increasingly important for many applications at all wavelengths, but particularly in the infrared as discussed in paragraphs 1.2.1 and 1.2.2. The challenge for researchers is to develop detectors that can efficiently convert light into electronic signals, without increasing the noise of the signal. Light detection has a fundamental role in consumer technology used in our everyday life, e.g. digital cameras, fibre optics, as well as to applications emerging in areas such as security, medicine, environmental science and terrain mapping. Less obvious, but important examples include gas sensing, defence/geoscience ranging, clinical thermography, rocket plume detection, and in

manufacturing monitoring which all rely on detection of near-IR wavelengths. This is the subject area of this thesis - optical measurement of low light levels at wavelengths greater than 1.6 μm.

1.2.1 Laser Ranging

Laser imaging detection and ranging (LIDAR) techniques are commonly used in the study of solid or gas targets. These techniques have been used to study profiles of gases in the atmosphere or mapping the earth surface, and can be adapted to include satellite-borne systems for global coverage [7]. The basic set-up of a LIDAR system can be conveniently divided into three subsystems: the transmitter, the receiver, and the detector. In Figure 1.2, a block diagram of a generic LIDAR system, shows how these subsystems fit together.

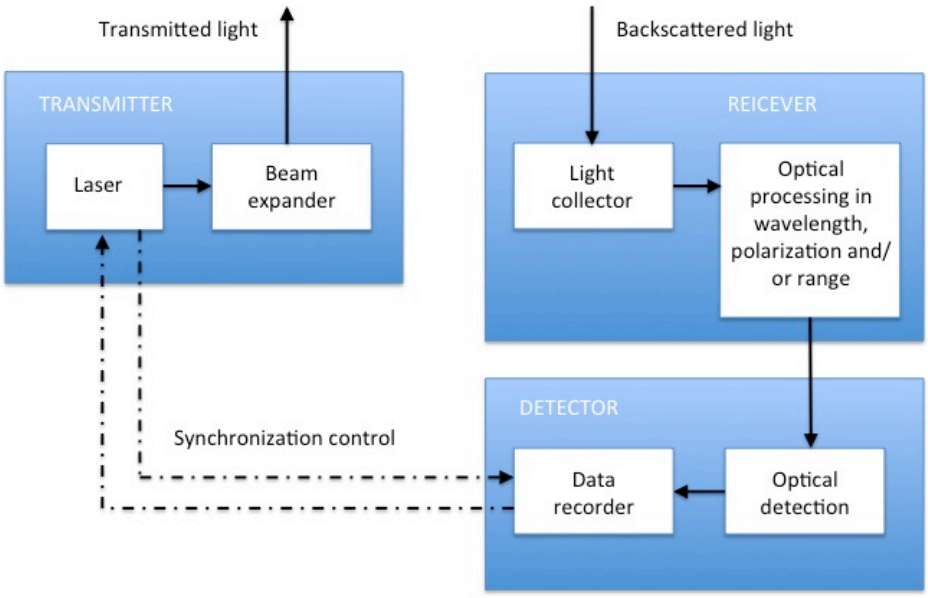

Figure 1.2 *Schematic diagram of a LIDAR system taken from [7]. The transmitter generates an optical pulse, an expander reduces the divergence of the laser beam before the transmission into the atmosphere. A receiver collects and processes the backscattered light and then directs it to a photodetector.*

In the transmitter unit, a laser generates optical pulses, and then a beam expander is usually used to control divergence of the light beam before it is directed into the atmosphere. The receiver collects photons backscattered from the target. It is usually

followed by an optical analysing system which, depending of the application, selects specific wavelengths or polarization states out of the collected light. The selected radiation is directed onto a detector, where the received optical signal is converted into an electrical signal.

LIDAR systems can be divided into two different configurations according to the arrangement of the transmitter and receiver: monostatic and bistatic. In the monostatic LIDAR the transmitter and the receiver are co-located, while in the bistatic system the source and the receiver may be separated by a large distance. These configurations are shown in Figure 1.3.

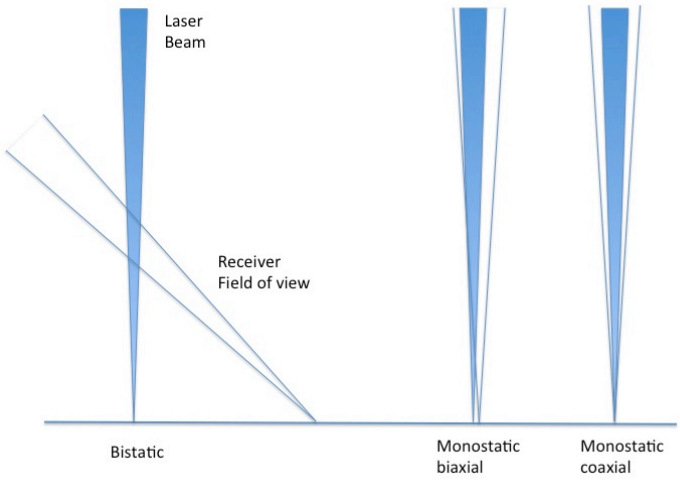

Figure 1.3 *Geometric arrangements of the LIDAR transmitter and receiver. In the bistatic case, the receiver is some distance from the transmitter, while in the monostatic case the receiver and transmitter are co-located. The monostatic configuration can be classified as coaxial when the receiver axis is in perfect alignment with the transmitter axis and biaxial when the receiver axis is slightly out of line with the transmitter axis.*

In the simplest form, the detected LIDAR signal can be written as

$$P(d)=KG_m(d)S(d)T(d) \tag{1.2}$$

The power P received from a distance d is made up of four factors. The first factor, K, is dependent upon the LIDAR system (as, for example, the system signal collection efficiency, detection efficiency, lens and filter transmittance, etc.), the second, $G_m(d)$, describes the range-dependent measurement geometry. These two factors are determined by the LIDAR set-up and can thus be controlled. $S(d)$, the backscatter coefficient at distance d, refers to the capacity of the target to scatter light back into the direction of the source. $T(d)$ relates to the absorption of the radiation from the atmosphere. Both $S(d)$ and $T(d)$ are target and environment dependent [8].

According to the measured characteristics, LIDAR can be divided into four subsections: time of flight, active triangulation, amplitude modulation and frequency modulation. Time of flight (TOF) is the LIDAR technique commonly used in single photon detection. TOF refers to the time it takes for a pulse of energy to travel from its transmitter to an observed object and then back to the receiver. In TOF LIDAR a short pulse of radiation is fired at the target. The time that the light takes to arrive and come back from the target is measured. The distance the light beam travels can then be calculated by multiplying the known velocity of the light by the time light takes to travel the distance. In this case, the measured time is representative of the round-trip distance and so has to be halved to give the actual range of the target. The accuracy of the system is dependent on the acquisition time: the more pulses detected; the more distance data can be collected in a histogram, increasing the resolution of the system.

1.2.1.1 Three-dimensional imaging using Time of flight laser ranging

Measuring the round trip time between a light pulse emission and the return of the pulse resulting from its reflectance off an object, it is possible to obtain details of the target and estimate its position [9]. Usually a high laser power is used in TOF LIDAR, which is particular true for analysing objects placed at long distances from the transmitter. Use of a high laser power helps to obtain a clear pulse back from the target, but on the other hand it can contribute to eye safety concerns. For this reason TOF ranging using single photon detection is becoming a field of increasing interest. It gives high sensitivity and the capability of low average power operation. Several groups have performed ranging experiments using single photon TOF experiments with targets positioned at kilometre scale distances. A response from a laser aimed at objects such as trees, cars and people can be detected allowing the calculation of the object's position, and details of the object can be

analysed with high depth resolution [10], [11], [12]. In Figure 1.4 the LIDAR scanning of cars and people is presented: on the left the 3D image of a Chevrolet van is shown with a depth accuracy of under 3 cm and 1 cm x and y resolution taken from a distance of 60 metres using a 532 nm wavelength micro-chip laser and an array of Si Single-photon avalanche diodes (SPADs) (4 × 4); on the right a 3D image of a person is shown with mm-scale depth accuracy, cm-scale x and y resolution taken from a range of 910 metres using a 1560 nm laser and superconductive nanowire single photon detector.

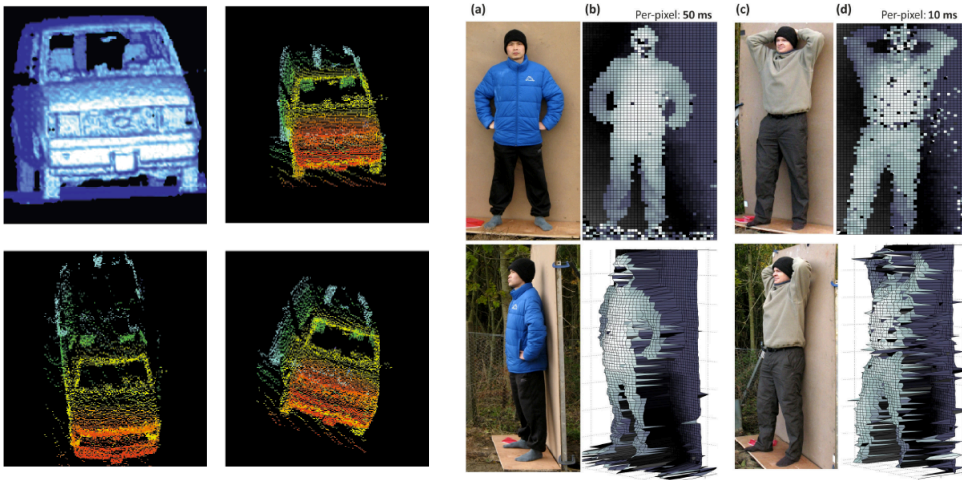

Figure 1.4 *On the left, single 128 × 128 pixel image recorded with the LIDAR looking at the front and right side of a Chevrolet van from a distance of 60 m, figure taken from [10]. On the right, examples of close-up photographs of human targets and corresponding depth profiles from a distance of 910 m, figure taken from [12].*

Most of the three-dimensional range imaging experiments performed use an operating wavelength at and below 1.55 μm. Recently, research has been conducted at longer wavelengths; in particular above 1.6 μm. At these wavelengths there is a lower solar background, the main source of noise in this application, as it is shown in Figure 1.5. The scattering of the illumination beam by small particulates is also reduced by moving to longer wavelength, increasing the utility of the LIDAR approach.

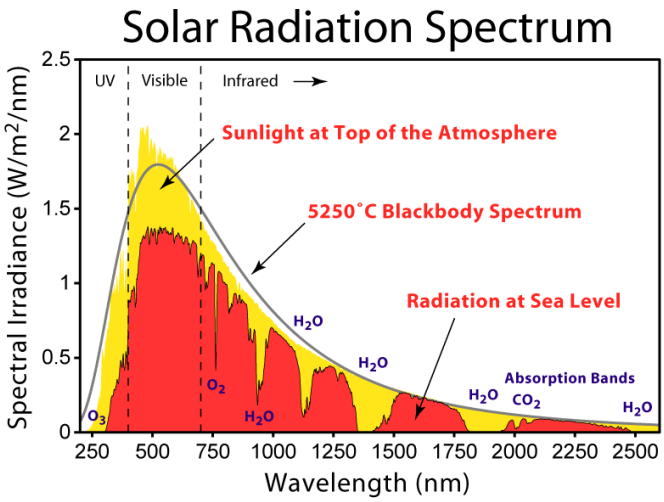

Figure 1.5 *Solar irradiance spectrum above the Earth's atmosphere (yellow curve) and at sea level (red curve) for wavelengths from 250 to 2500 nm. At sea level the spectral irradiance is lower because of the absorption of different molecules. Figure taken from [13].*

Very few papers have been published on ranging in the Mid Wave infrared (MWIR) range. One of the few in the literature is by Diagne *et al.* which showed three-dimensional range imaging with a 30 cm depth resolution at 20 m using an antimonide-based Geiger mode avalanche photodiode (APD) array and 2 μm illumination [14]. In this work the authors developed a 32 × 32 array of mesa diodes 30 μm in diameter and with a 100 μm pitch. The APDs are grown by MBE and have a separate absorption-multiplication (SAM) design that consists of a lattice-matched $In_{0.15}Ga_{0.85}As_{0.17}Sb_{0.83}$ long wavelength absorber and $Al_{0.55}Ga_{0.45}As_{0.05}Sb_{0.95}$ multiplication layer. The breakdown voltage map of the array shows less than 1 V of variation in breakdown voltage and an average dark count rate of 1.5 kHz with an overbias ranging from 3.1 to 4.1 V at 77 K. LIDAR experiments were carried out with a pulsed laser with up to 10 kHz repetition rate and at least 2 μJ pulse energy and 400 ps width at a wavelength of 2 μm. The system's time resolution was 2 ns, which corresponds to approximately 30 cm in range because the time of flight measured is round-trip time. The demonstrated three dimensional array imaging capability is shown in Figure 1.6. Research is ongoing to develop and integrate new detector technologies, such as the one just described, which detect at wavelengths where the solar emission is negligible.

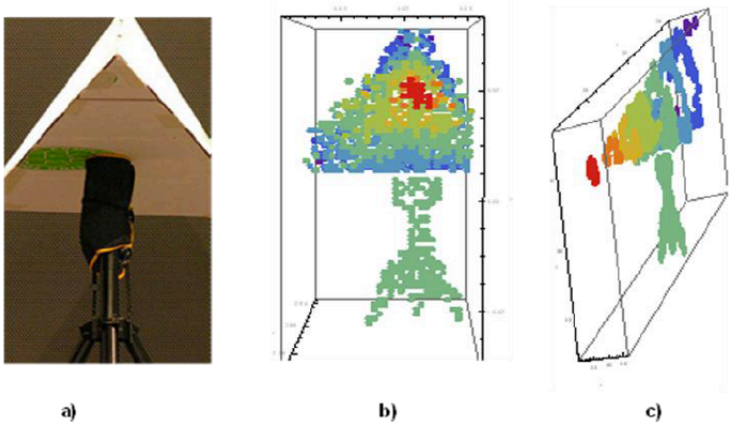

Figure 1.6 *LIDAR demonstration images obtained using a 32 × 32 mesa geometry* $In_{0.15}Ga_{0.85}As_{0.17}Sb_{0.83}$ */*$Al_{0.55}Ga_{0.45}As_{0.05}Sb_{0.95}$ *array at a wavelength of 2 μm. The imaged target consists of a pyramid mounted on a tripod at a range of approximately 20 m. The photo of the target is shown in (a), while the LIDAR 3D images of the target are shown in (b) and (c) with different angle of view. Figure taken from [14].*

Recently, LIDAR has been used over a very broad spectral range for mapping unknown areas of the earth or monitoring the enemy's movements in a military environment and is becoming a field of great interest [15]. For these applications the use of an operation wavelength where the solar background is low is very attractive.

1.2.1.2 Gas sensing with LIDAR

LIDAR technologies are not only useful in defence and geosciences, which typically rely on the probing of solid targets; they are also important for tracing gas profiles in the atmosphere, for example for monitoring greenhouse gases.

LIDAR can be used to study hurricanes [16], volcanic eruptions [17], desert dust [18], and forest fire smoke [19]. Greenhouse gas profiling is an important tool for environmental scientists for use in climate change analysis and prediction. Every molecule has a particular signature given from its absorption spectrum, so by studying the response at a particular wavelength it is possible to study the concentration of particular gases as a function of height, for example. By positioning a transmitter and a receiver, it is possible to probe the atmosphere and to gain information about the composition of the atmosphere in all directions as a function of time and use this information in models of atmospheric conditions [8].

High sensitivity detection of atmospheric gases is possible with a basic LIDAR technique called Differential Absorption LIDAR (DIAL). The DIAL technique is based on the same principal as TOF but with two different wavelengths involved; it uses single absorption lines or broad absorption bands of gases for analysing the atoms or molecules of interest in the atmosphere. In a DIAL system two laser pulses of slightly different wavelengths - one in the absorption window of the molecule under study and one just outside the absorption window (the reference signal) - are used to estimate the effect of the absorption and so the concentration of a particular molecule in the atmosphere. Figure 1.7 shows the DIAL system mechanism.

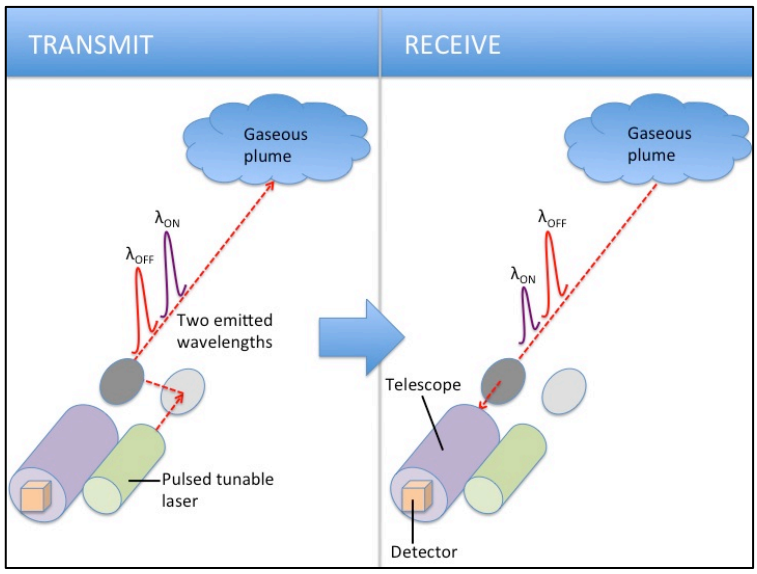

Figure 1.7 *Schematic diagram of a DIAL system mechanism. A pulsed tunable laser sends two laser pulses of the same amplitude but slightly different wavelengths -λ_{ON} in the absorption window of the molecule under study and λ_{OFF} just outside of the absorption window (the reference signal) - through to an optical system that directs the beams to the gaseous plume in the atmosphere. The two different wavelengths are reflected from the gaseous plume and are collected by a telescope which focuses the radiation on to the detector. By comparing these returning pulses it is possible to estimate the effect of the absorption and so the concentration of a particular molecule in the atmosphere.*

DIAL systems in the UV, visible and IR have been developed for Ozone and industrial emission [20], [21], [22]. In the MWIR range gases such as CO, CO_2, CH_4, N_2O and O_3 can be monitored.

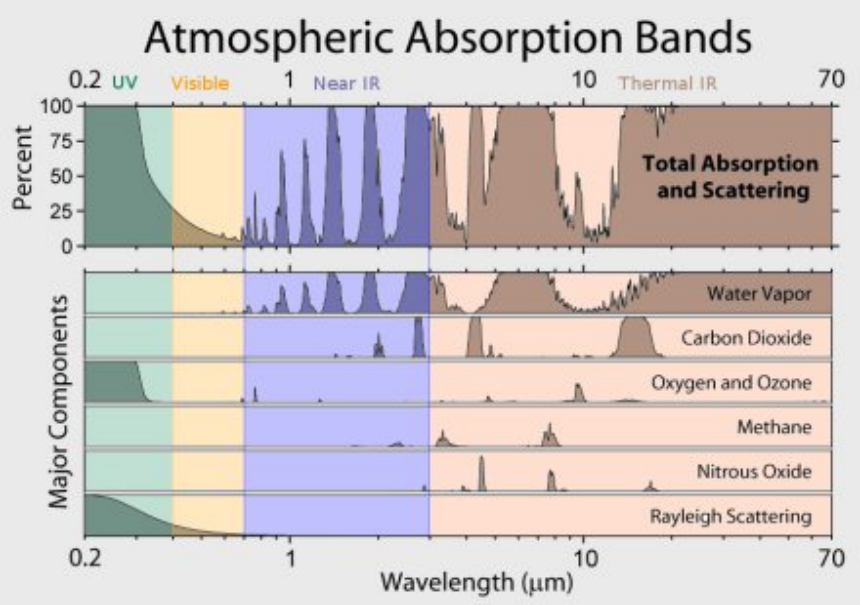

Figure 1.8 *Atmospheric absorption band diagram for some common atmospheric gasses at wavelengths between 0.2 and 70 μm. CO_2, CH_4, N_2O and O_3 show significant peaks in the MWIR range between 2 and 3.5 μm. Figure taken from [23].*

In Figure 1.8 CO_2, CH_4, N_2O and O_3 show distinct absorption bands in the IR above 2 μm. The deep absorption peaks for such atmospheric gases and also CO, and their band intervals in the range between 2 and 3.5 μm are listed in Table 1.1.

Gas	Centre wavelength of the absorption peak (λ(μm))	Band interval (λ(μm))
CO_2	2.7	2.9-2.6
	2.0	1.9-1.7
O_3	3.3	3.3-3.2
CH_4	3.3	4-3.1
	2.2	2.5-2.2
N_2O	2.87	3.0-2.86
CO	2.34	2.4-2.3

Table 1.1 *Summary of the absorption peaks CO_2, CH_4, N_2O, O_3 and CO and their band intervals at wavelengths in the range between 2 and 3.5 μm. Table taken from [24].*

At present use of DIAL for the detection of greenhouse gases is an important area of research. Greenhouse gases are assumed [25] to be the major cause of "global warming" - increase of the average surface temperature of the Earth. Greenhouse gases allow short wavelength radiation to reach the Earth, whilst infrared radiation from the planet's surface is captured and re-radiated back to Earth by these gases.

Technology has been developed for LIDAR gas sensing experiments to improve the performance of the transmitter and receiver. Further development is needed for atmospheric profiling, especially in the band between the wavelengths of 2 and 3.5 μm [26].

1.2.2 Thermometry

Thermometry is the study of measuring the temperature of a system. Radiation thermometry at wavelengths longer than the near infrared could be a very useful technique for applications such as medical diagnostics, rocket plume detection and manufacturing process monitoring.

Black body radiation from an object at a particular temperature is emitted according to Planck's law. Figure 1.9 shows the spectrum of black body radiation at different temperatures.

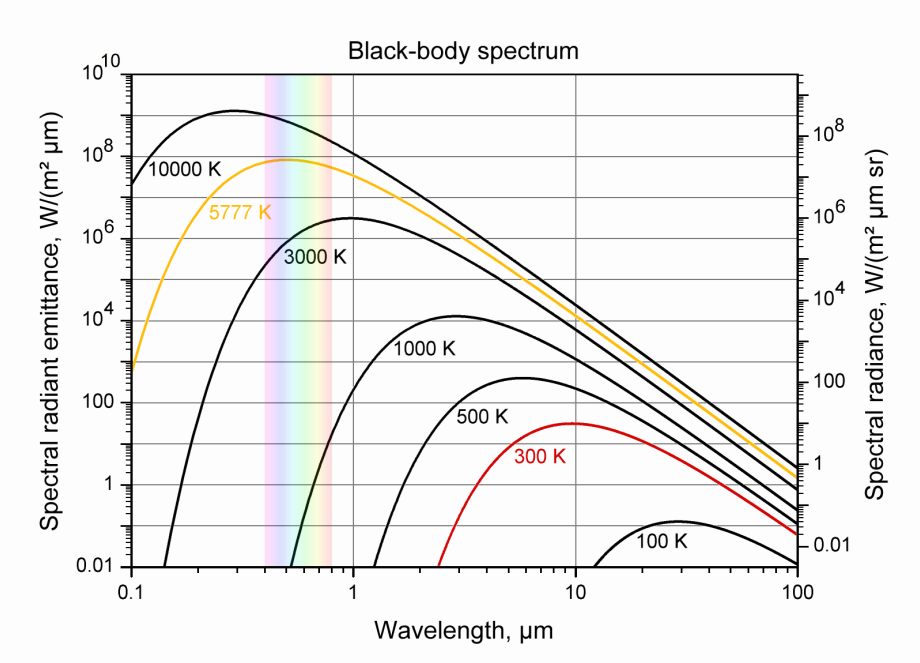

Figure 1.9 *Black-body spectral radiant emission as a function of wavelength at a selection of surface temperatures. The red and yellow lines are the radiation spectrum emitted from an object at approximately room temperature and from the Sun respectively. Figure taken from [27].*

1.2.2.1 Thermography for human diagnostic techniques

Humans have a temperature around 310 K, so assuming they can be treated as blackbody sources, they emit radiation with an emission peak around 9 µm. Thermography detects this emitted IR radiation and relates this to skin temperature, reporting anomalous temperature changes making it useful for early pre-clinical diagnosis and control during treatment of homeostatic imbalances. Thermography is a non-invasive, non-contact method and does not involve external radiation, resulting in a very safe technique. Presently thermography systems use LWIR cameras which detect at the emission peak for radiation emitted from the human body. However recent studies, using the rapid change of the spectral radiant emittance as a function of source temperature close to the lower cut off wavelength, demonstrate the advantage of analysing the human body radiation near 2 µm wavelength. Zhou *et al*. [28] demonstrated the potential of InAs photodiodes for thermometry measurements at temperature below 40 °C. They detected a blackbody temperature of 37 °C with a signal to noise ratio as high as 5.5.

Some of the most common applications of thermography are breast pathologies and the diagnosis of muscle strains, spinal injuries, inflammations and nerve problems and arthritis within vertebrae [29], [30]. In breast pathologies such as breast cancer it is not used as a screening tool (where other techniques such as mammography are used), but it can be a very useful technique for monitoring the cancer during its treatment [31]. Metastatic tumours create heat due to two separate processes. The first process is correlated to the metabolic activity of the tumour tissue and can be compared with the temperature of tissue adjacent to it, and in the opposite breast; while the second one concerns the production of a chemical, which promotes the development of blood vessels supplying the area where the cancer resides. Digital infrared imaging can detect this difference in temperature and make an image.

1.2.2.2 Rocket plume detection

Remote sensing can be used for the characterisation of terrestrial combustion phenomena such as forest fires and volcanic eruption or for civil and military applications. Detecting environmental combustion is suited for use in battlespace characterisation. Missile plumes, explosive fireballs and muzzle flashes emit strongly in the visible and the IR spectral regions and may be passively observed from airborne and space-based sensors [32]. A strong infrared radiation signature is also given by the exhaust chemicals from solid propellant rockets: they consist of high temperature gasses and solid particles which emit IR radiation. Solid particles can play a very important role in the propellant rockets: Al_2O_3 particles, for example, have a heating effect on the rocket gas flow, which greatly increases the temperature and so the infrared intensity of the plume and overall the energy available for the propulsion [33]. The study of the mechanism of the IR radiation emission, giving information about the temperature and so the energy rate produced by the rocket combustion chamber, can help to improve the propellant chemical formula and how it is stored in the rocket. Figure 1.10 shows the infrared plume temperature for two different propellants using a conical nozzle.

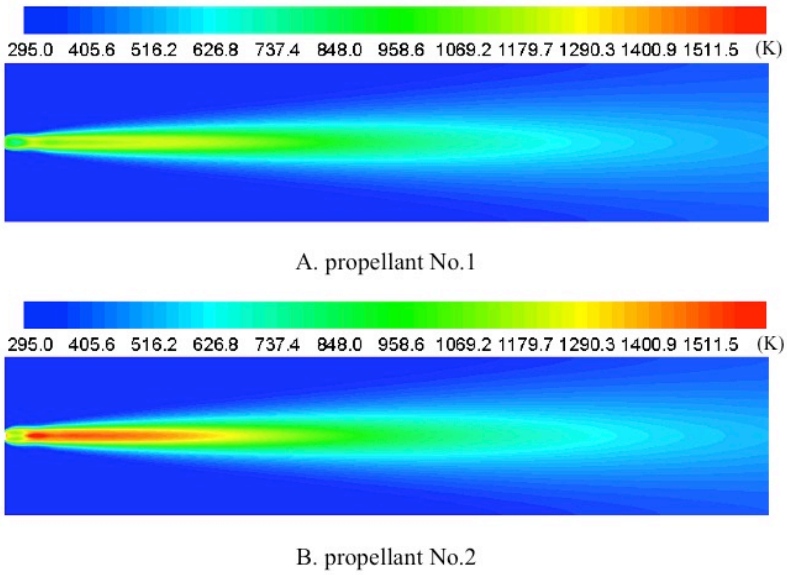

Figure 1.10 *Plume temperature for two different propellants, figure taken from [33]. Propellant 2, the one with Al_2O_3 particles, has higher plume temperature.*

In Figure 1.10, the plume temperature is higher for propellant 2, the one with Al_2O_3 particles, with respect to propellant 1. The authors allocate this result to two causes: propellant 2 has higher energy characteristics, which leads to higher temperature of the combustion chamber gas; the Al_2O_3 particles with high temperature can heat up the plume, and then further improve the flow field temperature.

1.2.2.3 Industry manufacturing and civil monitoring using thermometry

The monitoring of the condition of civil infrastructure or industrial equipment and associated processes is a very important area where IR thermometry is commonly used to prevent unplanned failure, reducing the associated hazard [34]. The identification of damage as change to the material or geometrical/electrical property can prevent major accidents that can damage human life or induce huge economic losses. IR thermometry can be used as a powerful non-destructive tool for detecting material alterations and therefore contributing to the quality control of civil infrastructure or industrial processes. Surface temperature is a useful parameter that can indicate the structural health of an object. So measuring the temperature of a body using infrared thermography to provide its thermal image can discover faults indicated by abnormal temperature distributions

allowing preventative maintenance before failure.

IR thermography has been successfully utilized for several applications such as assessing robustness of civil structures [35], inspection of electrical equipment [36], monitoring of plastic deformations [37], inspection of tensile deformation [38], evaluation of fatigue damage in materials [39], weld inspection [40].

Figure 1.11 is an example of a thermal image produced by an oxidized connection of a miniature circuit breaker.

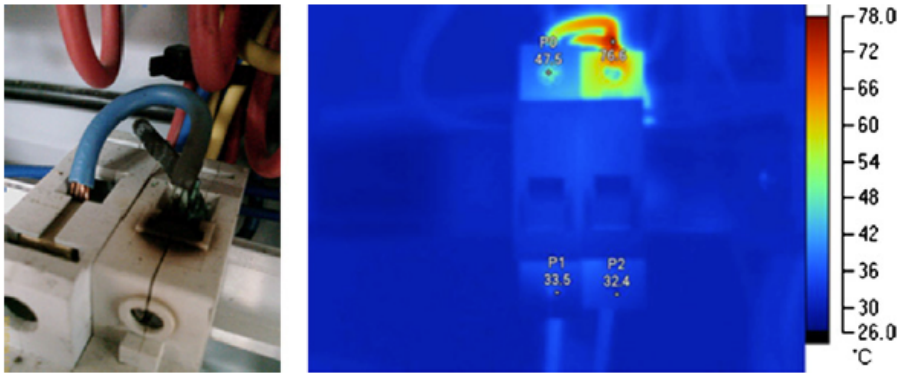

Figure 1.11 *Oxidized connection of a miniature circuit breaker (on the left) with its corresponding infrared image (on the right), figure taken from [36]. The different colours in the infrared image correspond to different temperatures as shown in the temperature scale (°C).*

1.3 Detection system overview

As described in section 1.2, infrared detection is essential for photonics applications which scan the Earth's surface, to check the manufacturing steps in industrial processes, to analyse the composition of the atmosphere and monitor the effect of medicine treating a patient. In many of these applications, the optical signal on the detector is very weak either for safety reasons or due to attenuation, so single photon detectors are often needed. When a photon is absorbed in a bulk semiconductor photodetector, an electron-hole pair is created in the crystal and will contribute to the detected photocurrent. Photons with energy greater or equal to the material bandgap can be absorbed causing an electron to be promoted from the valence band to the conduction band. The choice of semiconductor material depends on the detection wavelength range

required by the application. For example, silicon devices are the most mature material system, however Si detectors will have a cut off wavelength of 1.1 μm limiting their use to visible and near IR applications. InGaAs and Ge based detectors are often used for applications from 1 μm to 1.7 μm. For longer wavelengths, HgCdTe based detectors are often used [41], [42], [43]. Unfortunately HgCdTe is not easy to grow and process. New technologies are thus required for applications detecting beyond the near IR. For these purposes III-V materials are a possible solution, as will be discussed in Chapter Two. The next part of this Chapter is dedicated to the state of the art of single photon techniques and technology commonly used.

1.3.1 Single photon detection and the Time-Correlated Single-photon Counting technique

In many applications semiconductor photodiode detectors play a very important role. However, in some case, as the ones mentioned before, such detectors lack the necessary sensitivity in the infrared region, in particular. In photon-starved applications, where the optical signal is very weak, conventional semiconductor photodiodes have a limited sensitivity, and other technologies are often more appropriate - single photon detectors are needed. They have the capability to produce a measurable, macroscopic output pulse after the detection of a single photon: they can produce many thousands of electrons from the single electron-hole pair created by absorption of a single photon.

A well established and common technique coupled with single photon detectors is the Time-correlated-single-photon-counting (TCSPC) [44]. It was initially used in time-resolved fluorescence and photoluminescence, but nowadays it is becoming increasingly important in applications that involve fast optical signals and low light sensitivity, as for example LIDAR. TCSPC operates by measuring the arrival of single photons (which gives a STOP signal pulse) with respect to a reference signal (the START signal pulse), usually given by an external clock. A typical TCSPC set up is shown in Figure 1.12.

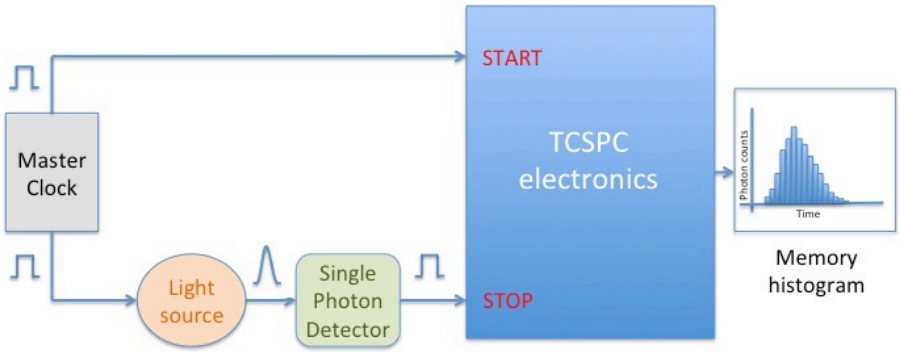

Figure 1.12 *A typical TCSPC set up. A master clock sends two pulses simultaneously, one (the reference signal) triggers the TCSPC electronics that start the timing, while the other triggers the light source. A single photon detector detects the emitted photon and sends a stop pulse to the TCSPC apparatus. The time between the photon arrival and the reference signal is measured and recorded in a histogram.*

The time measured for one START-STOP sequence is recorded in a histogram. TCSPC is a statistical method so a high measurement repetition rate is typically used in order to accumulate a sufficient number of photon events for statistical data precision. For statistical reasons it is important to ensure that the probability of detecting a photon for clock period (between the START and the next START) must be much less than unity. Multi photon events will cause a distortion in the histogram. This phenomenon is called pulse pile-up – there is a higher probability of observing photon counts in the early part of the timing window with respect to the latter part, altering the shape of the histogram. To avoid this problem the TCSPC STOP rate has to be less than 10% of the START rate. Figure 1.13 shows an experimental TCSPC histogram build up from $^1O_2$ time-resolved luminescence data taken by Gemmell *et al*. [45].

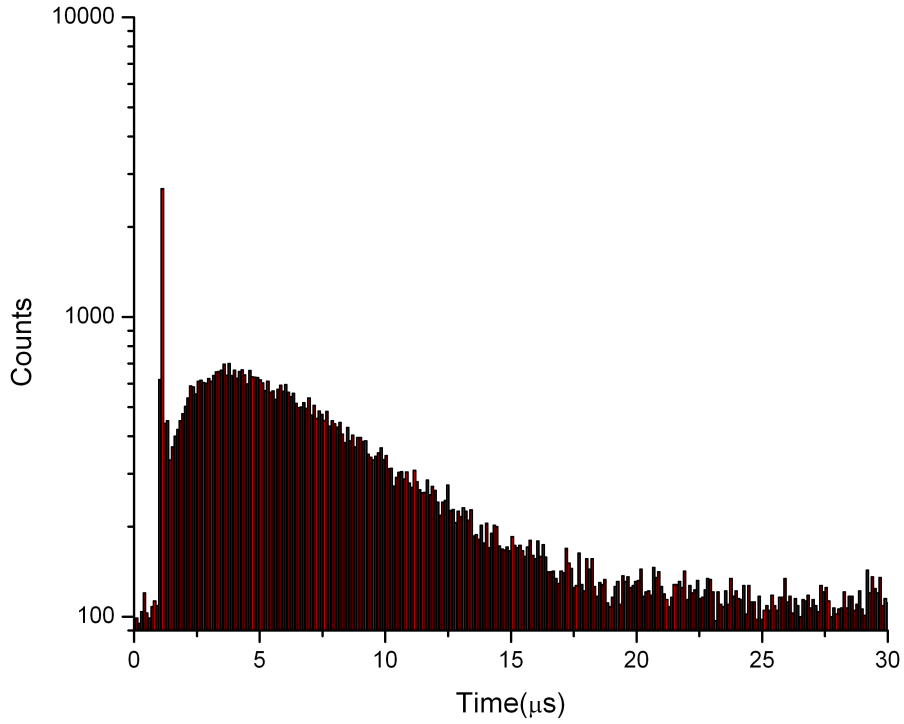

Figure 1.13 *Typical TCSPC histogram: every time a photon event is detected a count is added to the corresponding time bin. The histogram shown represents the 1270 nm wavelength time-resolved luminescence measurements of* $^1O_2$*. Data taken by Gemmell et al. [45]***.**

The main components of the TCSPC electronics are the constant fraction discriminator (CFD), the time to amplitude converter (TAC) and the analogue to digital converter (ADC). The CFD evaluates the pulse height of the incoming START and STOP pulses, allowing only pulses above a given threshold to be recorded. In this way the small amplitude noise pulses are eliminated. The ADC converts the TAC output to a digital form, suitable to be binned into a timing histogram.

1.3.2 Single photon key figures of merit

The key parameters for single-photon detectors are dark count rate (DCR), single photon detection efficiency (SPDE) and noise equivalent power (NEP). The DCR quantifies the rate at which the detector is triggered from non-photon induced events. Afterpulsing is a contribution to the DCR. Afterpulsing refers to dark counts that originate from carriers that were trapped in deep energy levels in the avalanche region during previous impact ionisation events and are later released, causing further avalanche events. The SPDE is the probability that, assuming the time between photon arrivals is greater than the dead-time of the detection system, an incident photon generates a measurable output pulse. The noise equivalent power

(NEP) is the measure of the detector sensitivity and is the minimum optical power that can be detected. The lower the NEP, the more sensitive the detector. It is defined as:

$$NEP = \frac{hc}{\lambda SPDE}\sqrt{2DCR} \tag{1.3}$$

where h is Planck's constant and λ is the wavelength of the incident photon.

Other important parameters that need to be taken into account in a photodetector include the time interval between the photon arrival and the detector output pulse - the timing jitter- and the gain [46], [47].

1.3.3 Single photon detectors

The most common single photon detectors are listed in the following sections.

1.3.3.1 Photomultiplier Tube

A photomultiplier tube (PMT) is a vacuum device that is able to convert low-light levels to electrical signals [48].

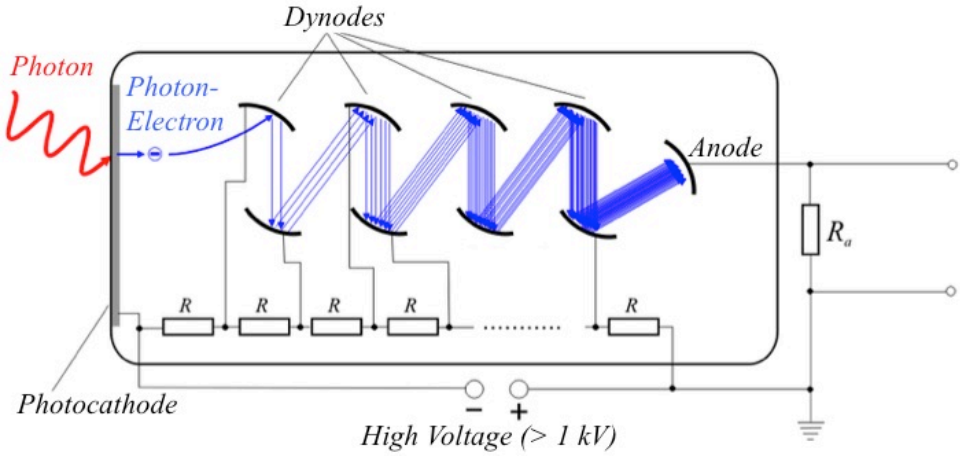

Figure 1.14 *Schematic representation of PMT taken from [49].*

As shown in Figure 1.14, the PMT consists of a photocathode, typically deposited as a thin layer on the inner wall of the entrance window of the photomultiplier, which converts the incident radiation to electrons using the photoelectric effect. Within the vacuum tube, a set of electrodes, known as dynodes, are arranged so that every dynode has a lower potential than

the following one. When a photon is absorbed, an electron is emitted from the photocathode via the photoemission process and then accelerated in the electric field to the first dynode. The electron has sufficient kinetic energy that on collision with the first dynode, it generates a number of low-energy electrons via secondary emission. These secondary electrons are accelerated to the next dynode where this secondary emission process is repeated. This process is repeated for a number of dynodes, creating a high level of multiplication.

The gain, defined as the number of electrons produced per photon absorbed, is given by:

$$G=\delta^{b} \tag{1.4}$$

where δ is the secondary electron emission factor of the dynodes and b is the number of dynodes. Ideally the device should give a constant gain for each electron at a particular energy that enters the dynode system, but clearly this is not possible because of the statistical nature of the secondary emission process.

The gain can be optimized using different dynode configurations. The most common are: Venetian blind, box and grid, linear focused and circular cage focused as shown in Figure 1.15

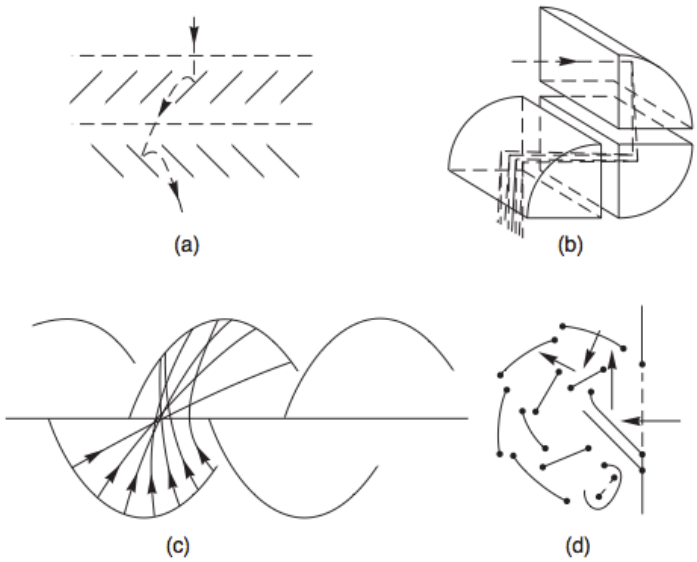

Figure 1.15 *Schematic representations of four different dynode configurations: a) venetian blind, b) box and grid, c) linear focused and d) circular cage focused. Typical trajectories of an electron through the systems are also shown. Figure taken from [50].*

Typically, PMT gain is in the range 10^4 to 10^7. Another important parameter in PMTs is the jitter. This is associated mainly with the variation in transit time of the electrons travelling from the photocathode to the anode (known also as transit time spread); this usually results from the initially different velocity of photoelectrons and their different emission angles resulting in different electron paths. The path of the electrons that are emitted along the axis of the dynode is much shorter than those taking a more off-axis route. This effect causes a difference in the transit time associated with the geometry of the system. The fluctuation in transit time from the cathode to the anode strongly influences the device timing jitter, which is around 1 ns for PMTs. To try to reduce the jitter, cathodes with spherical distributions of electric fields can be used to further accelerate the electrons that are emitted outside the axis of the dynode. Another disadvantage of PMTs is their poor SPDE. NWIR-PMTs have been reported from Hamamatsu with 2% SPDE at 1500 nm, a DCR of 10^5 Hz and gain of 10^6 at -60 ˚C using InP/InGaAs as photocathode material [51]. Moreover, because of the large number of dynodes required, they can be mechanically unstable and require biases as high as 1 kV. They also cannot easily be used for small volume applications due to their large dimensions but, having a larger active area than the other single photon detectors, they have a very high photon collection efficiency without external optics. Typical PMT light sensitive surfaces are 30-50 mm in diameter, but they can be up to 200 mm or even larger.

1.3.3.2 Microchannel plates

A microchannel plate (MCP) is a device that operates with principles similar to a PMT.

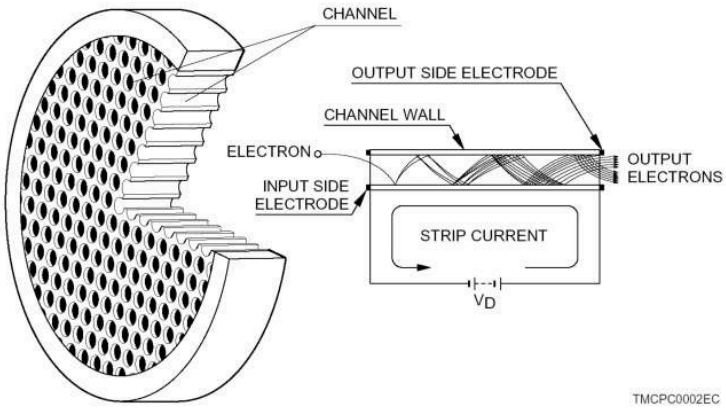

Figure 1.16 *MCP schematic diagram. A 2D array of thin glass capillaries are arranged in a disc. The wall of every capillary is coated with a photo emissive material and biased at each end so as to create a device with a continuous dynode. Figure taken from [48].*

It consists of a 2D array of thin glass capillaries (with internal diameter ranging from 6 to 20 μm each) arranged in a disc, as shown in Figure 1.16 [48]. The wall of every capillary is coated with a photo-emissive material and biased at each end. Thus it can be described as a device with a continuous dynode rather than a series of discrete dynodes. When an electron is accelerated inside a channel, it is able to create secondary electrons after a collision with the channel's wall. These secondary electrons can start further collisions along the length of the channel giving an exponential multiplication. As a strong electric field is applied almost parallel from the photocathode to the anode, the emission angle distribution and the initial velocity of photoelectrons, in contrast to PMTs, can be ignored. Moreover, since a MCP is used instead of conventional dynodes, the secondary electrons' transit times are very short, allowing an improvement in the transit time spread giving a jitter in the order of 20-30 ps. MCPs require voltages as high as 1 kV and have detector figure of merit values that are similar to PMTs. As with PMTs they are large in volume so they cannot be used for small volume applications. The main advantage of this type of detector is the 2D configuration that makes them suitable for image intensifiers or LIDAR systems.

1.3.3.3 Quantum dot based detectors

Quantum dots (QD) are man-made 3D "droplets" of material that can contain charges ranging from a single electron to a collection of several thousand. Their typical dimensions range from a few nanometres to a few micrometres, and their size, shape and interactions can be precisely controlled through the use of advanced nanofabrication technology. The physics of quantum dots shows many parallels with the behaviour of naturally occurring quantum systems in atomic physics. As in an atom, the energy levels in a quantum dot become quantized due to the electrons confinement. These artificial atoms can be very useful as a single photon source or a single photon detector.

Shields *et al.* [52] demonstrated the first quantum dot single-photon detector using a $GaAs/Al_{0.33}Ga_{0.67}As$ quantum dot field effect transistor – i.e. a field effect transistor (FET) with the gating provided by a QD layer. When a photon is detected, an electron is produced inside the device. The generated electron can be captured by a quantum dot causing a change in the shape of the electric field in the FET. In this way, a measurable change in the current between source and drain can be detected. Kardynal *et al*. demonstrate a detector that presents a detection efficiency SPDE of approximately 0.9% at a wavelength of 650 nm and a temperature of 77 K, resulting in a NEP of $2\times10^{-16}\,WHz^{-1/2}$ [53]. The same quantum dot FET structure was also used for photon number resolving by the same group allowing the detection of 2 or more photons [54]. A similar device was developed by Rowe *et al*. The details of this structure are shown in Figure 1.17. It operates at 4 K reaching a SPDE of 2-3% at a wavelength of 800 nm [55].

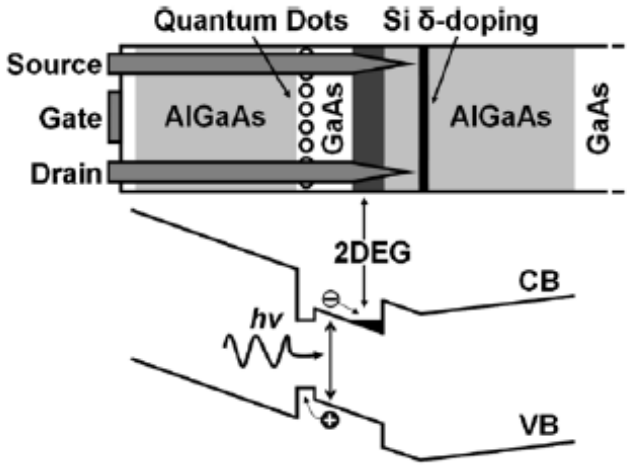

Figure 1.17 *Schematic diagram of a GaAs/$Al_{0.33}Ga_{0.67}$As quantum dot field effect transition developed by Rowe et al. [55]. When a photon is detected, an electron is produced inside the device and captured by a quantum dot causing a change in the shape of the FET's electric field that results in a measurable change in the current between source and drain.*

Another interesting structure is a QD resonant tunnelling diode demonstrated by Blakesley *et al.* in 2005 [56]. A schematic sketch of his band structure is given in Figure 1.18. The black line represents the band structure of the device under forward bias near the resonant condition; the red one is the band structure after photon absorption.

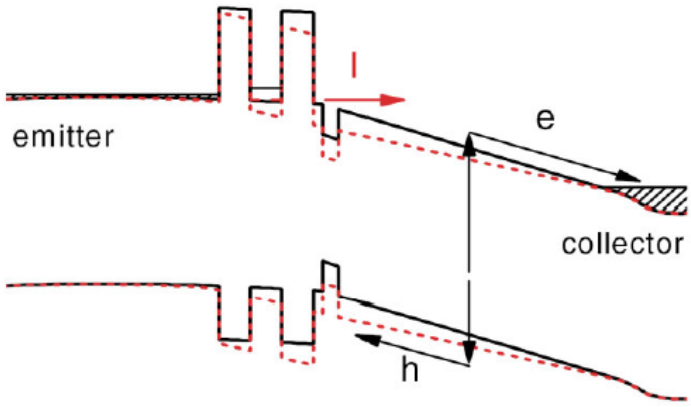

Figure 1.18 *Sketch of a QD resonant tunnelling diode demonstrated by Blakesley et al., figure taken from [56]. The current flows between emitter and collector by tunnelling through the double barrier. When the QD captures a photo-excited hole, the height of the barrier decreases (red dash line), the resonant tunnelling condition changes and a measurable change in current can be detected.*

Figure 1.18 shows that the current flows between emitter and collector by tunnelling through the double barrier. When the QD captures a photo-excited hole, the height of the barrier decreases, the resonant tunnelling condition changes and a measurable change in current can be detected. This device shows a timing jitter of around 150 ns when cooled to 4 K and irradiated with 550 nm wavelength incident radiation. A SPDE of 12.5%, a DCR of 2×10^{-3} s^{-1} and a NEP of 2×10^{-19} $WHz^{-1/2}$ was measured. In this type of device the dark counts are generated from electrons that escape from the QD. At this low temperature thermally activated escape is highly improbable, so tunnelling, depending on the confinement energy and the electric field over the barrier, is the only factor responsible for the dark counts. To increase the confinement and reduce the DCR, a material with a larger bandgap can be used in the semiconductor sandwich creating a higher barrier for electrons and holes and reducing the escape probability. For many applications it is preferable to have detectors operational in the low loss window of communication fibre at wavelengths of 1300 or 1550 nm. An InP based AlAs/$In_{0.53}Ga_{0.47}As$/AlAs quantum dot resonant tunnelling diode has been demonstrated by Li *et al.* [57] with an operational wavelength of 1310 nm. At a temperature of 4.5 K the device has a SPDE of 0.35% with a DCR of 1.58×10^{-6} ns^{-1} at a certain discriminator level. The author suggested that increasing the thickness of the absorption layer could help to increase the SPDE.

1.3.3.4 Superconducting detectors

The electrical resistivity of certain metals and alloys drops suddenly to zero when the sample under examination is cooled to a sufficiently low temperature, often a temperature in the liquid Helium range. This phenomenon, called superconductivity, was observed first by Onnes in 1911 whilst analysing a Mercury sample [58]. Superconductors can be characterised by a critical temperature T_c at which this phase transition occurs from a state of normal electrical resistivity to a superconducting state. It is this transition that is used to detect single-photons in a superconducting single-photon detector.

The most common single photon counting detectors based on superconductivity theory are transition edge sensors and superconductive nanowires.

Transition edge sensors (TES) are devices cooled just below their critical temperature T_c. When a photon is absorbed, the photoelectron produced results in a temperature increase,

which increases the temperature of the detector above T_c and causes a large change in resistance that can be readily detected. This change in the resistance can be detected by external circuitry to provide the detection of single photons [59]. In 1942, Andrews *et al*. applied a current to a fine tantalum wire operating in its superconducting transition region at 3.2 K and measured the change in resistance caused by an infrared signal [60]. This was the first demonstration of a TES bolometer. In 1949, the same researcher applied a current to a columbium nitride strip within its superconducting transition at 15 K and measured the voltage pulses when it was bombarded by alpha particles [61]. A new generation of TES with high SPDEs are being developed; Niobium and Tungsten are the most common materials used for infrared detection [62], [63]. At 1550 nm a 95% SPDE and low DCR of approximately 10 Hz was measured by Lita *et al.* [64].

The most attractive aspect of this type of structure is that it can be used for photon number resolving [65], [66]. By analysing the detector output pulse it is possible to determine if one, two, or three photons have been absorbed with jitter as low as 5 ns [67]. The very low operating temperature is the greatest drawback of TESs [47].

The superconductive nanowire is a single photon detector (SNSPD) based on a superconducting wire which is biased just below the critical current density. It was developed in 1991 by Golt'sman *et al*. [68]. This type of device, using long strips of superconductor as the absorber, was able to detect a measurable output pulse due to the creation of a resistive barrier along the wire. A schematic nanowire operational mechanism is shown in Figure 1.19.

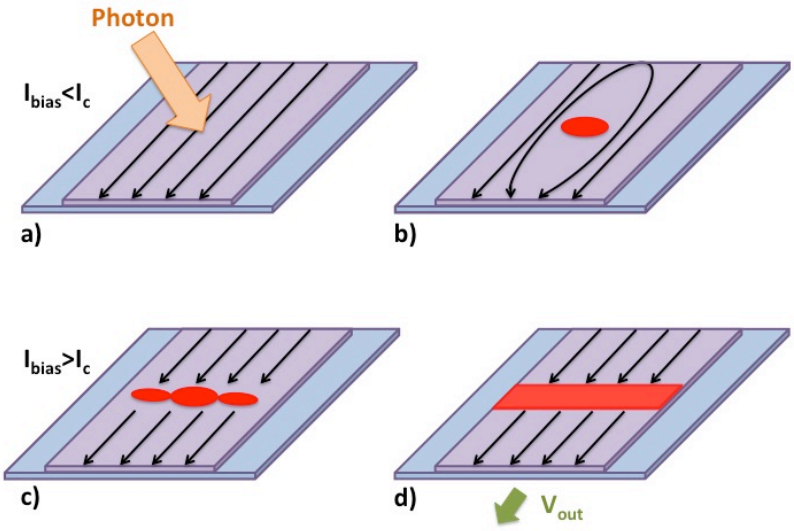

Figure 1.19 *Schematic nanowire operational mechanism. a) The photon is absorbed by a wire where a supercurrent is flowing through it with the bias current slightly less than the critical current, b) the absorption creates a hot spot that perturbs the supercurrent in the wire redirecting it around the spot, c) at the edges of the nanowire the current density is pushed above the critical current density, forming resistive regions d) this increases in width until a resistive barrier across the width of the strip is created.*

When a photon is absorbed, the temperature in the wire locally increases above T_c creating a resistive hot spot, proportional to the photon intensity. The hot spot perturbs the supercurrent in the wire redirecting it to other areas of the strip, this leads the current density in parts of the strip to exceed the critical current density and a resistive barrier along all the width of the strip is created. This allows a measurable voltage pulse to be detected. The wire then returns to its operating temperature due to electron-phonon scattering where the electrons lose their energy. This causes the hot spot to shrink rapidly removing the resistive barrier and the device returns to its superconductive status. Golt'sman's group are pioneers with this type of detector; they have been developing and testing single photon nanowires to optimise their performance for many years. In 2001 they demonstrated an ultrathin NbN strip with a thickness of 5 nm for ultrafast single-photon detection and counting of visible and infrared photons with an experimentally measured SPDE of 20% for photons with a wavelength of 810 nm and negligible dark counts. Their SNSPD SPDE is much lower due to the very low active area of the device compared to the optical spot size. To improve the SPDE the authors suggest using coupling optics which allow the incident photon beam to be focused to a

diffraction-limited spot size and, at the same time, varying the geometrical configurations of the detector to increase the active- area [69].

All the early superconductive nanowire detectors suffered from this low SPDE since they were designed with long straight wires, which did not match the illumination area created by incident light. To avoid this problem the width of the wire could be increased to increase the probability that a photon was detected. Unfortunately this is only a partial solution since the width of the wire cannot be increased indefinitely because of the small size of the hot spot created after the absorption. A more efficient structure was for this reason developed by Verevkin *et al.*: it consists of wire configured in a meander line style [70]. A meander design by Takesue *et al.* is shown in Figure 1.20 [71]. It consists of a 100 nm wide superconducting NbN meander wire detector covering a 10 μm × 10 μm area; this design ensures a 50% fill factor over the detector surface.

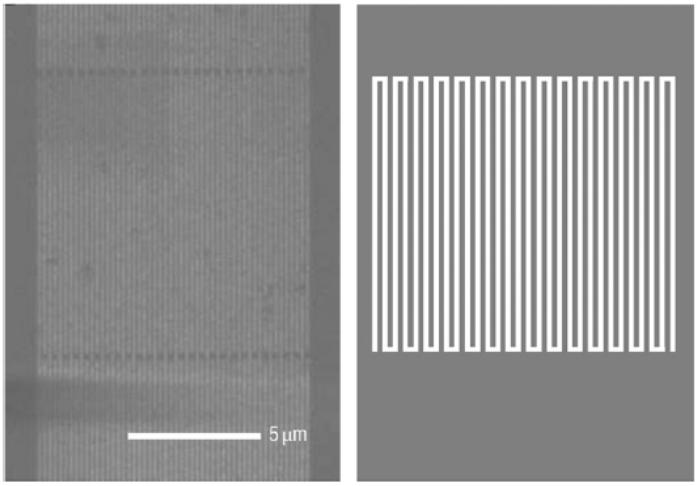

Figure 1.20 *On the left SNSPD close up image observed with scanning electron microscope (SEM) for a device that consists of 10 μm × 10 μm area meander with 100 nm wires at 200 nm pitch. On the right a schematic representation of portion of the meander line. Figures taken from [71], [46].*

Meander wire detectors with a larger active area have been use to achieve a high coupling efficiency between the nanowire and the optical fibre leading to a SPDE improvement. A detector with a small active area limits the number of optical modes that can be collected which is critical in applications where photons are distributed over many modes. Unfortunately the maximum count rate for an SNSPD decreases as its active area is increased

due to its kinetic inductance: a longer meander wire increases the overall inductance, leading to a detector dead time in the order of ns [72].

A further increase in SPDE can be obtained by using an optical cavity to increase the number of absorption passes for the photons [73]. Typical SPDE for a 100 nm wide and 4 nm thick NbN wire in cavity is 57% at 1550 nm [74]. A SPDE of up to 90% can be reached for a 20 nm wide and 10 nm thick NbN based detector at 1550 nm, as shown by Marsili *et al*. [75]. As the SPDE of the SNSPD is the product of the absorption coefficient of the meander (which increases with the thickness of the nanowire) and the probability of a photon inducing a resistive state formation in the nanowire (which increases with decreasing of cross sectional area of the nanowire), a thicker NbN film needs to be patterned with a thinner wire to increase a detector's SPDE.

Until now the most common material used in SNSPDs is NbN because of its fast response properties [76]. NbN SNSPDs need to be grown at high temperature (>600 °C) on lattice-matched substrates (sapphire or MgO) [47]; moreover they are not very robust with respect to structural defects and have limited compatibility with the structures that enhance the optical coupling and the absorption of the detector. High quality SNSPD devices have been developed on alternative superconductors such as NbTiN [77], [78] and WSi [79] on Si substrates allowing a much easier integration with the cavity. Marsili *et al.* developed a WSi superconductive nanowire detector with a system SPDE greater than 90% in the wavelength range 1.52-1.61 μm, a low dark count rate of less than 1 Hz, a low timing jitter of less than 100 ps and a short reset time of less than 100 ns [79]. An advantage of using WSi with respect to NbN is that WSi allows higher sensitivity at longer wavelengths.

All the SNSPD detectors can be used to detect radiation with wavelengths up to 3 μm, and possibly longer wavelengths. Moreover, they can be used in photon number resolving: the wires can be arranged in parallel providing an electrical output proportional to the photon numbers. Marsili *et al.* reported a detector capable of counting up to four photons at telecommunication wavelengths [80], [81].

The disadvantages of superconducting nanowire detectors are the very low operating temperature, around 4 K for NbN or even cooler (mK) for WSi.

1.3.3.5 Avalanche Photodiodes

One of the most common technologies for low light level detection is based on the avalanche photodiode (APD). The next chapter describes in detail the operating principles of the avalanche photodiode, its key characteristics and reviews the common materials used in these types of detectors. Single-photon avalanche diodes (SPADs) are introduced and their operating principles are described in Chapter Two.

1.4 Conclusion

This Chapter discussed the detection of low levels of light, but in particular in the infrared region at wavelengths above 1.6 μm. The particular focus of this Chapter was single-photon detectors, and a review of the most significant literature was presented.

Light detection has a fundamental role in consumer technology used in our everyday life, e.g. digital cameras, fibre optics, to emerging applications such as security, medicine, environmental science, terrain mapping, and space applications. Less obvious, but important examples, analysed in detail in this chapter, include gas sensing, defence/geoscience ranging, clinical thermography, rocket plume detection, and industry manufacturing monitoring which all rely on detection of near-infrared wavelengths. In many of these applications, the optical signal on the detector is very weak either for safety reasons, or due to high levels of optical loss during the transmission of light. The most common single photon detectors were introduced: Photomultiplier tubes; microchannel plates; quantum dot based detectors; and superconducting detectors were described in detail. This included their operating mechanisms, their properties, along with typical values of their single-photon detection figures of merit. A well-established and common technique, known as Time-correlated-single-photon-counting (TCSPC), coupled with single photon detectors was also introduced. It was initially used in time-resolved fluorescence and photoluminescence, but nowadays it is becoming increasingly important in applications that involve fast optical signal and low light sensitivity. The operational principles of TCSPC were described: it is based on the detection of single photons and the measurement of their arrival (STOP signal pulse) with respect to a reference signal (START signal pulse), usually given by an external clock.

1.5 Thesis overview and motivation

This thesis is primarily concerned with optical measurement at wavelengths greater than 1.6 μm performed with InAs detectors. InAs is a material that shows excellent properties for APD operation: low excess noise factor and excellent multiplication characteristics. Moreover, it possesses a narrow bandgap (E_g=0.36 eV) at room temperature, and thus it can be used to detect light efficiently in the MWIR (wavelengths of up to 3.5 μm).

The scope and the motivation for the individual chapters are given below in detail.

Chapter Two describes the operating principles of the APD, its main characteristics and reviews the main materials used in these types of detectors highlighting what are the advantages and disadvantages of all these different materials in an APD. Finally, SPADs are introduced. The fundamental differences between SPADs and APDs are described.

Chapter Three is dedicated to InAs and in particular to the unique characteristics of InAs APDs. It reviews some of the previous work accomplished in InAs and describes in detail the main properties that make an InAs APD a unique device in terms of its impact ionisation characteristics.

Chapter Four presents the first InAs mesa APD prototypes grown at the University of Sheffield in the National Centre of III-V Technologies. In this chapter a brief description of the post-growth processing is reported with particular attention to the passivation layer step. Preliminary dark current results on detectors of different sizes are reported using different passivation materials such as SU8 photoresist, SiN and Al_2O_3. Results show that SU8, at present, is more suitable than SiN and Al_2O_3, although it presents poor characteristics during the device packaging process due to poor adhesion between the metal contacts and the SU8. A new mask set has been designed combining SU8 with another insulating material which has good adhesion with the top metal contact and is used under the external bondpad.

Chapter Five presents a study of II-VI material as the passivation layer on InAs mesa photodiodes. II-VI semiconductors can be grown on InAs resulting in solid and reliable structures where contacts can be easily deposited (good adhesion between II-VI and metal

contact). This chapter describes initially the growth and the characterization of binary compounds as ZnSe, ZnTe and CdSe on InAs (ZnSe: 5.668 Å, ZnTe: 6.103 Å, CdSe: 6.050 Å, InAs: 6.058 Å). The study of the II-VI material on InAs is then further extended to ternary compounds such as CdMgSe with different Mg concentrations. Both binary and ternary compounds were initially grown on InAs substrates giving crystalline layers which had well-defined X-ray diffraction (XRD) and photoluminescence (PL) peaks. A pre-growth surface oxide removal study is carried out to improve surface morphology of II-VI layers grown on InAs substrates. Optimizing the process with an InAs substrate, the study is then extended to examine sidewall passivation on processed mesa photodiode devices so as to produce detectors with low leakage current.

Chapter Six presents laboratory based LIDAR experiments, with ranges of around 0.5 m stand-off distance using InAs avalanche photodiodes. Time-of-flight measurements were performed at wavelengths from 1300 nm to 2370 nm. Preliminary characterisation analyses were conducted on n-i-p and p-i-n InAs structures; dark currents, multiplication, responsivity and detector output pulse arrival time were studied. InAs n-i-p structures were further available during the ranging experiment, and were used in linear multiplication mode. Here, the laser beam was incident on the edge of the device (rather than the top of the mesa) in order to achieve a mixed carrier injection and thus higher gain. A 6 mm ranging error was observed in the experiment. A total system jitter of less than 50 ps has been observed in the InAs devices at room temperature and at low gain.

Chapter Seven summarises the conclusions of the research presented and proposes possibilities of future work in the same field.

1.6 References

[1] T. Young, "The Bakerian lecture: On the theory of light and colours," *Philosophical transactions of the Royal Society of London,* vol. 92, pp. 12-48, 1802.

[2] Wikipedia. Electromagnetic Spectrum http://en.wikipedia.org/wiki/File:EM_spectrum.svg

[3] A. Einstein, "Über einen die Erzeugung und Verwandlung des Lichtes betreffenden heuristischen Gesichtspunkt," *Annalen der Physik,* vol. 322, pp. 132-148, 1905.

[4] R. A. Millikan, "A direct photoelectric determination of Planck's h," *Physical Review,* vol. 7, pp. 355-388, 1916.

[5] A. H. Compton, "A quantum theory of the scattering of X-rays by light elements," *Physical Review,* vol. 21, pp. 483-502, 1923.

[6] D. Halliday, R. Resnick, and K. S. Krane, "PHYSICS", Vol. 2, John Wiley & Sons, 1992.

[7] E. Browell, S. Ismail, and W. Grant, "Differential absorption lidar (DIAL) measurements from air and space," *Applied Physics B,* vol. 67, pp. 399-410, 1998.

[8] C. Weitkamp, "Lidar: range-resolved optical remote sensing of the atmosphere" vol. 102, Springer, 2005.

[9] M.-C. Amann, T. Bosch, M. Lescure, R. Myllyla, and M. Rioux, "Laser ranging: a critical review of usual techniques for distance measurement," *Optical Engineering,* vol. 40, pp. 10-19, 2001.

[10] M. A. Albota, B. F. Aull, D. G. Fouche, R. M. Heinrichs, D. G. Kocher, R. M. Marino*, et al.*, "Three-dimensional imaging laser radars with Geiger-mode avalanche photodiode arrays," *Lincoln Laboratory Journal,* vol. 13, pp. 351-370, 2002.

[11] B. F. Aull, A. H. Loomis, D. J. Young, R. M. Heinrichs, B. J. Felton, P. J. Daniels*, et al.*, "Geiger-mode avalanche photodiodes for three-dimensional imaging," *Lincoln Laboratory Journal,* vol. 13, pp. 335-349, 2002.

[12] A. McCarthy, N. J. Krichel, N. R. Gemmell, X. Ren, M. G. Tanner, S. N. Dorenbos*, et al.*, "Kilometer-range, high resolution depth imaging via 1560 nm wavelength single-photon detection," *Optics Express,* vol. 21, pp. 8904-8915, 2013.

[13] Wikipedia. Solar Irradiance Spectrum
http://en.wikipedia.org/wiki/File:Solar_Spectrum.png

[14] M. Diagne, M. Greszik, E. Duerr, J. Zayhowski, M. Manfra, R. Bailey*, et al.*, "Integrated array of 2-μm antimonide-based single-photon counting devices," *Optics Express,* vol. 19, pp. 4210-4216, 2011.

[15] A. Axelsson, "Rapid topographic and bathymetric reconnaissance using airborne LiDAR," in *Security+ Defence*, 2010, pp. 783503-10, 2010.

[16] D. Whiteman, K. Evans, B. Demoz, D. C. Starr, E. Eloranta, D. Tobin*, et al.*, "Raman lidar measurements of water vapor and cirrus clouds during the passage of Hurricane Bonnie," *Journal of Geophysical Research: Atmospheres (1984–2012),* vol. 106, pp. 5211-5225, 2001.

[17] G. Pappalardo, A. Amodeo, L. Mona, M. Pandolfi, N. Pergola, and V. Cuomo, "Raman lidar observations of aerosol emitted during the 2002 Etna eruption," *Geophysical Research Letters,* vol. 31, pp. L05120 1-4, 2004.

[18] Z. Liu, A. Omar, M. Vaughan, J. Hair, C. Kittaka, Y. Hu*, et al.*, "CALIPSO lidar observations of the optical properties of Saharan dust: A case study of long‐range transport," *Journal of Geophysical Research: Atmospheres (1984–2012),* vol. 113, pp. D07207 1-20, 2008.

[19] M. Fromm, J. Alfred, K. Hoppel, J. Hornstein, R. Bevilacqua, E. Shettle*, et al.*, "Observations of boreal forest fire smoke in the stratosphere by POAM III, SAGE II, and lidar in 1998," *Geophysical Research Letters,* vol. 27, pp. 1407-1410, 2000.

[20] H. Edner, K. Fredriksson, A. Sunesson, S. Svanberg, L. Uéus, and W. Wendt, "Mobile remote sensing system for atmospheric monitoring," *Applied Optics,* vol. 26, pp. 4330-4338, 1987.

[21] P. F. Ambrico, A. Amodeo, P. Di Girolamo, and N. Spinelli, "Sensitivity analysis of differential absorption lidar measurements in the mid-infrared region," *Applied Optics,* vol. 39, pp. 6847-6865, 2000.

[22] M. Uchiumi, N. J. Vasa, M. Fujiwara, S. Yokoyama, M. Maeda, and O. Uchino, "Development of DIAL for CO_2 and CH_4 in the atmosphere," vol. 4893, pp. 141-149, 2003.

[23] Absorption Band.
http://globalcoolingplan.org/methane/massextinct.html

[24] Absorption by atmospheric gases in the IR, visible and UV spectral regions. (Lecture)

http://irina.eas.gatech.edu

[25] J. G. Titus, "Greenhouse effect and global warming," *Encyclopedia of Coastal Science*, Springer, pp. 494-501, 2005.

[26] T. F. Refaat, M. N. Abedin, O. V. Sulima, S. Ismail, and U. N. Singh, "III-V compound detectors for CO_2 DIAL measurements," in *Optics & Photonics 2005*, pp. 588706-28, 2005.

[27] Blackbody spectrum
http://www.sun.org/encyclopedia/black-body-radiation

[28] X. Zhou, I. Sandall, M. J. Hobbs, B. S. White, C. H. Tan, and J. R. Willmott, "Evaluation of InAs photodiodes for radiation thermometry," in *Semiconductor and Integrated Optoelectronics Conference,* Cardiff, 2013.

[29] E. Ring and K. Ammer, "Infrared thermal imaging in medicine," *Physiological Measurement,* vol. 33, pp. R33-R46, 2012.

[30] J. Christensen, L. H. Matzen, M. Væth, S. Schou, and A. Wenzel, "Thermography as a quantitative imaging method for assessing postoperative inflammation," *Dentomaxillofacial Radiology,* vol. 41, pp. 494-499, 2012.

[31] E. Ng and E. Kee, "Advanced integrated technique in breast cancer thermography," *Journal of medical engineering & technology,* vol. 32, pp. 103-114, 2008.

[32] B. J. Steward, K. W. Bauer, and G. P. Perram, "Remote discrimination of large-caliber gun firing signatures," *Journal of Applied Remote Sensing,* vol. 6, pp. 063607 1-15, 2012.

[33] W. Zhang, Q.-q. Ye, S.-p. Li, and N.-f. Wang, "Numerical study on the influence of aluminum on infrared radiation signature of exhaust plume," *ISPDI 2013-Fifth International Symposium on Photoelectronic Detection and Imaging*, pp. 890729-10, 2013

[34] S. Bagavathiappan, B. Lahiri, T. Saravanan, J. Philip, and T. Jayakumar, "Infrared Thermography for Condition Monitoring-A Review," *Infrared Physics & Technology,* vol. 60, pp. 35-55, 2013.

[35] M. Clark, D. McCann, and M. Forde, "Application of infrared thermography to the non-destructive testing of concrete and masonry bridges," *NDT & E International,* vol. 36, pp. 265-275, 2003.

[36] M. S. Jadin and S. Taib, "Recent progress in diagnosing the reliability of electrical equipment by using infrared thermography," *Infrared Physics & Technology,* vol. 55, pp. 236-245, 2012.

[37] C. Badulescu, M. Grédiac, H. Haddadi, J.-D. Mathias, X. Balandraud, and H.-S. Tran, "Applying the grid method and infrared thermography to investigate plastic deformation in aluminium multicrystal," *Mechanics of Materials,* vol. 43, pp. 36-53, 2011.

[38] J. Kumar, S. Baby, and V. Kumar, "Thermographic studies on IMI-834 titanium alloy during tensile loading," *Materials Science and Engineering: A,* vol. 496, pp. 303-307, 2008.

[39] M. Pastor, X. Balandraud, M. Grédiac, and J. Robert, "Applying infrared thermography to study the heating of 2024-T3 aluminium specimens under fatigue loading," *Infrared Physics & Technology,* vol. 51, pp. 505-515, 2008.

[40] B. Lahiri, S. Bagavathiappan, T. Saravanan, K. Rajkumar, A. Kumar, J. Philip*, et al.*, "Defect Detection in Weld Joints by Infrared Thermography," *Proc. of the International Conference on Non Destructive Evaluation for Steel and Allied Industries - NDESAI 2011,* pp. 191-197, 2011.

[41] J. W. Beletic, R. Blank, D. Gulbransen, D. Lee, M. Loose, E. C. Piquette*, et al.*, "Teledyne Imaging Sensors: Infrared imaging technologies for Astronomy & Civil Space," *High Energy, Optical, and Infrared Detectors for Astronomy III,* vol. 7021, pp. 70210H 1-14, 2008.

[42] M. Jack, J. Asbrock, S. Bailey, D. Baley, G. Chapman, G. Crawford*, et al.*, "MBE based HgCdTe APDs and 3D LADAR sensors," *Infrared Technology and Applications XXXIII,* vol. 6542, pp. 65421A 1-12, 2007.

[43] J. Beck, C. Wan, M. Kinch, J. Robinson, P. Mitra, R. Scritchfield*, et al.*, "The HgCdTe electron avalanche photodiode," *Journal of Electronic Materials,* vol. 35, pp. 1166-1173, 2006.

[44] W. Becker, "Advanced time-correlated single photon counting techniques" (Series in chemical physics), Vol. 81, Springer-Verlag, 2005.

[45] N. R. Gemmell, A. McCarthy, B. Liu, M. G. Tanner, S. N. Dorenbos, V. Zwiller*, et al.*, "Singlet oxygen luminescence detection with a fiber-coupled superconducting nanowire single-photon detector," *Optics Express,* vol. 21, pp. 5005-5013, 2013.

[46] G. S. Buller and R. J. Collins, "Single-photon generation and detection," *Measurement Science and Technology,* vol. 21, pp. 012002 1-28, 2010.

[47] R. H. Hadfield, "Single-photon detectors for optical quantum information applications," *Nature Photonics,* vol. 3, pp. 696-705, 2009.

[48] Hamamatsu, "Photomultiplier Tubes: Basics and Applications. Third Edition ".

http://www.hamamatsu.com/resources/pdf/etd/PMT_handbook_v3aE.pdf

[49] Wikipedia. Photomultiplier. http://commons.wikimedia.org/wiki/File:Photomultiplier_schema_de.png

[50] S. Flyckt and C. Marmonier, "Photomultiplier tubes: principles and applications," *Photonis*, 2002.

[51] Hamamatsu. Photomultiplier Tube. http://www.hamamatsu.com/resources/pdf/etd/H10330B-25_-45_-75_TPMO1056E01.pdf

[52] A. J. Shields, M. OSullivan, I. Farrer, D. Ritchie, R. Hogg, M. Leadbeater*, et al.*, "Detection of single photons using a field-effect transistor gated by a layer of quantum dots," *Applied Physics Letters,* vol. 76, pp. 3673-3675, 2000.

[53] B. Kardynal, A. Shields, M. O'Sullivan, N. Beattie, I. Farrer, D. Ritchie*, et al.*, "Detection of single photons using a field effect transistor with a layer of quantum dots," *Measurement Science and Technology,* vol. 13, pp. 1721-1726, 2002.

[54] B. Kardynał, S. Hees, A. Shields, C. Nicoll, I. Farrer, and D. Ritchie, "Photon number resolving detector based on a quantum dot field effect transistor," *Applied Physics Letters,* vol. 90, pp. 181114 1-3, 2007.

[55] M. Rowe, E. Gansen, M. Greene, R. Hadfield, T. Harvey, M. Su*, et al.*, "Single-photon detection using a quantum dot optically gated field-effect transistor with high internal quantum efficiency," *Applied Physics Letters,* vol. 89, pp. 253505 1-3, 2006.

[56] J. Blakesley, P. See, A. Shields, B. Kardynał, P. Atkinson, I. Farrer*, et al.*, "Efficient single photon detection by quantum dot resonant tunneling diodes," *Physical Review Letters,* vol. 94, pp. 067401 1-4, 2005.

[57] H. Li, B. Kardynał, P. See, A. Shields, P. Simmonds, H. Beere*, et al.*, "Quantum dot resonant tunneling diode for telecommunication wavelength single photon detection," *Applied Physics Letters,* vol. 91, pp. 073516 1-3, 2007.

[58] H. K. Onnes, "Further experiments with liquid helium. C. On the change of electric resistance of pure metals at very low temperatures etc. IV. The resistance of pure mercury at helium temperatures," *in KNAW,* pp. 1910-1911, 1911.

[59] K. Irwin and G. Hilton, "Transition-edge sensors," *Cryogenic Particle Detection*, Springer, pp. 63-150, 2005.

[60] D. Andrews, W. Brucksch, W. Ziegler, and E. Blanchard, "Attenuated Superconductors I. For Measuring Infra−Red Radiation," *Review of Scientific Instruments,* vol. 13, pp. 281-292, 1942.

[61] D. Andrews, R. Fowler, and M. Williams, "Effect of alpha particles on a superconductor," *Physical Review,* vol. 76, pp. 154-155, 1949.

[62] J. Skidmore, J. Gildemeister, A. Lee, M. Myers, and P. Richards, "Superconducting bolometer for far-infrared Fourier transform spectroscopy," *Applied Physics Letters,* vol. 82, pp. 469-471, 2003.

[63] D. Rosenberg, A. E. Lita, A. J. Miller, and S. W. Nam, "Noise-free high-efficiency photon-number-resolving detectors," *Physical Review A,* vol. 71, pp. 061803 1-4, 2005.

[64] A. E. Lita, A. J. Miller, and S. W. Nam, "Counting near-infrared single-photons with 95% efficiency," *Optics Express,* vol. 16, pp. 3032-3040, 2008.

[65] D. Fukuda, G. Fujii, T. Numata, A. Yoshizawa, H. Tsuchida, H. Fujino*, et al.*, "Photon number resolving detection with high speed and high quantum efficiency," *Metrologia,* vol. 46, pp. S288-S292, 2009.

[66] D. Rosenberg, A. Lita, A. Miller, S. Nam, and R. Schwall, "Performance of photon-number resolving transition-edge sensors with integrated 1550 nm resonant cavities," *IEEE Transactions on Applied Superconductivity,* vol. 15, pp. 575-578, 2005.

[67] A. Lamas-Linares, T. Gerrits, N. A. Tomlin, A. Lita, B. Calkins, J. Beyer*, et al.*, "Transition edge sensors with low timing jitter at 1550 nm," in *Quantum Electronics and Laser Science Conference*, p. QTu3e.1, 2012.

[68] G. Goltsman, A. Semenov, Y. P. Gousev, M. Zorin, I. Godidze, E. Gershenzon*, et al.*, "Sensitive picosecond NbN detector for radiation from millimetre wavelengths to visible light," *Superconductor Science and Technology,* vol. 4, pp. 453-456, 1991.

[69] G. Goltsman, O. Okunev, G. Chulkova, A. Lipatov, A. Semenov, K. Smirnov*, et al.*, "Picosecond superconducting single-photon optical detector," *Applied Physics Letters,* vol. 79, pp. 705-707, 2001.

[70] A. Verevkin, J. Zhang, R. Sobolewski, A. Lipatov, O. Okunev, G. Chulkova*, et al.*, "Detection efficiency of large-active-area NbN single-photon superconducting detectors in the ultraviolet to near-infrared range," *Applied Physics Letters,* vol. 80, pp. 4687-4689, 2002.

[71] H. Takesue, S. W. Nam, Q. Zhang, R. H. Hadfield, T. Honjo, K. Tamaki, *et al.*, "Quantum key distribution over a 40-dB channel loss using superconducting single-photon detectors," *Nature photonics,* vol. 1, pp. 343-348, 2007.

[72] A. J. Kerman, E. A. Dauler, W. E. Keicher, J. K. Yang, K. K. Berggren, G. Goltsman, *et al.*, "Kinetic-inductance-limited reset time of superconducting nanowire photon counters," *Applied Physics Letters,* vol. 88, pp. 111116 1-3, 2006.

[73] G. Gol'Tsman, O. Minaeva, A. Korneev, M. Tarkhov, I. Rubtsova, A. Divochiy, *et al.*, "Middle-infrared to visible-light ultrafast superconducting single-photon detectors," *IEEE Transactions on Applied Superconductivity,* vol. 17, pp. 246-251, 2007.

[74] K. M. Rosfjord, J. K. Yang, E. A. Dauler, A. J. Kerman, V. Anant, B. M. Voronov, *et al.*, "Nanowire single-photon detector with an integrated optical cavity and anti-reflection coating," *Optics Express,* vol. 14, pp. 527-534, 2006.

[75] F. Marsili, F. Najafi, E. Dauler, H. Korre, V. Anant, K. Sunter, *et al.*, "Cavity-Integrated Ultra-Narrow Superconducting Nanowire Single-Photon Detector Based on a Thick Niobium Nitride Film," in *Quantum Electronics and Laser Science Conference*, p. QTu3E.3, 2012.

[76] K. Ilin, M. Lindgren, M. Currie, A. Semenov, G. Goltsman, R. Sobolewski, *et al.*, "Picosecond hot-electron energy relaxation in NbN superconducting photodetectors," *Applied Physics Letters,* vol. 76, pp. 2752-2754, 2000.

[77] S. Dorenbos, E. Reiger, U. Perinetti, V. Zwiller, T. Zijlstra, and T. Klapwijk, "Low noise superconducting single photon detectors on silicon," *Applied Physics Letters,* vol. 93, pp. 131101 1-3, 2008.

[78] M. G. Tanner, C. Natarajan, V. Pottapenjara, J. OConnor, R. Warburton, R. Hadfield, *et al.*, "Enhanced telecom wavelength single-photon detection with NbTiN superconducting nanowires on oxidized silicon," *Applied Physics Letters,* vol. 96, pp. 221109 1-3, 2010.

[79] F. Marsili, V. Verma, J. Stern, S. Harrington, A. Lita, T. Gerrits, *et al.*, "Detecting single infrared photons with 93% system efficiency," *Nature Photonics,* vol. 7, pp. 210-214, 2013.

[80] A. Divochiy, F. Marsili, D. Bitauld, A. Gaggero, R. Leoni, F. Mattioli, *et al.*, "Superconducting nanowire photon-number-resolving detector at telecommunication wavelengths," *Nature Photonics,* vol. 2, pp. 302-306, 2008.

[81] F. Marsili, D. Bitauld, A. Gaggero, S. Jahanmirinejad, R. Leoni, F. Mattioli, *et al.*, "Physics and application of photon number resolving detectors based on superconducting parallel nanowires," *New Journal of Physics,* vol. 11, pp. 045022 1-21, 2009.

Chapter Two

2. Avalanche Photodiodes in the Near and Mid-infrared

2.1 p-n and p-i-n junctions

The role of a photodetector is to convert incident light into a useful electrical response. One of most common type of devices, used from X-ray to the infrared wavelength, is the photodiode which is a p-n or p-i-n structure operated under zero or reverse bias. Electron-hole pairs are created through optical absorption when the diode is illuminated by light. Because of the combination of built-in and applied electric field, electrons and holes in the depletion region accelerate in opposite directions and drift to the surrounding n- and p-cladding regions, respectively, generating a photocurrent. This resulting current I_{ph} is proportional to the incident optical power P_{in} according to the formula $I_{ph} = R_p(\lambda)P_{in}$, where R_p is the responsivity of the device at wavelength λ [1]. Figure 2.1 shows the current-voltage characteristic of photodiodes; the bias region 1 is defined as the operating regime of the photodiode.

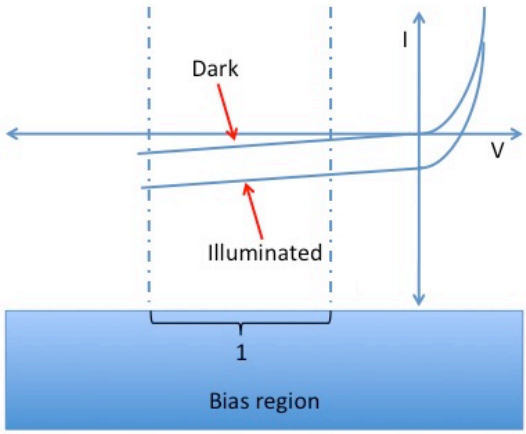

Figure 2.1 *Current-Voltage characteristic of photodiodes: the bias region 1 is defined as the operating regime of the photodiode. When the diode is operated under reverse bias and is illuminated by light, a current $I_{ph,}$ proportional to the incident optical power $P_{in,}$ is created.*

2.2 Avalanche photodiodes (APDs)

In a number of applications, for example time-resolved fluorescence [2], the ability to detect only very few photons with high temporal resolution is required. Typically, when the photon flux is low, the photocurrent in the photodiode junction operating in Region 1 of Figure 2.1 is correspondingly low and external amplification is needed to detect these small detector output signals. Such external amplification can introduce noise, particularly when high bandwidths or gains are required. One solution to this problem is to use avalanche photodiodes (APDs), where the current is amplified within the detector itself, which can give a better noise performance than the use of the external amplification electronics.

The physical phenomenon which causes the APD internal current gain is impact ionisation [3]. In the presence of an electric field the primary carriers, generated through absorption of photons, can acquire sufficient kinetic energy to excite (by collision) bound electrons into the conduction band, leaving holes in the valence band. After the collision, electrons and holes drift in the electric field and may initiate further impact ionisation events. In this way it is possible to generate many secondary electrons and holes, all of which contribute to the photocurrent and are subject to further impact ionisation. The rate of this carrier generation depends on the impact ionisation coefficients α for the electrons, and β for the holes. Their numerical values depend on the semiconductor material and on the electric field. The inverse coefficients $1/\alpha$ and $1/\beta$ give the mean distance between impact ionisation events for electrons and holes respectively. Another important parameter is the ionisation coefficient ratio k, which is defined as either α/β or β/α depending on whether holes or electrons form the primary photocurrent respectively. The avalanche multiplication (M) is defined as the ratio between the multiplied and the un-multiplied photocurrents. For pure electron injection and for only electron impact ionisation, M is given by [4]:

$$\boldsymbol{M = \frac{\alpha - \beta}{\alpha\, exp\{(\beta - \alpha)w\} - \beta}} \qquad (2.1)$$

Where w is the thickness of the depletion region, α and β are the impact ionisation coefficients for electrons and holes, respectively.

Avalanche multiplication in APDs does not only multiply the initial current and its associated noise, but adds further multiplication noise, which is characterised by the excess noise factor, F. The impact ionisation process is stochastic rather than deterministic, with each injected carrier undergoing a different level of multiplication. The contribution to gain noise caused by these fluctuations in the multiplication for the different injected carriers, is characterised by F. If an electron injection is considered, F is given by [5]:

$$\boldsymbol{F = kM + (1 - k)\left(2 - \frac{1}{M}\right)} \tag{2.2}$$

where M is the average multiplication generated by the electron injection and k is the impact ionisation ratio. Using this equation it is possible to find that F has its minimum value, tending to 2 for large M, for k=0. The equation (2.2) doesn't consider dead space effects that can cause decrease of F at specific M. When k=0 the variance in the multiplication for different injected carriers is limited because only one type of carrier, for example electrons, can undergo impact ionisation. In this case the secondary holes created cannot impact ionise (i.e. β=0) and provide feedback to create new electrons. Figure 2.2 shows schematically what happens inside the depletion region (thickness w) of an APD when an electron is injected and β=0.

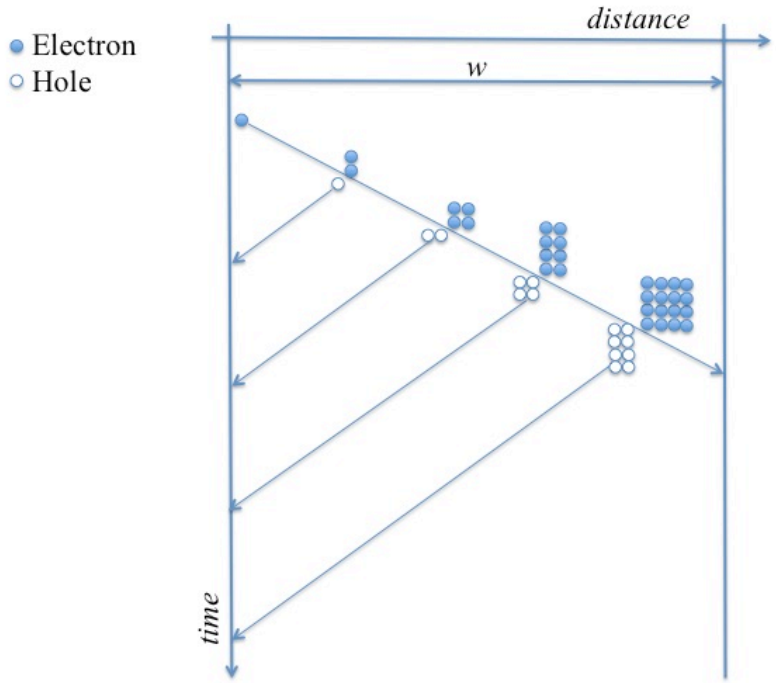

Figure 2.2 *Schematic representation of the time versus distance along the avalanche region for a possible avalanche of impact ionisation events initiated by electrons when k=0. The injected electron undergoes impact ionisation creating secondary electrons and holes. While the secondary electrons undergo impact ionisation, the holes do not. This reduction in feedback from holes leads to a more deterministic process and reduces F. For clarity, all the electrons are shown to impact ionise after the same distance (and time) interval, whereas in real devices this is not the case as the process is stochastic and the impact ionisation coefficients only represent a mean distance between impact ionisation events.*

When k=0.3 for example, in contrast to k=0, the electrons and also some holes contribute to the impact ionisation process, as shown in Figure 2.3: the injected electron generates electrons and holes which subsequently both undergo impact ionisation and contribute to the avalanche photocurrent. This mechanism, unfortunately, causes an increase of the variance in the multiplication and so an increase in F. This also reduces the speed of the device: the time taken for the entire avalanche process is longer because carriers will drift across the multiplication region several times during the avalanche build-up.

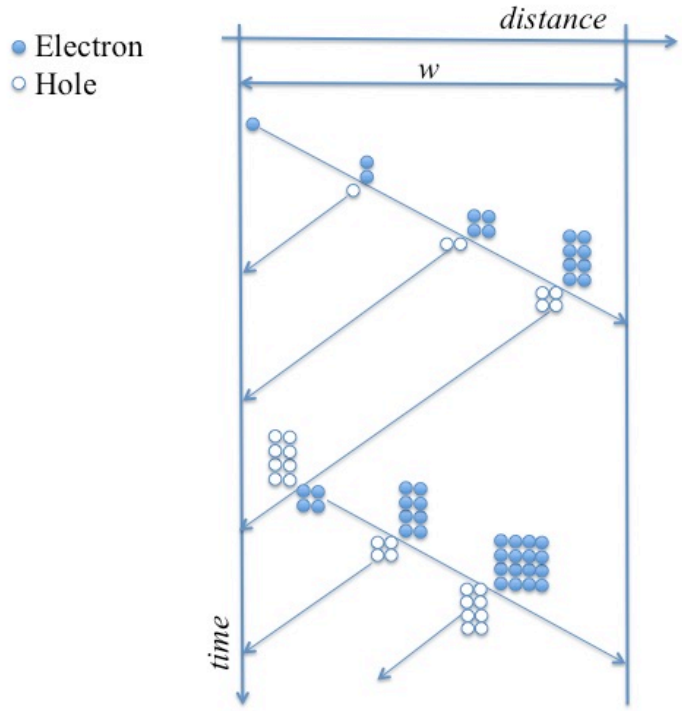

Figure 2.3 *Schematic representation of the time versus distance along the avalanche region for a possible avalanche of impact ionisation events initiated by an electron when k=0.3. In this case, electrons and also some holes contribute to the multiplication. The figure is drawn as if all the electrons and holes impact ionise at the same position after the same time intervals. In real devices the impact ionisation coefficients represent the reciprocal of the mean distance between impact ionisation events. This system presents less determinism due to the increasing variance in the multiplication and so a larger noise factor F.*

To achieve fast and low noise APDs it is advantageous for the values of α and β to differ significantly. These coefficients depend on the material used in the depletion region and the electric field used.

2.3 Single-photon Avalanche photodiodes

In order to detect single photons, the usual route is to operate the APD above avalanche breakdown, in order that a single carrier can initiate an avalanche that has sufficient hole and electron impact ionisation that the avalanche photocurrent is self-sustaining. When operated above avalanche breakdown, the device is known as a Single Photon Avalanche Diode (SPAD) detector. The fundamental design difference between SPADs

and APDs is that SPADs are reverse biased diodes designed to operate with a reverse bias voltage well above the breakdown voltage, as shown in Figure 2.4.

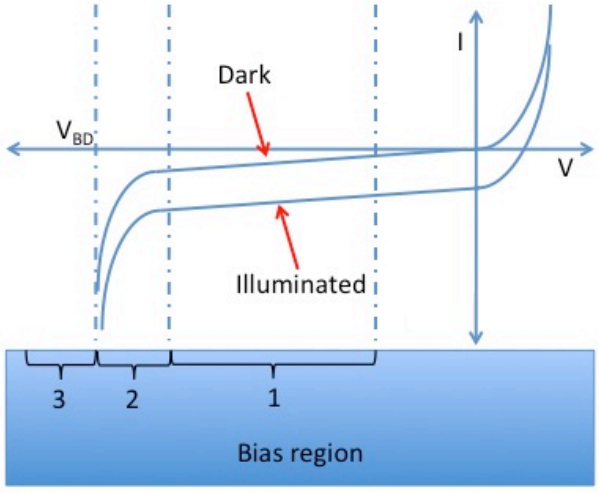

Figure 2.4 *Current-Voltage characteristic of both photodiodes. SPADs are reverse biased detectors designed to operate with a reverse bias voltage well above the breakdown voltage (bias region 3), while APDs operate below it (bias region 2). The usual photodiode response is in Bias Region 1.*

When biased above breakdown, a single carrier injected into the multiplication region can trigger a self-sustaining avalanche – this mode of operation is often described as the Geiger mode. The current created inside the device rises swiftly to a macroscopic level (milliampere range) and continues until the avalanche is quenched, at which point external circuitry is used to decrease the bias to below the breakdown voltage. SPAD quenching approaches are used to decrease the electric field in the device so that it is below the field required for avalanche breakdown thus inhibiting further impact ionisation events and inhibiting the avalanche photocurrent, and resetting the detector to its quiescent state. After quenching, the bias is then raised again above the breakdown voltage and the SPAD is ready to detect another photon [6], [7]. The most common quenching circuits are gated quenching mode, passive quenching and active quenching:

- In the gated quenching mode the SPAD is reversed biased by a voltage V_i just below the breakdown voltage (V_{BD}). A short voltage pulse is applied so that the device is periodically biased above the breakdown voltage for a specific time interval where, if a carrier is present in the depletion region, a self-sustaining avalanche may start. If an avalanche occurs during the gate duration, it will be

quenched at the end of the voltage pulse when the detector returns to a level below avalanche breakdown. Gated mode quenching is usually triggered by an external clock so that the detector gating is coincident with the expected photon arrival.

- Passive quenching circuits are composed of a single resistor R in series with the SPAD. In this quenching circuit, the device is reversed biased above V_{BD}. When an avalanche current is initiated, it also flows through R, which causes the voltage across the SPAD to drop to a level below the breakdown voltage of the SPAD. The avalanche is stopped and, after voltage recovery, the detector will be ready to detect another photon. In this case the reset time is limited by the product of the value of R and the device capacitance.
- In active quenching circuits a very fast comparator is used. In this quenching circuit, the device is reverse biased above V_{BD}. When a photon is absorbed by the photodiode, the avalanche will start. The comparator senses the avalanche current and provides a digital voltage that switches the bias below V_{BD}, quenching the avalanche. In this case, the reset time can largely be determined by the pulse duration from the comparator circuit.

2.4 APD and SPAD design

The basic design of APDs and SPADs is a p-n or p-i-n junction. The choice of material in the junction layers has a crucial role: the absorption region material determines the operational wavelength range of the detector, the multiplication region material affects the detector avalanche performance. The simplest design uses the same material for all the layers; unfortunately the use of the same material for the absorbing region and multiplication region is not always possible, and separate absorption and multiplication devices are commonly used, for example the InGaAs/InP APD and SPAD geometry [8] which are described below.

Infrared avalanche photodiode devices require an absorber material with a high absorption coefficient at long wavelengths. Unfortunately, few materials offer this characteristic in conjunction with a high multiplication, low dark current and low excess noise factor (properties fundamental for a good multiplication region material). One of the main issues is that the multiplication layer requires a very high electric field, and this often causes band-to-band tunnelling across the relatively narrow band-gap. Silicon, for example, is a mature material system, but it can detect effectively at wavelengths

only up to 1.1 μm. More sophisticated APD and SPAD designs have been developed for infrared detection. The most common is a separate absorption multiplication region (SAM) structure; in this design the most appropriate absorber material is chosen according to the required application wavelength and a separate multiplication region material is chosen for the multiplication region to ensure high detector performance. A separate charge sheet layer is also usually included to guarantee that the electric field is high enough to achieve a high avalanche gain in the multiplication region whilst keeping the field low in the absorber to minimize the tunnelling and impact ionisation processes. This type of structure is referred to as a separate absorption, charge and multiplication region (SACM) structure. In this design, in order to maximise detection efficiency it is vital that the absorber layer is fully depleted at the operational voltage in order to avoid unwanted recombination. The lowest reverse-bias voltage at which the absorber is first depleted is known as the punch-through voltage.

2.5 Material choice in APDs and SPADs

Different semiconductor material properties have been studied to find the best design that can be used for APDs and SPADs according to the required wavelength. At present a number of materials are used for operation in the infrared: Ge and InGaAs devices are common, but there is also research in the Ge-on-Si, InSb and HgCdTe material systems. Their characteristics depend on the operating temperature, their precise composition and material quality. In the following paragraphs the main characteristics of common APDs and SPADs are summarised.

2.5.1 Ge photodiodes

Ge photodiodes can effectively detect light in the infrared up to around 1.6 μm wavelength at 300 K [9]. Figure 2.5 shows the absorption coefficient of Ge at 300 K and at 77 K published by Dash *et al.* [9].

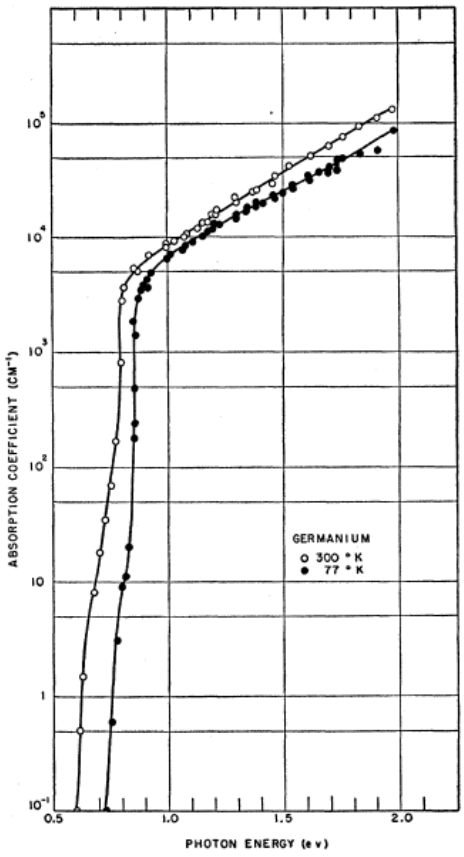

Figure 2.5 *Absorption coefficient of Ge at 300 K (open circles) and 77 K (closed circles). With decreasing photon energy, the absorption coefficient initially decreases gradually until an energy of around 0.81 eV (λ=1530 nm) 300 K and 0.88 eV (λ=1409 nm) at 77 K, after which it drops rapidly. Figure taken from [9].*

The earliest APDs capable of detecting light in the low attenuation optical fibre communication windows at λ = 1.3 μm and 1.55 μm, were based on Ge [10], [11]. Unfortunately a fundamental limitation in Ge avalanche photodiodes is the ratio of the electron and hole impact ionisation coefficient: as α and β values are similar [12], k is close to unity [13] leading to a high excess noise factor F. Moreover, since the bandgap is narrow the thermal generation rate of electron-hole pairs is high, limiting the sensitivity and avalanche gain that can be obtained [3]. High-purity materials, uniform doping concentrations and low dislocation density are important parameters that help to keep dark current low. Hence for SPAD operation, some form of cooling system is also required. A major issue with Germanium SPADs is that these devices exhibit afterpulsing effects caused by carrier trapping in the high field region of the device, increasing the DCR [14], [15]. Because of this high concentration of trapping centres, the afterpulsing effect is strong; the traps have an emission lifetime of microseconds at

the low operation temperatures. In 2007, Tosi *et al*. [16] reported Germanium SPADs that, at 77 K and with an excess bias of 1.5 V, had a DCR of 3 Mcps and a timing jitter of 80 ps using a 1310 nm wavelength laser. The same authors measured a SPDE of about 30% at 1310 nm and, because of the low operating temperature, the efficiency was only around 1% at 1550 nm wavelength.

An alternative to the homojunction devices, such as Ge APDs, is the SAM structure APDs in which the Ge is the absorber and alternative, wider gap semiconductors are used for the multiplication layer. The most promising material that can be coupled with Ge and has high performance multiplication properties is silicon. Although Ge and Si have a 4% lattice mismatch that can result in a high concentration of dislocations and potentially increased dark current, careful processing and device design can reduce the effect of these hetero-interface dislocations. Ge on Si SACM APD structures with a p-doped charge layer have been studied. *k* of around 0.09 and a gain-bandwidth product of 340 GHz at a wavelength of 1310 nm was measured by Kang *et al.* [17]. The sketch of the analysed structure is shown in Figure 2.6. At room temperature, the dark current density was less than 19 $mAcm^{-2}$ at biases up to -5 V and increased to 175 $mAcm^{-2}$ when biased at 90% of breakdown voltage (25 V) with a gain of 8.

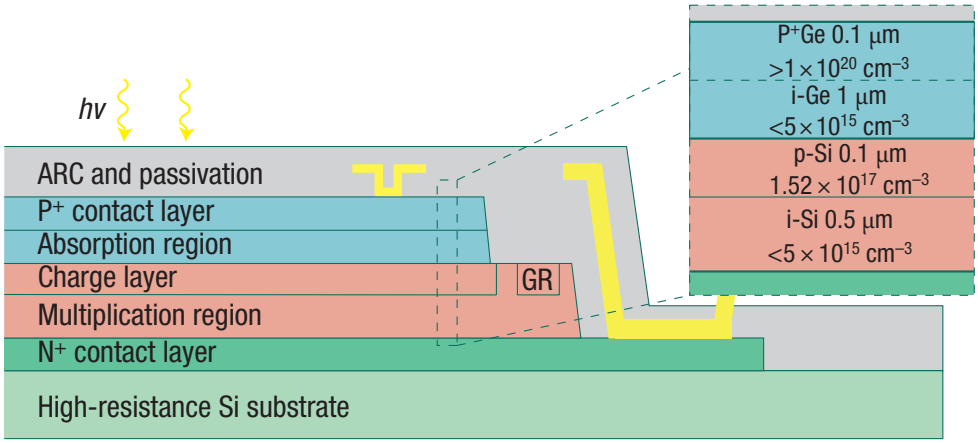

Figure 2.6 *Schematic cross-sections of the SACM germanium/ silicon APD by Kang et al. [17]. The structure includes a floating guard ring (GR) to prevent premature breakdown along the device perimeter and an anti-reflection coating (ARC). The offset shows in detail the thicknesses and the doping densities of the different Germanium and Silicon layers respectively.*

Geiger mode operation of Ge-on-Si SACM APDs has also been demonstrated [18], [19]. In 2013, Warburton *et al.* [19] demonstrated a Ge on Si SACM SPAD with a DCR of 10^6-10^7 Hz at 100 K. The authors characterise the device at two different wavelengths, 1310 nm (at 100 K) and 1550 nm (at 125 K). They reported a 4% SPDE and 300 ps timing jitter at 10% excess bias at 1310 nm, and a 0.15% SPDE and 420 ps timing jitter at 6% excess bias at 1550 nm. The NEP measured was 1×10^{-14} $WHz^{-1/2}$ at 1310 nm wavelength and 5×10^{-12} $WHz^{-1/2}$ at 1550 nm.

2.5.2 InGaAs and InGaAs/InP avalanche photodiodes

$In_{0.53}Ga_{0.47}As$ is used as an absorbing material in APDs, as it can be grown lattice matched on InP substrates. It is a direct bandgap semiconductor with a bandgap of 0.75 eV and can detect light with wavelengths up to 1.65 μm.

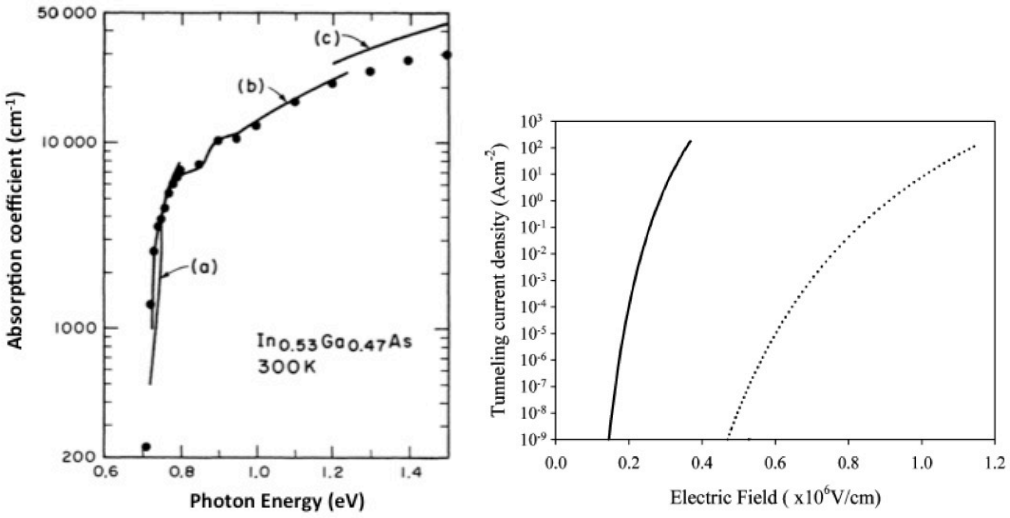

Figure 2.7 *Left, the absorption coefficient of $In_{0.53}Ga_{0.47}As$ at 300 K; figure taken from [20]. The data points are taken from Backer et al. [20], while solid lines are from (a) Zielinski et al. [21], (b) Humphreys et al. [22] and (c) Burkhard et al. [23]. Right, tunnelling current density for $In_{0.53}Ga_{0.47}As$ (solid line) taken from [24] and InP (dotted line) taken from [25].*

Figure 2.7 shows the absorption coefficient of $In_{0.53}Ga_{0.47}As$ at 300 K. $In_{0.53}Ga_{0.47}As$ has a high absorption coefficient compared to other materials of comparable bandgap. At a wavelength of 1.55 μm, for example, its value is 7000 cm^{-1} at room temperature, an order of magnitude larger than that of Ge [22] at this wavelength. This means that in a layer only 1.5 μm thick, more than 70% of the incident photons can be absorbed.

Unfortunately, it suffers from interband tunnelling at the electric fields necessary for impact ionisation, resulting in very high leakage currents in an all-InGaAs APD. $In_{0.53}Ga_{0.47}As$, with its narrow bandgap and small electron effective mass, begins to tunnel at fields as low as 150 kV/cm and increases rapidly with increasing field as shown on the right of Figure 2.7. As a high electric field cannot be reached, no significant avalanche gain can be obtained for this type of structure: electric fields in excess of 350 kV/cm, in fact, would be required for any appreciable gain in a 1 μm thick structure, and in such a situation the high tunnelling currents compromise the noise performance, making the device insensitive and impractical. This problem was overcome by the development of a SAM APD structure. In this design, a wide bandgap semiconductor such as InP is used for the high field multiplication region, which gives a negligible tunnelling current, and the absorption occurs in the adjacent $In_{0.53}Ga_{0.47}As$ layer. A charge sheet layer is used to control the electric field in the absorber region. The avalanche gain and the excess noise are determined by the ionisation coefficients of InP. Values of β and α for InP and $In_{0.53}Ga_{0.47}As$ are plotted in Figure 2.8.

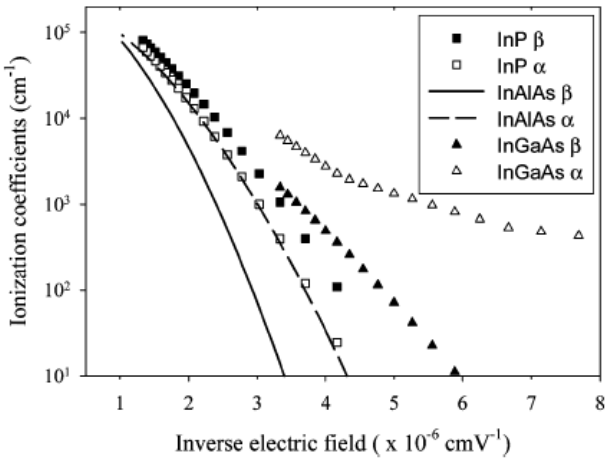

Figure 2.8 *Hole (α) and electron (β) impact ionisation coefficient values for InP and $In_{0.53}Ga_{0.47}As$, along with $In_{0.52}Al_{0.48}As$. Figure taken from [13].*

Unfortunately, the $In_{0.53}Ga_{0.47}As$/InP SAM APD design presents another problem: because it has a large bandgap discontinuity between InP and $In_{0.53}Ga_{0.47}As$, the carriers created in the InGaAs layer are trapped at the heterojunction interface and have difficulty in reaching the InP layer. There have been several improvements to the basic SAM APD to solve this problem. The approach that has been most widely adopted utilises a transition region consisting of one or more latticed-matched intermediate-

bandgap $In_xGa_{1-x}As_{1-y}P_y$ layers to prevent carrier trapping [26]. This type of SAM structure has been modelled, fabricated and characterised for $In_{0.53}Ga_{0.47}As$ /InP SPADs [8]; their energy band diagram and cross section are shown in Figure 2.9.

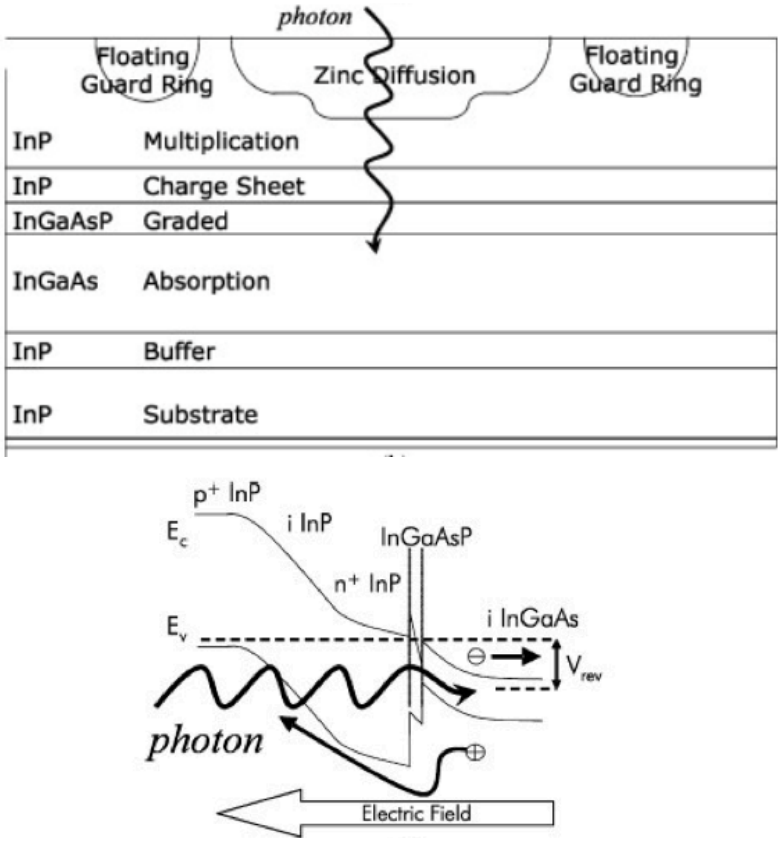

Figure 2.9 *Top, schematic cross-section of a planar $In_{0.53}Ga_{0.47}As/InP$ SPAD with a InGaAsP transition region between $In_{0.53}Ga_{0.47}As$ and InP. One floating guard ring is incorporated in the structure to avoid edge breakdown. Bottom, energy band diagram of the device under reverse bias condition. The intermediate bandgap InGaAsP quaternary layer helps the transfer of the holes, created after the photon absorption, across the large valence band discontinuity. Figure taken from [8].*

The effect of the InGaAsP quaternary layer on the device performance was studied thoroughly: samples with one (SPAD-1Q) or three (SPAD-3Q) InGaAsP layers were grown and clear improvements in the detector efficiency were demonstrated. At 175 K, a dark current of around 10 pA was found for a 20 μm diameter SPAD-3Q device just below the breakdown (around 90 V). It was found that the breakdown voltage decreases with temperature with a rate of 0.17 V/K. A SPDE of 10% and a NEP of 6×10^{-16} $WHz^{-1/2}$ were also measured at 200 K at a wavelength of 1.55 μm [8].

To extend the useful operating wavelength beyond a wavelength of 1600 nm, in $In_xGa_{1-x}As$ absorber photodiodes, an In mole fraction higher than 0.53 is required. Unfortunately, as the indium concentration is raised above x=0.53, then InGaAs cannot be grown lattice-matched with InP. The mismatch causes dislocations in the absorption region that greatly deteriorate the device's electrical and optical performance. A buffer layer scheme is required to accommodate the lattice mismatch with the underlying substrate: by introducing a compositionally graded buffer layer the lattice constant is changed and crystalline defects are predominantly confined to the buffer. Typical buffer layer materials used in this type of structures are InAlAs and InAsP. Joshi *et al.* [27] used an InAsP graded buffer layer on top of an InP substrate and demonstrated an $In_{0.72}Ga_{0.28}As$ p-i-n photodiode with low dislocation defect density in the absorber, despite 2% lattice mismatch with the InP substrate. At room temperature a 45 μm diameter device had a responsivity of 1.34 A/W and a dark current of 400 nA was measured at -5 V bias at a wavelength of 2.05 μm. Based on this structure the authors developed 16 element and 32 element $In_{0.72}Ga_{0.28}As$ photodiode linear arrays having a cut-off wavelength of 2.2 μm. Based on the dark current data of a single photodiode, dark currents of less than 50 nA per pixel at -5 V were predicted when the array was cooled to 200 K [28].

A linearly graded InAlAs buffer is used by Zhao-Bing *et al*. [29] to incorporate an $In_{0.85}Ga_{0.15}As$ absorber layer to fabricate a photodiode with a cut-off wavelength of approximately 2.7 μm. The detector, 300 μm in diameter, exhibited a dark current of 7.68 μA and 291 nA at 290 K and 150 K respectively at a reverse bias of 10 mV. The measured specific detectivity peak of the device was 4.96×10^9 $cmHz^{1/2}/W$ at 300 K. The specific detectivity is defined as:

$$D^* = \frac{\sqrt{A\Delta f}}{NEP} \tag{2.3}$$

where A is the device area and Δf frequency bandwidth.

For comparison a shorter wavelength (2.5 μm) detector was also designed. It showed lower dark current and higher peak detectivity, when compared to the longer wavelength detector, indicating that dislocations, introduced by the larger lattice

mismatch in the absorption layer of the 2.7 μm device, are not effectively confined in the buffer layer and that further optimization of the buffer layer structure was needed.

Strained InGaAs offers the prospect of longer wavelength photodiode detectors, which are available commercially. Hamamatsu manufactures a G12183 series of p-i-n photodiodes with cut-off wavelengths from 2.55 to 2.6 μm. In terms of dark current, the best non-cooled type has a dark current of 400 nA at -0.5 V and at 298 K, while the best thermo electrically (TE) cooled type has a dark current of 85 nA at -0.5 V and at 253 K [30]. Details of the microstructures used in these commercial devices are not available.

2.5.3 Mid-IR range photodiodes

2.5.3.1 Type II superlattice photodiodes

Band structure engineering in heterostructures can permit photodiode operation at longer wavelength spectral regions. By using repeats of two or more dissimilar materials organised in a periodic structure with layer thicknesses of the order of nanometres it is possible to form quantum confined structures that operate at particular wavelength ranges.

In 1970, Esaki and Tsu proposed, for the first time, the fabrication of this artificial periodic structure which they termed a superlattice (SL) [31]. Due to its periodic structure, the superlattice has a periodic potential. It can be considered as a set of quantum wells with finite potential barrier height repeated periodically along the growth direction of the SL and barrier width thin enough for electrons to tunnel through, so that the electrons see the alternating layers as a periodic potential. This superperiodic potential, coming from the superperiodic lattice structure, acts on the conduction electrons and holes to create new Brillouin zones and mini energy bands superimposed on the band structures of the constituent layers [32].

SLs can be classified according the confinement scheme of their electrons and holes. Given two semiconductors A and B forming the structure of B/A/B/A…, three scenarios, as shown in Figure 2.10, can be obtained. These confinement schemes are usually labelled type I and type II. In type I, electrons and holes are both confined within layer A which is the potential well for both electrons and holes. In type II superlattices, electrons are confined in layer (A) and holes are confined in layer B. In

addition, a superlattice formed by semiconductors in which the conduction band of one material overlaps the valence band of the other is sometimes also referred to as a type III superlattice [33].

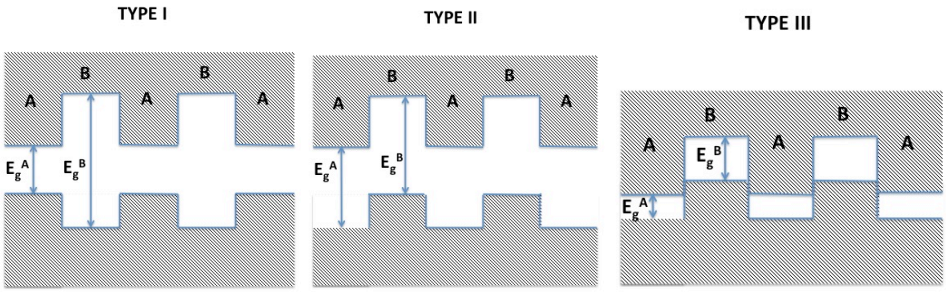

Figure 2.10 *Schematic diagram of three arrangements of the confinement of electrons and holes formed by two semiconductors A and B.*

Type II superlattices can be used for IR detection by engineering a narrow bandgap structure from two larger bandgap semiconductor materials. Typical materials used in Type II photodetectors for short and mid wave IR detection are InGaAs/GaAsSb and InAs/GaAs.

InGaAs/GaAsSb superlattices have been shown to detect efficiently at wavelengths up to 3.4 μm. P-i-n diodes, grown on InP substrates, with an i-region consisting of a SL of $In_{0.53}Ga_{0.47}As/GaAs_{0.51}Sb_{0.59}$ with layer thickness of 5 nm were demonstrated by Sidhu *et al.* and Inada *et al.* [34], [35]. Both papers present a room temperature cutoff wavelength of around 2.4 μm. Their room temperature peak responsivities were 0.77 A/W and 0.6 A/W, respectively, at $\lambda = 2.23$ μm. Dark currents at -1 V bias were in the order of 100 nA for both structures at room temperature, and decreased to as low as 100 pA at 200 K. This result is more than an order of magnitude lower than comparable bulk HgCdTe and suggests that the InGaAs/GaAsSb SL material system has potential as a candidate for room temperature operation. In 2006 Sidhu *et al.* [36] continued their studies developing an InP-based separate absorption-multiplication (SAM) APD using the $In_{0.53}Ga_{0.47}As/GaAs_{0.51}Sb_{0.59}$ type II SL as absorber and InP in the avalanche multiplication region. The room temperature dark current at the punchthrough voltage of 37 V was 130 nA for a 44 μm-device. The dark current drops rapidly with temperature, and at 225 K, is approximately 10 nA giving a current density of 0.66 mA/cm^2 at 90% of the breakdown. The device exhibits a multiplication gain in excess

of 30 at room temperature and in excess of 200 at 225 K. A similar structure, with $In_{0.52}Al_{0.48}As$ used as the material for the multiplication region, instead of InP, was reported by Ong *et al.* [37]. In this paper, $In_{0.52}Al_{0.48}As$ is preferred to InP for the avalanche material because it has weaker breakdown-voltage temperature dependence which allows more APD design tolerance: the breakdown-voltage temperature dependence is 40 mV/K, which is much smaller than 88 mV/K observed by Sidhu *et al*. for InP [36]. The APD exhibits an absorption cut-off wavelength of 2.5 μm and gain multiplication factor above 50 at 290 K and 150 at 200 K. A responsivity of 0.47 A/W (without gain) for the APD at a wavelength of 2004 nm was also demonstrated. The temperature-dependent dark current density- voltage data of a 90 μm diameter APD is shown in Figure 2.11.

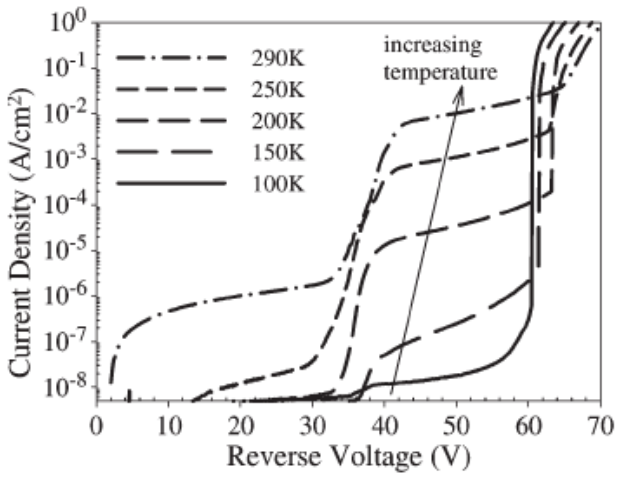

Figure 2.11 *Temperature-dependent dark current density-voltage data of a 90 μm diameter mesa geometry SAM APD with $In_{0.53}Ga_{0.47}As/GaAs_{0.51}Sb_{0.59}$ (150 pairs) type II SL and $In_{0.52}Al_{0.48}As$ as absorber and multiplication regions, respectively. Figure taken from [37].*

For longer wavelengths an InGaAs/GaAsSb SL with different compositions can be used. An example of how the spectral absorption range varies with the InGaAs/GaAsSb SL composition is presented by Chen [38]. In this paper, the comparison of InP based p-i-n photodiodes for the NWIR/MWIR spectral regions using a strain compensated $In_{0.34}Ga_{0.66}As/GaAs_{0.25}Sb_{0.75}$ SL (where the compressively strained $GaAs_{0.25}Sb_{0.75}$ layers are strain compensated by tensile strained $In_{0.34}Ga_{0.66}As$) and a lattice matched $In_{0.53}Ga_{0.47}As/GaAs_{0.5}Sb_{0.5}$ SL is presented. It was found that the device with the absorption region formed from 100 periods of 7 nm thick $In_{0.34}Ga_{0.66}As$ and 5 nm thick

$GaAs_{0.25}Sb_{0.75}$ strain compensated type II SL has an optical response up to 3.4 μm, while the device with 100 periods of 7 nm thick $In_{0.53}Ga_{0.47}As$ and 5 nm thick $GaAs_{0.5}Sb_{0.5}$ lattice matched type II superlattice has an optical response up to 2.8 μm. The dark current densities shown by the strained and the matched structure were 9.7 mA/cm^2 and 1.66 mA/cm^2 respectively at 290 K under -0.5 V reverse bias. The strain compensated device shows a specific detectivity of 2.0×10^8 cmHz$^{1/2}$W^{-1} at wavelength of 3 μm at 290 K and 1.0×10^9 cmHz$^{1/2}$W^{-1} at 200 K.

An InAs/GaSb SL is another common structure used for mid-IR photodetectors. An InAs/GaSb SL APD with a cut off wavelength which varies from 4.14 μm at 77 K to 4.92 μm at 300 K was reported by Mallick *et al*. [39]. To improve the performance of the device a ZnS layer was deposited as passivation material for the APD. The dark current measured at reverse bias of -1 V is 2 μA at room temperature and decrease down to 1 μA at 77 K. A maximum multiplication gain of 600 at reverse bias of -20 V at 77 K was achieved; it was calculated as the difference between the photocurrent and the dark current normalized to the unity gain dark current. In 2009 Cervera *et al.* [40] demonstrated a p-i-n photodiode with a cut off wavelength of 4.9 μm at 80 K. The structure had a 1 μm thick absorbing region (220 SL periods) and had a responsivity of 360 mA/W at 4.5 μm and at 80 K. The dark current density measured was as low as 0.1 μA/cm^2 at -50 mV. P-i-n based detectors for the longer wave MWIR spectral region using a type II strained layer InAs/GaSb SL were reported by Khoshakhlagh *et al.* [41]. In this paper, the authors designed and fabricated a p-i-n structure that gave a cutoff wavelength of 8 μm. A study of how the device performance changed as a function of the absorber doping was also carried out. It was found that by p-doping the InAs layer in the absorption region of the device, the dark current of the p-i-n photodiodes decreases due to the decreasing of the total dark current density associated with diffusion and generation recombination process. At the same time the p-i-n responsivity and detectivity increase. Table 2.1 summarises the data obtained by Khoshakhlagh *et al*. at 77 K for the three p-i-n photodiodes with the same SL design varying the absorber doping concentration (absorber thickness 1.9 μm for all the diodes).

Sample	Dark Current Density (A/cm^2) |0.1| V	Responsivity (at λ=7 μm) (A/W) |0.2| V	Detectivity (at λ=7 μm) ($cm\ Hz^{1/2}W^{-1}$) |0.1| V
P-i-n (no intentional doping)	0.2	0.62	1.3×10^{9}
P-i-n (1×10^{16} cm^{-3})	0.11	0.8	4.2×10^{9}
P-i-n (5×10^{15} cm^{-3})	0.08	1.03	6.1×10^{9}

Table 2.1 *Summary of dark current density, responsivity and detectivity measured at 77 K at 7 μm wavelength for p-i-n detectors using type II strained InAs/GaSb SL. Table taken from [41].*

2.5.3.2 HgCdTe photodiodes

HgCdTe is a unique type of infrared detector material. The bandgap of HgCdTe can be tuned by over an order of magnitude by varying the Mercury and Cadmium composition to give a bandgap of less than 0.1 eV to greater than 1.5 eV, allowing to tune to wavelengths from 2 to 24 μm.

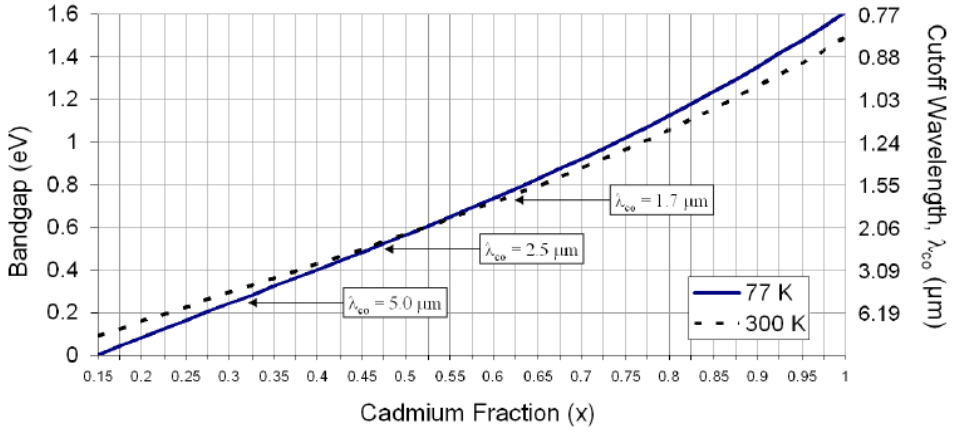

Figure 2.12 *Bandgap and cutoff wavelength of $Hg_{1-x}Cd_xTe$ as a function of Cd fraction, x at temperatures of 77 K and 300 K. Figure taken from [42].*

Due to the temperature dependence of the bandgap, it is important to define the temperature of operation as well as wavelength range of operation when fabricating

HgCdTe material. Figure 2.12 compares the Cd fraction x required to obtain a particular bandgap value at 77 K and at room temperature.

A significant characteristic for this detector is the excess noise factor, which can reach very low levels for electron injection avalanche structures in short to long wave IR. Early work by Alabedra *et al*. [43] on HgCdTe APDs with 0.92 eV bandgap (cutoff wavelength of 1.35 μm) showed an excess noise that corresponded to a k of around 10 for a hole injected device under illumination of light at 1.3 μm. Leveque *et al*. [44] calculated that HgCdTe presents hole or electron majority multiplication, depending on the Cd fraction x, with a ratio of ionisation factors β/α that changes rapidly with a maximum of 30 for x=0.6 and a minimum of 0.06 for x=0.41. The lowest excess noise has been observed by Beck and co-workers [45] for electron initiated multiplication in $Hg_{0.7}Cd_{0.3}Te$ which has at 77 K a bandgap of around 0.28 eV that corresponds to a 4.3 μm cutoff wavelength. An almost pure exponential increase in gain with voltage was obtained when the APD was illuminated by 1.55 μm light, suggesting that only electrons were subjected to impact ionisation. A gain of more than 1000 at 13.1 V and a gain normalised dark current density of 3.4 $nAcm^{-2}$ at 12.5 V has been observed at cryogenic temperature. For this type of structure the excess noise had a value of 1 and was independent of gain. Similar noiseless gain has been obtained with HgCdTe with a bandgap of 0.13 eV corresponding to a cutoff wavelength of 9.7 μm. At 77 K and at 5 V this device has a gain of more than 100 and a normalised dark current density of 0.58 $mAcm^{-2}$ with no tunnelling observed. Wider bandgap 0.56 eV HgCdTe gives a 2.2 μm wavelength cutoff and shows similar exponential gain behaviour; however, unlike the narrower band gap compositions, it could be operated at room temperature at higher operating voltages and with an excess noise of 2. At 77 K, the process is deterministic and the excess noise factor can reach a value close to unity, while at room temperature phonon interactions randomize the gain process with the result that the excess noise factor is increased (around 2) but still shows the gain independent behaviour of the k=0 APD. The reason for the extremely low noise in HgCdTe for these compositions is attributed to the unique band structure in this material. The higher L and X satellite valleys are significantly above the Γ minimum. Electrons can therefore gain energy rapidly in the low scattering environment of the Γ valley and impact ionise more readily in the first conduction band without transferring to the higher conduction bands where the scattering rates are significantly higher. This coupled with the large hole scattering rate that prevent holes from impact ionising leads to very large α/β ratio. This means

that avalanche breakdown, where the gain goes to an extremely high value, has not been observed and low excess noise has been achieved. Figure 2.13 shows the band structures for CdTe and HgTe; the $Hg_{1-x}Cd_xTe$ bandgap structure is a combination between the CdTe and HgTe depending on the Cd fraction.

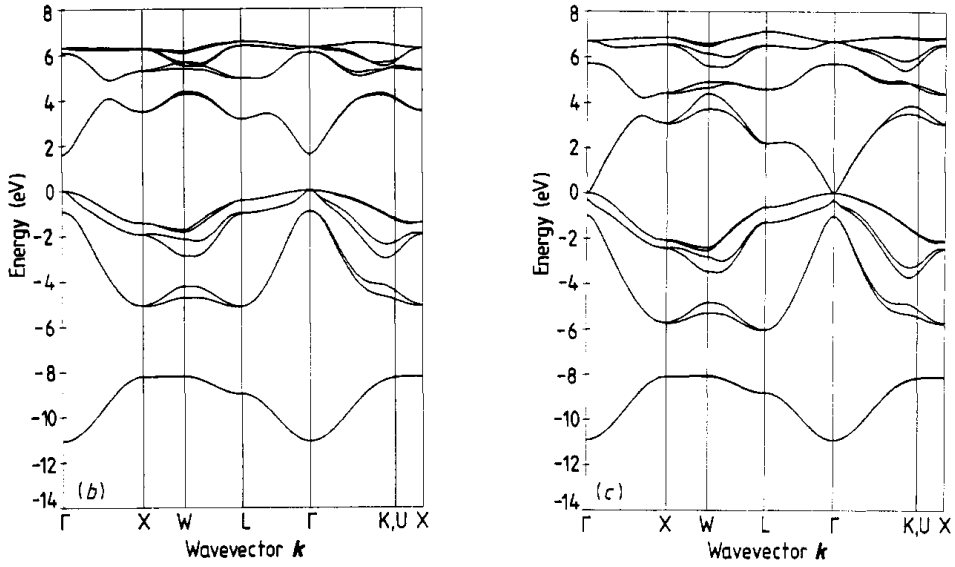

Figure 2.13 *Band structures for CdTe (left) and HgTe (right) [46]. Both materials present a relatively flat valence band and a conduction band with high X and L valley separation energies with respect to the Γ valley minimum. The $Hg_{1-x}Cd_xTe$ bangap structure is a combination between the two and dependent on the Cd fraction. Due to the high valley separation energies and the low phonon scattering in $Hg_{1-x}Cd_xTe$, the electrons can impact ionise within the Γ valley. On the other hand, while the electrons can easily acquire the required energy for impact ionisation, the holes cannot: the relatively flat heavy hole band limits the rate at which holes can gain energy.*

2.5.3.3 InSb photodiodes

Another material that can detect light at wavelengths in the mid infrared is InSb, whose energy gap at room temperature is 0.18 eV which corresponds to a cutoff wavelength of 7 μm [47]. The InSb band structure is very similar to HgCdTe, it presents a high X and L valley separation energies with respect to the Γ valley minimum (more than twice the band gap energy) [48]. Due to the high valley separation energies and the low phonon scattering in InSb, the electrons can impact ionise within the Γ valley [49]. At present,

InSb technology for SPADs is immature and few avalanche photodiodes have been developed so far. In 2013 Ueno *et al*. [50] developed an InSb p-i-n photodiode that operated at wavelengths from 2 to 7 μm at room temperature. To optimise the detector performance in terms of dark current, the authors carried out doping density studies in the different layers to find the best configuration and incorporated an AlInSb barrier layer to suppress the effect of the diffusion current. N-type doping concentrations from 2×10^{16} to 8×10^{18} were studied showing that, when the carrier density exceeds 4.3×10^{18}, over 80% of the infrared radiation with a wavelength of 3 μm or more can penetrate InSb. Careful analysis of the AlInSb barrier thickness and Al composition were also presented showing a dark current of around 0.15 mA at a reverse bias of 0.5 V for the structure having an AlInSb barrier 20 nm thick with 18 % Al concentration.

Theoretical studies have been carried out on InSb diodes and APDs by Abautret *et al*. [51]. In the case of an electron initiated avalanche process, the authors studied different APD designs in order to decrease the band to band tunnelling current. The p-type absorber doping level and, in particular, the multiplication layer thickness have been found to be critical parameters to reduce the level of band to band tunnelling. The best simulated results have been obtained for an InSb structure with a 2 μm p-type linear graded doping layer from 5×10^{16} cm^{-3} to $1\times10^{18}cm^{-3}$ and 3 μm n-type multiplication layer with a background doping level under 1×10^{15} cm^{-3}. The advantage of this structure is that it leads to a reduction of electric field inducing a weaker available energy for the tunnelling process. 77 K dark current density data show that in this design tunnelling starts at 2.5 V: the dark current density is dominated by tunnelling from 2.5 V, it increases from a value around 10^{-4} A/cm^2 at 2.5 to 1 A/cm^2 at 4.5 V. Under illumination of 1.55 μm wavelength light (0.01 W/cm^{-2}), it achieves a gain value higher than 10 at 4.5 V and at 77 K. Impact ionisation processes in InSb have been studied theoretically by Herbert *et al*. [52]. A p-i-n InSb structure with i-layer 3.2 μm thick has been simulated. The doping concentration in the p and n layers is 1×10^{17} cm^{-3} while in the i layer it is 1×10^{14} cm^{-3}. The simulations show that, for fields below 6×10^{3} Vcm^{-1}, the ratio of electron to hole ionisation coefficients k (α/β) is greater than 10^2. This implies that very low excess noise can be expected for fields in this range. At room temperature the excess noise factor of the simulated structure approaches a value around 2 at a gain of 60. Gain of around 60 was obtained, at room temperature, when the diode was reverse biased up to 2.5 V. These low noise and high gain characteristics show some potential for InSb to be used for for e-APDs.

2.6 Conclusions

Reverse biased p-n or p-i-n junctions are commonly used to detect light from X-ray to the infrared wavelengths. For low level radiation detection APDs or SPADs can be used to provide internal gain due to the impact ionisation phenomenon. The simplest design for APDs or SPADs uses the same material for the whole structure. For infrared detection, unfortunately, few materials offer a high absorption coefficient in conjunction with a high multiplication, low dark current and low excess noise factor (properties fundamental for a good multiplication region material). One of the main issues is that the multiplication layer requires a very high electric field, and this often causes band-to-band tunnelling across the relatively narrow band-gap. Thus, sophisticated APD and SPAD designs have been developed for infrared detection. The most common is a separate absorption multiplication region (SAM) structure. In this design the most appropriate absorption material is chosen according to the required application wavelengths and a separate material is chosen for the multiplication region to ensure high detector performance in terms of gain, dark current and excess noise factor. In the infrared range above 1.7 μm type II semiconductor superlattices, HgCdTe and InSb photodetectors are promising technologies. Typical materials used in Type II photodetectors for short and mid wave IR detection are InGaAs/GaAsSb and InAs/GaAs. The device properties vary depending on the choice of superlattice materials, and the structures in which they can be used. However, processing and engineering of device structures incorporating these superlattices is extremely challenging, though APDs with low dark current and high gain have been demonstrated. HgCdTe has a bandgap that can be tuned according to the Cd concentration, allowing the detection of light from 0.83 μm to greater than 12 μm. It can be used to produce extremely low noise, high gain APDs, mainly due to its unique band structure: while electrons can easily acquire the requisite energy to impact ionise, holes cannot leading to an electron APD. This reduction in feedback from holes leads to a more deterministic impact ionisation process and reduces the excess noise factor. Unfortunately, HgCdTe is not easy to grow or process. thus making device quality reproducibility difficult. InSb has an energy gap of 0.18 eV at room temperature, corresponding to a cut-off wavelength of 7 μm. The InSb band structure is very similar to HgCdTe, so it can also be used to produce electron APDs. At present, although it promises high gain and low noise, InSb technology for SPADs is immature and few avalanche photodiodes have been developed so far. APD designs require further development to decrease the band to band tunnelling current.

Another material that allows detection up to a wavelength of 3.5 μm which has shown excellent electron multiplying behaviour is InAs. InAs photodetectors will be discussed in detail in Chapter Three.

2.7 References

[1] G. P. Agrawal, "Fiber-optic communication systems″, vol. 222, John Wiley & Sons, 2010.

[2] W. Becker, "Advanced time-correlated single photon counting techniques" (Series in chemical physics), vol. 81, Springer-Verlag, 2005.

[3] G. Stillman and C. Wolfe, "Avalanche photodiodes," *Semiconductors and semimetals,* vol. 12, pp. 291-393, 1977.

[4] G. Rees and J. David, "Nonlocal impact ionization and avalanche multiplication," *Journal of Physics D: Applied Physics,* vol. 43, pp. 243001 1-17, 2010.

[5] A. R. J. Marshall, "The InAs electron avalanche photodiode and the influence of thin avalanche photodiodes on receiver sensitivity," *PhD Thesis,* 2009.

[6] S. Cova, M. Ghioni, A. Lacaita, C. Samori, and F. Zappa, "Avalanche photodiodes and quenching circuits for single-photon detection," *Applied Optics,* vol. 35, pp. 1956-1976, 1996.

[7] S. Cova, M. Ghioni, A. Lotito, I. Rech, and F. Zappa, "Evolution and prospects for single-photon avalanche diodes and quenching circuits," *Journal of Modern Optics,* vol. 51, pp. 1267-1288, 2004.

[8] S. Pellegrini, R. E. Warburton, L. J. J. Tan, J. S. Ng, A. B. Krysa, K. Groom*, et al.*, "Design and performance of an InGaAs-InP single-photon avalanche diode detector," *IEEE Journal of Quantum Electronics,* vol. 42, pp. 397-403, 2006.

[9] W. Dash and R. Newman, "Intrinsic optical absorption in single-crystal germanium and silicon at 77 K and 300 K," *Physical Review,* vol. 99, pp. 1151-1155, 1955.

[10] H. Melchior and W. Lynch, "Signal and noise response of high speed germanium avalanche photodiodes," *IEEE Transactions on Electron Devices,* vol. 13, pp. 829-838, 1966.

[11] H. Ando, H. Kanbe, T. Kimura, T. Yamaoka, and T. Kaneda, "Characteristics of germanium avalanche photodiodes in the wavelength region of 1-1.6 μm," *IEEE Journal of Quantum Electronics,* vol. 14, pp. 804-809, 1978.

[12] T. Mikawa, S. Kagawa, T. Kaneda, Y. Toyama, and O. Mikami, "Crystal orientation dependence of ionization rates in germanium," *Applied Physics Letters,* vol. 37, pp. 387-389, 1980.

[13] J. P. R. David and C. H. Tan, "Material considerations for avalanche photodiodes," *IEEE Journal of Selected Topics in Quantum Electronics,* vol. 14, pp. 998-1009, 2008.

[14] A. Lacaita, P. Francese, F. Zappa, and S. Cova, "Single-photon detection beyond 1 μm: performance of commercially available germanium photodiodes," *Applied Optics,* vol. 33, pp. 6902-6918, 1994.

[15] G. Buller, S. Fancey, J. Massa, A. Walker, S. Cova, and A. Lacaita, "Time-resolved photoluminescence measurements of InGaAs/InP multiple-quantum-well structures at 1.3 μm wavelengths by use of germanium single-photon avalanche photodiodes," *Applied Optics,* vol. 35, pp. 916-921, 1996.

[16] A. Tosi, A. Dalla Mora, F. Zappa, and S. Cova, "Germanium and InGaAs/InP SPADs for single-photon detection in the near-infrared," in *Optics East 2007*, 2007, pp. 67710P 1-12, 2007.

[17] Y. Kang, H.-D. Liu, M. Morse, M. J. Paniccia, M. Zadka, S. Litski*, et al.*, "Monolithic germanium/silicon avalanche photodiodes with 340 GHz gain–bandwidth product," *Nature Photonics,* vol. 3, pp. 59-63, 2008.

[18] Z. Lu, Y. Kang, C. Hu, Q. Zhou, H.-D. Liu, and J. C. Campbell, "Geiger-mode operation of Ge-on-Si avalanche photodiodes," *IEEE Journal of Quantum Electronics,* vol. 47, pp. 731-735, 2011.

[19] R. E. Warburton, G. Intermite, M. Myronov, P. Allred, D. R. Leadley, K. Gallacher*, et al.*, "Ge-on-Si Single-Photon Avalanche Diode Detectors: Design, Modeling, Fabrication, and Characterization at Wavelengths 1310 and 1550 nm," vol. 60, pp. 3807-3813, 2013.

[20] F. Bacher, J. Blakemore, J. Ebner, and J. Arthur, "Optical-absorption coefficient of $In_{1-x}Ga_xAs/InP$," *Physical Review B,* vol. 37, pp. 2551-2557, 1988.

[21] E. Zielinski, H. Schweizer, K. Streubel, H. Eisele, and G. Weimann, "Excitonic transitions and exciton damping processes in InGaAs/InP," *Journal of Applied Physics,* vol. 59, pp. 2196-2204, 1986.

[22] D. Humphreys, R. King, D. Jenkins, and A. Moseley, "Measurement of absorption coefficients of $Ga_{0.47}In_{0.53}As$ over the wavelength range 1.0–1.7 μm," *Electronics Letters,* vol. 21, pp. 1187-1189, 1985.

[23] H. Burkhard, H. Dinges, and E. Kuphal, "Optical properties of $In_{1-x}Ga_xP_{1-y}As_y$, InP, GaAs, and GaP determined by ellipsometry," *Journal of Applied Physics,* vol. 53, pp. 655-662, 1982.

[24] J. S. Ng, J. P. R David, G. J. Rees, and J. Allam, "Avalanche breakdown voltage of $In_{0.53}Ga_{0.47}As$," *Journal of Applied Physics,* vol. 91, pp. 5200-5202, 2002.

[25] L. J. J. Tan, J. S. Ng, C. H. Tan, and J. P. R. David, "Avalanche noise characteristics in submicron InP diodes," *IEEE Journal of Quantum Electronics,* vol. 44, pp. 378-382, 2008.

[26] J. C. Campbell, "Recent advances in telecommunications avalanche photodiodes," *Journal of Lightwave Technology,* vol. 25, pp. 109-121, 2007.

[27] A. Joshi and D. Becker, "High-speed low-noise p-i-n InGaAs photoreceiver at 2 μm wavelength," *IEEE Photonics Technology Letters,* vol. 20, pp. 551-553, 2008.

[28] A. Joshi and S. Datta, "High-Speed, Large-Area, p-i-n InGaAs Photodiode Linear Array at 2 μm Wavelength," in *Infrared Technology and Applications XXXVIII,* vol. 8353, pp 85533D 1-9, 2012.

[29] T. Zhao-Bing, G. Yi, W. Kai, and Z. Yong-Gang, "Gas source MBE-grown metamorphic InGaAs photodetectors using InAlAs buffer and cap layers with cut-off wavelength up to 2.7 μm," *Chinese Physics Letters,* vol. 25, pp. 2292-2295, 2008.

[30] Hamamatsu. Strained InGaAs. http://www.hamamatsu.com/resources/pdf/ssd/g12183_series_kird1119e02.pdf

[31] L. Esaki and R. Tsu, "Superlattice and Negative Differential Conductivity in Semiconductors," *IBM Journal of Research and Development,* vol. 14, pp. 61-65, 1970.

[32] C. Kittel, "Introduction to Solid State Physics", Eight Edition ed., John Willey & Sons, 2005.

[33] J. H. Davies, "The physics of low-dimensional semiconductors: an introduction", Cambridge University press, 1998.

[34] R. Sidhu, N. Duan, J. C. Campbell, and A. L. Holmes, "A long-wavelength photodiode on InP using lattice-matched GaInAs-GaAsSb type-II quantum wells," *IEEE Photonics Technology Letters,* vol. 17, pp. 2715-2717, 2005.

[35] H. Inada, K. Miura, Y. Nagai, M. Tsubokura, A. Moto, Y. Iguchi*, et al.*, "Low Dark Current SWIR Photodiode with InGaAs/GaAsSb Type II Quantum Wells grown on InP Substrate," in *2009 IEEE 21st International Conference on Indium Phosphide & Related Materials,* pp. 149-152, 2009.

[36] R. Sidhu, L. Zhang, N. Tan, N. Duan, J. Campbell, A. Holmes, *et al.*, "2.4 μm cutoff wavelength avalanche photodiode on InP substrate," *Electronics Letters,* vol. 42, pp. 181-182, 2006.

[37] D. S. G. Ong, J. S. Ng, Y. L. Goh, C. H. Tan, S. Y. Zhang, and J. P. R. David, "InAlAs Avalanche Photodiode With Type-II Superlattice Absorber for Detection Beyond 2 μm," *IEEE Transactions on Electron Devices,* vol. 58, pp. 486-489, 2011.

[38] B. L. Chen, W. Y. Jiang, J. R. Yuan, A. L. Holmes, and B. M. Onat, "SWIR/MWIR InP-Based p-i-n Photodiodes with InGaAs/GaAsSb Type-II Quantum Wells," *IEEE Journal of Quantum Electronics,* vol. 47, pp. 1244-1250, 2011.

[39] S. Mallick, K. Banerjee, S. Ghosh, J. B. Rodriguez, and S. Krishna, "Midwavelength infrared avalanche photodiode using InAs-GaSb strain layer superlattice," *IEEE Photonics Technology Letters,* vol. 19, pp. 1843-1845, 2007.

[40] C. Cervera, J. B. Rodriguez, R. Chaghi, H. Ait-Kaci, and P. Christol, "Characterization of midwave infrared InAs/GaSb superlattice photodiode," *Journal of Applied Physics,* vol. 106, pp. 024501 1-5, 2009.

[41] A. Khoshakhlagh, S. Myers, H. Kim, E. Plis, N. Gautam, S. J. Lee, *et al.*, "Long-Wave InAs/GaSb Superlattice Detectors Based on nBn and Pin Designs," *IEEE Journal of Quantum Electronics,* vol. 46, pp. 959-964, 2010.

[42] J. W. Beletic, R. Blank, D. Gulbransen, D. Lee, M. Loose, E. C. Piquette, *et al.*, "Teledyne Imaging Sensors: Infrared imaging technologies for Astronomy & Civil Space," in *High Energy, Optical, and Infrared Detectors for Astronomy III,* vol. 7021, pp. 70210H 1-14, 2008.

[43] R. Alabedra, B. Orsal, G. Lecoy, G. Pichard, J. Meslage, and P. Fragnon, "An $Hg_{0.3}Cd_{0.7}Te$ avalanche photodiode for optical-fiber transmission systems at λ= 1.3 μm," *IEEE Transactions on Electron Devices,* vol. 32, pp. 1302-1306, 1985.

[44] G. Leveque, M. Nasser, D. Bertho, B. Orsal, and R. Alabedra, "Ionization energies in $Cd_xHg_{1-x}Te$ avalanche photodiodes," *Semiconductor Science and Technology,* vol. 8, pp. 1317-1323, 1993.

[45] J. Beck, C. Wan, M. Kinch, J. Robinson, P. Mitra, R. Scritchfield, *et al.*, "The HgCdTe electron avalanche photodiode," *Journal of Electronic Materials,* vol. 35, pp. 1166-1173, 2006.

[46] A. Chen, Y. Lai-Hsu, S. Krishnamurthy, and M. Berding, "Band structures of HgCdTe and HgZnTe alloys and superlattices," *Semiconductor Science and Technology,* vol. 5, pp. S100-S102, 1990.

[47] A. Rogalski, "Infrared photon detectors," *SPIE Optical Engineering Press*, vol 1, 1995.

[48] IOFFE. InSb band structure. http://www.ioffe.ru/SVA/NSM/Semicond/InSb/bandstr.html.

[49] C. Anderson and C. Crowell, "Threshold energies for electron-hole pair production by impact ionization in semiconductors," *Physical Review B,* vol. 5, pp. 2267-2272, 1972.

[50] K. Ueno, E. G. Camargo, T. Katsumata, H. Goto, N. Kuze, Y. Kangawa*, et al.*, "InSb Mid-Infrared Photon Detector for Room-Temperature Operation," *Japanese Journal of Applied Physics,* vol. 52, pp. 092202 1-6, 2013.

[51] J. Abautret, J. Perez, A. Evirgen, F. Martinez, P. Christol, J. Fleury*, et al.*, "Electrical modeling of InSb PiN photodiode for avalanche operation," *Journal of Applied Physics,* vol. 113, pp. 183716 1-7, 2013.

[52] D. Herbert, P. Childs, R. A. Abram, G. Crow, and M. Walmsley, "Self-consistent 2-d monte carlo simulations of InSb APD," *IEEE Transactions on Electron Devices,* vol. 52, pp. 2175-2181, 2005.

Chapter Three

3. InAs Avalanche Photodiodes

3.1 InAs crystal and band structures

The choice of different semiconductor materials in a APD configuration is not only important for setting its operating wavelength range but also required for optimisation of detector performance. For these reasons the choice of a particular material is made with reference to its application. For example, Si APDs are good optical detectors for applications that detect photons up to wavelengths of 1.1 μm or lower, whereas InGaAs, Ge on Si and HgCdTe APDs have been used at long wavelengths. In recent years, the infrared spectral range between 1.55 and 3.55 μm has become increasingly important for many applications including eye-safe LIDAR imaging, gas sensing, thermometry, free space communications in the NWIR and MWIR ranges. Within this spectral range III-V compounds can be grown and processed to be good candidates for avalanche infrared detectors. One material that shows very promising properties for APD and SPAD operation is InAs because of its unique band structure respect the other III-V semiconductors. Although commercially available InAs photodiodes exist, there are currently no APDs on the market.

InAs is a semiconductor composed of indium (III) and arsenic (V) grown in a zinc blende structure. In this type of binary compound structure, the arrangement of the atoms is the same as diamond -i.e. two face centred cubic (FCC) lattices displaced from each other by one quarter of a body diagonal, but with the two species In and As alternating. The crystal structure of InAs is shown in the Figure 3.1 (the black and white atoms are In and As respectively):

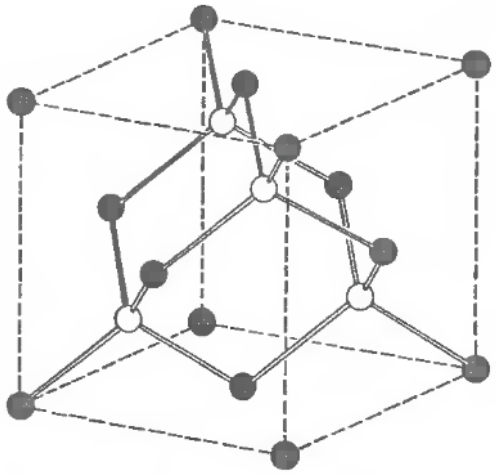

Figure 3.1 *InAs zinc blende crystal structure. The black and white atoms are In and As respectively. Figure taken from [1].*

InAs is a narrow direct bandgap semiconductor with E_g=0.36 eV at room temperature [2] allowing photons with wavelengths up to 3.5 μm to promote electrons to the conduction band, leaving behind holes. The InAs bandstructure is different from wider bandgap III-V materials [3]. InAs shares more similarities with $Hg_xCd_{1-x}Te$, (range of composition from x=0.7 to 0.2). In particular it has the same single carrier type impact ionisation initiated solely by electrons [4], [5], [6]. Some of the interesting behaviour of InAs can be explained by consideration of its bandstructure and, in particular, the confinement of electrons in the first conduction band Γ valley [7]. As shown in Figure 3.2 InAs, in contrast with large gap III-V materials such as InP or GaAs, shows high X and L valley separation energies with respect to the Γ valley minimum (at least twice the band gap energy). In both InP or GaAs electrons must escape the first conduction band Γ valley before they can achieve the ionisation threshold energy. Due to the high valley separation energies and the low phonon scattering in InAs, the electrons can impact ionise within the Γ valley at moderate reverse bias fields. On the other hand, while the electrons can easily acquire the required energy for impact ionisation, the holes cannot: the relatively flat heavy hole band limits the rate at which holes can gain energy. This contrast leads to preferential electron impact ionisation. As explained in Chapter Two, this causes disparate ionisation coefficients α (for electrons) and β (for holes), leading to low excess noise F in InAs avalanche photodiodes.

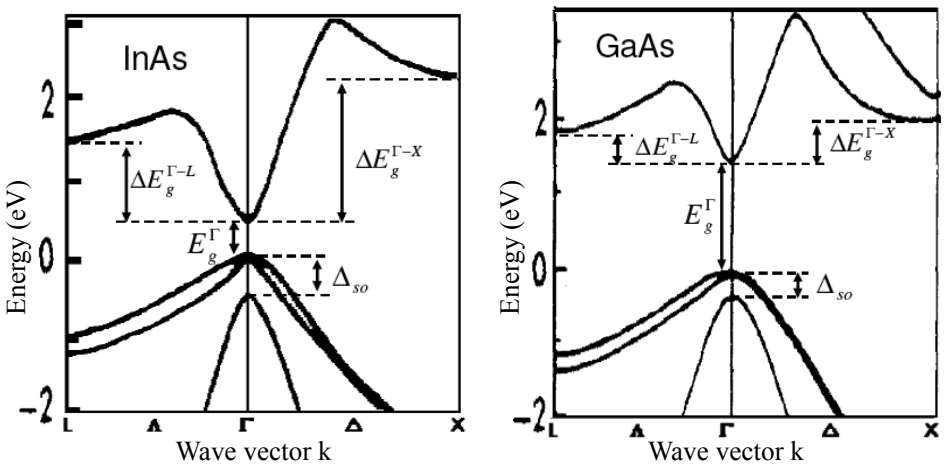

Figure 3.2 *Portion of InAs (on the left) and GaAs (on the right) band structures centred at the Γ-point. The difference in the valence and conduction bands between the two materials are clearly shown: the InAs Γ valley bandgap energy (E_g^{Γ}) is smaller than that of GaAs, while the X and L valley separation energies with respect to the* Γ *valley minimum are smaller for GaAs than InAs. Figures taken from [2], [8].*

3.2 InAs Avalanche Photodiodes multiplication

The properties described in section 3.1 make InAs APDs very promising devices with regards to the single photon detection of infrared light. Interesting results have been achieved by Andrew Marshall and co-workers at the University of Sheffield [2], [4], [9], [10], [11]. In this work a thorough study of both p-i-n and n-i-p InAs diodes was made: growth and processing techniques were analysed and compared to get an InAs APD with as low a leakage current as possible. In Marshall's work the photomultiplication measurements from n-i-p and p-i-n diodes confirm that the electron impact ionisation coefficient α is greater than the hole impact ionisation coefficient β in InAs at room temperature and 77 K. Figure 3.3 shows the carrier injection for reversed bias n-i-p and p-i-n mesa structures under top light illumination: the created photo-holes (h) and electrons (e) travel to the cathode and anode respectively. For a n-i-p geometry junction, for example, the photo-generated hole diffuses from the p into the depletion region, where it is accelerated by the electric field and undergoes impact ionisation.

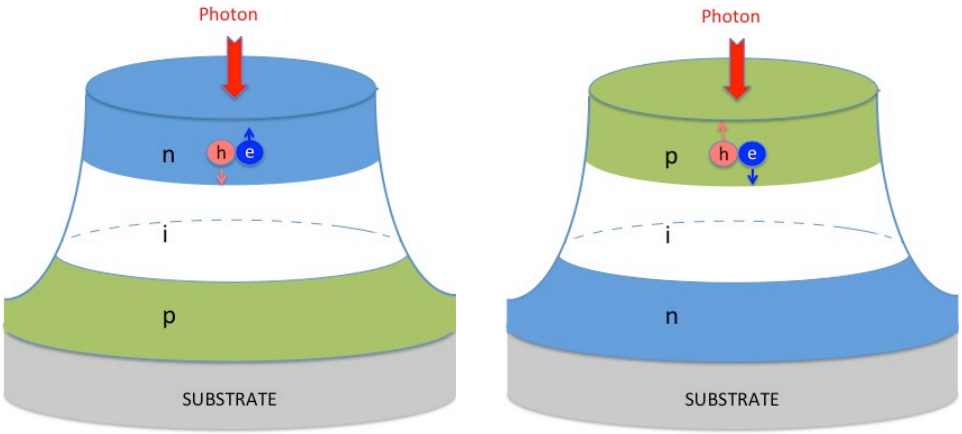

Figure 3.3 *InAs n-i-p (on the left) and p-i-n (on the right) structures under top illumination and reverse bias. The incident photon is absorbed and a hole-electron pair is generated in the device: the blue and pink dots represent an electron and a hole respectively.*

Using lasers with different wavelengths, Marshall *et al.* [4], [2] studied the diode multiplication under pure hole/electron or mixed injection conditions. Close to pure electron injection into the depletion region was achieved by focused p-side illumination of a p-i-n diode with a laser of 633 nm wavelength to ensure that almost all the light was absorbed in the p-type cap layer. According to available spectral absorption data [12], [13], it is expected that less than 1% of the incident light penetrated the p region to reach the i region of the diode. Likewise hole injection into the depletion region was obtained by similar n-side illumination of n-i-p diodes. The variation in the profile of the carrier injection was achieved by illuminating both p-i-n and n-i-p diodes with a 3390 nm wavelength laser. At longer wavelengths the laser penetrates further into the structure creating carriers in all the three layers of the structure, giving mixed injection into the high field depletion region. The experimental results are shown in the Figure 3.4 (N.B the detailed discussion of how *M* is measured are given in connection with our own measurements in Chapter Six).

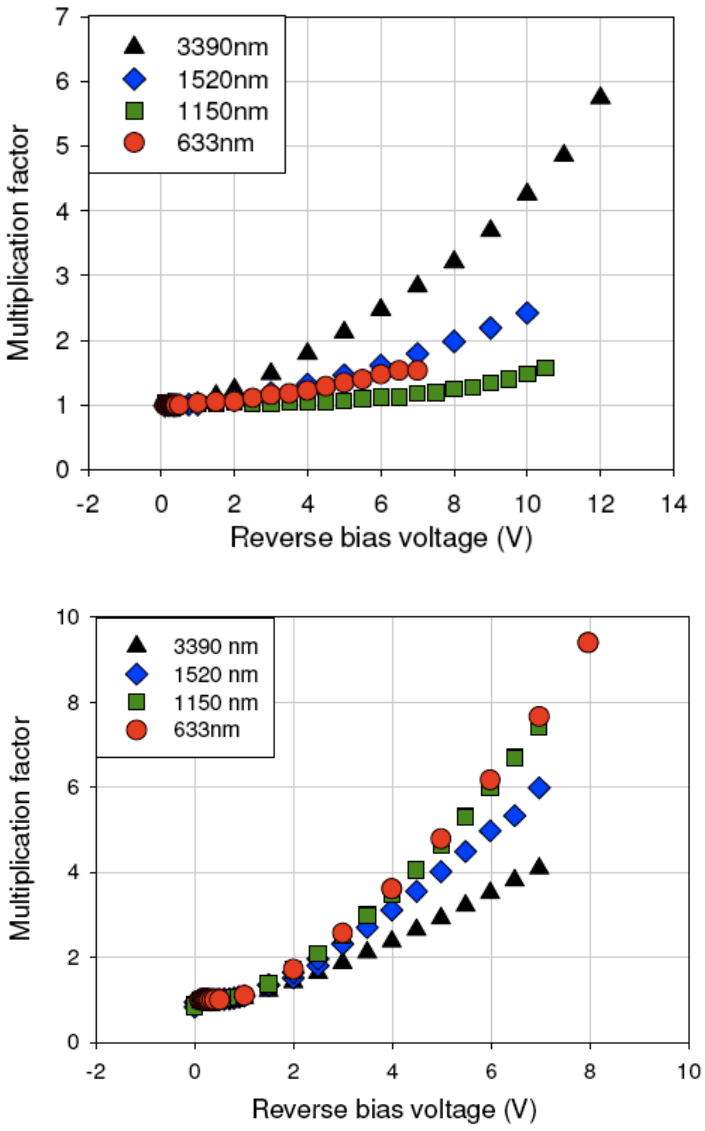

Figure 3.4 *Photomultiplication versus applied reverse bias for 400 μm diameter n-i-p (top) and p-i-n (bottom) diodes using incident light at wavelengths of 3390 nm, 1520 nm, 1150 nm and 633 nm at room temperature. Figures taken from [2].*

In the n-i-p structure, pure hole injection gives a low multiplication. The multiplication is increased by the presence of electrons when a longer wavelength laser is used to illuminate the device to achieve mixed injection. In contrast to expectation, Figure 3.4 shows higher multiplication for the 633 nm laser with respect to the 1150 nm laser: this is due to the high percentage of hole recombination in the cladding when the shorter wavelength laser illuminates the sample.

In the p-i-n structure, pure electron injection gives the highest multiplication, which is reduced by the presence of holes when a longer wavelength laser is used to illuminate the device.

These measurements, performed at different laser wavelengths, provide strong evidence that in InAs the electrons initiate the vast majority of avalanche events, with α several orders of magnitude greater than β. In effect these devices experience electron only impact ionisation and have been termed e-APDs [6]. Marshall's results contradict the previous report by Mikhailova *et al*. [14], based on experimental work on InAs at 77 K, in which they claimed that β is approximately 10 times greater than α. Furthermore, other published work on impact ionisation in InAs also support the argument that the results presented by Mikhailova *et al*. are erroneous. Satyanadh *et al*. [15] modelled the multiplication in p-i-n diodes using a Monte Carlo method at 300 K. They modelled device multiplication for various intrinsic junction widths. However, this model used a physically unrealistic photocurrent injection, as they consider a constant number of photo-generated carriers per unit length within the intrinsic region. However, in agreement with Marshall's work, they found a similar multiplication characteristic shape and very low excess noise. Brennan and Mansour [16], using Monte Carlo modelling at 77 K, were unable to match α modelled by Mikhailova *et al.*: their α was significantly higher and falls more slowly with decreasing electric field than the corresponding Mikhailova coefficient. Although the modelled electron multiplication rises more rapidly, the shape of the multiplication characteristic is much more similar to that presented in Marshall's work and modelled by Satyanadh *et al*., than to that modelled using the coefficients of Mikhailova *et al*. These results are illustrated in Figure 3.5.

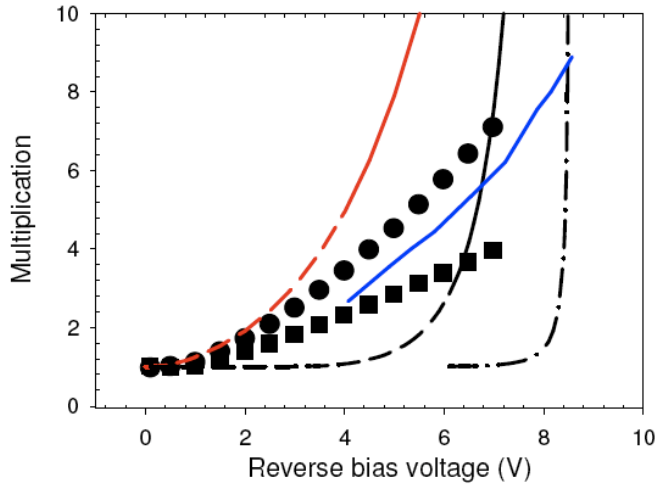

Figure 3.5 *Experimental and modelled multiplication factors found by different authors. Figure taken from [2]. The black circles and black squares represent Marshall's experimental results for* M_e *and* M_{mixed} *when illuminated with 1150 nm and 3390 nm wavelength lasers, respectively; the red solid/dashed line is* M_e *modelled using α from Brennan and Mansour [16] and β=0 (solid line within the published field range and dashed line extrapolated); the black solid/dashed line and black dot dashed line are,* M_h *and* M_e *respectively when modelled using the parameterised α and β from Mikhailova [14]; the blue line is the modelled mixed injection multiplication from Satyanadh [15] for a p-i-n diode with 4 μm intrinsic width [2].*

All previous reports, with the sole exception of those reported by Mikhailova *et al.* [14], demonstrate that the main mechanism for multiplication in an InAs APD is electron impact ionisation.

3.3 InAs Avalanche Photodiodes excess noise

One of most important aspects of impact ionisation dominated by only one carrier type is the effect that it has on the excess noise. Noise measurements on InAs samples are also useful for studying the impact ionisation coefficients. A thorough characterisation of excess noise in both p-i-n and n-i-p InAs diodes has been made in Marshall's research. In these works [2], [10], [11], all the measurements on n-i-p and p-i-n diodes confirm that electron impact ionisation coefficient α is greater than hole impact ionisation coefficient β in InAs. The excess noise measured is shown in Figure 3.6.

(a) N-I-P

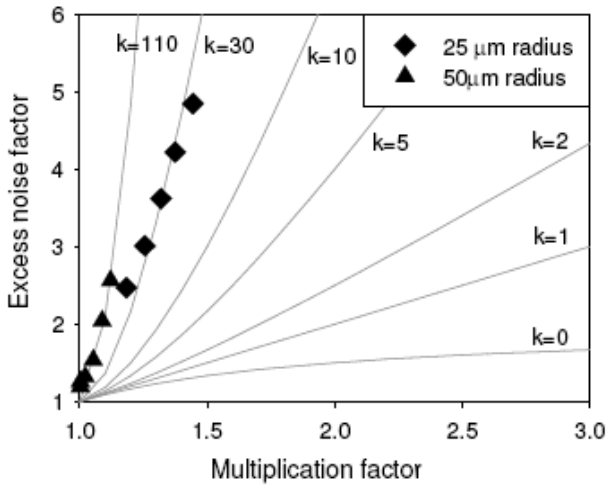

(b) P-I-N

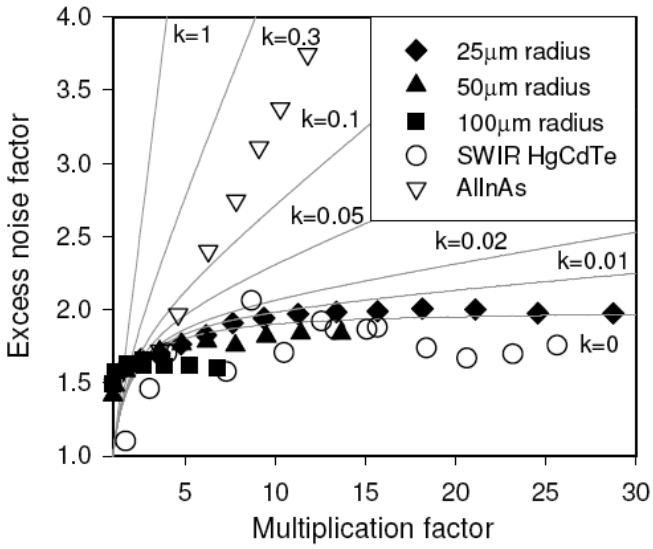

Figure 3.6 *(a) Excess noise results from majority hole injection in InAs n-i-p diodes with different radii. (b) A comparison between the excess noise measured on InAs p-i-n diodes with different radii using majority electron injection and HgCdTe and AlInAs based APDs. Figures taken from [2].*

In Figure 3.6 excess noise measurements for a n-i-p structure show a very high *F* due to the large variation in gain of the injected holes, indicating a low hole impact ionisation rate with respect to that of electrons. The variation between the two curves is likely caused by a greater level of electron contamination in the smallest device. This contamination was due to the electron generation by radiation incident on the i region

since the laser spot size is larger than the top of the mesa. For the same reason, p-i-n excess noise measurements in Figure 3.6 (b) shows only a small variation with the device area.

It must be concluded for the n-i-p diodes, that with truly pure hole injection F would be greater. P-i-n excess noise measurements, instead, show a very low excess noise indicating high electron impact ionisation that confirms the large α/β ratio in InAs. The excess noise results in Figure 3.6 are the lowest reported for III-V materials and are noteworthy. In contrast with other III-V materials, in which the excess noise factor is high and continues to rise with increasing gain (in the figure the excess noise for a InAlAs p-i-n diode is shown too), InAs shares with HgCdTe a comparable low excess noise due to electron only avalanche multiplication.

3.4 InAs ionisation coefficients and avalanche breakdown

Marshall's excess noise characterisation has confirmed that β is essentially zero in InAs and so the InAs APD is an electron multiplying APD: the electron ionisation coefficient α, thus, is the main parameter that causes the carrier generation during the avalanche. Marshall's work [2], [4], [11] uses the multiplication data taken on p-i-n diodes to calculate the value of α. This is dependent on the electric field (ξ) and is given, at room temperature, by:

$$\alpha(\xi) = Ae^{\left(-\frac{B}{|\xi|}\right)^C} \tag{3.1}$$

where at room temperature:

$A=4.621\times10^6$ m^{-1}
$B=1.388\times10^7$ Vm^{-1}
$C=0.3778$

for fields between 5kV/cm and 60 kV/cm.

Figure 3.7 shows the comparison between the newest α calculated by Marshall and published data from Brennan and Mansour [16], Bude and Hess [17], and Mikhailova *et al.* [14].

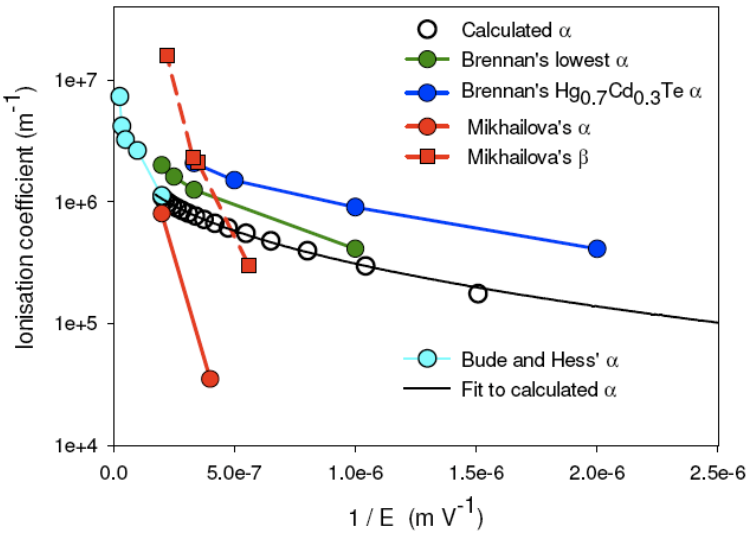

Figure 3.7 *Comparison between the InAs electron ionisation coefficient α calculated by Marshall (empty circles) [2] and published data from Brennan and Mansour (full green circles) [16], Bude and Hess (full cyan circles) [17] and Mikhailova et al. (full red circles) [14]. The graph also shows α for HgCdTe by Brennan (full blue circles) and β by Mikhailova (full red squares). Figure taken from [2].*

In Figure 3.7 it is clear how, in contrast with Mikhailova, the electron ionisation coefficient α calculated by Marshall *et al.* is in good accordance with the other published values of α.

Most of the published works on impact ionisation in InAs, support the argument that the avalanche multiplication is essentially dominated by electron impact ionisation with a negligible contribution from hole impact ionisation [4]. This means, in contrast with large bandgap III-V and Silicon APDs, they show a progressive rise in multiplication with no avalanche breakdown detected because the holes do not contribute to impact ionisation and do not provide the contribution necessary for the avalanche to rapidly increase to breakdown as the bias is increased. Figure 3.8 shows a comparison between the multiplication characteristics of different group IV, III-V and II-VI APDs.

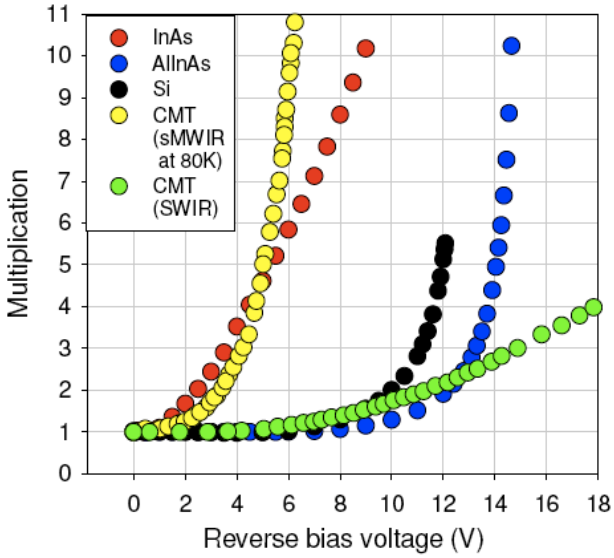

Figure 3.8 *Comparison between the multiplication characteristics of different group IV, III-V and II-VI APDs. Figure taken from [2] - InAs (red circles), AlInAs (blue circles) [18], Si (black circles) [19], sMWIR CMT at 80 K (yellow circles) and SWIR CMT at 297 K (green circles) [6].*

Figure 3.8 clearly shows that, while AlInAs APDs and silicon APDs exhibit a sharp rise in multiplication to breakdown with an operating voltage in excess of 15-20 V and 10 V respectively, InAs APDs have a progressive increase in gain without avalanche breakdown below 10 V. A multiplication factor as high as 25 was demonstrated by Ker *et al.* [20] at room temperature and 77 K biasing the photodetector at 13 V and 19.5 V respectively. In this work, a p-i-n diode was used, where the p layer consisted of a highly doped (Be > 2×10^{18} cm^{-3}) layer of thickness 0.1 µm InAs, a 0.2 µm thick $AlAs_{0.16}Sb_{0.84}$ electron diffusion blocking layer and 0.7 µm thickness of InAs absorption layer to provide pure electron injection at visible wavelength (633 nm). The structure had an undoped region of 3.5 µm followed by an n- region of 2 µm thickness.

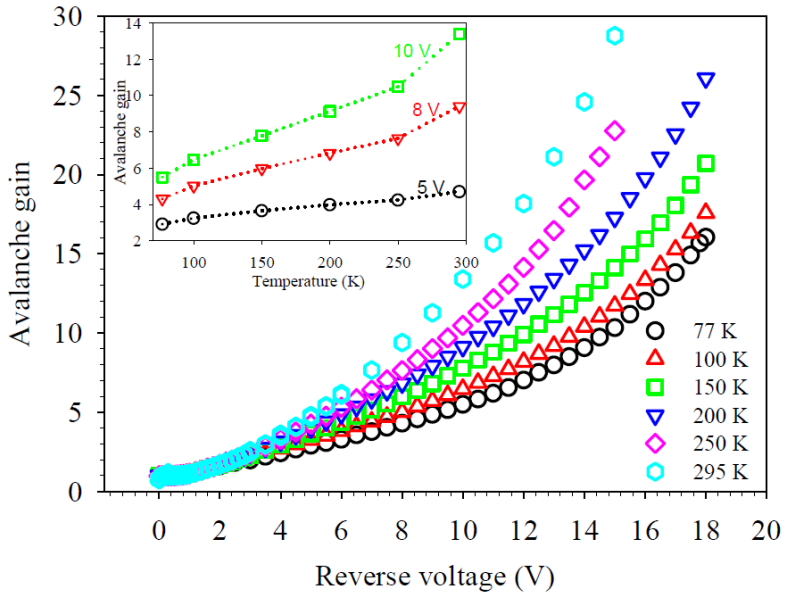

Figure 3.9 *Avalanche gain of an InAs p-i-n diode at 77 K (black circles), 100 K (red triangles), 150 K (green squares), 200 K (blue triangles), 250 K (pink rhombuses) and 295 K (cyan circles). Inset shows the temperature dependent avalanche gain at different reverse bias voltages. Figure taken from [20].*

Figure 3.9 shows a characteristic of InAs that differs when compared to wider bandgap semiconductors such as GaAs and Si: its gain is reduced with decreasing temperature. As the temperature of a semiconductor lattice decreases the total carrier phonon scattering rates decreases significantly. Consequently, the carriers will undergo less phonon scattering (which reduces the carriers' kinetic energy for a given ξ). However, as the temperature reduces, the bandgap also increases thus increasing the threshold energy for impact ionisation. For large gap III-V materials the first mechanism has a greater effect and much higher gain is observed as the temperature is reduced. In InAs the increase in bandgap has a greater effect than the decrease in phonon scattering and it exhibits the opposite behaviour with lower gains observed at 77 K compared with those at room temperature.

In general with all APDs, a reduction in temperature reduces the probability of inter-band excitation and reduces the dark current. Thus, a compromise between gain and DCR has to be found to achieve the best InAs APD operation according to the requirement of the application. A study of dark current as a function of the temperature is shown in Figure 3.10.

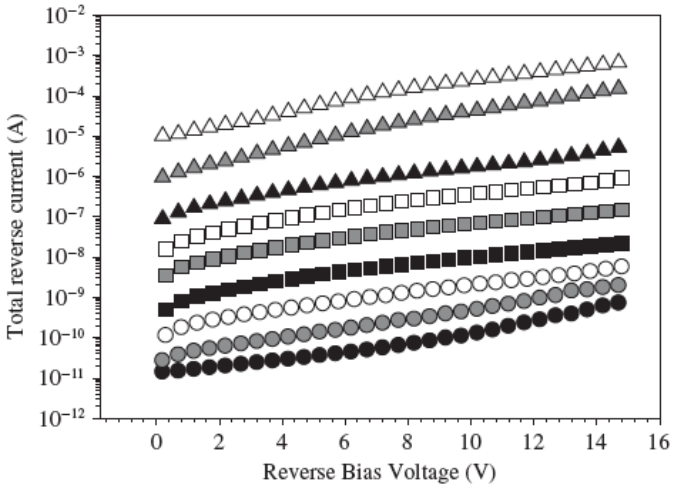

Figure 3.10 *Reverse bias dark current for n-i-p InAs diodes with a diameter of 110 μm at temperature of 77 K (black circles), 100 K (grey circles), 125 K (white circles), 150 K (black squares), 175 K (grey squares), 200 K (white squares), 220 K (black triangles), 250 K (grey triangles), and 290 K (white triangles). Figure taken from [21].*

Very similar results have been recently obtained by the University of Virginia [22], [23]. Dark current, gain and excess noise factor measurements were taken on two different InAs p-i-n structures: a p ungraded (constant uniform doping in the p region) structure and a p graded (graded doping in the p region) structure. The ungraded structure contains 6 μm of nominally intrinsic material surrounded by n^+ and p^+ claddings doped at 1×10^{18} cm^{-3} and 5×10^{18} cm^{-3}, respectively, whereas for the graded structure, in place of the 6 μm i-region is a 4 μm i-region followed by a 2 μm graded p region and a 0.7 μm uniform p region. The graded p region was achieved by ramping the Beryllium (acceptor material) cell temperature in order to form a graded p-type doping between 1×10^{17} and 5×10^{14} cm^{-3} in a 2 μm thickness. The graded structure was designed to reduce the peak electric field. A dark current as low as that reported by Ker *et al.* [21], [24] has been shown by the ungraded structure, with lower dark current achieved using the graded structure due to a reduced diffusion current. The gain reported by the University of Virginia is high for the two different structures and increases exponentially with bias, showing no sign of breakdown, suggesting that k=0 (i.e. β=0). At room temperature a gain of 30 is demonstrated for the ungraded structure when the reverse bias was increased up to 10 V before reaching the measurement limit; while a gain of 70 was shown for the graded structure at 12 V. The slightly lower dark

current in the graded structure allows the device to be biased to higher voltages allowing higher gains to be measured than for the ungraded structure.

3.5 High frequency behaviour of InAs avalanche photodiodes

Another important characteristic observed in InAs APDs is the absence of a gain-bandwidth (inverse transit time) product limit. In contrast with high gap conventional APDs, InAs presents bandwidths that remain constant at different gains. This is due to the constant transit time regardless of gain for single carrier APDs. A gain-bandwidth product of 430 GHz and 580 GHz has been demonstrated at room temperature and at 77 K respectively by Marshall *et al.* [25] as shown in Figure 3.11.

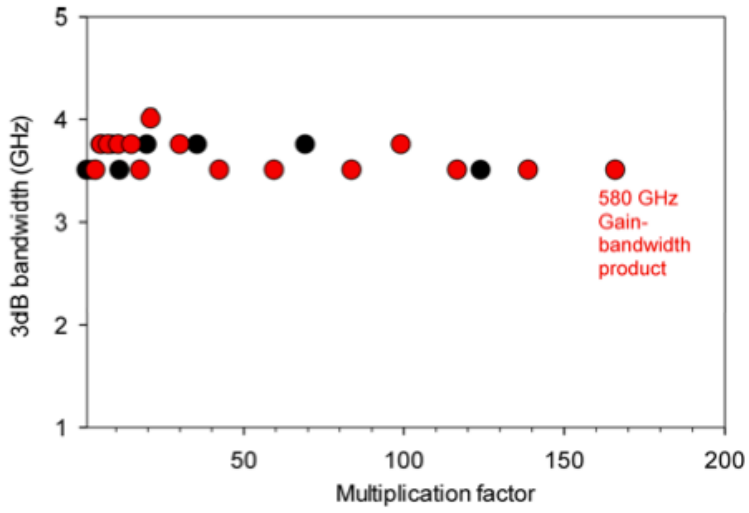

Figure 3.11 *Measured 3 dB bandwidth of InAs n-i-p e-APD as a function of device gain at room temperature (black circles) and at 77 K (red circles), figure taken from [25]. To ensure the best performance for the e-APD, only photogenerated electrons enter the i-region with high electric field.*

These properties, together with the low excess noise due to the relatively deterministic nature of the electron avalanche, make InAs a material with potential benefits for SPAD detectors. The possibility of achieving high gain at low electric fields and to work in linear mode operation makes the InAs diode a photodetector in which the breakdown probability and the SPAD quenching circuits are no longer relevant. The current, created inside the device after the photon detection rises to a macroscopic level as the electron avalanche builds up during the single transit of the multiplication region, and

falls when the electrons arrive at the edge of the multiplication region. Quenching circuitry is not required. The single electron transit time across the multiplication region for each incident photon will also lead to reduced jitter compared to conventional SPADs due to the reduction in variance in the avalanche build up time. Low excess noise, high gain and linear mode operation are also relevant properties for a photon number resolving detector: InAs photodiodes are thus a potential technology to distinguish avalanches simulated by different numbers of photon-excited carriers, since they give an output signal proportional to the number of photons in the incident pulse. Generally, avalanche diodes biased above breakdown are used in Geiger mode, where the device emits a binary output indicating the presence or absence of photons, and cannot resolve the number of photons incident on the device. Recently Toshiba demonstrated that avalanche photodiodes can be capable of resolving photon number, using a technique to measure very weak avalanches at the early linear stage of their development. Under such conditions the output signal from the avalanche photodiode is proportional to the number of incident photons. By measuring the avalanche current before it saturates in the device, it is possible to distinguish avalanches simulated by different numbers of photon-excited carriers, so they are a competitive technology for photon number resolving experiments. InGaAs APDs were used by Toshiba researchers [26], [27] showing, under a pulsed 1550 nm laser illumination, photon number resolving with very low excess noise factor: varying the average detected flux of photon per pulse Toshiba studied the distribution peak output signal voltage, showing clearly a series of maxima corresponding to the avalanche current due to a different number of photons. This technology is very promising but, as it is based on the InGaAs detector, it can be used only for near infrared application. For longer wavelength, instead, InAs could be the solution, especially as the more deterministic avalanche is formed in the predominantly electron injection device,

3.6 Conclusions

In this Chapter the most important characteristics of InAs and a review of the most significant papers about InAs photodetectors are presented.

InAs is a III-V narrow bandgap material allowing photons with wavelengths up to 3.5 μm to be absorbed. The InAs bandstructure shares similarities with HgCdTe, in particular it has the same single carrier type impact ionisation. In this case impact

ionisation is initiated solely by electrons. It is found that under the electric fields the electron impact ionisation dominates the avalanche multiplication and hole multiplication plays only a small role. Recent experimental works carried out independently by groups in the University of Sheffield and University of Virginia, contradicting earlier published results by Mikhailova, agreed that the avalanche process is electron impact ionisation dominated. Cross-checked experiments on both p-i-n and n-i-p diodes show that the electron impact ionisation coefficient α is much greater than the hole impact ionisation coefficient β. Such single carrier type dominated multiplication leads to a low associated excess noise factor. InAs APDs have highly desirable characteristics, unique among the III-V materials so far studied but comparable to HgCdTe. The possibility of achieving high gain at low electric fields and to operate in linear mode gives InAs APDs potential for photon number resolving technology. Furthermore, since the device will not have a self-sustaining avalanche, the absence of long reset times associated with external quenching circuitry could result in potentially very high maximum count rates.

3.7 References

[1] C. Kittel, "Introduction to Solid State Physics", Eight Edition ed., John Willey & Sons, 2005.

[2] A. R. J. Marshall, "The InAs electron avalanche photodiode and the influence of thin avalanche photodiodes on receiver sensitivity," *PhD Thesis,* 2009.

[3] I. Vurgaftman, J. Meyer, and L. Ram-Mohan, "Band parameters for III–V compound semiconductors and their alloys," *Journal of Applied Physics,* vol. 89, pp. 5815-5875, 2001.

[4] A. R. J. Marshall, C. H. Tan, M. J. Steer, and J. P. R. David, "Electron dominated impact ionization and avalanche gain characteristics in InAs photodiodes," *Applied Physics Letters,* vol. 93, pp. 111107 1-3, 2008.

[5] F. Ma, X. Li, J. C. Campbell, J. D. Beck, C.-F. Wan, and M. A. Kinch, "Monte Carlo simulations of $Hg_{0.7}Cd_{0.3}Te$ avalanche photodiodes and resonance phenomenon in the multiplication noise," *Applied Physics Letters,* vol. 83, pp. 785-787, 2003.

[6] J. Beck, C. Wan, M. Kinch, J. Robinson, P. Mitra, R. Scritchfield*, et al.*, "The HgCdTe electron avalanche photodiode," *Journal of Electronic Materials,* vol. 35, pp. 1166-1173, 2006.

[7] IOFFE. InAs Band Structure. http://www.ioffe.ru/SVA/NSM/Semicond/InAs/bandstr.html.

[8] J. R. Chelikowsky and M. L. Cohen, "Nonlocal pseudopotential calculations for the electronic structure of eleven diamond and zinc-blende semiconductors," *Physical Review B,* vol. 14, pp. 556-582, 1976.

[9] A. R. J. Marshall, C. H. Tan, J. P. R. David, J. S. Ng, and M. Hopkinson, "Fabrication of InAs Photodiodes with reduced surface leakage current," *Optical Materials in Defence Systems Technology,* vol. 6740, pp. H7400 1-9, 2007.

[10] A. R. J. Marshall, C. H. Tan, M. J. Steer, and J. P. R. David, "Extremely Low Excess Noise in InAs Electron Avalanche Photodiodes," *IEEE Photonics Technology Letters,* vol. 21, pp. 866-868, 2009.

[11] A. R. J. Marshall, J. P. R. David, and C. H. Tan, "Impact Ionization in InAs Electron Avalanche Photodiodes," *IEEE Transactions on Electron Devices,* vol. 57, pp. 2631-2638, 2010.

[12] S. Adachi, "Optical dispersion relations for GaP, GaAs, GaSb, InP, InAs, InSb, $Al_xGa_{1-x}As$, and $In_{1-x}Ga_xAs_yP_{1-y}$," *Journal of Applied Physics,* vol. 66, pp. 6030-6040, 1989.

[13] J. R. Dixon and J. M. Ellis, "Optical properties of n-type indium arsenide in the fundamental absorption edge region," *Physical Review,* vol. 123, pp. 1560-1566, 1961.

[14] M. P. Mikhailova, N. N. Smirnova, and S. V. Slobodchikov, "Carrier Multiplication in InAs and InGaAs P-N-Junctions and Their Ionization Coefficients," *Soviet Physics Semiconductors-Ussr,* vol. 10, pp. 509-513, 1976.

[15] G. Satyanadh, R. Joshi, N. Abedin, and U. Singh, "Monte Carlo calculation of electron drift characteristics and avalanche noise in bulk InAs," *Journal of Applied Physics,* vol. 91, pp. 1331-1338, 2002.

[16] K. F. Brennan and N. S. Mansour, "Monte Carlo calculation of electron impact ionization in bulk InAs and HgCdTe," *Journal of Applied Physics,* vol. 69, pp. 7844-7847, 1991.

[17] J. Bude and K. Hess, "Thresholds of impact ionization in semiconductors," *Journal of Applied Physics,* vol. 72, pp. 3554-3561, 1992.

[18] Y. L. Goh, D. J. Massey, A. R. J. Marshall, J. S. Ng, C. H. Tan, W. K. Ng*, et al.*, "Avalanche multiplication in InAlAs," *IEEE Transactions on Electron Devices,* vol. 54, pp. 11-16, 2007.

[19] C. H. Tan, J. P. R. David, G. J. Rees, R. C. Tozer, and D. C. Herbert, "Treatment of soft threshold in impact ionization," *Journal of Applied Physics,* vol. 90, pp. 2538-2543, 2001.

[20] P. J. Ker, J. P. R. David, and C. H. Tan, "Temperature dependence of gain and excess noise in InAs electron avalanche photodiodes," *Optics Express,* vol. 20, pp. 29568-29576, 2012.

[21] P. J. Ker, A. R. J. Marshall, A. B. Krysa, J. P. R. David, and C. H. Tan, "Temperature Dependence of Leakage Current in InAs Avalanche Photodiodes," *IEEE Journal of Quantum Electronics,* vol. 47, pp. 1123-1128, 2011.

[22] W. Sun, Z. Lu, X. Zheng, J. Campbell, S. Maddox, H. Nair*, et al.*, "High Gain InAs Avalanche Photodiodes," *IEEE Journal of Quantum Electronics,* vol. 49, pp. 154-161, 2013.

[23] S. J. Maddox, W. Sun, Z. Lu, H. P. Nair, J. C. Campbell, and S. R. Bank, "Enhanced low-noise gain from InAs avalanche photodiodes with reduced dark

current and background doping," *Applied Physics Letters,* vol. 101, pp. 151124 1-3, 2012.

[24] P. J. Ker, "Development of high speed low noise InAs electron avalanche photodiodes," *PhD Thesis,* 2012.

[25] A. R. J. Marshall, P. J. Ker, A. Krysa, J. P. R. David, and C. H. Tan, "High speed InAs electron avalanche photodiodes overcome the conventional gain-bandwidth product limit," *Optics Express,* vol. 19, pp. 23341-23349, 2011.

[26] B. E. Kardynal, Z. L. Yuan, and A. J. Shields, "An avalanche-photodiode-based photon-number-resolving detector," *Nature Photonics,* vol. 2, pp. 425-428, 2008.

[27] Z. L. Yuan, J. F. Dynes, A. W. Sharpe, and A. J. Shields, "Evolution of locally excited avalanches in semiconductors," *Applied Physics Letters,* vol. 96, pp. 191107 1-3, 2010.

Chapter Four

4. InAs photodiodes: post growth processes, mask set design and preliminary passivation results.

4.1 Introduction

The devices studied in this thesis have been grown at the University of Sheffield in the National Centre of III-V technologies. As was seen in Chapter Three, InAs offers very attractive properties that can be very useful for an APD [1], [2]; but unfortunately it suffers from high surface leakage current [3]. In this chapter a brief description of the post-growth processing is reported. To achieve the best detector performance in a mesa geometry, a good passivation layer deposited on top of the InAs devices is essential. In this way it is possible to prevent the formation of electron states within the InAs bandgap that are the origin of the increasing dark current. The aim of the work described in this Chapter is to find the best passivation process that can be used to produce packaged InAs APDs. Preliminary dark current results on InAs mesa detector prototypes of different sizes will be reported using different passivation materials such as SU8 photoresist, SiN and Al_2O_3. Results show that SU8, at present, is more suitable than SiN and Al_2O_3, although it can cause issues during the device packaging process due to poor adhesion between the metal contacts and the SU8. To alleviate this, a new mask set has been designed combining SU8 with another insulating material that has good adhesion with the top metal contact and is used under the external bondpad. Details of the new mask set are reported. A higher bonding yield in our InAs mesa APDs has been observed when SiN is used underneath the bondpad, instead of SU8.

4.2 Growth and post-growth processing: etching processes, passivation coating and device packaging

The p-i-n and n-i-p InAs junctions were grown by the National Centre of III-V technologies at the University of Sheffield by either Molecular Beam Epitaxy (MBE) or Metalorganic Vapour Phase Epitaxy (MOCVD) techniques.

After the growth the sample is processed to form the mesa structures. Trials have shown

that the best recipe for mesa etching is in 1:1:1 H_3PO_4: H_2O_2: H_2O solution followed by 30 s in a 1:8:80 H_2SO_4: H_2O_2: H_2O solution [4]. Once the InAs mesas are formed, they are exposed to the atmosphere; without passivation the mesa surface can degrade, leading to increased leakage currents due to an accumulation of electrons on the surface [5] leading to device failure. This problem is particularly significant for APDs where the high electric fields can make them especially vulnerable to degradation. Therefore, the introduction of a passivation layer is needed to protect the sample surface without increasing the surface leakage current [3]. This dielectric layer is also crucial for the deposition of the device's external bondpads to avoid stressing the mesa structure during packaging. Figure 4.1 shows a diagram of a mesa structure after the processing of a n-i-p wafer. A passivation layer is deposited on top of the mesa to protect the detector surface along with a circular metal top contact and metal track that allows the devices to be connected to the external bondpad.

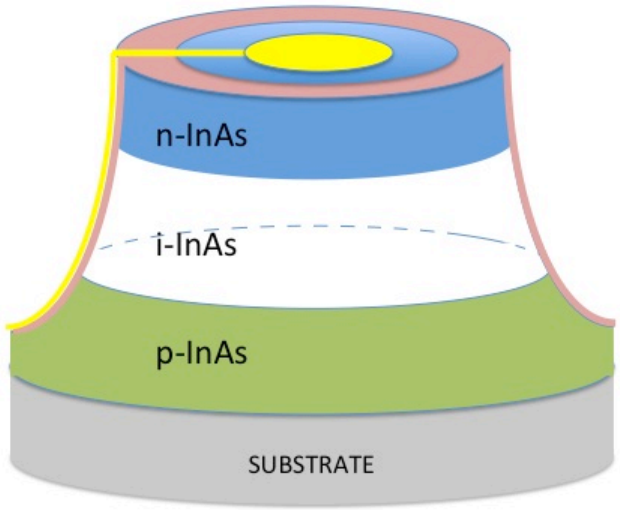

Figure 4.1 *InAs n-i-p structure with a passivation layer (in pink) used to protect the mesa wall after etching. A circular gold top contact and a gold track (in yellow) that connect the device to the bondpad area are also shown in the sketch.*

Figure 4.2 clearly shows the decrease in leakage current density for a passivated sample; the passivation layer material used in this case is SU8, a very viscous polymer commonly used as a negative photoresist. I-V curves were taken using a Source-Measure Unit (SMU), Keithley 236, that allows DC reverse bias to be applied to the photodiode while simultaneously measuring the current flowing through it.

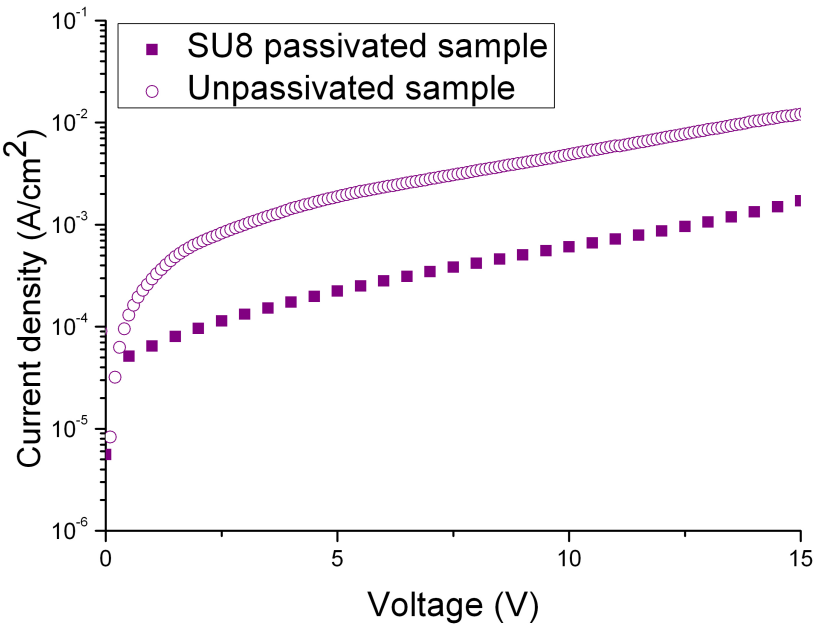

Figure 4.2 *Example of dark current density results for an unpassivated (open circles) and SU8-passivated (closed squares) InAs detectors at 77 K.*

SU8 is currently used for InAs passivation by some researchers [6], [7], however it is not an ideal material for wire bonding as the metal contacts have a poor adhesion to the SU8. Because the top metal contact does not adhere well to the SU8 layer, the gold/aluminium bonding process pulls the metal contact from the chip during the bonding and no packaged devices can be produced. Figure 4.3 clearly shows circular areas without metal on the bondpads where bonding attempts were carried out using a ball bonding machine.

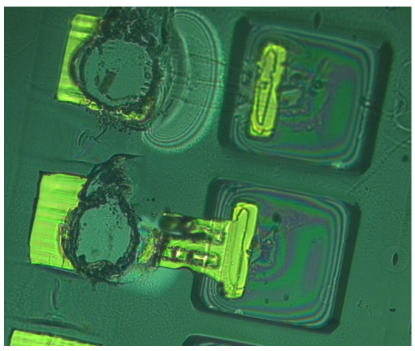

Figure 4.3 *Optical microscope image of InAs square mesa devices with external bondpads produced at the University of Sheffield. The damage from the gold ball-bonding attempts are clearly visible as circular areas without the top contact metal.*

This is a limitation for the use of SU8 as passivation for InAs devices. Therefore other materials have been researched to find a stable and robust passivation layer which protects the mesa surface. Lin *et al.* [8] reported on InAs mesa diode passivation using SiO_2. Their results show the difficulty in passivating InAs with the samples exhibiting an increased leakage current compared to an unpassivated sample. Increased leakage current was also observed by Marshall [4] in diodes which were passivated by SiN_x and SiO_2. B-stage Bisbenzocyclobutene (BCB) was also used by the same authors showing that BCB passivated diodes did not show significantly lower dark current compared to the unpassivated samples.

SiN, Al_2O_3 and II-VI semiconductors have been studied as passivation materials in this thesis. II-VI semiconductors can be deposited epitaxially on InAs structures. The performance of InAs mesa diodes with II-VI materials as passivation layers are very promising and it will be discussed in detail in Chapter Five.

SiN and Al_2O_3 are materials commonly used for passivation purposes [9], [10]. Good quality layers of hundreds of nm of SiN and Al_2O_3 have been deposited using the facilities of the external company, Helia Photonics Ltd., keeping the sample temperature below 100°C to avoid any temperature related device degradation. Electron beam evaporation techniques were used for Al_2O_3 deposition. Figure 4.4 shows the reflectivity verses wavelength behaviour for Al_2O_3 coated InAs mesa samples. The deposited Al_2O_3 passivation layer thickness is around 502 nm.

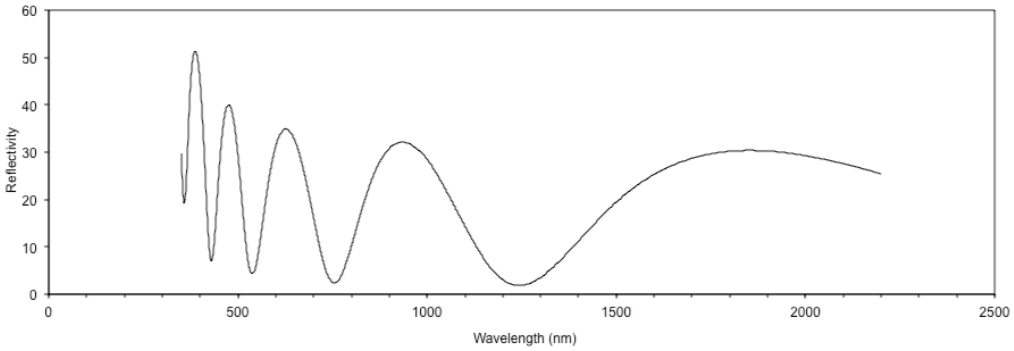

Figure 4.4 *Reflectivity (in percentage) as a function of wavelength behaviour for Al_2O_3 InAs mesa coated sample. The final Al_2O_3 thickness deposited was around 502 nm. Data taken by Helia Photonics Ltd..*

At room temperature, the current-voltage characteristic of this sample shows an increase in dark current of one order of magnitude with respect to the as grown device. This poor performance, possibly caused by aluminium on the mesa sidewall shorting the diode, precludes the use of Al_2O_3 as a passivation layer for InAs detectors.

SiN was also used as a possible passivation layer for InAs structures. It was deposited by pulsed DC sputtering. A study of detector performance was carried out as a function of the relative fraction of Si and N by varying the flow rate of N_2 inside the chamber. Table 4.1 summarises the characteristics of the three SiN layers deposited, the flow rate of N_2 is measured in standard cubic centimetres per minute (sccm).

	N_2 flow rate	SiN thickness
Sample1	5 sccm	230 nm
Sample2	10 sccm	205 nm
Sample3	15 sccm	300 nm

Table 4.1 *Characteristics of SiN layers deposited on InAs mesa devices.*

Figure 4.5 is an example of the reflectivity as a function wavelength for one of these SiN coatings.

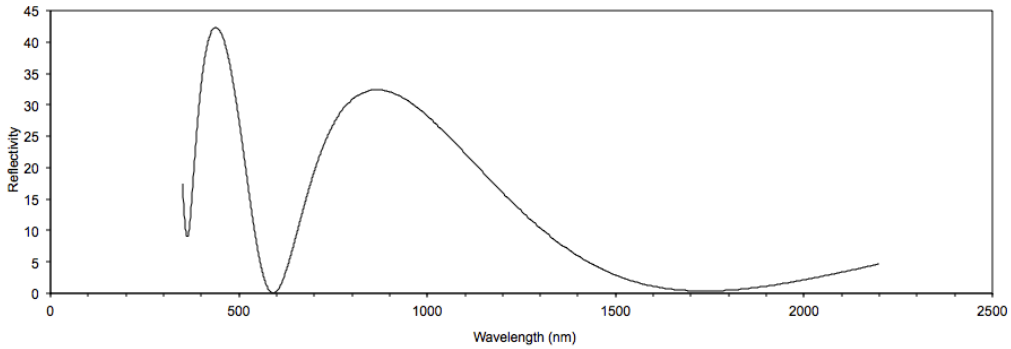

Figure 4.5 *Example of reflectivity (in percentage) as a function of wavelength for an InAs mesa sample coated with SiN. The N_2 flow rate is 5 sccm and the thickness deposited is around 230 nm. Data taken by Helia Photonics Ltd..*

The best results have been found for Sample 1, where the sample has been coated with the lowest N_2 flow rate. The room temperature dark current characteristics for these SiN coated devices are lower than the Al_2O_3 coated ones, but still higher when compared to the data from the SU8 passivated structures: the best one reaches 10 mA of dark current at around 7 V.

A new mask set is required to combine SU8 with another insulator material that, having good adhesion with the top metal contact, can be used under the external bondpad to give a high chip bonding yield. Bond tests conducted by the author, in parallel with the University of Sheffield, demonstrate that SiN can be used as the bondpad passivation material.

4.3 New mask design for InAs detector

SU8 is a good passivation layer for mesa devices but is not reliable for the bonding process. SiN, in contrast, is a very good insulating material that can be used under the bondpad giving very good bonding rate, but, as described in the previous section, not a useful passivation layer. A mask set featuring both these materials was designed with SiN deposited under the bondpad and SU8 on the sidewalls of the devices.

The photolithographic mask set was designed using Wavemaker software to have circular devices with diameters of 200, 100, 75, 50, and 25 μm. For each device size, there are three diodes with various distances between the bondpad and the device: distances of 75 μm, 150 μm and 200 μm are used to reduce any stress on the mesa from

the bonding process. Figure 4.6 shows the final mask set design in Wavemaker.

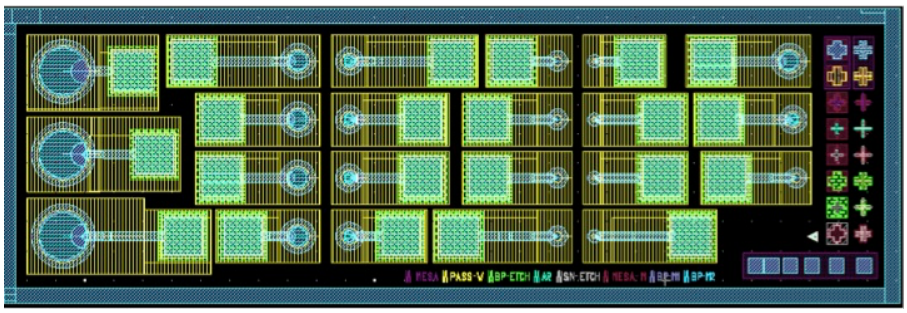

Figure 4.6 *Image of the new mask set designed in Wavemaker. The* circular *devices have diameters of 200, 100, 75, 50, and 25 µm. For each device size, there are three diodes with various distances between the bondpad and the device: distances of 75 µm, 150 µm and 200 µm are used to reduce any stress on the mesa from the bonding process.*

As shown in Figure 4.6, each cell also contains alignment marks between the different masks (on the right) and Transmission line method (TLM) pads (bottom right). The TLM pads are spaced, from the left to the right at distances, d_t, of 5, 15, 25, 35 and 45 µm respectively and were designed to measure the InAs contact resistance. The contact resistance of a semiconductor can be measured according the equation (4.1) [11]:

$$R_{measured}=2R_{PAD}+R_{semiconductor}+R_{system} \quad (4.1)$$

where R_{PAD} is the resistance between the TLM pad and the semiconductor, $R_{semiconductor}$ is the resistance along the length of the semiconductor and R_{system} is the resistance of the measurement set-up used for the current-voltage measurements. R_{system} can be obtained from preliminary calibration measurements, while R_{PAD} can be found by extrapolating the plot of $R_{measured}$ verses d_t, to d_t=0.

The mask set consists of seven masks:

Mask 1: Mask 1 is used during the top metal contact deposition as shown in Figure 4.7. A positive photoresist was deposited on the sample and patterned using mask 1 and UV radiation. Metal contacts consisting of 20 nm of Ti and 200 nm of Au were evaporated everywhere and finally the sample was rinsed in acetone to remove the resist and the metal from the unpatterned regions.

Step1

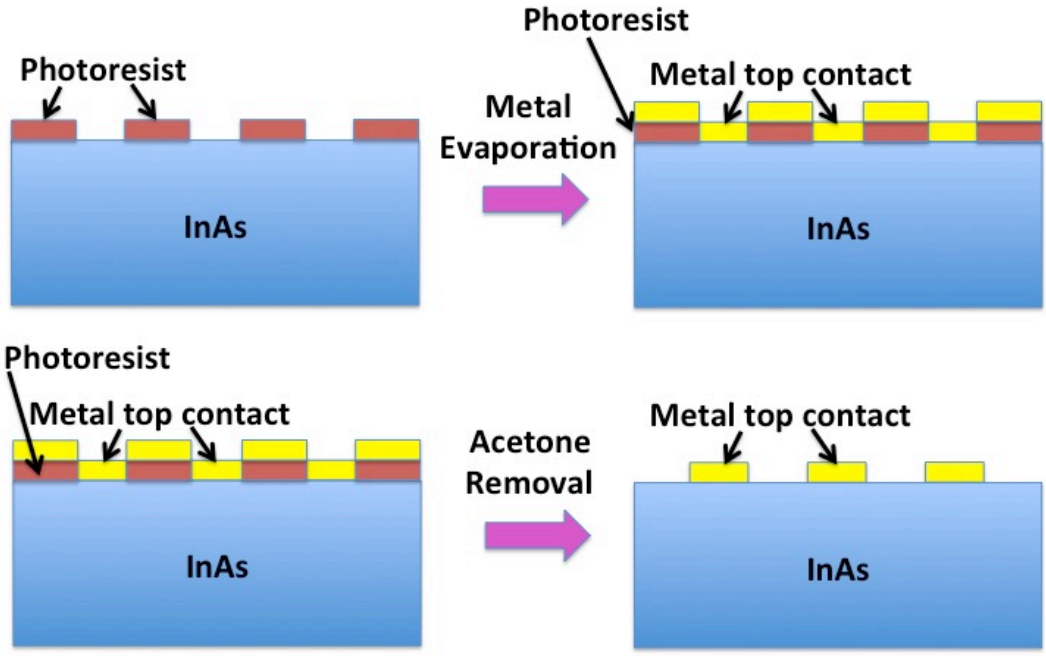

Figure 4.7 *A photoresist is deposited on top of InAs wafer and patterned with UV radiation leaving uncovered areas (top left). The metal is evaporated everywhere (top right and bottom left), the sample is then rinsed in acetone to remove the resist and the metal from the unpatterned regions (bottom right).*

Mask 1 was designed so that the 200, 100, and 75 μm diameter devices had a top contact ring with a width of 5 μm, and for the 50 μm, and 25 μm devices the top contacts were a 20 and 10 μm diameter circular structure respectively. A screengrab from Wavemaker of Mask 1 in Figure 4.8 shows the top metal contact design for all the devices. The green features are open windows where the gold is deposited forming the metal contact.

Figure 4.8 *Screengrab from Wavemaker in which the 200, 100, and 75 µm diameter devices show a top contact ring with a width of 5 µm, while the 50 µm, and 25 µm devices a 20 and 10 µm diameter circular structure respectively.*

Mask 2: Mask 2 is used to define the bondpad areas prior to the bondpad etch as shown in Figure 4.9. A positive photoresist is deposited on the sample and patterned using mask 2. The uncovered areas were etched to form the bondpad areas and finally the sample was rinsed in acetone to remove photoresist from the unpatterned regions.

Step2

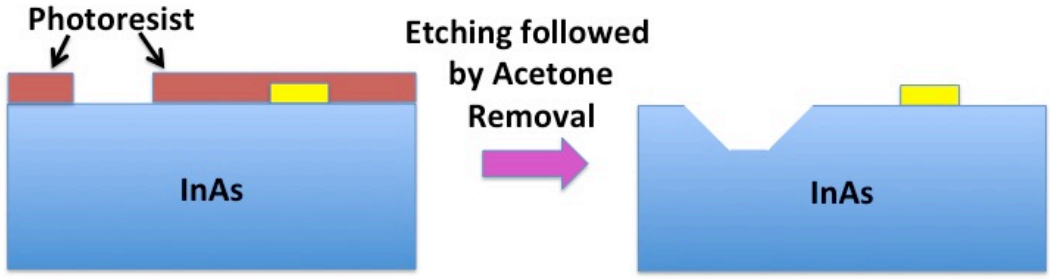

Figure 4.9 *A photoresist is deposited on top of InAs wafer and patterned with UV radiation leaving uncovered areas (left). The uncovered areas are etched to form a bondpad region, the sample is then rinsed in acetone to remove the photoresist (right).*

A screengrab from Wavemaker of Mask 2 in Figure 4.10 shows the bondpad etched areas for all the devices. The black features are open windows where the etching occurs, forming the bondpad area.

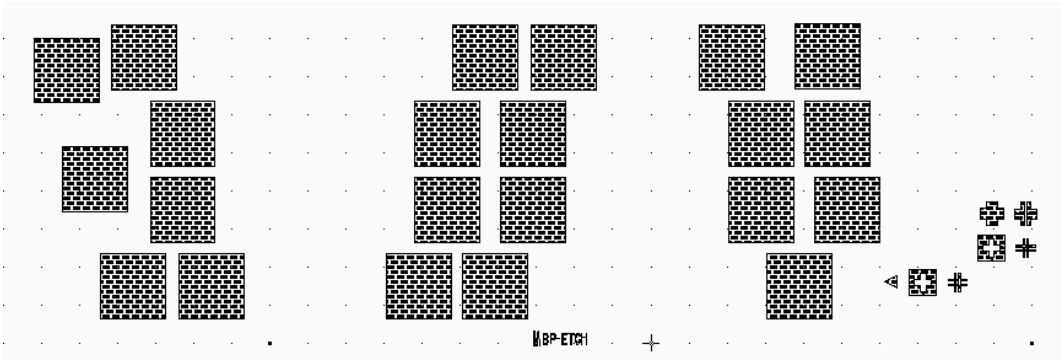

Figure 4.10 *Screengrab from Wavemaker in which the bondpad regions (black features) are defined.*

At this point SiN is deposited by Plasma-enhanced chemical vapor deposition (PECVD) on top of the entire wafer, as illustrated in Figure 4.11.

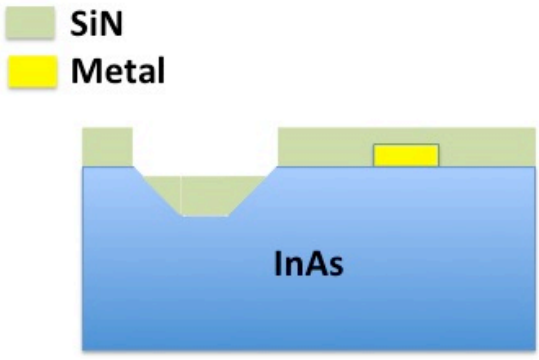

Figure 4.11 *SiN deposition using PECVD*

Mask 3: Mask 3 is used to protect the SiN on the bondpad area during the SiN etching process as shown in Figure 4.12. A positive photoresist is deposited on the wafer and then mask 3 and UV radiation were used to pattern the sample to leave the SiN on the bondpad area protected. The unprotected SiN is then etched to the required thickness of the antireflection coating (if present).

Step3

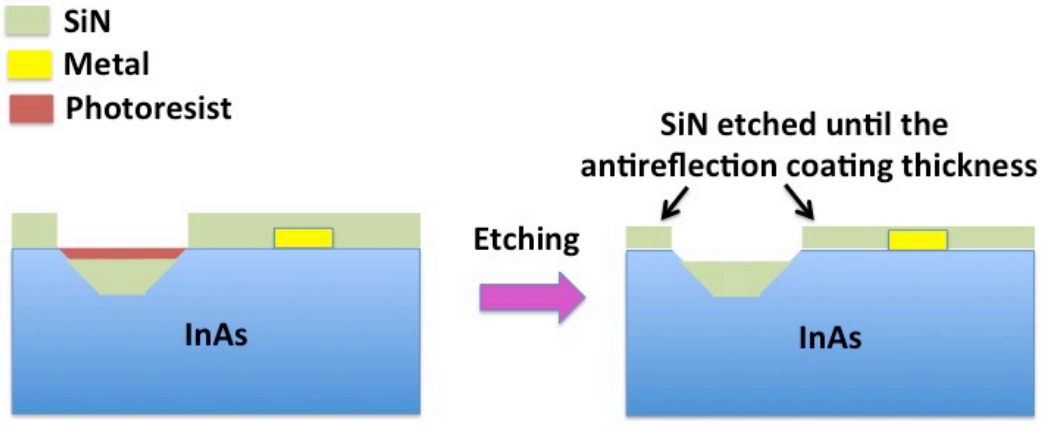

Figure 4.12 *SiN etching process first step. The SiN on the bondpad area is protected by the photoresist (left), the rest is etched until the thickness for a suitable antireflection coating is reached (right).*

A screengrab from Wavemaker of Mask 3 is shown in Figure 4.13: the shaded features are covered windows that protect the bondpad areas from SiN etch.

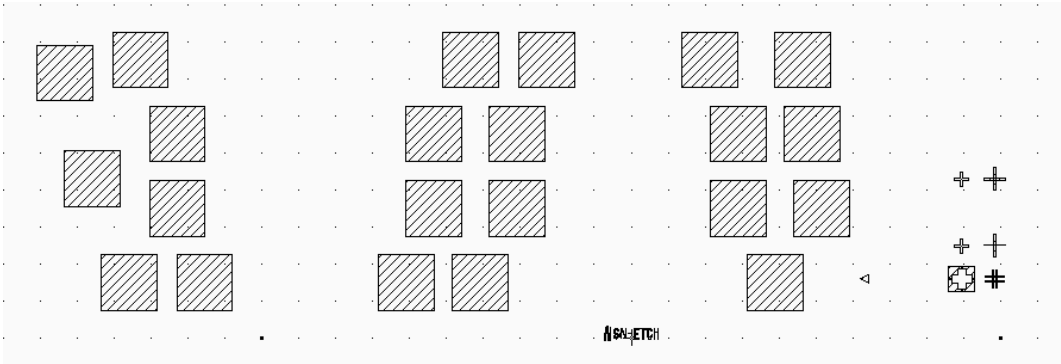

Figure 4.13 *Screengrab from Wavemaker in which the bondpad areas (shades features) are protected from the SiN etch.*

Mask 4: Mask 4 is used to form an antireflection coating on top of the devices as shown in Figure 4.14. A positive photoresist is deposited on the sample and patterned using mask 4 and UV radiation to protect the SiN on the bondpad area and on the regions inside the metal contacts for the 200, 100, and 75 μm devices. The unprotected SiN was then etched and removed.

Step4

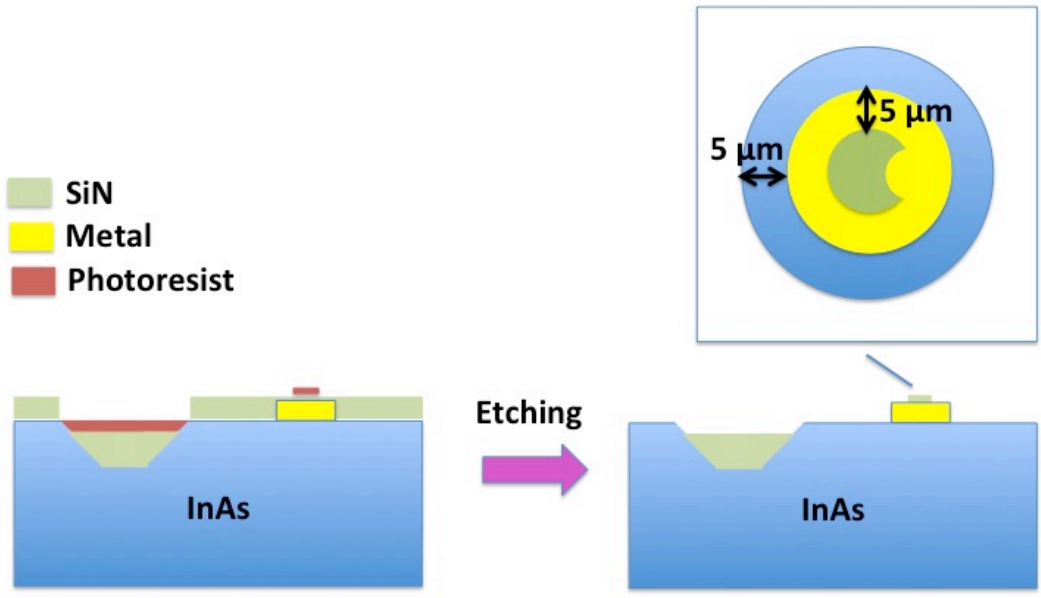

Figure 4.14 *The second SiN step. The SiN is etched away from all areas apart from the bonpad areas and the areas on top of the devices in order to form an antireflection coating (right).*

A screengrab from Wavemaker of Mask 4 is shown in Figure 4.15: the red features are covered windows that protect, from the SiN etch, the bondpads and regions inside the top metal contacts where an antireflection coating are formed.

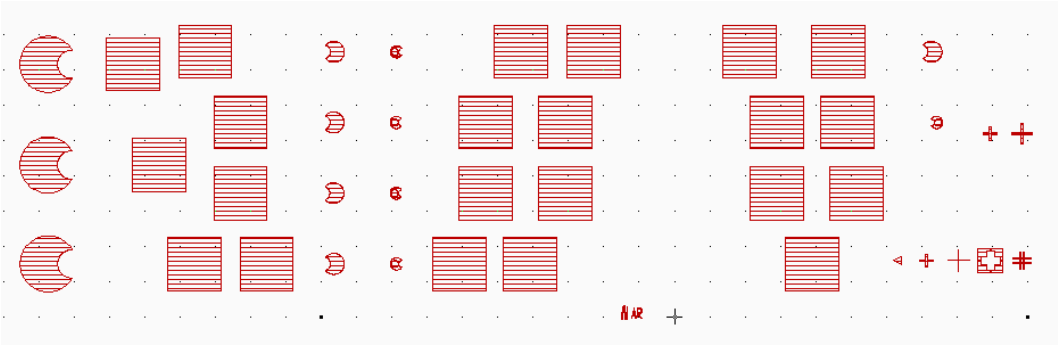

Figure 4.15 *Screengrab from Wavemaker in which the bondpads and regions inside the metal contacts for the 200, 100, and 75 µm devices are protected from the SiN etch by covered windows (red features). This also provides an anti-reflection coating for the mesa photodetectors.*

Mask 5: Mask 5 is used during the mesa etching process as shown in Figure 4.16. A positive photoresist is deposited on the wafer and then patterned using mask 5 and UV

radiation to define the mesas centred on the top contacts. The sample was then etched using 1:1:1 H_3PO_4:H_2O_2:H_2O followed by 1:8:80 H_2SO_4:H_2O_2:H_2O sample solutions to form the mesa structures. To allow for the effects of the etching on the mesa sidewalls the circular opening window radius in the mask is 10 μm larger than the final mesa radius; this assumes a 10 μm etch with a 45° bevel angle. The deposited SiN protects the bondpad areas from the etch.

Step5

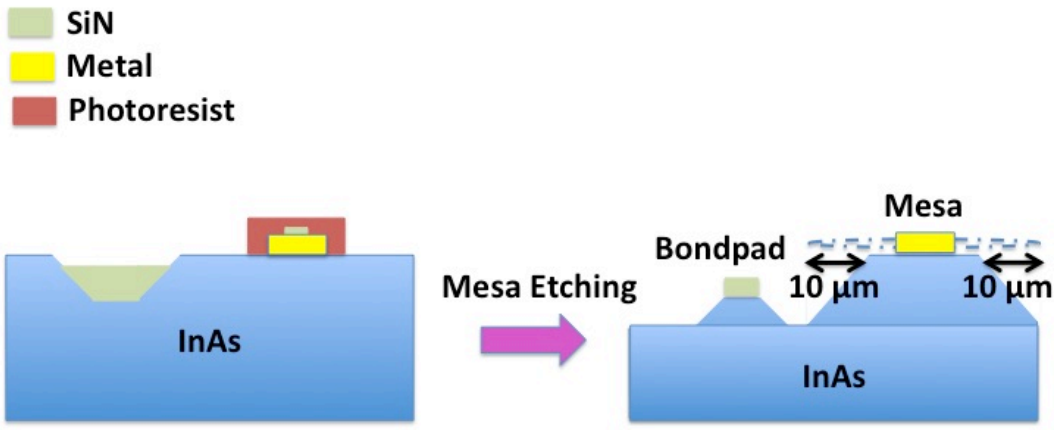

Figure 4.16 *Mesa isotropic etching. The photoresist is patterned over the devices centred on the top contact (left), the SiN protects the bondpad region from the etching. The sample is etched to form the mesa structure (right).*

A screengrab from Wavemaker of Mask 5 is shown in Figure 4.17: the green features are covered windows that protect the top of the mesa during the mesa etch process.

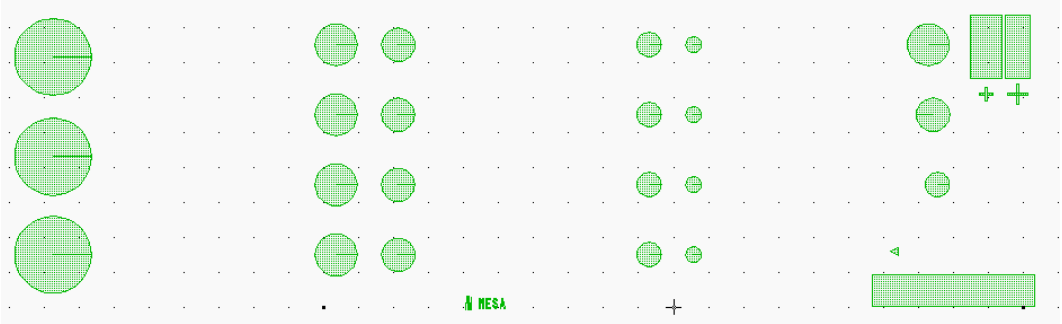

Figure 4.17 *Screengrab from Wavemaker for the mesa isotropic etching process. The circular opening window radius in the mask is 10 μm larger than the final mesa radius. The opening windows are the green circular features.*

Mask 6: Mask 6 is used during the SU8 deposition as shown in Figure 4.19. The negative photoresist SU8 is deposited upon the sample, and cured using UV radiation and baking the sample. Mask 6 is used to pattern the SU8 with UV radiation so that the mesa sidewalls are covered but not the optical windows or the bondpads. The optical window openings in mask 6 were designed with a 2 μm tolerance for the mesa etch - as shown in Figure 4.18. Mask 6 also opens the SU8 around each device to prevent any cracks from propagating across the SU8 layer and to allow the bottom gold contact to be deposited around each cell.

Step6

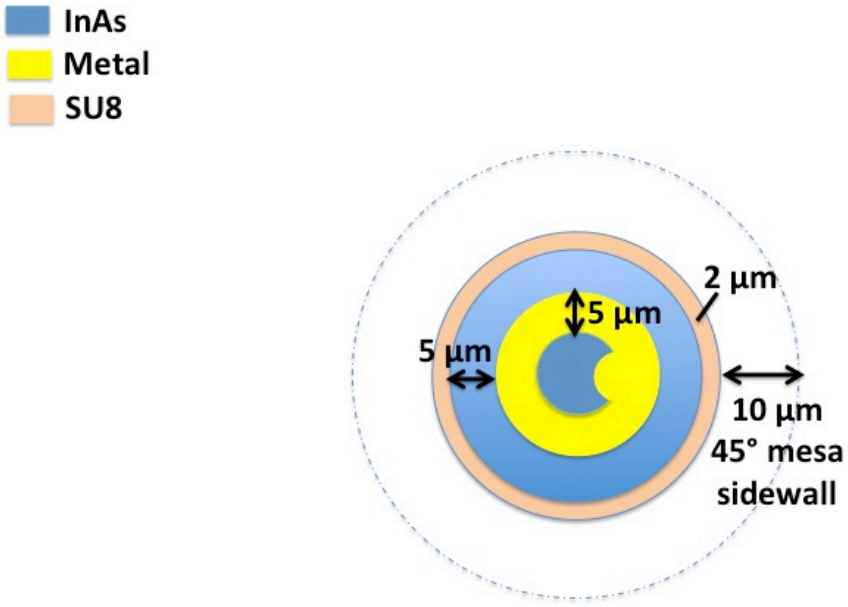

Figure 4.18 *Diagram of the mesa from a top view. The 2 µm tolerance in the optical window opening for the mesa etch is shown.*

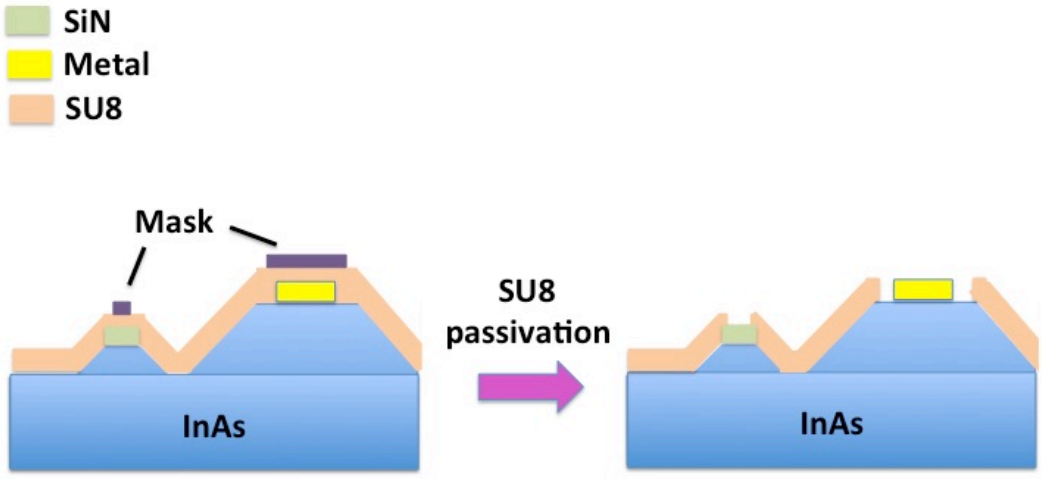

Figure 4.19 *SU8 passivation layer. The negative photoresist SU8 is deposited on the sample (left), then the SU8 is patterned to cover the mesa sidewalls but not the optical windows or the bondpads (right).*

A screengrab from Wavemaker of Mask 6 is shown in Figure 4.20: the shaded features are the regions where the SU8 is deposited.

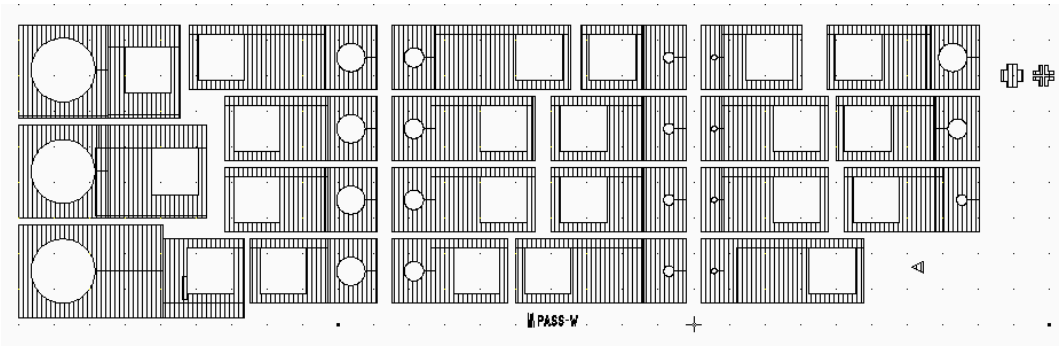

Figure 4.20 *Screengrab from Wavemaker in which the regions covered with SU8 (shaded features) are defined.*

Mask 7: Mask 7 is used during the bondpad and track metal deposition as shown in Figure 4.21. A positive photoresist was deposited on the sample. Mask 7 and UV radiation were used to define the pattern for the bondpads and tracks on the SiN and SU8 passivation layers respectively. Then the metal was deposited by evaporation and finally the sample was rinsed in acetone to remove resist and metal from unpatterned regions.

Step7

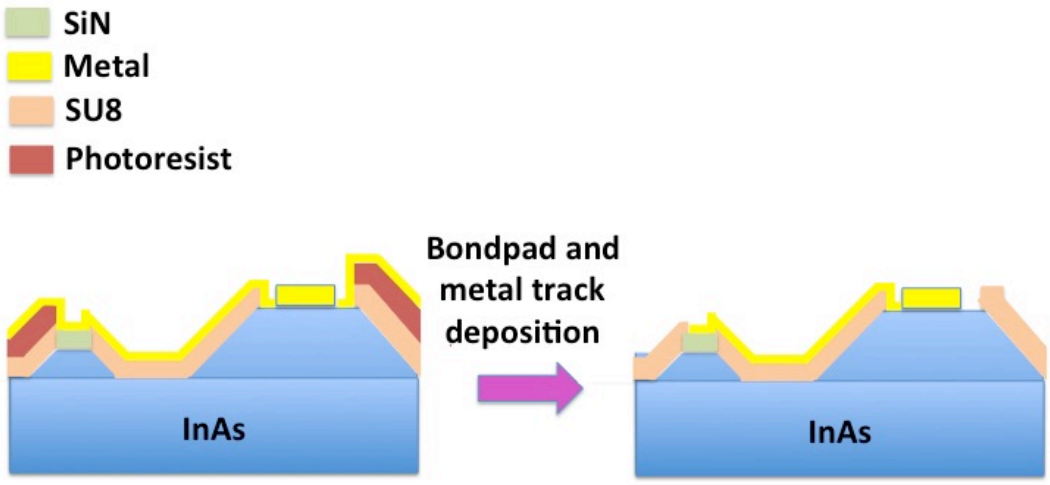

Figure 4.21 *Bondpad and track deposition. A positive photoresist was deposited on the sample and mask 7 was used to define the pattern for the bondpads and tracks (left). The metal was deposited upon the sample with the photoresist and metal removed from the unpattern regions using an acetone rinse (right).*

A screengrab from Wavemaker of Mask 7 is shown in Figure 4.22: the shaded features

are the regions where the metal is deposited.

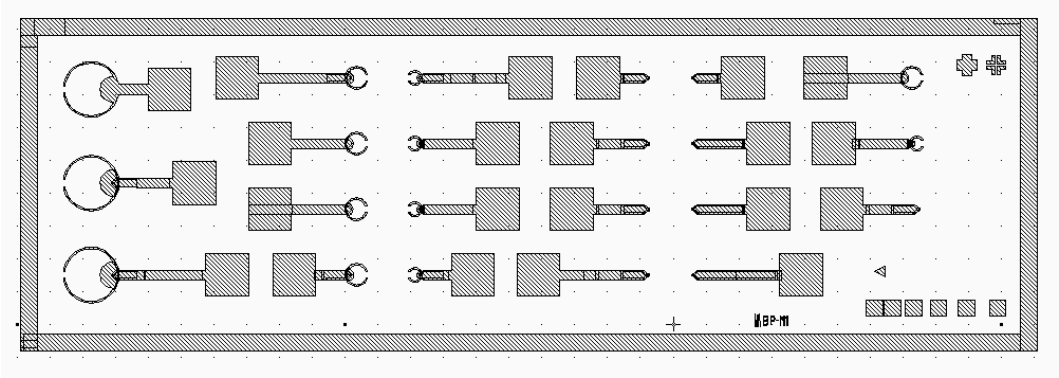

Figure 4.20 *Screengrab from Wavemaker in which the pattern for the bondpads and tracks (shaded features) is defined.*

Mask 7 was designed to give bondpad contacts with an area of 130 μm × 130 μm. Tracks with a width of 20 μm connect the bondpad with the top contacts of the devices. At this stage, the metal was again deposited on top of the mesa to ensure a good overlap with the track metal.

4.4 Conclusion

The photodiodes studied in this thesis were grown at the University of Sheffield in the National Centre of III-V technologies. After growth the InAs wafer was etched into mesas. The recipe used for mesa etching was 1:1:1 H_3PO_4, H_2O_2, H_2O solution (phosphoric acid, hydrogen peroxide, DI water) followed by 30 s in a 1:8:80 H_2SO_4, H_2O_2, H_2O solution (sulphuric acid, hydrogen peroxide, DI water). InAs offers very interesting properties for an APD but unfortunately suffers of high surface leakage current in particular in mesa geometry photodetectors. The surface exposed to the atmosphere can degrade due to the formation of electronic states within its bandgap increasing the dark current. A passivation layer was deposited on the samples to avoid any surface degradation. At the present the most suitable passivation layer for InAs APDs is SU8 although it is not possible to achieve a high bonding yield due to the poor adhesion between SU8 and the top metal contact. It was found very hard to produce packaged devices when SU8 has been used underneath the external bondpads. The ability to produce packaged devices is very important so, for this reason, other possible materials for device passivation, namely SiN and Al_2O_3, have been studied. Unfortunately neither SiN nor Al_2O_3 suppress the surface leakage current so they cannot be used for our purposes. Current-voltage characteristics for these coated samples show

increased dark current that compromises device performances. A new mask set has been designed to combine the excellent passivation properties of SU8 with another insulating material that can be used under the external bondpad. Using SiN for this purpose gave a high bonding yield. With the new mask set design, InAs packaged APDs have been finally achieved. This solution, unfortunately, is unstable due to the use of SU8, a better solution is the use of II-VI semiconductors as passivation layer. The performance of InAs mesa diodes with II-VI materials as passivation layers are very promising and it will be discussed in detail in Chapter Five.

4.6 References

[1] A. R. Marshall, J. P. David, and C. H. Tan, "Impact ionization in InAs electron avalanche photodiodes," *IEEE Transactions on Electron Devices,* vol. 57, pp. 2631-2638, 2010.

[2] A. R. J. Marshall, P. Vines, P. J. Ker, J. P. David, and C. H. Tan, "Avalanche multiplication and excess noise in InAs electron avalanche photodiodes at 77 K," *IEEE Journal of Quantum Electronics,* vol. 47, pp. 858-864, 2011.

[3] P. J. Ker, A. R. Marshall, A. B. Krysa, J. P. David, and C. H. Tan, "Temperature dependence of leakage current in InAs avalanche photodiodes," *IEEE Journal of Quantum Electronics,* vol. 47, pp. 1123-1128, 2011.

[4] A. R. Marshall, "The InAs electron avalanche photodiode and the influence of thin avalanche photodiodes on receiver sensitivity," *PhD Thesis,* 2009.

[5] D. Tsui, "Observation of surface bound state and two-dimensional energy band by electron tunneling," *Physical Review Letters,* vol. 24, pp. 303-306, 1970.

[6] A. R. Marshall, C. H. Tan, J. P. David, J. S. Ng, and M. Hopkinson, "Fabrication of InAs photodiodes with reduced surface leakage current," in *Optics/Photonics in Security and Defence*, pp. 67400H 1-9, 2007.

[7] S. Maddox, W. Sun, Z. Lu, H. Nair, J. Campbell, and S. Bank, "Enhanced low-noise gain from InAs avalanche photodiodes with reduced dark current and background doping," *Applied Physics Letters,* vol. 101, pp. 151124 1-13, 2012.

[8] R.M. Lin, S.F. Tang, S.C. Lee, C.H. Kuan, G.S. Chen, T.P. Sun*, et al.*, "Room temperature unpassivated InAs pin photodetectors grown by molecular beam epitaxy," *IEEE Transactions on Electron Devices,* vol. 44, pp. 209-213, 1997.

[9] M. A. Itzler, R. Ben-Michael, C.F. Hsu, K. Slomkowski, A. Tosi, S. Cova*, et al.*, "Single photon avalanche diodes (SPADs) for 1.5 μ m photon counting applications," *Journal of Modern Optics,* vol. 54, pp. 283-304, 2007.

[10] O. Salihoglu, A. Muti, K. Kutluer, T. Tansel, R. Turan, C. Kocabas*, et al.*, "Atomic layer deposited Al_2O_3 passivation of type II InAs/GaSb superlattice photodetectors," *Journal of Applied Physics,* vol. 111, pp. 074509 1-4, 2012.

[11] P. J. Kerr, "Development of high speed low noise InAs electron avalanche photodiodes," *PhD Thesis,* 2012.

Chapter Five

5. ZnSe, CdSe, CdMgSe and ZnTe as alternative passivation layers for InAs photodiodes.

5.1 Introduction

Mesa photodiodes without surface passivation can degrade when exposed to the atmosphere, leading to increased leakage currents due to an accumulation of electrons on the surface and, eventually to device failure. This problem is particularly important for avalanche photodiodes (APDs) where the high electric fields can make them vulnerable to degradation. The introduction of a passivation layer is primarily needed to protect the sample surface to prevent an increase in the surface leakage current. The passivation is also crucial for the deposition of device external bondpads so that stress on the mesa structure is avoided during sample packaging (in particular, the forces applied during the wire bonding process can damage the structure). A passivation layer with resistivity much higher than that of the photodiode material must be used to avoid any leakage current through the external bondpads. Thus, although InAs APDs have been previously achieved, for these reasons no packaged InAs APDs have been demonstrated.

As mentioned in Chapter Four, we have used the photoresist SU8 as a passivation layer for InAs APDs. However, the packaging yield is low for SU8-passivated InAs mesa detectors. II-VI semiconductors can have a high bandgap and they can be grown epitaxially on InAs [1] resulting in solid and reliable structures where contacts can be easily deposited due to good adhesion between the II-VI semiconductor and the metal contact [2]. So, in principle, they can be used as an alternative passivation layer to SU8.

The main characteristics that make the II-VI layers useful for our purposes are: a high conduction band offset with respect to InAs, a complete coverage of the InAs surface and the presence of no defects that can conduct. Electrical measurements then provide the final pass/fail test. All the characterisation techniques described in this Chapter are used to assess these characteristics of the II-VI layers.

The aim of the work in this Chapter is to determinate whether any of the II-VI compounds reduce the leakage current in InAs mesa structures. We have carried out an initial study of II-VI materials as passivation layers for InAs mesa photodiodes with external bondpads. The resistivity of a material increases as its bandgap is increased [3], so we studied II-VI materials which have bandgaps much larger than InAs. This Chapter describes the initial growth and characterisation of binary compounds such as ZnSe, CdSe and ZnTe and ternary compounds such as CdMgSe and ZnSeTe on InAs. A study of the II-VI layers in terms of bandgap and lattice constant was also conducted. We grew both binary and ternary compounds initially on InAs substrates obtaining crystalline layers which had well-defined X-ray diffraction (XRD) and photoluminescence (PL) peaks. After we optimised the process on InAs substrates, we then extended the study to examine sidewall passivation on processed mesa photodiodes to produce detectors with low leakage currents.

This is the first study of growth of II-VI materials on InAs mesa structures showing that this novel technique gives promising results in term of device passivation, and hence represents an important achievement in device processing even if further investigations are required. A pre-growth surface oxide removal and passivation study was also carried out to improve surface morphology of these materials grown on InAs. A standard heat clean process could damage the mesa samples due to the high temperature involved so we developed a chemical cleaning method ensuring the samples were not exposed to high temperatures during growth.

5.2 Relevance to other work on II-VI layers for InAs diode passivation

Figure 5.1 shows the variation of the bandgap energy of different materials as a function of their lattice constant. CdSe has the closest lattice constant to that of InAs, with a value of 6.050 Å.

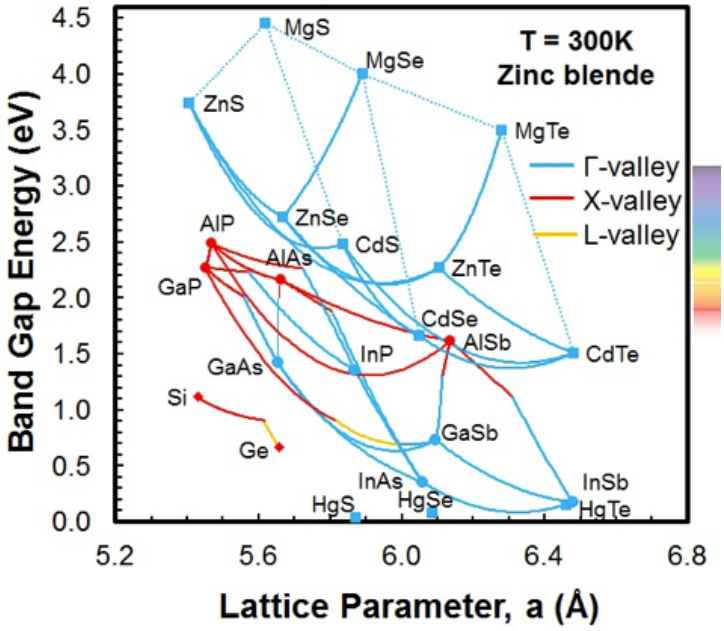

Figure 5.1 *A graph showing the variation of the bandgap energy of different materials as a function of their lattice constants [4].*

Table 5.1 shows in detail the values of the lattice constant and bandgap at 300 K for the main compounds analysed in this Chapter.

	Lattice Constant (Å)	Bandgap Energy at 300 K (eV)
ZnSe	5.668	2.72
CdSe	6.050	1.69
MgSe	5.890	4
ZnTe	6.103	2.29
InAs	6.058	0.36
GaAs	5.653	1.42

Table 5.1 Values of the lattice constant and bandgap at 300 K for the main compounds analysed in this Chapter [5], [6], [7].

Previous studies have demonstrated high quality II-VI epitaxial growth on InAs substrates [1], [8]. Ivanov *et al.* [1] successfully grew several II-VI semiconductors including CdSe on InAs substrates using two MBE growth chambers. Their method required InAs homoepitaxial buffer layers deposited in a dedicated III-V system, followed by an As cap layer. This served as a passivating layer which protected the surface from atmospheric contamination and oxidation during transfer to the II-VI MBE chamber. II-VI compounds were then grown after annealing the sample in the II-VI chamber to remove the As layer.

Ouyang *et al.* also successfully grew ZnTe on different substrates [8], [9], including InAs in a MBE system with separate III-V and II-VI growth chambers connected via an ultrahigh-vacuum transfer module. Here substrates were deoxidized in the III-V chamber under As overpressure, followed by the growth of the corresponding buffer layers, and then transferred under vacuum to the II-VI chamber for the ZnTe growth. This technique gives high quality growth but does not allow the use of InAs substrates in a dedicated II-VI chamber. To remove the oxide without As overpressure, heating the substrate above its congruent evaporation temperature occurs, with high densities of In droplets forming during oxide removal.

ZnSe is not a common II-VI semiconductor grown on InAs due to the large lattice mismatch with InAs. As is shown in Figure 5.1, ZnSe has a similar lattice constant to GaAs, and for this reason ZnSe films are usually grown on GaAs substrates [10], [11]. The novel results reported in this Chapter demonstrate that it is possible to deposit high quality single crystalline ZnSe directly on InAs.

In this thesis for the first time we report the achievement of high quality single crystal II-VI passivation layers on InAs mesa structures. Despite the large lattice mismatch with InAs, we show that ZnSe successfully terminates the InAs mesa devices preventing atmospheric oxidation. This novel use of ZnSe as a device passivation agent prevents any deep level traps forming within the InAs bandgap that are the origin of the surface currents. ZnSe is at the same time an ideal material for producing InAs mesa packaged devices because of its high bandgap. We report the first ZnSe-passivated InAs mesa packaged photodiodes. Better II-VI compounds that can be used for the same purpose are ZnTe and CdMgSe; they still present a reasonably high bandgap and at the same time they are almost lattice matched with InAs. We have found that ZnTe also successfully passivates InAs mesa structures showing negligible surface leakage currents, and mesa packaged photodiodes have been produced for the first time. The growth of CdMgSe on top of mesa samples is still a challenge; the complexity of a ternary compound has to be investigated in more detail to try to find the best growth parameters for the II-VI layer. More studies and analysis have to be conducted for a better understanding of the CdMgSe/InAs heterostructure. CdMgSe-passivated InAs mesa samples have not yet been demonstrated. This new idea to use II-VI layers for passivation techniques can be extended to every III-V semiconductors-based device.

5.3 Characterisation techniques

5.3.1 X-ray Diffraction

Crystal structures can be studied through the diffraction of X-ray photons, neutrons and electrons. [12]. When the beam is incident on the sample, a strong interaction takes place with the periodic electrical potential of the crystal: the beam is scattered by each atom in the periodic crystal, which generates spherical scattered waves. The spherical waves interfere and constructive interference can be observed at particular directions. The superposition of the waves, scattered elastically by the atoms, gives information about layer thickness, composition and quality of the epitaxial structures.

X-ray diffraction (XRD) is a non-contact, non-destructive technique that allows the sample's characterisation by studying the diffracted X-ray beams from a crystal. It uses high-energy photons with wavelengths comparable with or smaller than the lattice constant of the material studied. Bragg's law forms the foundation of X-ray diffraction and states that it can be viewed as the reflection of plane waves off successive crystal planes. The incident waves are specularly reflected from parallel planes of the atoms in the crystal, with each plane reflecting only a small fraction of the radiation. The specular reflection is elastic so that the angle of incidence is equal to the angle of reflection. Reflections from the parallel planes of atoms interfere constructively. This process normally takes place without any energy loss (i.e. elastic scattering) and is known as X-ray diffraction. A diagrammatic explanation of the Bragg equation is shown in Figure 5.2.

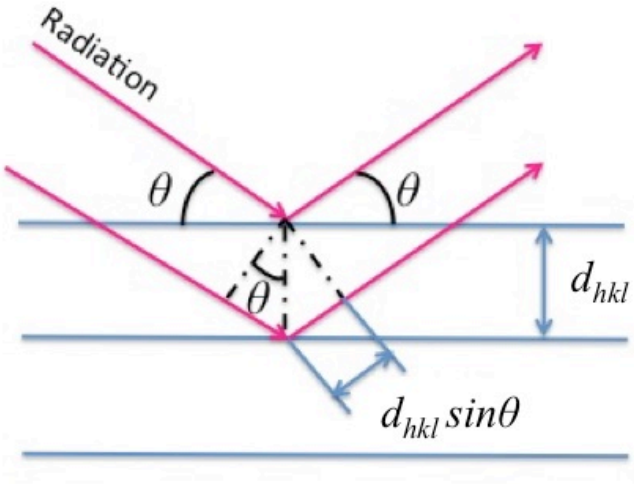

Figure 5.2 *Derivation of Bragg's law. Here d_{hkl} is the spacing between parallel atomic plane and θ is the incident angle. The radiation is drawn as pink arrows.*

If parallel lattice planes spaced d_{hkl} are considered, the path difference for rays reflected from adjacent planes is $2d_{hkl}\sin\theta$, where θ is measured from the plane. Constructive interference of the radiation from successive planes occurs when the path difference is equal to the wavelength λ:

$$2d_{hkl}\sin\theta=\lambda \tag{5.1}$$

Equation (5.1) is known as Bragg's law. For certain values of θ, (corresponding to integral multiples of λ) the reflections from all periodic parallel planes will add up in phase to give a strong diffracted beam.

A schematic diagram of the geometry of the X-ray diffracted system used in this thesis is shown in Figure 5.3.

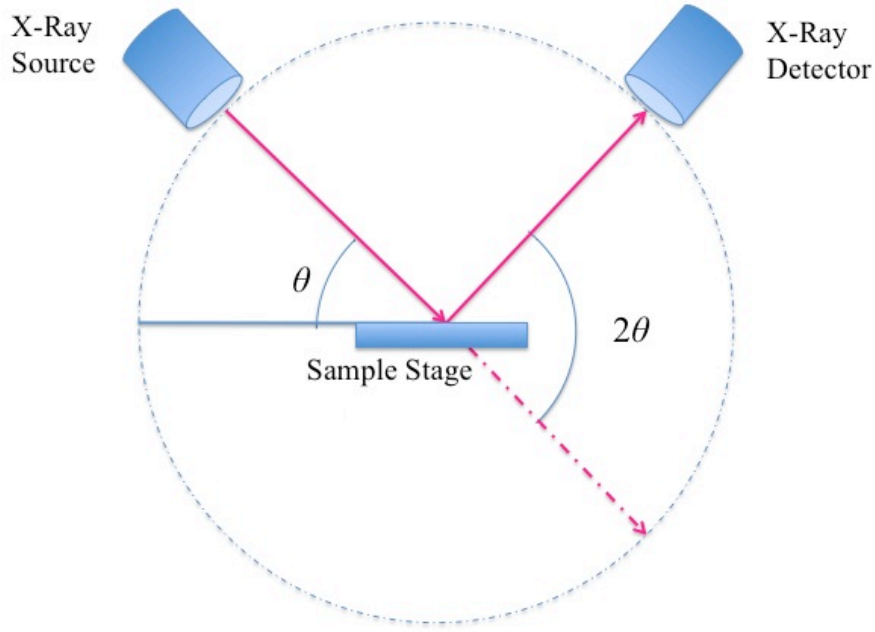

Figure 5.3 *Geometry of the X-ray diffraction system used in this thesis. The scan procedure during the acquisition process is so that the sample and detector angles are in a θ/2θ alignment.*

The X-ray beam, generated from electron bombardment of a copper target that produces radiation at the Cu Kα line with a wavelength of 1.54 Å, is directed at the sample stage with an incident angle θ. After the interaction with the crystal structure of the sample, the reflected beam is collected by the X-ray detector which is connected to a PC where the counts are recorded [13]. The position of the X-ray detector with respect to the sample stage is shown in Figure 5.3.

A rocking curve is a plot of diffracted intensity versus angular position (θ) of the sample [14]. It is obtained by rotating the sample through small angles around the vertical rotation axis of the sample stage. The X-ray data presented in this thesis were collected by using the $\theta/2\theta$ scan: as the stage was rotated through a range of many arcsec the detector is moved simultaneously maintaining the same $\theta/2\theta$ alignment. During the scan, the detector aperture was restricted with a slit for reducing background and scattered radiation.

5.3.2 RHEED Oscillation technique

Reflection High Energy Electron Diffraction (RHEED) is one of the most useful analytical tools used for characterising layers during MBE growth. It is based on the

study of the diffracted pattern of an electron beam from a crystal [12]. As with X-rays, the diffraction phenomenon can be explained in terms of Bragg's law. In the RHEED technique a beam of high energy electrons is directed upon a crystal surface at very small glancing angles of incidence (<5°). The beam is diffracted from the crystal after penetrating only a few atomic layers, resulting in a diffraction pattern that is determined by the periodicity of the crystal surface. This diffraction pattern can be monitored on a phosphor screen.

A RHEED system consists of an electron gun and a fluorescent phosphor screen as shown in Figure 5.4.

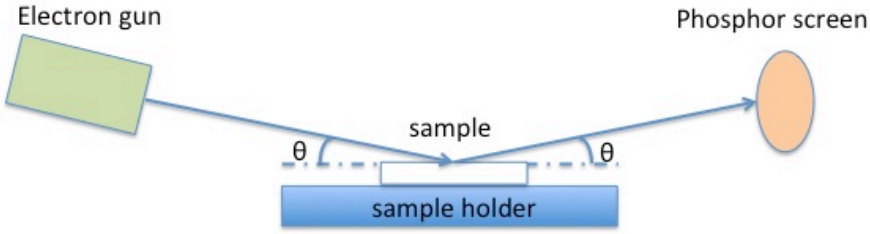

Figure 5.4 *Schematic diagram of a RHEED system setup. An electron beam, emitted by a gun, is diffracted according to Bragg's law by the sample under analysis. The diffracted beam is then monitored on a fluorescent screen.*

The electron gun emits high-energy electrons in the range 10 – 15 keV. A phosphor coated lead glass screen is located opposite to the electron gun. This fluorescent screen converts the intensity of the diffracted RHEED pattern into visible light [15].

RHEED can be used to study sample morphology and to estimate the growth rate during a MBE growth [16]. In this thesis RHEED was used to evaluate the thickness of the samples grown. RHEED oscillation measurements were only available in New York as will be shown in section 5.5.1.1. Monitoring a diffraction maximum, it is possible to estimate the growth rate as shown in Figure 5.5.

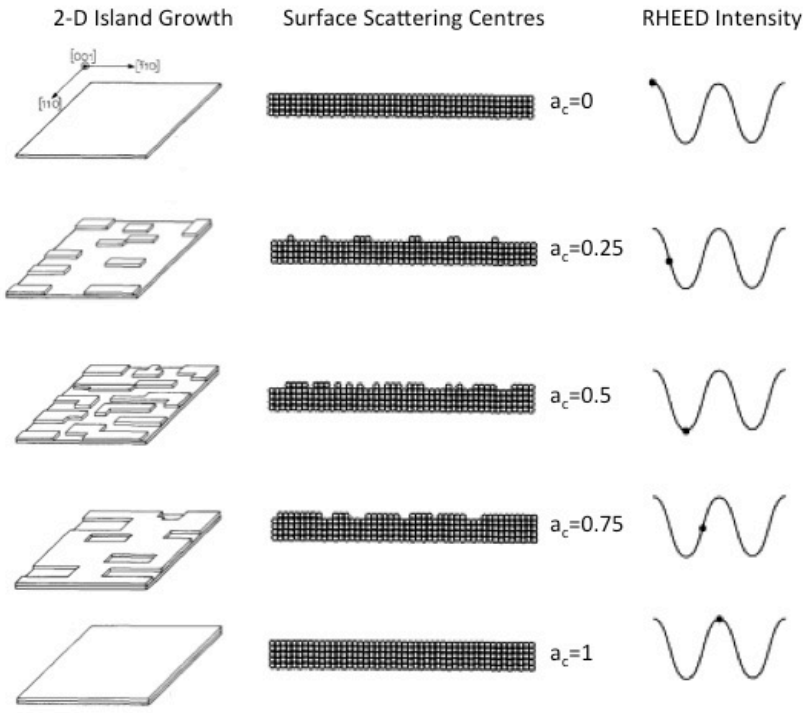

Figure 5.5 *Schematic diagram of the correlation of the surface coverage of 2D clusters with idealised RHEED oscillations. a_c is the fractional layer coverage. The graphs on the right show the RHEED intensity as a function of time [16].*

During the deposition process atoms arrive at the sample and nucleate. At the beginning the sample is smooth and the scattered waves interfere constructively showing a maximum in the RHEED pattern. When the atoms arrive on this smooth surface, they start to nucleate in 2D islands forming steps that increase the sample roughness. The rougher surface causes more diffuse scattering of the RHEED beam, leading to a lower intensity of the diffracted beam. Other arriving atoms will migrate to the step (edge) of this 2D island thus bond building up a monolayer. A monolayer contains one layer of each atomic species involved in the growth. Increasing the number of atoms that arrive on the surface, the diffracted intensity decreases until a minimum observed for a fractional layer coverage a_c equal to 0.5 corresponding to a maximum surface roughness. From this stage of the monolayer growth, further atoms smooth the surface. A maximum in RHEED intensity is observed when the monolayer is completed. Thus the surface cycles between smooth and atomically rough, with a period corresponding to the time to complete a monolayer of growth. The correlation between the RHEED

oscillation period and the monolayer growth rate allows the thickness of the layer to be evaluated.

5.3.3 Ellipsometry spectroscopy

Ellipsometry spectroscopy is a non destructive optical characterization technique that allows the investigation of film properties such as thickness, roughness, optical constants and composition. It measures the change of polarisation after the light is reflected from the sample under analysis. Light polarised parallel to the plane of incidence is called *p* polarised, while light polarised in the perpendicular direction is called *s* polarised. A schematic of the ellipsometry set up is shown in Figure 5.6.

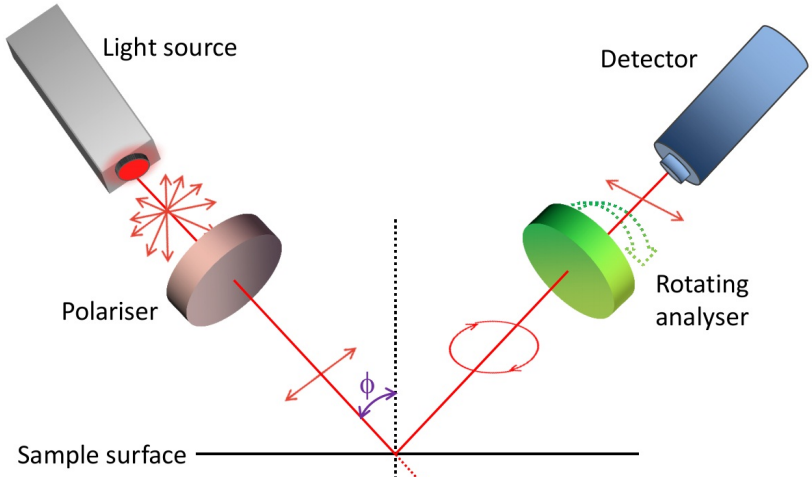

Figure 5.6 *Sketch of a rotating analyser ellipsometry set up [13]. In this configuration, the linearly polarised light reflects from the sample surface, becomes elliptically polarised, and travels through a continuously rotating polariser referred to as the analyser. The rotating analyser then produces a detector output intensity as a function of polarisation angle.*

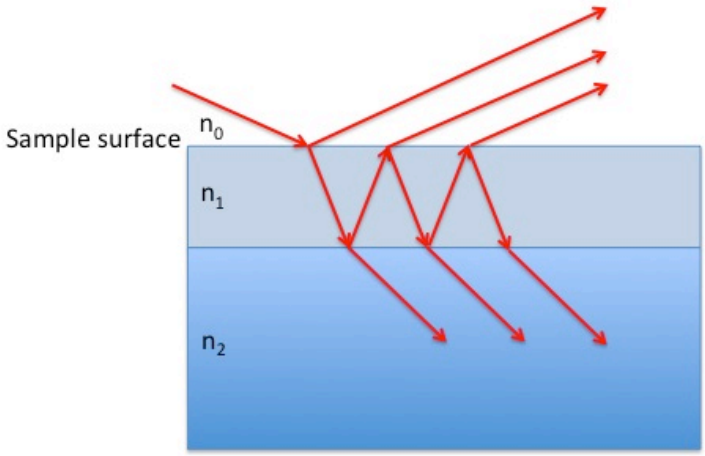

Figure 5.7 *Light reflects and refracts at each interface of the sample structure leading to interference in the reflected light measured by the detector. Interference between beams depends on relative phase and amplitude of the electric fields. Fresnel reflection and transmission coefficients can be used to calculate the response from each contributing beam.*

The light emitted from the source is made parallel, linearly polarised by a polariser, and incident on the sample. This light is then reflected by the sample according to Snell and Fresnel laws. Fresnel reflection and transmission coefficients are applicable at each interface of the sample as shown in Figure 5.7. The beam, after multiple reflections and transmissions, then passes through an analyser and is focused onto a detector, giving an electronic signal determining the details of the reflected polarization. This information is compared to the known input polarisation to determine the polarisation change caused by the sample reflection. The polarisation change is represented as an amplitude ratio ψ and phase difference Δ. These experimental values are compared with theoretical values extrapolated from a model built up to describe the material structure. The model is used to calculate the predicted response from Fresnel's equations, which describes each material in the structure giving an estimation of its thickness, optical constants and other properties. Finding the best match between the model and the experiment is typically achieved through regression where the mean squared error is used to quantify the difference between curves. The unknown parameters are allowed to vary until the minimum error is reached.

5.3.4 Photoluminescence Spectroscopy

Photoluminescence spectroscopy (PL) is a characterisation technique that allows sensitive analysis of the material quality. It is a non-contact, non-destructive method used for analysing the electronic structure of semiconductors.

The sample under analysis is illuminated by a laser with photon energy greater than the band-gap of the semiconductor sample. The incident photons excite the sample's electrons from the valence to the conduction band. Simultaneously holes are created in the valence band. If the electron in the conduction band is normally excited to a state above the conduction band minimum, it is then subjected to a process known as thermalisation: the excited electron can lose some of its energy via non-radiative processes by undergoing phonon interactions with the lattice. This non-radiative interaction takes place in a few picoseconds. Finally the excited electron falls from the conduction band into a hole in the valence band and releases its energy as radiation. This radiative processed is called luminescence and it is studied in the PL spectra; the radiative interaction takes place in a few nanoseconds. The intensity of the PL depends on the crystalline quality of the material. In high quality "direct gap" materials, the band-to-band transition dominates and the energy of the emitted photon gives information about the material bandgap. The PL spectra can also provide details on the material strain [15]. Furthermore, radiative processes can involve localised defect and impurity levels resulting in photon emission at lower energies. The study of the light emitted from these energy levels can be used to identify specific defects in a material [17]. Figure 5.8 is an example of a PL spectrum where a deep level defect is visible [18]

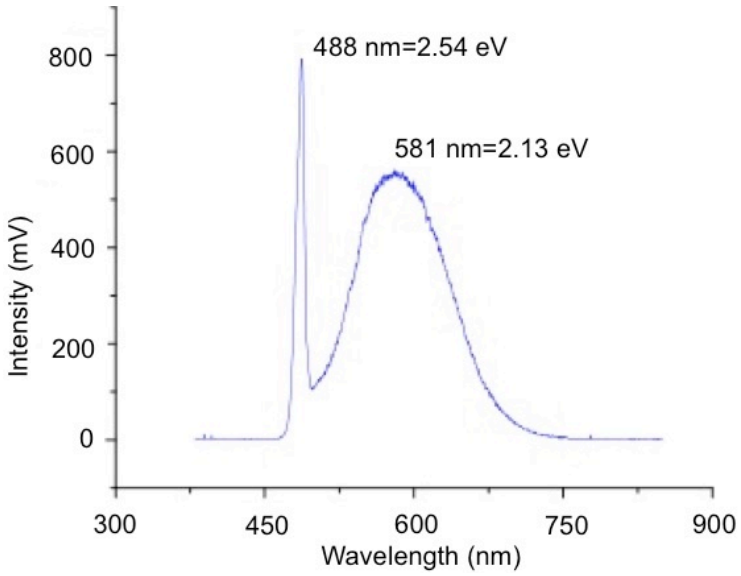

Figure 5.8 *PL spectrum from a ZnCdSe quantum well. The ZnCdSe PL peak centred at 2.54 eV is visible as well as a deep level defect peak at 2.13 eV [18].*

The experimental set up used for the PL measured in this Thesis is shown in Figure 5.9. A diode laser with a wavelength of 375 nm, is used as the excitation source. The laser beam is directed to a mirror and then to a 75 mm focal length lens (Lens 1) that focuses the light onto the sample placed in a cryostat. A cryostat allows measurements to be carried out at temperature between 77 K and room temperature. The luminescence emitted from the sample passes again through Lens 1 and then to Lens 2 (75 mm focal length) that couples the light to a fibre and to the monochromator. At the monochromator exit, a charge coupled device (CCD) array detects the emission as a function of wavelength. Computer software sets the CCD exposure time and analyses the PL spectra collected.

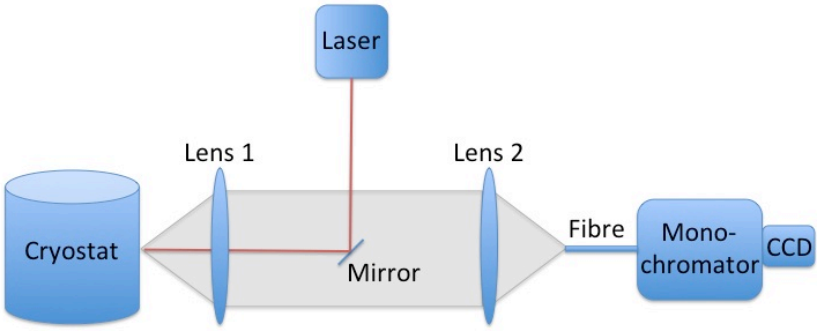

Figure 5.9 *Experimental set up for the PL measurements The sample is inside a cryostat and its luminescence is collected by a monochromator CCD detector.*

5.3.5 Atomic Force Microscopy

Atomic force microscopy (AFM) is a high resolution microscopy technique that utilises the detection of a small force between a small probe and the sample surface [12]. With this technique, mechanical contact force, Van der Waals forces, capillary forces, chemical bonding, electrostatic forces, Casimir forces and solvation forces can be measured. It consists of a millimetre-sized cantilever with a sharp tip (probe) at its end that is used to scan the sample. The cantilever is typically silicon with a tip radius of curvature of the order of nanometres. When the tip is brought into proximity with a sample surface, forces between the tip and the sample lead to a deflection of the cantilever according to Hooke's law. The cantilever behaves as a simple harmonic oscillator with angular frequency given by:

$$\omega_0 = \sqrt{\frac{C}{m}} \tag{5.2}$$

where m is mass of the cantilever and C is the cantilever's force constant. The force F_c exerted on the tip by the sample deflects the cantilever:

$$F_c = C\Delta z \tag{5.3}$$

where Δz is the displacement of the cantilever and is measured as a function of tip position by using the back of the cantilever as a reflector for a laser beam. Motion of the reflector changes the path of the laser beam, which is collected using a detector, as is shown in Figure 5.10. Picometre-scale displacements can easily be measured with this microscopy technique.

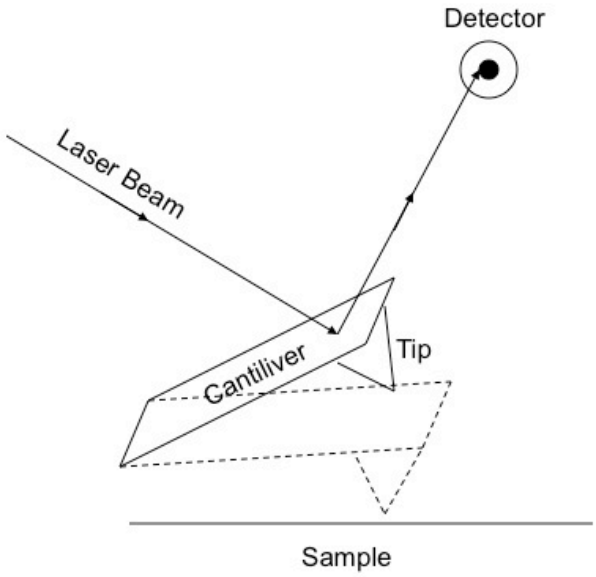

Figure 5.10 *Sketch of AFM operational mechanism. The cantilever deflects according to the force that the sample exerts on it. The displacement in the cantilever is measured using a laser beam. The motion of the cantilever changes the path of the laser beam, which is collected using a detector.*

According to the AFM mode of operation, attractive or repulsive forces can be studied. Figure 5.11 shows the force involved in the system versus tip-to-sample separation.

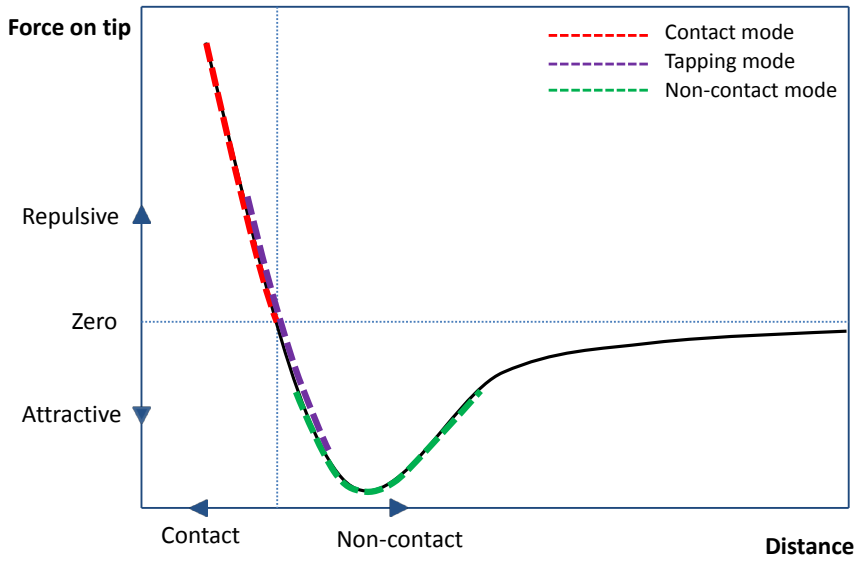

Figure 5.11 *Force involved in the AFM system versus tip-to-sample separation distance. Attractive or repulsive forces can be studied with the different AFM mode of operation: contact mode (red dash line), tapping mode (purple dash line) and non-contact mode (green dash line) [13].*

At the right side of the curve of Figure 5.11 the tip and sample are separated. As the tip and the sample are gradually brought together, their atoms begin to weakly attract each other mainly through the Van der Waals effect (noncontact mode). This attraction increases until the atoms are so close together that their electron clouds begin to repel each other. This electrostatic repulsion progressively weakens the attractive force as the separation continues to decrease. The total force goes through zero and finally becomes positive (repulsive). The slope of the curve is very steep in the repulsive regime (contact mode). This force balances and surpasses almost any force that attempts to push the atoms closer together.

The simplest mode of operation of an AFM is contact mode, where the tip is dragged along in contact with the surface. The sample under the tip is gently moved, the contact/repulsion forces cause the cantilever to bend to accommodate changes in the topography and the cantilever deflection is measured. When the cantilever pushes the tip against the sample, the cantilever bends rather than forcing the tip atoms closer to the sample atoms. AFM in contact mode gives a good measure of the sample topography, but it can damage the sample. This mode of operation has not been used to study the samples analysed in this thesis.

Noncontact or tapping (intermittent-contact) imaging modes are less invasive, and they also can give information about the long-range forces between the sample and the tip (largely a result of Van der Waals interactions). In these techniques, the cantilever oscillates just above the sample due to an applied driving force of amplitude F_ω near the cantilever resonance frequency ω_0. The parameters characterizing the oscillating cantilever are sensitive to the forces that occur between the tip and the sample. The interaction shifts the resonance frequency ω_0 or equivalently changes the vibration amplitude. These changes are recorded and used to construct an image.

In tapping mode, the cantilever is driven to oscillate up and down near to its resonance frequency by a small piezoelectric element mounted in the AFM tip holder. The amplitude of this oscillation is usually greater than 20 nm [13]. The interaction of forces acting on the cantilever when the tip comes close to the surface such as Van der Waals force, dipole-dipole interaction and electrostatic forces cause the amplitude of this oscillation to decrease as the tip gets closer to the sample. An electronic servo uses the piezoelectric actuator to control the height of the cantilever above the sample. The servo adjusts the height to maintain a set cantilever oscillation amplitude as the cantilever is scanned over the sample. A tapping mode AFM image is therefore produced by imaging the force of the intermittent contacts of the tip with the surface. Tapping mode has become an important AFM technique as it overcomes some of the limitations of both contact and non-contact AFM. One of the major advantages of tapping mode is related to limitations that can arise due to the thin layer of liquid that forms on most sample surfaces in an ambient imaging environment (i.e., in air or some other gas). The amplitude of the cantilever oscillation in tapping mode is typically of the order of a few tens of nanometres, which ensures that the tip does not get stuck in this liquid layer. The amplitude used in non-contact AFM is much smaller. As a result, the non-contact tip often gets stuck in the liquid layer unless the scan is performed at a very slow speed. In general, tapping mode is much more effective than non-contact AFM, but especially for imaging larger areas of the sample that may include greater variation in topography. Tapping mode can be performed in gases and non-corrosive liquids.

5.3.6 Optical and Electron Microscopies

Optical and electron microscopies use the interaction of particles, photons and electrons respectively, to probe the object under study and create an image [12].

In the bright field optical microscopy a collimated beam of photons is focused though optical lenses onto the sample, the scattered and the reflected photons from the sample are then collected by a camera building up the sample image.

In the bright field electron microscopy a collimated beam of electrons is accelerated by high voltages and focused using a series of electrostatic and magnetic lenses onto the sample. In a Scanning Electron Microscope (SEM), a high-energy (100 V to 100 kV) focused beam is scanned over the sample. The number of secondary electrons generated by the beam that comes from the sample depends on the local composition and topography of the sample. A detector collects these electrons. Plotting the detector signal as a function of the beam location, an image of the sample surface can be formed. Another electron microscopy technique is the Transmission Electron Microscopy (TEM) where the electron beam travels through the sample giving information about the internal structure of the sample. In this thesis the samples were analysed using SEM.

Both optical and electron microscopies have an ultimate resolving distance depending on the wavelength of the probe source which in the case of electron microscopy is given by the de Broglie wavelength of the electron:

$$\lambda = \frac{h}{p} \tag{5.4}$$

where p is the momentum of the electron.

Optical and electron microscopies can be used in the dark field microscopy method. Dark field microscopy takes into account only the scattered beam that comes from the sample [19]. In this thesis dark field images were taken using the optical microscope. In dark field measurements, a disk blocks the light used to illuminate the sample leaving only an outer ring of illumination focused on the samples. When the light ring hits the sample most is reflected and some is scattered. While the scattered light can enter the objective lens, the reflected light is blocked and does not reach the objective. In the dark field mode only the scattered light

produces the image. Small, low-contrast or transparent samples, that are not visible in bright field microscopy, are visible with the use of a dark-field microscopes. In dark field images the weak light that scatters off the side of a feature is visible allowing sample details to be revealed without any additional preparation. The main limitation of this method is that it needs high intensity illumination to see properly the sample features and this could damage the sample under analysis.

5.4 Growth of II-VI compounds on InAs conducted at Heriot-Watt University

All the II-VI compounds presented in this section were grown at Heriot-Watt University in a VG V80H MBE system using 6N sources of Zn, Cd, Mg and Se. The usual substrate temperature during II-VI growths, to achieve good quality II-VI layer deposition, is in the range 240 °C to 270 °C [20], [21]; in the present study the growth temperature was 240 °C. The InAs deoxidation temperature is around T_S=540 °C [22]. All the growths have been done in collaboration with the group of Dr. Kevin Prior, in particular with the help and the expertise of Dr Richard Moug. We do not have Te at Heriot-Watt so we made alternative arrangements for ZnTe (see below). Finally, and importantly, the only structures available were n-i-p InAs mesas (i.e. the hole conduction structure). A sketch and a picture of the MBE system used are shown in Figure 5.12.

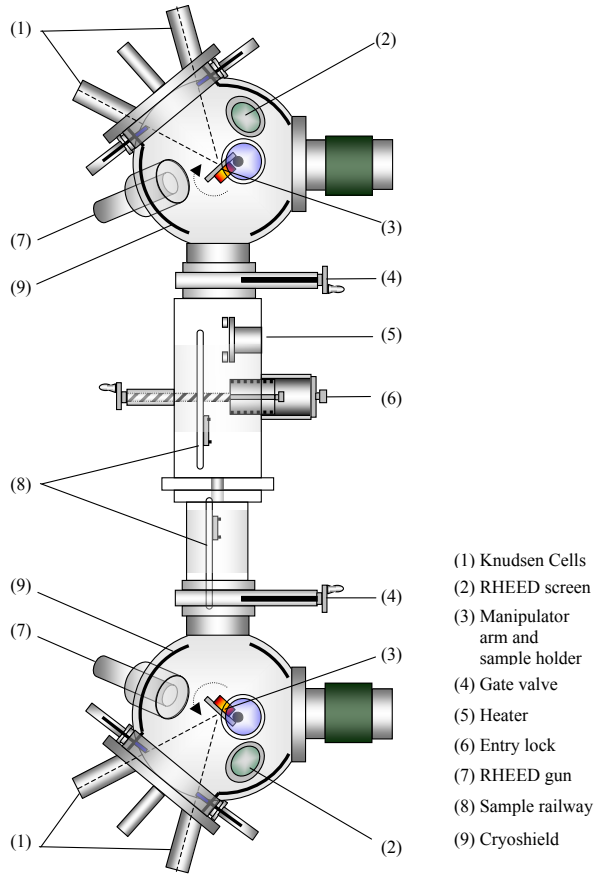

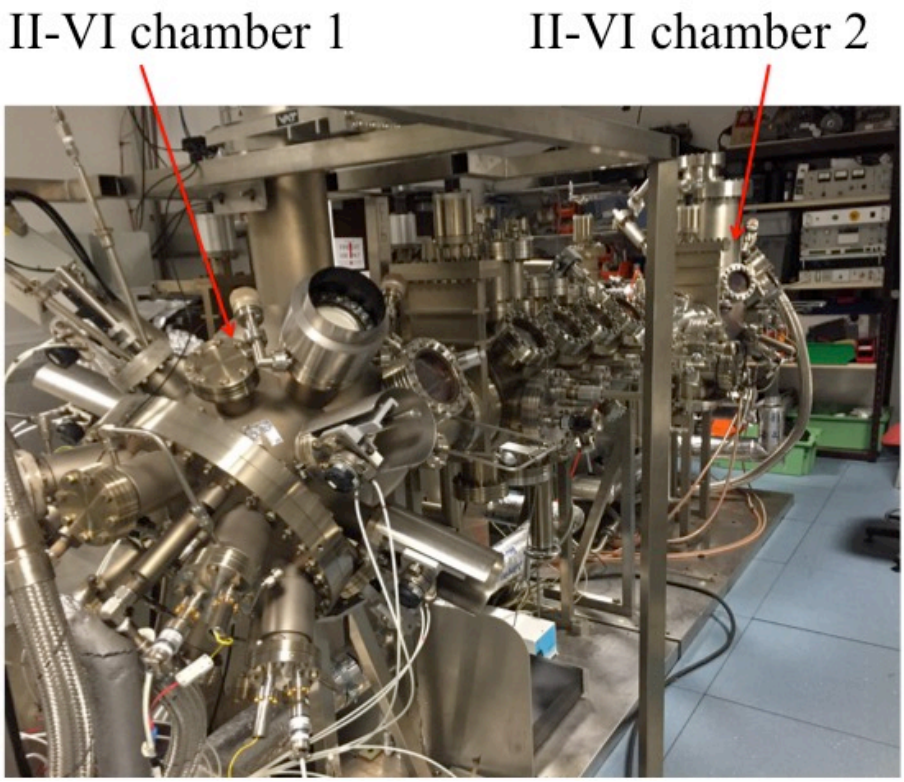

Figure 5.12 Top, schematic representation of the Heriot-Watt MBE system. The main components are numbered and listed [15]. Bottom, picture of the system.

As shown in Figure 5.12, the Heriot-Watt MBE system has two separate II-VI growth chambers connected via an ultrahigh-vacuum transfer module. The samples were inserted in the system using the entry lock (6), then moved to one of the growth chambers using the sample railway (8). Inside the II-VI chamber the sample was placed into the sample holder (3) facing the element sources, the Knudsen cells (1). Every cell is shielded from the sample by shutters. The whole system is under Ultra High Vacuum (around 10^{-9} torr) using a combination of rotary, turbo and ion pump, and the use of a liquid nitrogen shroud. This very low pressure is needed so that the mean free path of the particles between collisions is much larger than the width of the chamber: the beam particle travels in a straight line without collision until it hits the sample. For the elements involved in our growth, the use of only one chamber was needed.

5.4.1 Growth of ZnSe on InAs

The simplest method of estimating the band alignment and band offsets of intrinsic heterostructure is Anderson's rule [23]. Any doping will result in charge transfer and band bending at the interface, to maintain a common Fermi level, but we ignore this here to get the basic band offsets. Anderson's rule is based on the electron affinity, χ, of the materials, which is defined as the energy required to promote an electron from the bottom of the conduction band to the vacuum level where it can escape from the crystal. According to this rule, the vacuum levels of the materials in the heterostructure are aligned, so the conduction band offset (ΔE_C) between the two materials under consideration is given by the difference of their electron affinities. In the particular case of InAs and ZnSe, χ^{InAs}=4.9 eV [6] and χ^{ZnSe}=4.09 eV [24] (every value is subjected to at least 50 meV experimental error [23]) so $\Delta E_C{}^{InAs/ZnSe}$=0.81 eV. The InAs/ZnSe heterostructure alignment is shown in Figure 5.13. The ZnSe barrier confines carriers within the InAs diode, the thermal energy is not sufficient to let the carrier pass to the ZnSe: this avoids any leakage current through the external bondpads.

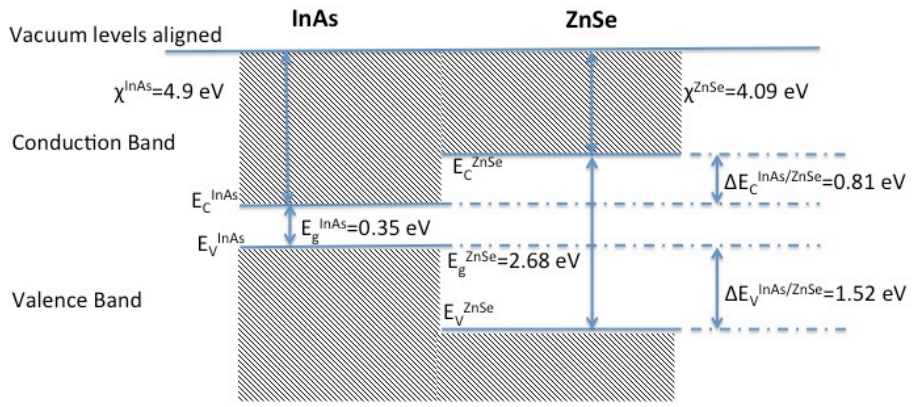

Figure 5.13 *Band structure alignment at heterojunction between InAs and ZnSe, calculated using Anderson's rule which is based on aligning the vacuum* levels.

5.4.1.1 ZnSe growth on heat cleaned InAs samples

Initially the sample was prepared by heating the InAs substrates to the deoxidation temperature of T_s=540 °C while monitoring with RHEED. Following oxide removal the substrate was then cooled to the growth temperature of T_s=240 °C, and the ZnSe layer was grown.

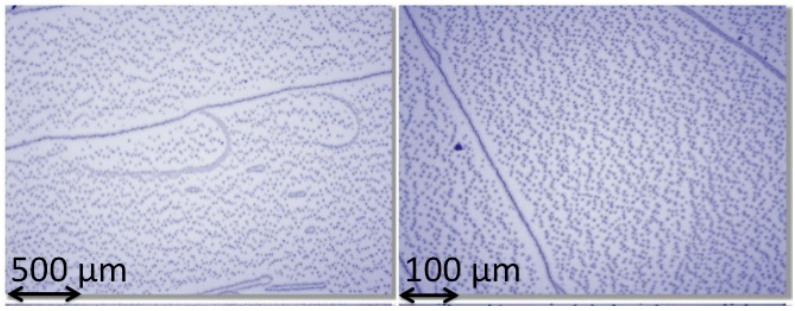

Figure 5.14 *Bright field optical microscope images of the ZnSe heat-cleaned sample. The sample area displayed is 2 × 2.7 mm for the image on the left, and 0.5 × 0.7 mm for the image on the right.*

Figure 5.14 shows bright field optical microscope images of the ZnSe/InAs sample. Pinholes are visible in the images as black spots, and are due to In droplets forming on the substrate during the high temperature removal of the oxide. The presence of pinholes in the sample surface can degrade its performance as the II-VI layer does not grow on top of the pin holes leaving areas without any passivation. This can firstly

cause an increase of surface leakage current and, secondly, short circuits when contacts are deposited. This problem can be solved by removing the oxide in As overpressure, although unfortunately this facility was not available at the Heriot-Watt MBE facility. As expected, the In droplets can be removed with an HCl etching solution.

We carried out X-ray diffraction measurements at room temperature on the sample. A well-defined XRD peak was shown demonstrating the good single crystalline quality of the ZnSe layer, as shown in Figure 5.15.

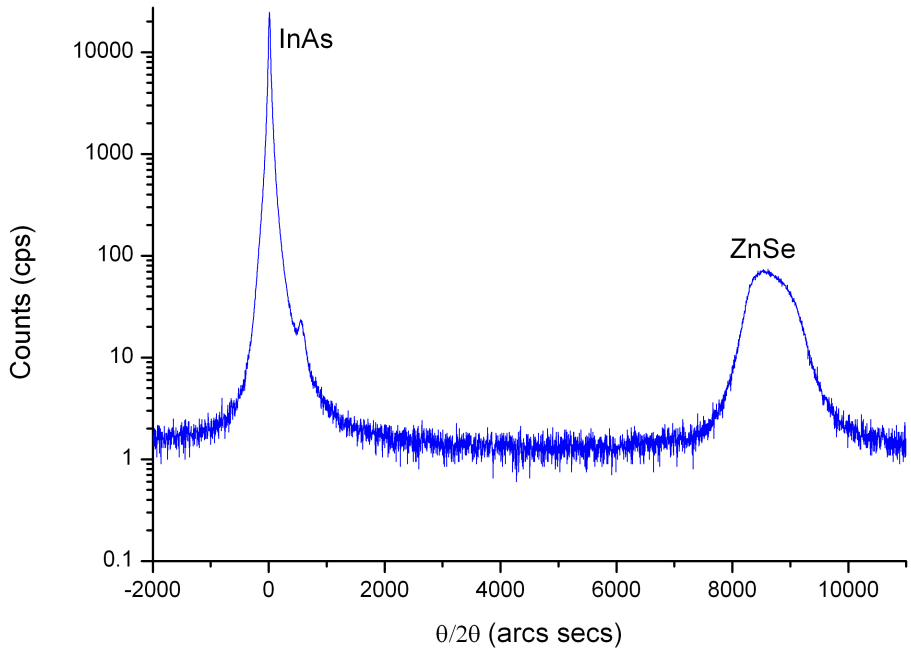

Figure 5.15 *XRD patterns from the ZnSe/InAs heat cleaned sample (room temperature).*

The XRD patterns show two diffraction peaks, one from the InAs substrate and the other from the thin ZnSe layer (the layer thickness determined from ellipsometry measurement is 380 nm). The ZnSe lattice mismatch with the InAs substrate is 6.4%, consequently the ZnSe layer is relaxed showing a symmetrical X-ray peak.

We carried out PL measurements as a function of temperature on the sample. A ZnSe PL peak has been observed. Figure 5.16 shows the normalised PL spectrum at 77 K from the heat cleaned ZnSe sample.

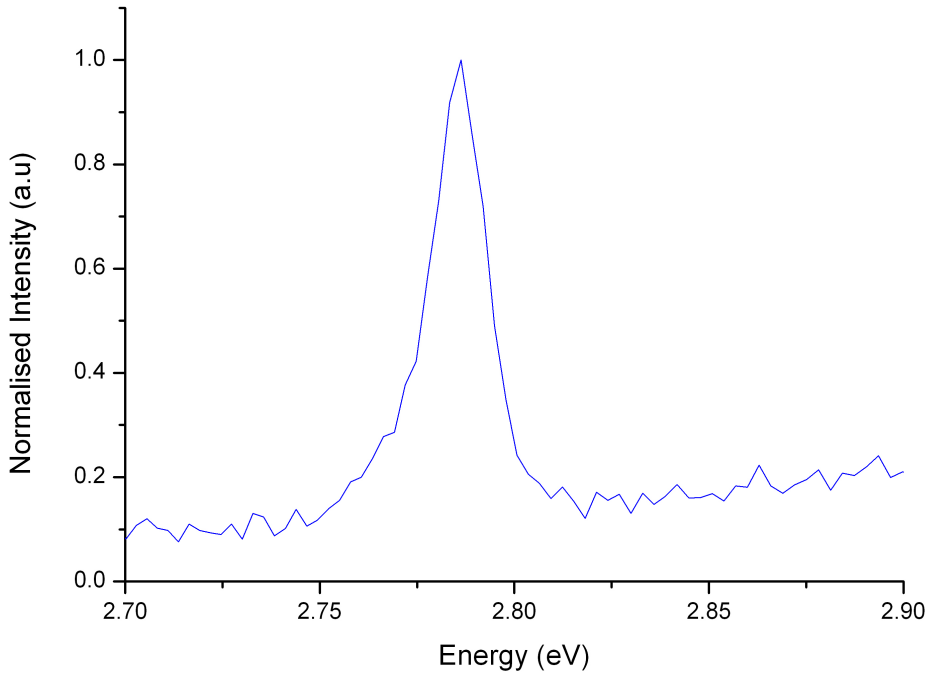

Figure 5.16 *PL spectrum from the ZnSe/InAs heat cleaned sample (77 K).*

The PL peak observed at 2.78 eV with a FWHM of 14 meV demonstrates that ZnSe with a good crystalline quality has been deposited. A deep level luminescence peak was also detected (not shown), probably caused by the formation of deep level states produced by the large lattice mismatch between ZnSe and InAs.

We studied an alternative method (below) to the heat cleaning oxide removal to prevent the sample being exposed to high temperatures. Low temperature II-VI deposition is important to avoid any sort of damage, as for example doping diffusion, caused by the heat on the sample and, at the same time, to avoid the formation of pinholes and so have also a better reproducibility.

5.4.1.2 ZnSe growth on chemically cleaned InAs samples

As seen in Figure 5.14 the heat cleaning treatment causes pinholes to form in the ZnSe layers. To avoid this an *ex situ* sample preparation is used. Therefore, instead of performing heat cleaning inside the MBE chamber, a chemical etch cleans the sample surfaces. Three solutions: HCl, H_3PO_4: H_2O_2: H_2O in the ratio of 1:1:1 and H_2SO_4: H_2O_2: H_2O in the ratio of 1:8:80 were compared using a step profile to measure the etch rates. These results are shown Table 5.2.

Etching solution	**Etch µm/min**
HCl	≈0.04
H_3PO_4, H_2O_2, H_2O (1:1:1)	≈1
H_2SO_4, H_2O_2, H_2O (1:8:80)	≈0.3

Table 5.2 *Etch rates for the etchants*

A combination of 1:1:1 H_3PO_4, H_2O_2, H_2O and 1:8:80 H_2SO_4, H_2O_2, H_2O solutions is known to remove the oxide layer from InAs and produce a clean surface [25], [26]. In the present study samples were etched for 30 s in each solution. However, when the sample was mounted on the substrate heater using indium at 160-180 °C a new oxide layer is formed on the InAs surface, meaning no improvement was observed. To eliminate any re-oxidation, we used two strategies. First, a sulphur layer was deposited on top of the InAs surface to passivate the layer. Second, the In used to mount the sample was replaced by a Ga-In alloy which allowed a lower temperature (~80 °C) mounting. After the samples were etched, they were transferred to a $(NH_4)_2S_x$ (ammonium polysulphide) solution to allow a sulphur layer to form on the substrate surface preventing oxide formation [27], [28]. We carried out tests to find the optimum conditions for the formation of the sulphur passivation layer. The samples were compared under a microscope which showed that 1 hour at 21 ˚C is the best preparation, as shown in Table 5.3.

Time (hour)	Temperature °C	Surface quality
0.5	21	Good
0.5	35	Good
0.5	75	Cloudy
1	21	Best
24	21	Bad

Table 5.3 *Sulphur treatment as a function of temperature and time.*

We grew ZnSe on top of the chemically cleaned InAs substrates. In this case the samples were heated to T_s=300 °C before cooling to the growth temperature of T_s=240 °C. The growth time was kept the same as the heat cleaned sample so as to have a II-VI layer of around the same thickness.

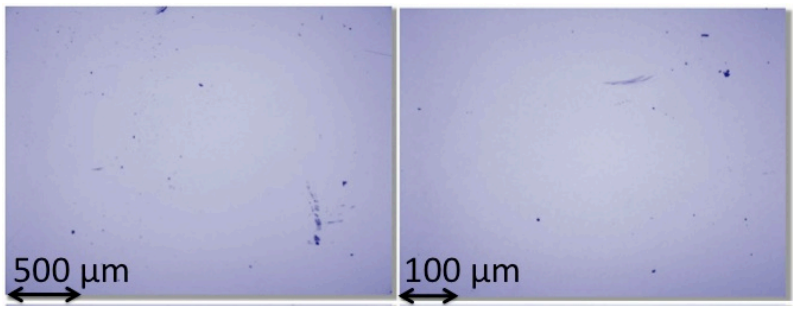

Figure 5.17 *Bright field optical microscope images of the ZnSe chemical cleaned sample. The sample area displayed is 2 × 2.7 mm (left), and 0.5 × 0.7 mm (right).*

Figure 5.17 shows bright field optical microscope images of the samples after growth. Due to the absence of the high temperature heat cleaning step, pinholes are not present in the samples over areas of many square mm, demonstrating that very good crystalline quality ZnSe can be grown on a sulphur passivated InAs substrate. XRD results at room temperature from these samples are shown in Figure 5.18.

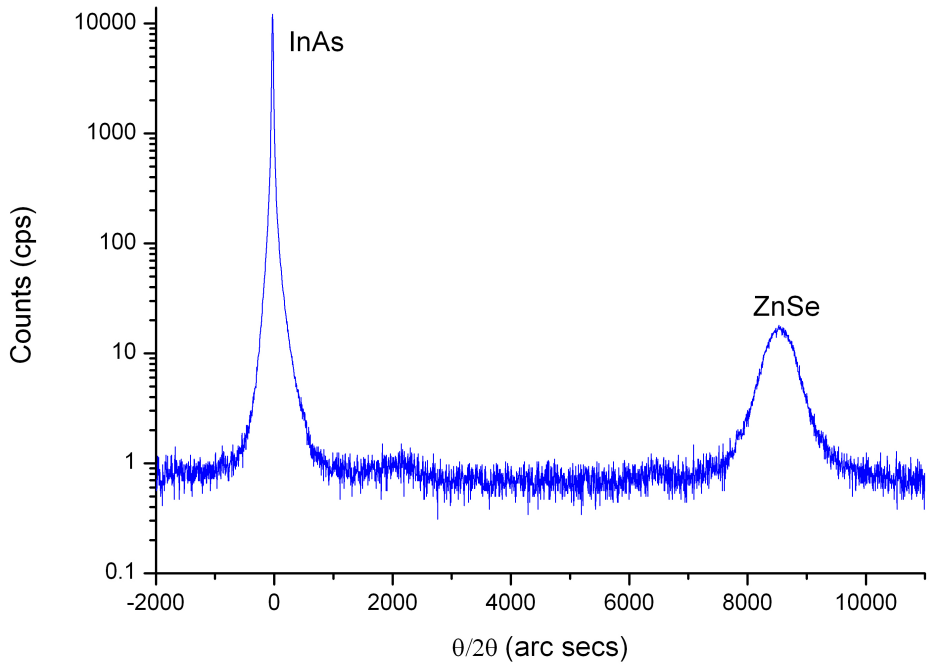

Figure 5.18 *XRD patterns from the chemically cleaned ZnSe/InAs sample (room temperature).*

Again XRD shows two very clear diffraction peaks, one feature representing the InAs substrate and the other representing the ZnSe film. The ZnSe layer is completely relaxed showing a symmetrical X-ray peak. The well-defined peaks show that this chemical treatment has not prevented single crystal epitaxial growth.

Figure 5.19 shows the normalised PL spectrum from the chemically cleaned ZnSe sample at 77 K.

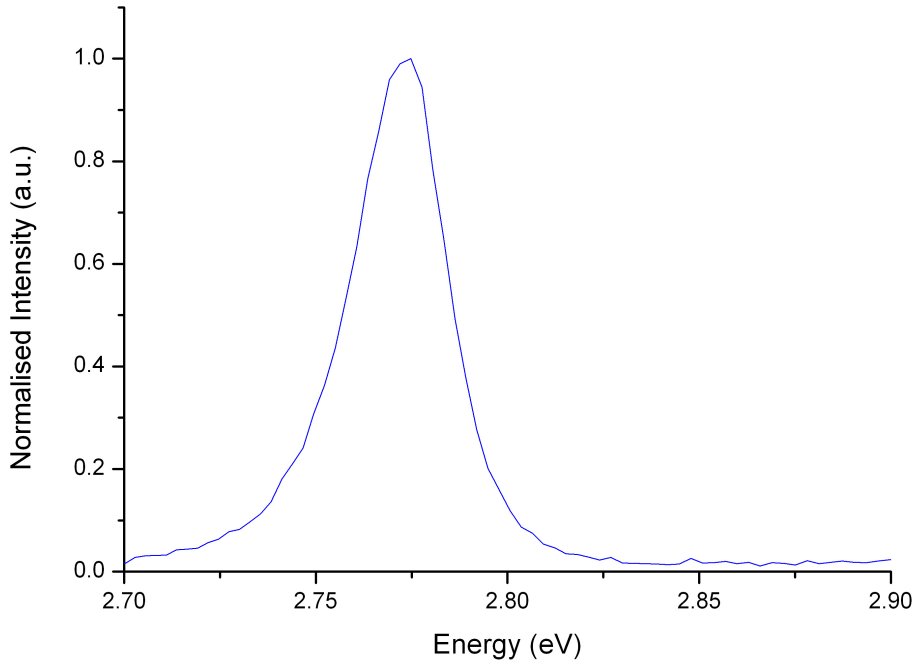

Figure 5.19 *PL spectrum from the ZnSe/InAs chemically cleaned sample (77 K).*

A clear ZnSe PL peak at 2.77 eV with FWHM of 29 meV is observed. The large lattice mismatch between ZnSe and InAs causes the formation of deep levels that result in a detectable additional PL peak at lower energy (not shown).

Once the growth of ZnSe on the InAs substrate was optimised, we grew ZnSe on top of an InAs mesa sample which had been chemically cleaned. The samples were heated to T_s=300 °C before cooling to the growth temperature of T_s=240 °C. An AFM image of the ZnSe/InAs mesa sample is shown in Figure 5.20: the picture shows in detail a 50 μm device. Figure 5.21 and Figure 5.22 shows images of the same sample taken with the SEM.

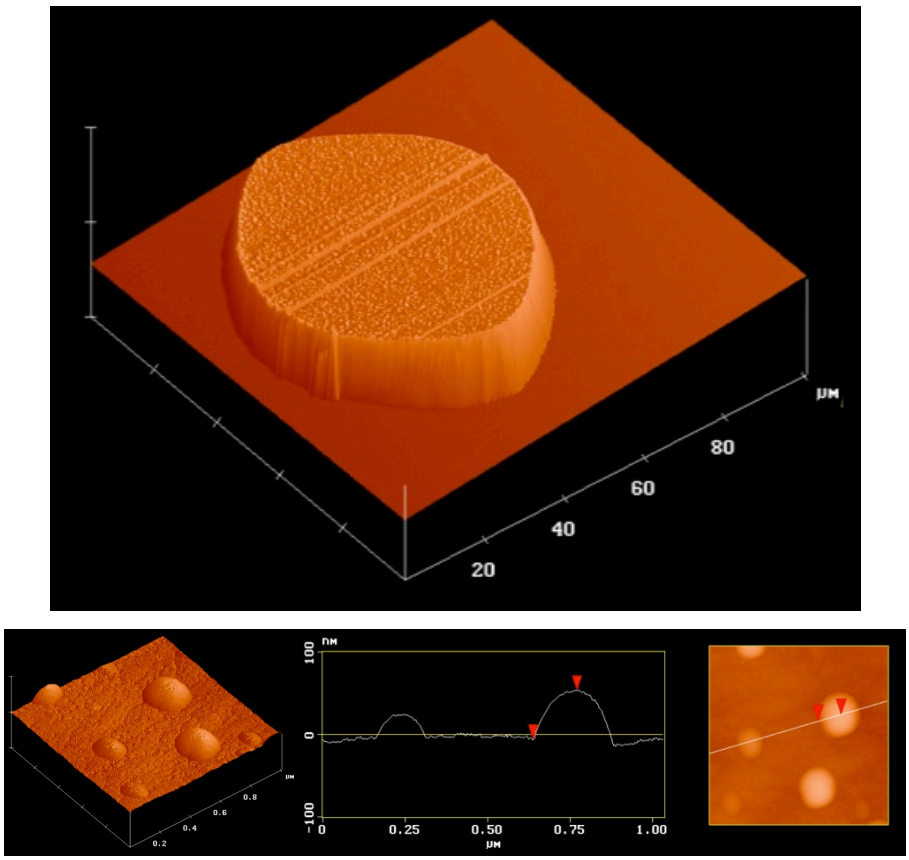

Figure 5.20 *Top, an AFM image of a 50 µm diameter ZnSe-passivated mesa device. The sample area analysed is 100 × 100 µm. Bottom, zoom of 1 µm^2 area on top of the ZnSe-passivated mesa device. The surface is smooth with some Selenium clusters 50-200 nm in diameter and 20-60 nm in height. These clusters are due to the exposure of the Se contaminated sample surface layer to the atmosphere [29]. The sample has Se on its surface because of the Se background in the chamber which is important when the sample cools after growth. At Heriot-Watt the background of the II-VI chamber is mainly Se with a little sulphur.*

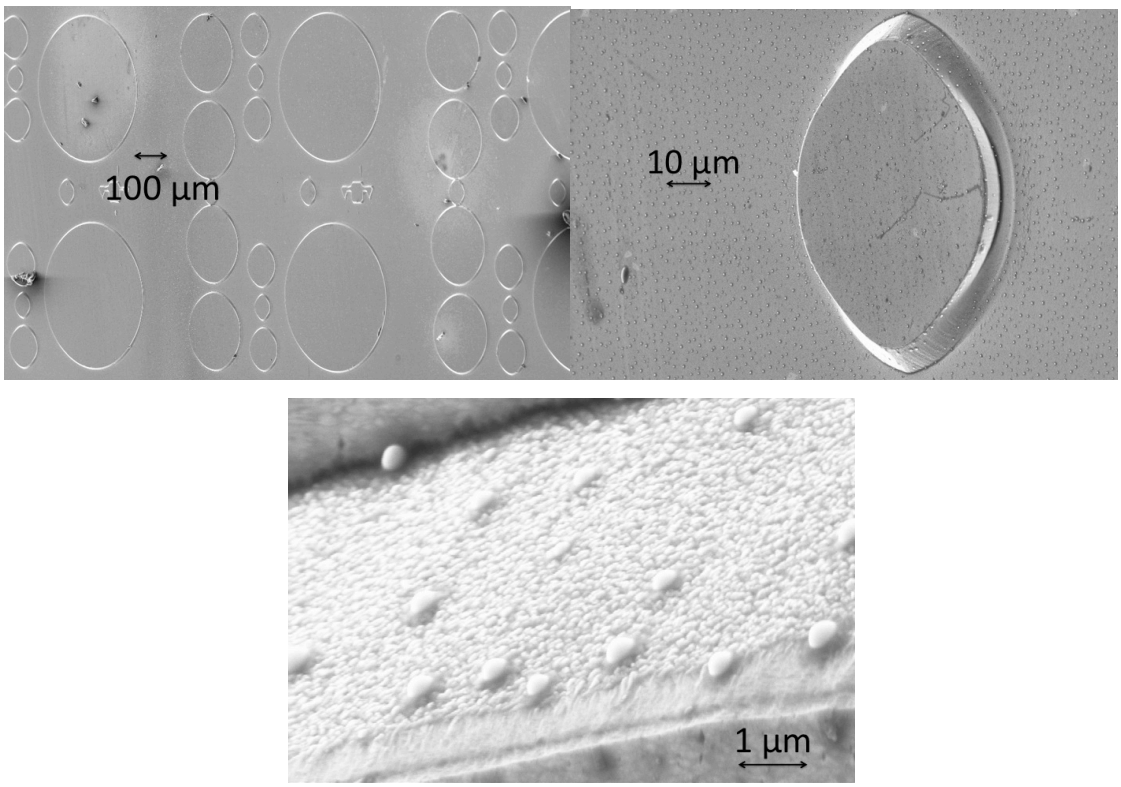

Figure 5.21 *SEM images of the sample at different magnifications. The electron beam energy is 10 kV. Top left, cluster of ZnSe-passivated mesa devices with diameters ranging between 50 to 400 µm. Top right, zoom of a 50 µm diameter ZnSe-passivated mesa device. Bottom, zoom of a 400 µm diameter ZnSe-passivated mesa device sidewall. The ZnSe on the sidewall grows in 3D perpendicular to the etched surface. Selenium clusters are present on the sidewall surface.*

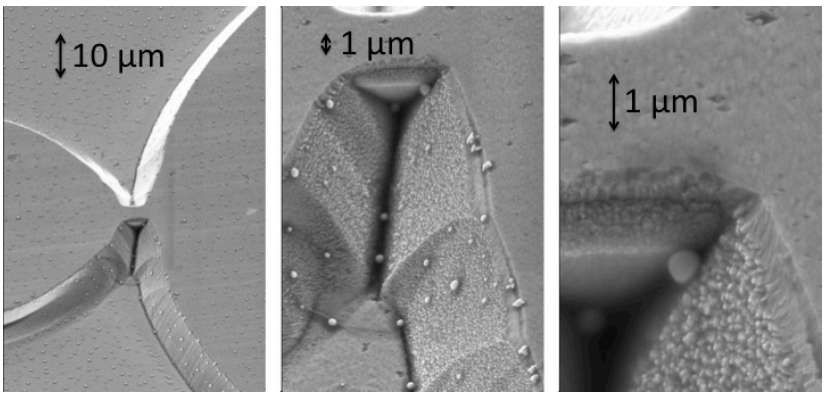

Figure 5.22 *SEM images of the sample at different magnifications. The electron beam energy is 10 kV. The pictures show the detail of a bridge that connects two ZnSe-passivated mesa devices, caused by incomplete etching. The shape of the mesa sidewall can be clearly seen. Because of the bevel angle 3D ZnSe growth is observed on the sidewall. 2D growth is observed on top of the mesa where the ZnSe grows on a flat surface. Selenium clusters are present on the surface.*

We performed PL on the ZnSe chemically cleaned mesa sample and XRD analysis. Well-defined XRD peaks and PL peaks were found demonstrating the good crystalline quality of ZnSe layers. XRD shows clear ZnSe peaks, illustrating that the chemical treatment on the mesa sample has not prevented single crystal epitaxial growth. At 77 K the PL peak is centred at 2.78 eV with a FWHM as low as 19 meV. This demonstrates that ZnSe with a good crystalline quality has been deposited. In the spectrum, a deep level peak is also present (not shown). Figure 5.23 shows the XRD (top) and the normalised PL spectrum at 77 K (bottom) from the chemically cleaned ZnSe mesa sample.

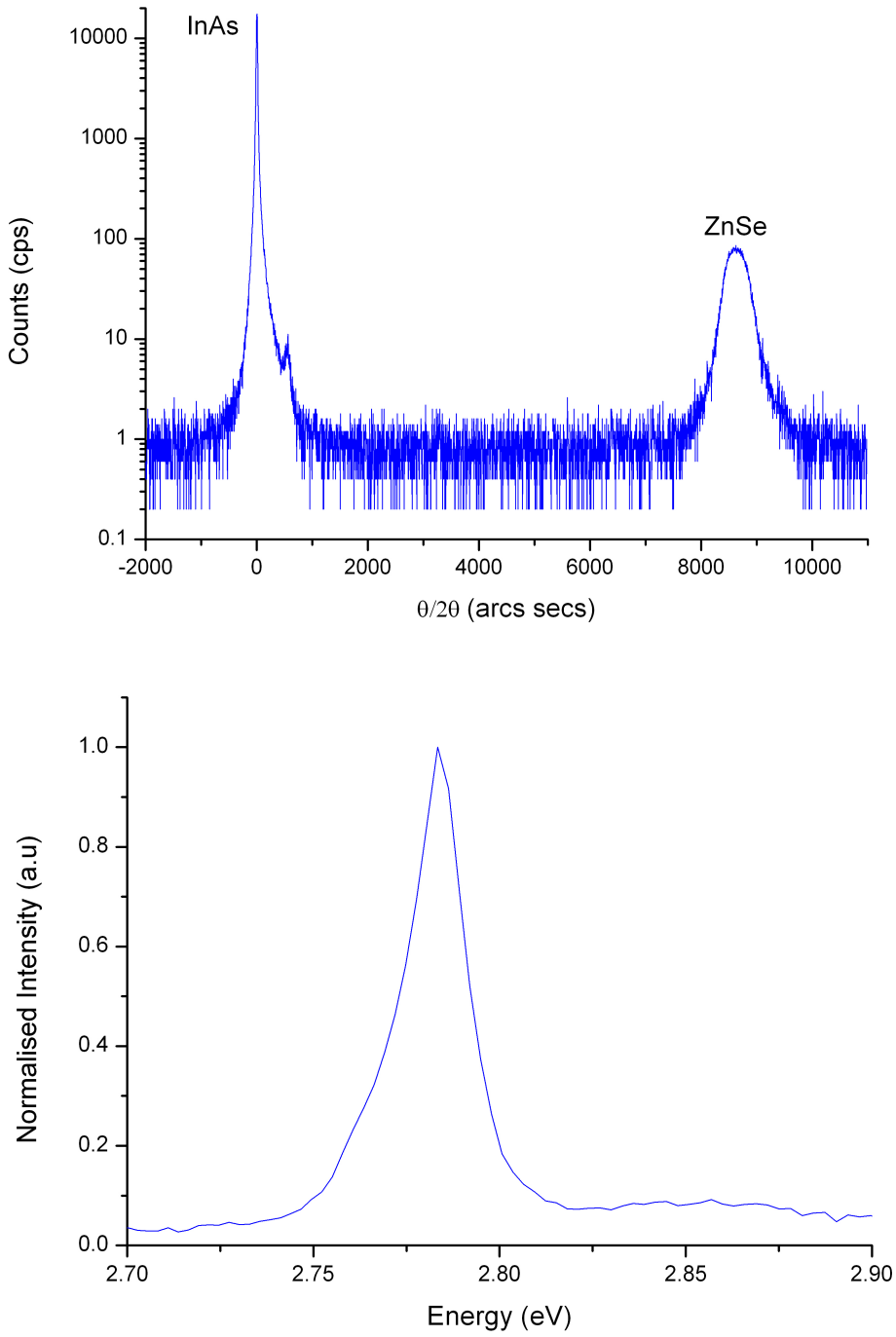

Figure 5.23 *Top, XRD patterns from the ZnSe/InAs chemically cleaned mesa sample (room temperature). Bottom PL spectrum from the same mesa sample (77 K).*

The ZnSe overgrowth successfully terminates the InAs mesa structure preventing atmospheric oxidation of the surface layers which form the deep level traps within the InAs bandgap that are likely to be the origin of the surface currents. Since ZnSe has a much larger bandgap than InAs it provides a high resistivity layer which prevents any additional leakage currents. This result is in agreement with the conduction band

alignment between ZnSe and InAs shown in Figure 5.13. This type of structure allows metallisation to be performed during device processing and packaging. The ZnSe passivation layer also provides a robust and solid layer for device to chip bonding.

Dark current measurements of the ZnSe-passivated mesas at room temperature show that the diode dark current scales with device area, Figure 5.24, indicating that surface leakage currents are negligible at this temperature. At room temperature bulk effects are present (above 1 V) and a high dark current is observed for the ZnSe-passivated sample with respect to the unpassivated reference. Further investigations at 77 K have to be conducted to study the electrical behaviour of the sample at low temperature.

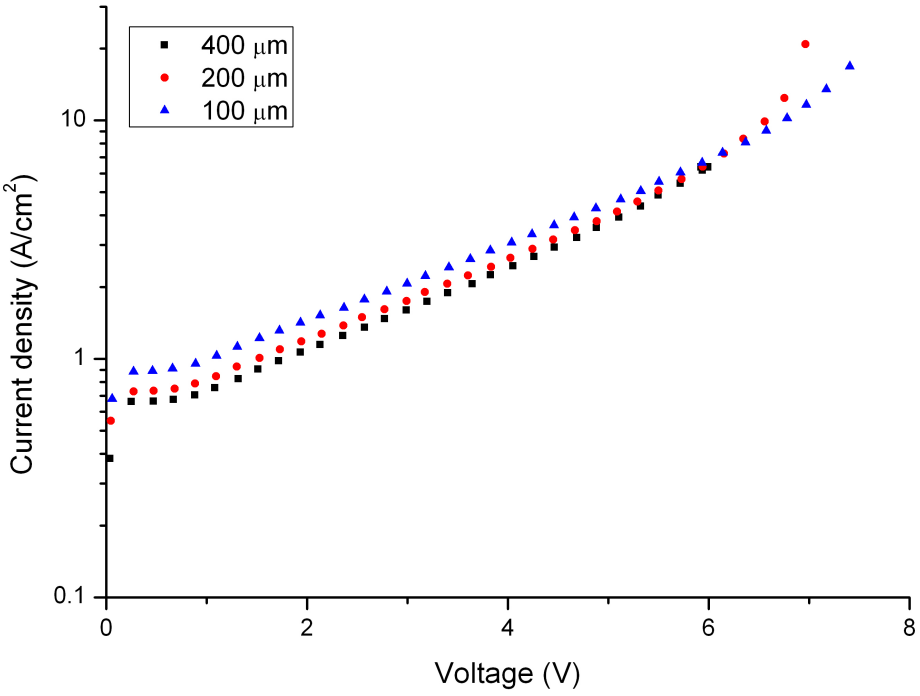

Figure 5.24 *Current density as a function of reverse bias for a ZnSe-passivated InAs mesa diode up to 8 V reverse bias at room temperature. The diameters of the devices plotted are 400 μm (black squares), 200 μm (red dots) and 100 μm (blue triangles).*

These results show that ZnSe is a good passivation layer for packaged InAs mesa APDs although its lattice constant is very different from the InAs one.

We continued our studies using the II-VI binary and ternary compounds to find a material that has similar properties to ZnSe and that, at the same time, is also lattice

matched with InAs. CdSe is the II-VI binary compound that has the closest lattice constant to that of InAs, with a value of 6.050 Å.

5.4.2 Growth of CdSe on InAs

According to Anderson's rule, in the CdSe/InAs heterostructure the conduction bands of the two materials are in close alignment as shown in Figure 5.25. χ^{InAs}=4.9 [6] and χ^{CdSe}=4.95 [30] (every value is subjected to at least 50 meV experimental error [23]) so $\Delta E_C{}^{InAs/CdSe}$=0.05 eV. This near-zero conduction band offset, possibly type II, will lead to results quite different from those found in ZnSe (section 5.4.1). The electrons require very little energy to move between the two materials, and leakage current through the external bondpads could be observed.

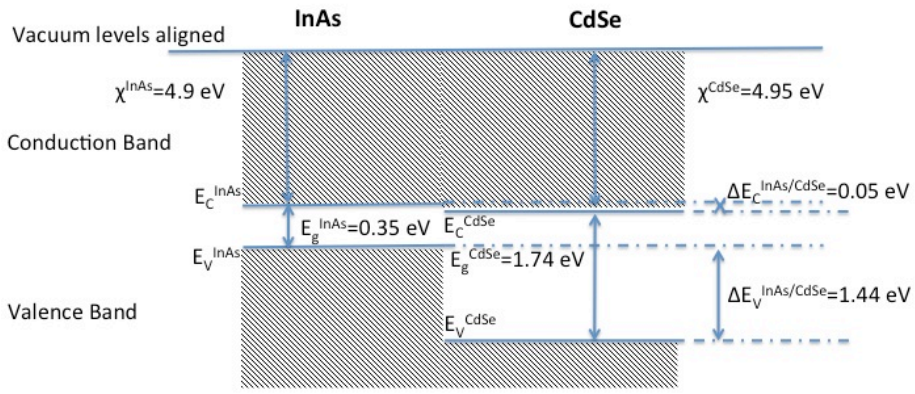

Figure 5.25 *Band structure of a heterojunction between InAs and CdSe, based on aligning the vacuum levels using Anderson's rule. There is a near-zero conduction band offset, and possibly type II band alignment (N.B. This is not expected to show a reduction in leakage current).*

5.4.2.1 CdSe growth on heat cleaned InAs samples

Initially the sample was prepared by heating the InAs substrates to the deoxidation temperature of T_s=540 °C while monitoring with RHEED. Following oxide removal the substrate was then cooled to the growth temperature of T_s=240 °C, and the CdSe layer was grown.

As with ZnSe, pinholes are present on the sample due to the high oxide removal temperature, as is visible in Figure 5.26.

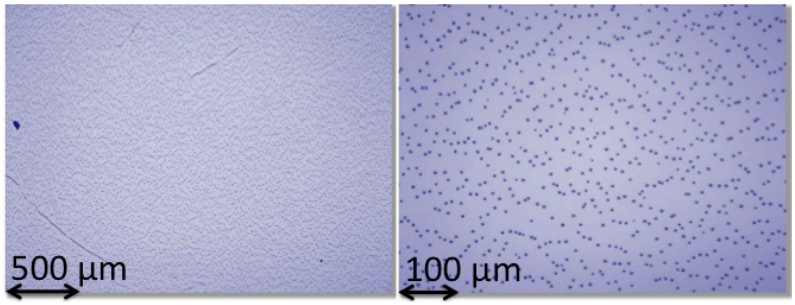

Figure 5.26 *Bright field optical microscope images of the CdSe heat-cleaned sample. The sample area displayed is 2 × 2.7 mm for the images on the left, and 0.5 × 0.7 mm for the images on the right.*

We carried out PL measurements as a function of temperature and XRD analysis also on this sample. Well-defined XRD peaks and intense PL peaks were found demonstrating the crystalline quality of CdSe layers. Figure 5.27 shows the X-ray diffraction pattern at room temperature and the PL spectrum at 77 K from the heat cleaned CdSe sample.

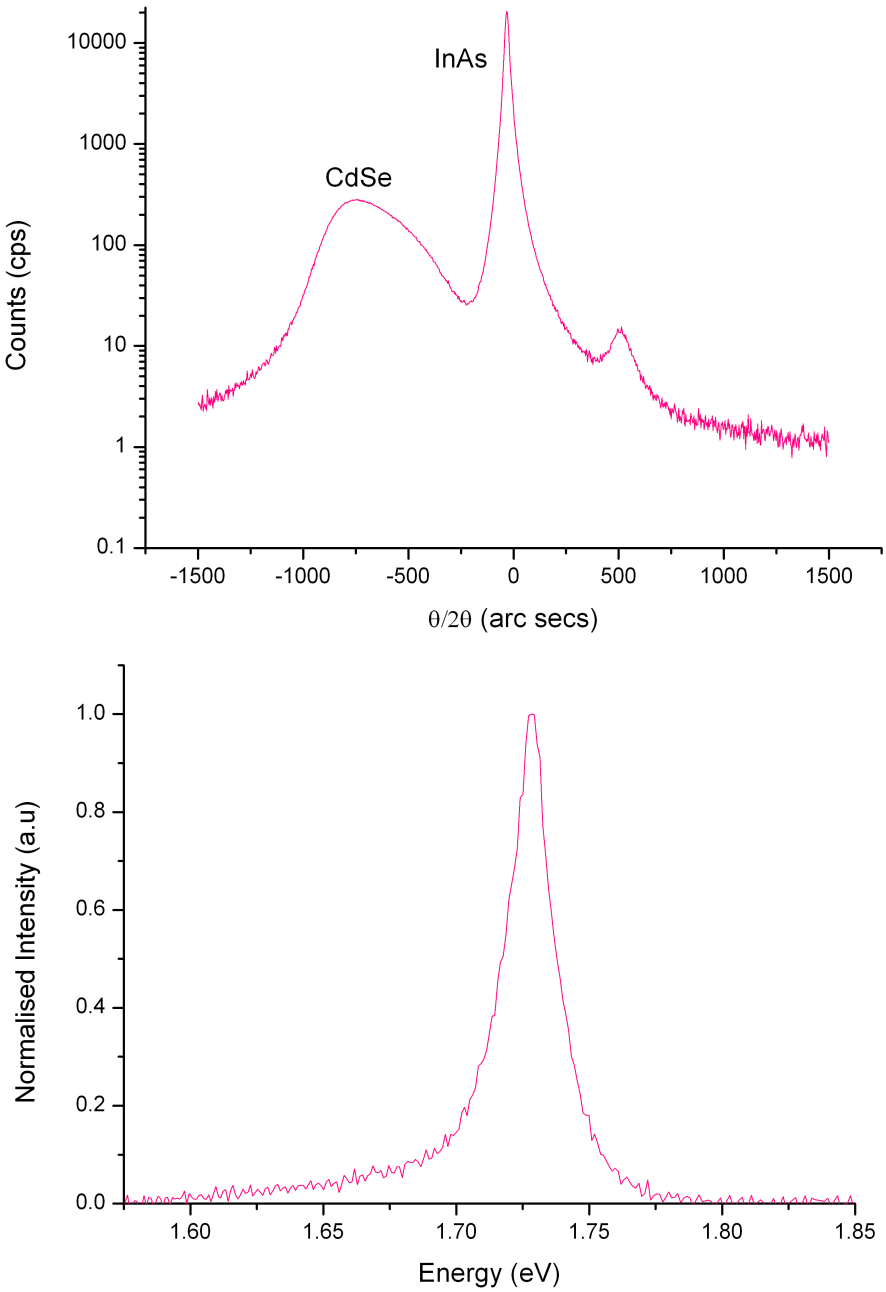

Figure 5.27 *Top, XRD patterns from the heat cleaned CdSe/InAs sample (room temperature). Bottom PL spectrum from the same sample (77 K).*

The XRD patterns show two diffraction peaks corresponding to the InAs substrate and the thin CdSe (CdSe thickness from ellipsometry measurement is 430 nm) epitaxial layer respectively. It also shows a weak peak (around 500 arc secs) which arises from the beam interacting with the Al sample holder when the sample size is small [18]. For CdSe the lattice mismatch with the InAs substrate is 0.13%, consequently the CdSe layer has a broad asymmetric X-ray peak, indicating that the layer has only partially relaxed. In the PL spectrum, the clear peak at 1.73 eV with FWHM of 19 meV is due to the CdSe luminescence.

Luminescence from any deep level defect has not been observed, indicating a good material quality.

To eliminate any pinholes from the sample and to avoid the high oxide removal temperatures that can damage a full InAs mesa photodiode, we also adopted the chemical treatment in this case.

5.4.2.2 CdSe growth on chemically cleaned InAs samples

The *ex situ* sample preparation used has been described in detail in section 5.3.1.2. Also in this case, the samples were heated to T_s=300 °C before cooling to the growth temperature of T_s=240 °C. The growth duration was similar to that of the heat cleaned sample to give a II-VI layer of around the same thickness.

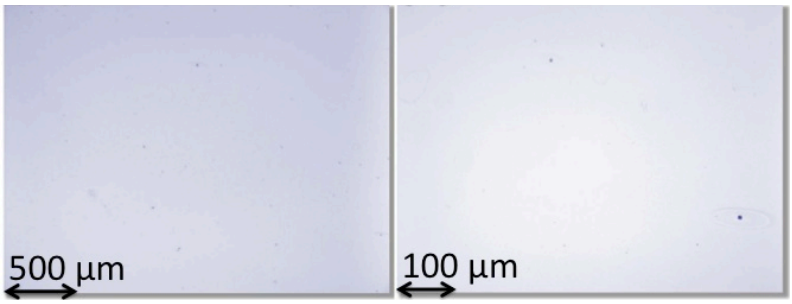

Figure 5.28 *Bright field optical microscope images of the CdSe chemically cleaned sample. The sample area displayed is 2 × 2.7 mm (left), and 0.5 × 0.7 mm (right).*

Figure 5.28 shows bright field optical microscope images of the samples after growth. As expected pinholes are not present.

XRD results at room temperature and the PL spectrum at 77 K from these samples are shown in Figure 5.29.

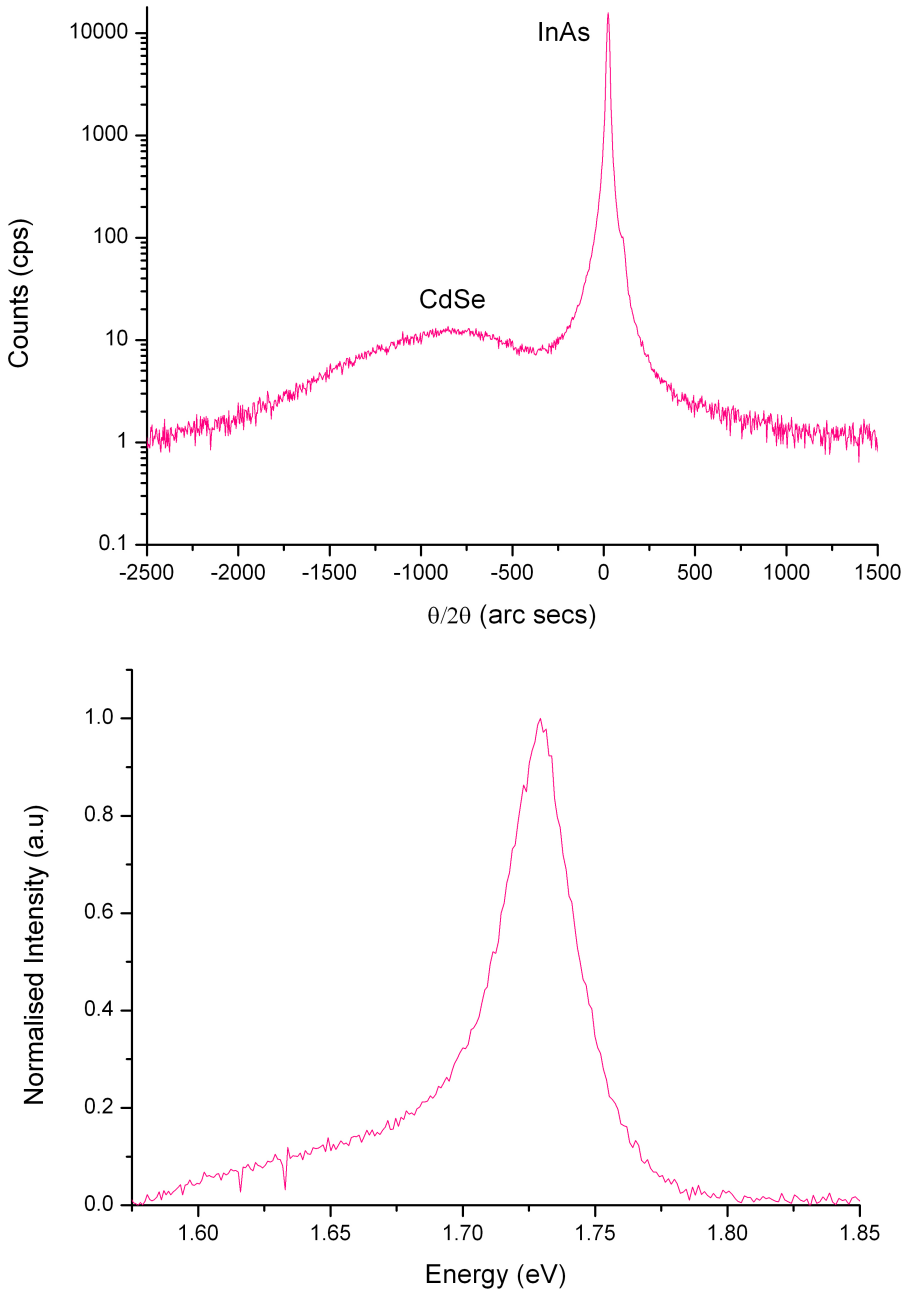

Figure 5.29 *Top, X-ray diffraction patterns from the chemically cleaned CdSe/InAs sample (room temperature). Bottom PL spectrum from the same sample (77 K).*

XRD shows two very clear diffraction peaks, for the InAs substrate and the CdSe layer. The CdSe XRD peak for the chemically cleaned sample is less intense and much broader with respect to the heat cleaned sample. As CdSe is almost lattice matched with InAs not many defects are incorporated in the heterostructure, consequently no other PL peaks are observed except the CdSe one, centred at 1.73 eV with FWHM of 33 meV.

The well-defined XR and PL peaks show that this chemical treatment has not prevented single crystal epitaxial growth.

The *ex situ* treatment, therefore, was used to clean the surface of an InAs mesa detector before the CdSe deposition. The CdSe growth parameters were kept as for the previous samples. Figure 5.30 shows images of the same sample taken with the SEM.

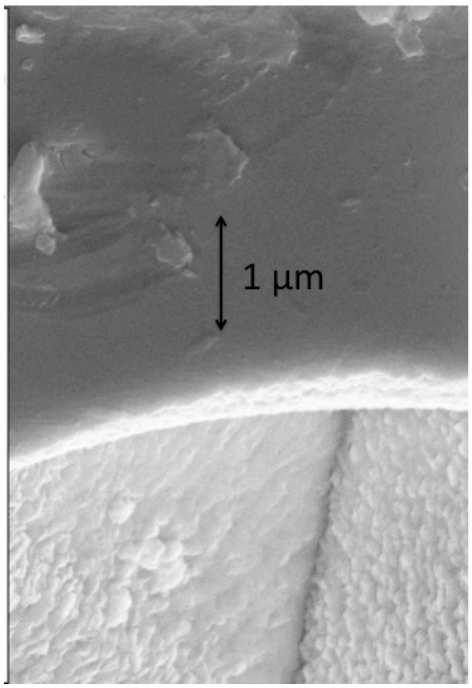

Figure 5.30 *SEM image of CdSe-passivated sample. The electron beam energy is 10 kV. The picture show the detail of a bridge that connects two CdSe-passivated mesa devices, caused by incomplete etching. Because of the bevel angle a 3D CdSe growth is observed on the sidewall. 2D growth is observed on top of the bridge where the CdSe grows on a flat surface.*

The CdSe-passivated mesa structure was then characterised using XRD and PL. Figure 5.31 shows the XRD (top) and the normalised PL spectrum at 77 K (bottom) from the chemically cleaned CdSe mesa sample.

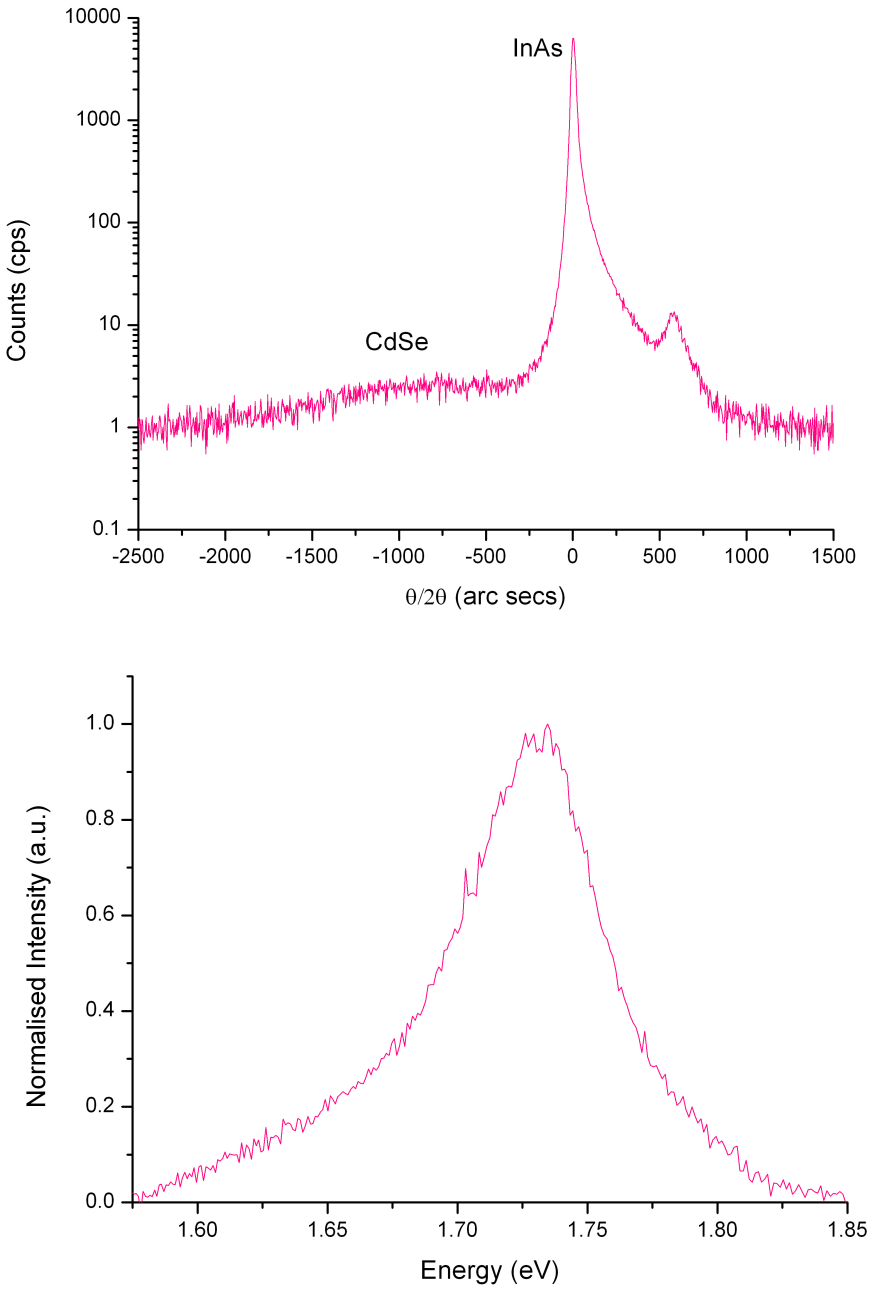

Figure 5.31 *Top, X-ray diffraction patterns from the chemically cleaned CdSe/InAs mesa sample (room temperature). Bottom PL spectrum from the same sample (77 K).*

A weak and broad CdSe XRD peak has been observed. Chemical treatment on the mesa sample has not prevented single crystal epitaxial growth, but a lower quality CdSe film (with respect to the one grown on the substrates) has been produced. The quality problem is possibly due to tilting of the crystal planes that must come from extended defects as for example dislocations. A CdSe PL peak centred at 1.74 eV with FWHM as

broad as 66 meV has also been found in this sample confirming the same conclusion as the XRD measurements regard the CdSe film quality.

We carried out a study of the full width at half maximum (FWHM) of the CdSe peaks to evaluate the effects of the two treatments used. The resulting normalised CdSe peak at 77 K for every treatment is shown in Figure 5.32.

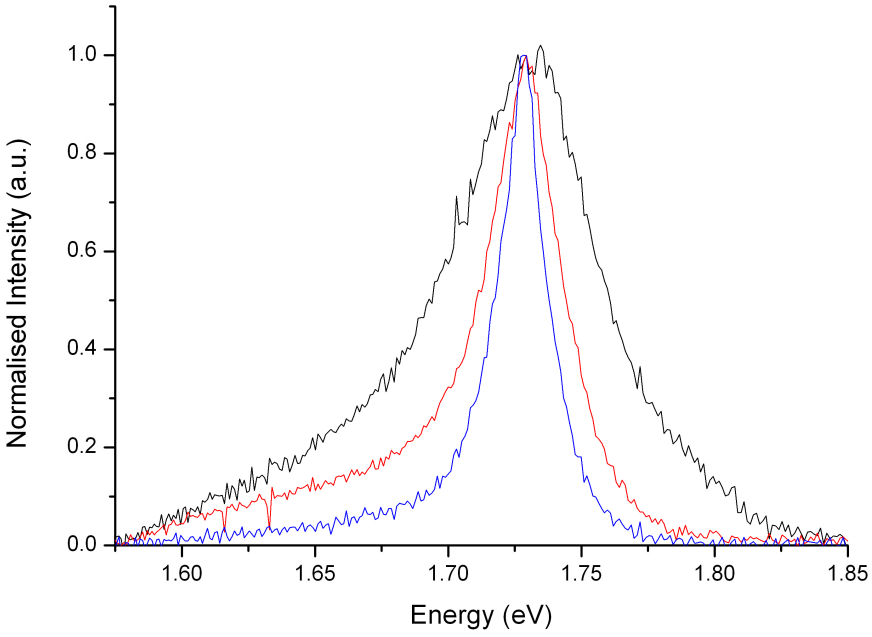

Figure 5.32 *PL peaks for the CdSe mesa chemically cleaned (black line), the CdSe substrate chemically cleaned (red line) and the CdSe substrate heat cleaned (blue line) at 77 K. The FWHM is smaller for the heat cleaned sample with respect to the chemically cleaned ones showing that a better II-VI crystal quality is achieved with the heat cleaning approach.*

The heat cleaning treatment appears to give a good quality sample surface to grow on (FWHM of the CdSe peak about 19 meV), but suffers from pinholes and poor reproducibility. The developed alternative chemical process looks to be a good alternative in term of surface cleaning, the CdSe FWHM observed is about 33 meV (slightly higher than for the heat cleaned substrate). Due to the rougher surface under the II-VI layer, the FWHM increases to 66 meV in the mesa structure. It was found that the chemical treatment in terms of XRD and PL is not as good as the heat cleaning at the present, but it removes the pinholes giving reproducible layers of usable quality; it could be improved further.

The results of the previous study are summarised in Table 5.4

	PL peak (eV)	FWHM (meV)
CdSe chemical cleaning mesa	1.74	66
CdSe chemical cleaning substrate	1.73	33
CdSe heat cleaning substrate	1.73	19

Table 5.4 *Comparison between the position of the centre of the PL peak and FWHM for the CdSe mesa chemical cleaned, CdSe substrate chemical cleaning and CdSe substrate heat cleaning at 77 K.*

Experimental dark current measurements taken on the CdSe-passivated mesas at room temperature show that the dark current is much larger than for unpassivated mesa devices as shown in Figure 5.33.

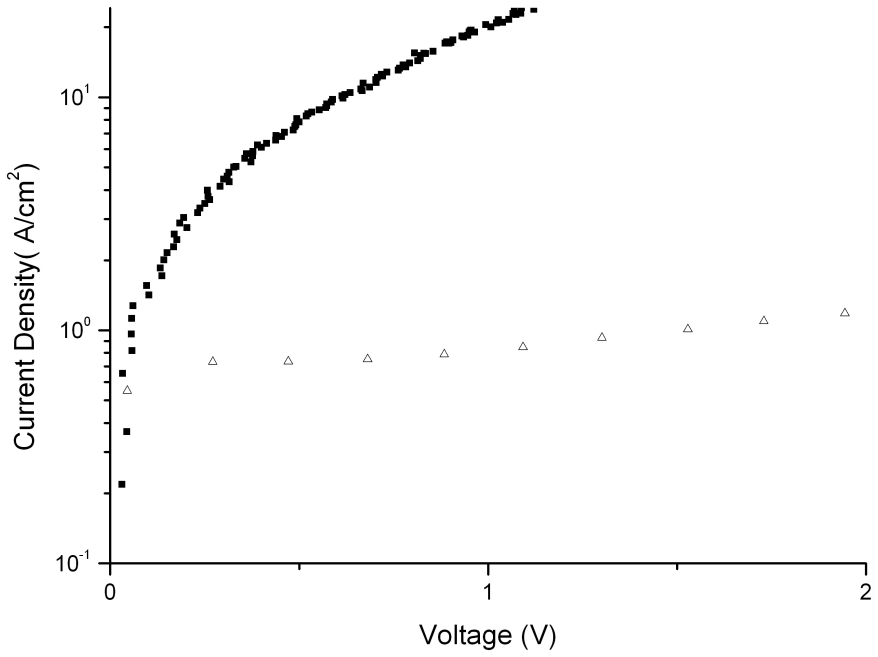

Figure 5.33 *Current density as a function of reverse bias for a CdSe-passivated InAs mesa diode (solid squares) up to 2 V reverse bias at room temperature. Current density data for the corresponding unpassivated mesa diodes (open triangles) is shown for comparison.*

Dark current measurements taken by the University of Sheffield on CdSe-passivated mesas show that the surface leakage currents have not been reduced; the dark current is

much higher with respect to the unpassivated sample, this could be mainly due to fabrication problems. The magnitude is clearly anomalous and needs further investigation. The II-VI etching recipe could play an important role in the InAs mesa photodiode fabrication and so optimisation.

CdSe is almost lattice matched with InAs but its band alignment is such that it is not a good passivation layer for InAs photodiodes because it could lead additional leakage current through the external bondpads. For this reason we have studied the incorporation of another element in CdSe to give a ternary compound with a similar lattice constant but a higher bandgap. The incorporation of Mg should be ideal for our purpose.

5.4.3 Growth of CdMgSe on InAs

The addition of a small percentage of Mg in CdSe will result in a ternary compound with a lattice constant almost matched to InAs but with a higher bandgap than CdSe. The Mg should increase the conduction band barrier while little change is observed in the valence band. This is due to the common anion rules [31]; it establishes that the valence band states are derived predominantly from p-like atomic orbitals of the anion, so in the CdMgSe this is only from the Se. According to Anderson's rule and the common anion approximation, a sketch of the CdMgSe band structure has been drawn, as shown in Figure 5.34.

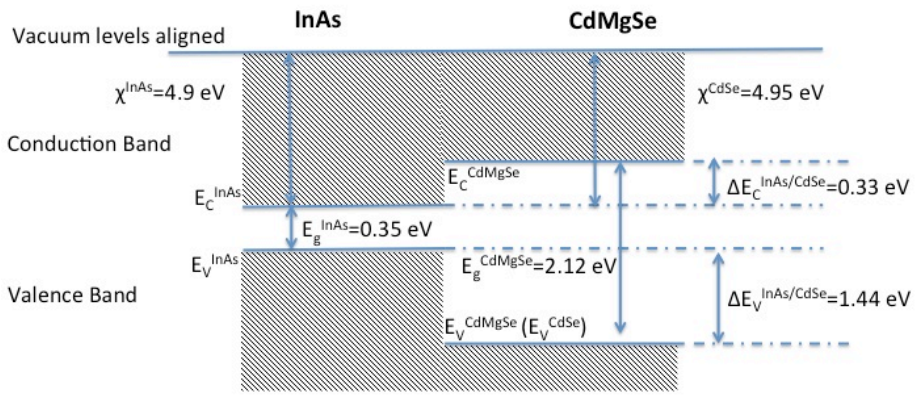

Figure 5.34 *Band structure of a heterojunction between InAs and* $Cd_{0.79}Mg_{0.21}Se$*, based on aligning the vacuum levels.*

In the InAs/CdMgSe heterostructure the conduction bands of the two materials form a barrier, proportional to the Mg concentration, which should be great enough to prevent electron transport from InAs to CdMgSe.

5.4.3.1 CdMgSe growth on heat cleaned InAs samples

Initially samples were prepared by heating the InAs substrates to the deoxidation temperature of T_s=540 °C while monitoring with RHEED. Following oxide removal the substrate was then cooled to T_s=180 °C where a low temperature CdSe buffer was grown for 3 mins. Finally the substrate was heated up to the growth temperature of T_s=240 °C. After the CdSe was grown for 3 minutes the Mg shutter was opened to start the CdMgSe growth. The different Mg compositions were obtained by varying the Mg cell temperature in each growth. 6 samples with 6 different Mg compositions were grown. The CdMgSe film thickness between the 6 samples varies from around 300 to around 450 nm (the thickness was determinated from ellipsometry measurement) depending on the Mg composition. The thickness decreases as the Mg concentration is decreased.

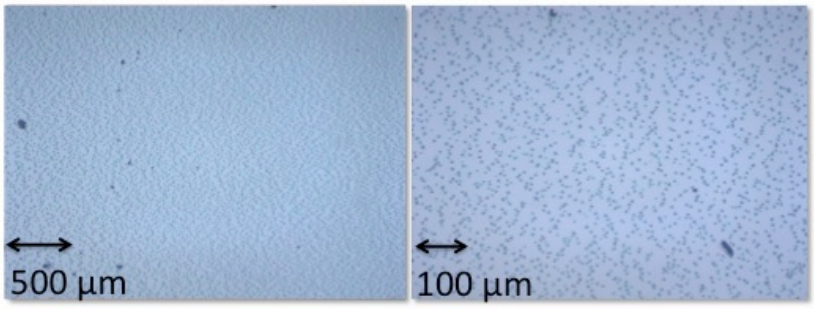

Figure 5.35 *shows bright field optical microscope images of one of the CdMgSe samples (sample HWC 585 with a composition of $Cd_{0.83}Mg_{0.17}Se$). The sample area displayed is 2 × 2.7 mm (left), and 0.5 × 0.7 mm (right).*

As with CdSe and ZnSe samples, pinholes are visible in Figure 5.35.

We found well-defined XRD peaks and intense PL peaks in all samples, demonstrating the very good crystalline quality of CdMgSe layers with different Mg compositions. An example of the strong luminescence from the II-VI film which is bright enough to be seen by eye, is shown in the photograph in Figure 5.36.

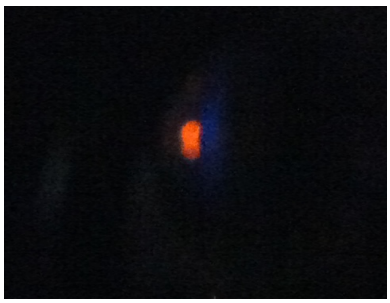

Figure 5.36 *Visible PL from one of the CdMgSe layers grown on an InAs substrate. A clear orange light is emitted from this sample (sample HWC 585 with a composition of* $Cd_{0.83}Mg_{0.17}Se$*).*

Figure 5.37 is an example of XRD and normalised PL peaks measured from one of the CdMgSe samples, the sample analysed is named HWC587. The PL spectrum was collected at 77 K.

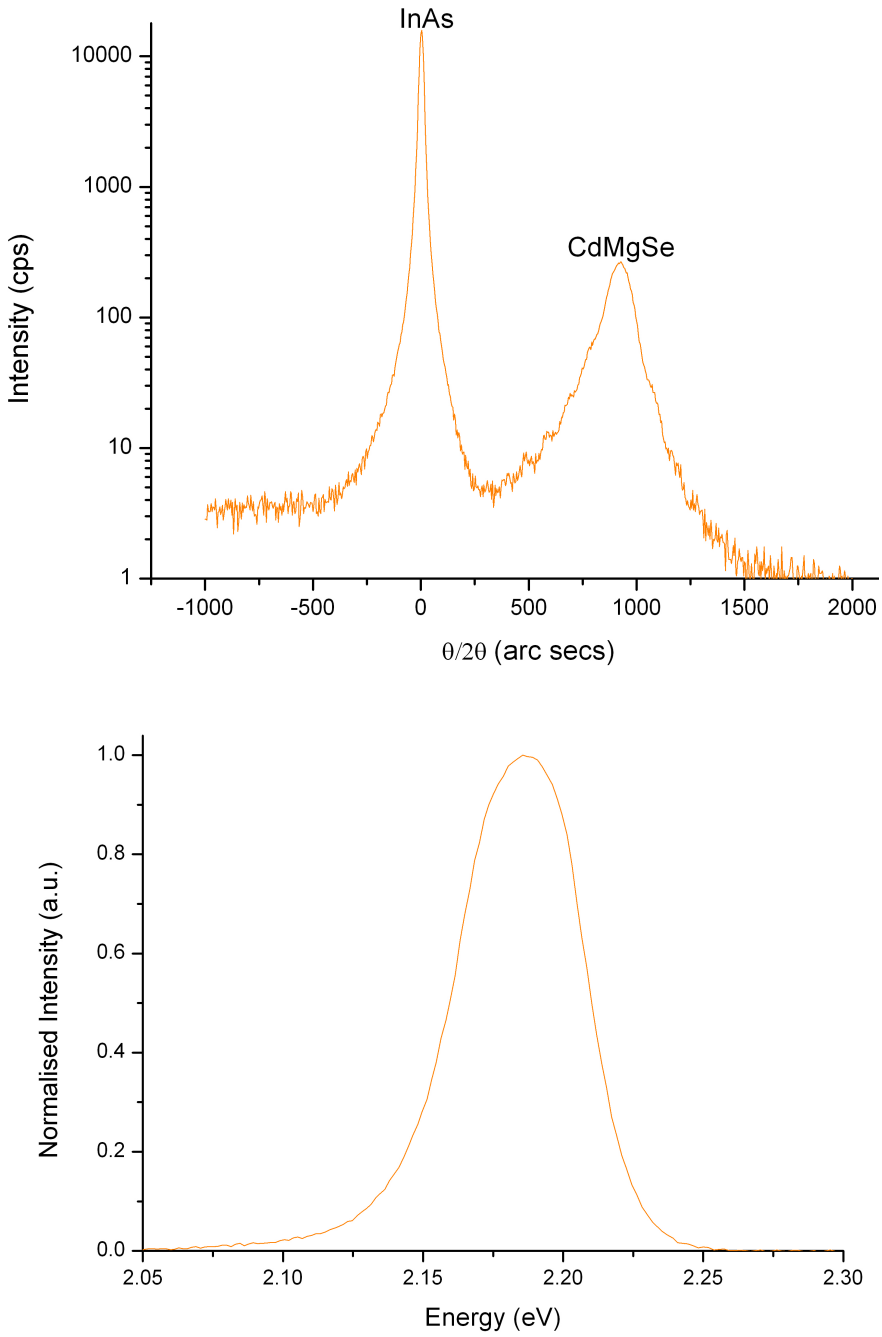

Figure 5.37 *Top, XRD from one of the heat cleaned CdMgSe/InAs samples (sample HWC587 with a composition of* $Cd_{0.79}Mg_{0.21}Se$*) at room temperature. Bottom PL spectrum from the same sample at 77 K.*

XRD shows two very clear diffraction peaks, for the InAs substrate and the CdMgSe film. The CdMgSe peak shifts as the Mg concentration is varied: higher values of $\theta/2\theta$ have been observed for higher Mg fraction. No other relevant PL peaks are observed except for the CdMgSe one, centred at 2.18 eV with FWHM of 50 meV. The well-defined XRD and PL peaks show that the heat treatment has provide a good surface on top of which single crystal epitaxial CdMgSe can be grown easily.

We carried out a study of the PL peak energy as a function of temperature for each CdMgSe sample, as is shown in Figure 5.38. The Mg composition *x* has been calculated from the PL data according the equation published by Kaygorodov *et al*. [32]:

$$E_G^{Cd_{1-x}Mg_xSe}(x)=xE_G^{MgSe}+(1-x)\,E_G^{CdSe}-Cx(1-x) \qquad (5.5)$$

where $E_G^{Cd_{1-x}Mg_xSe}$, E_G^{MgSe} and E_G^{CdSe} are the CdMgSe, MgSe and CdSe bandgap values respectively. E_G^{CdMgSe} and E_G^{CdSe} values have been estimated from our PL measurements at 77 K, assuming the PL peak energy equals the bandgap. Values of E_G^{MgSe} =4.05 eV and C=0.2 eV have been taken from Kaygorodov *et al* [32]. Table 5.5 summarises the six different Mg concentrations for the six CdMgSe films.

Sample name	Mg concentration
HWC583	0.22
HWC584	0.20
HWC585	0.17
HWC586	0.24
HWC587	0.21
HWC588	0.16

Table 5.5 *Mg concentrations in the CdMgSe layers grown on top of heat cleaned InAs substrates.*

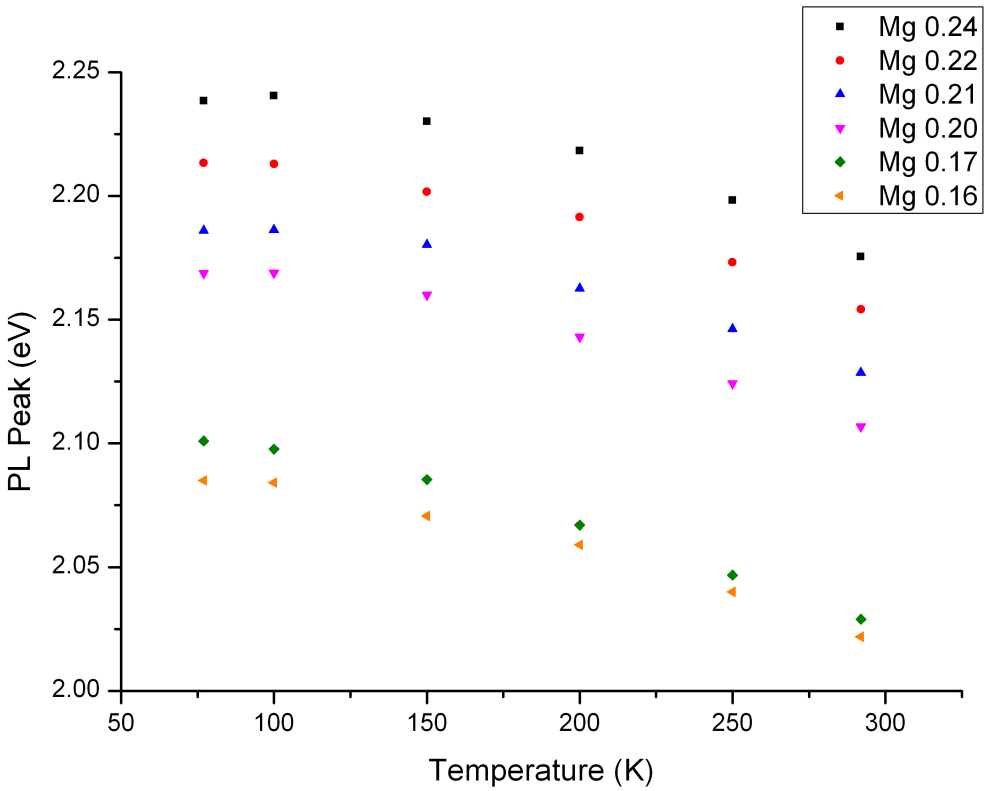

Figure 5.38 *PL peak energies as a function of temperature for the CdMgSe samples. The samples have been grown with Mg concentrations of 0.24 (black squares), 0.22 (red circles), 0.21 (blue up triangles), 0.20 (pink down triangles), 0.17 (green rhombuses) and 0.16 (orange left triangles). The PL peak from all the CdMgSe samples decreases with increasing temperature; this is due to the decrease in bandgap energy.*

For all the CdMgSe samples the PL peak energy decreases when increasing the temperature because of the reduction in bandgap energy. Fits to the data show that the Varshni equation [33] cannot be used. Similar behaviour has been found in other semiconductors [34], [35]. Figure 5.38 shows also how slight changes in Mg concentration result in different bandgap values. Therefore CdMgSe could be an interesting material that can be used to fabricate tunable light sources from blue to red, only changing the Mg composition in the II-VI sample.

To eliminate any pinholes from the sample and to avoid the high oxide removal temperatures that can damage a full InAs mesa photodiode, we also adopted the chemical treatment in this case.

5.4.3.2 CdMgSe growth on chemically cleaned InAs samples

After the successful growth of CdMgSe on the InAs heat cleaned substrate, a CdMgSe layer was deposited directly on top of a mesa sample. The sample was heated to T_s=300 °C before cooling to the buffer temperature T_s=180 °C and then heated up to the growth temperature of T_s=240 °C. The growth time was kept the same as the heat cleaned sample to give a II-VI layer of around the same thickness.

The CdMgSe-passivated structure was then characterised using the photoluminescence spectroscopy. The spectrum that was collected at 77 K is shown normalised in Figure 5.39.

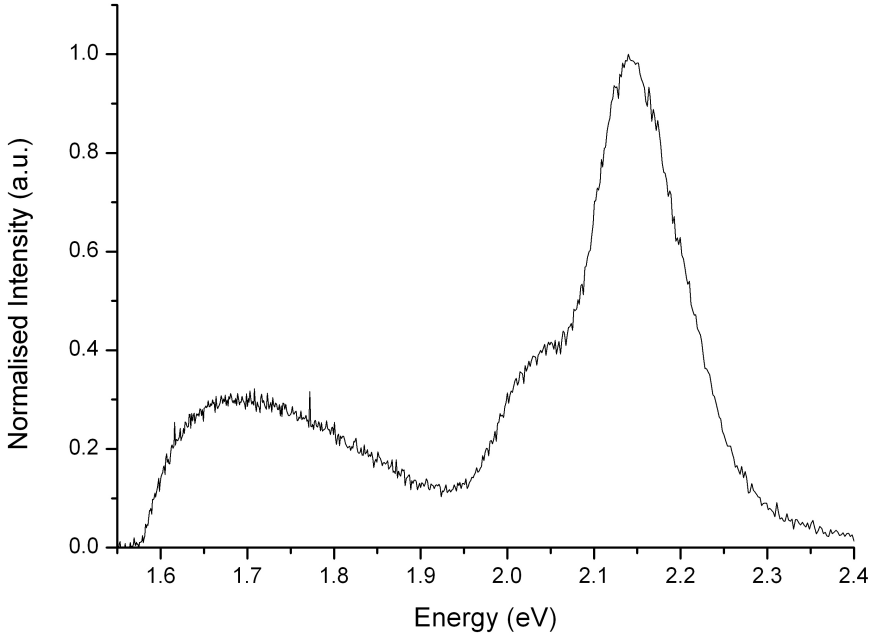

Figure 5.39 *PL spectrum from the CdMgSe/InAs chemically cleaned mesa sample (77 K).*

The PL spectrum of CdMgSe on chemically cleaned InAs mesa samples shows a CdMgSe peak at 2.14 eV with two lower intensity subsidiary peaks at 1.7 eV and 2.04 eV. Using equation 5.5, the Mg composition x has been calculated from the 77 K PL data as illustrated in detail in the previous paragraph. The Mg composition for this II-VI layer has been estimated as 0.19. Figure 5.40 shows the normalised CdMgSe PL spectrum in comparison with the two heat cleaned substrate samples with the nearest Mg concentration.

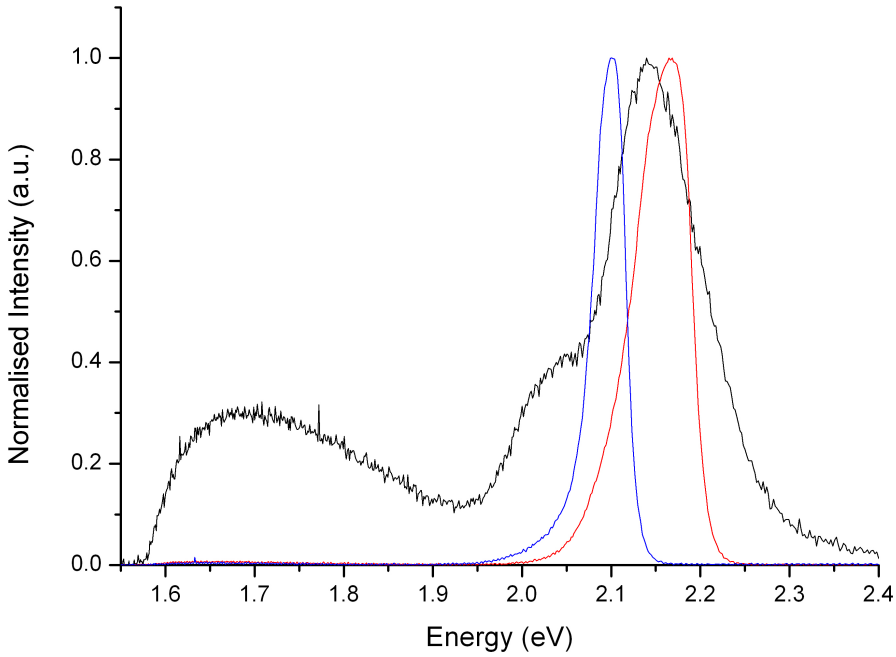

Figure 5.40 *Comparison between the PL spectra (77 K) from CdMgSe/InAs chemical cleaned mesa sample with a Mg concentration of 0.19 (black) and the two heat cleaned substrates with the nearest Mg concentration Mg concentration 0.20 (red) and 0.17 (blue).*

As shown in Figure 5.40, the CdMgSe grown on the mesa sample indicates the CdMgSe peak and two other clear PL peaks centred at 1.7 eV and 2.04 eV, both of which were absent when the same layer was grown on top of the heat cleaned substrate. The mesa structure configuration, where different crystal planes are involved (100 and 110 if a bevel angle of 45° is considered), could explain this different result. The peak at 2.04 eV could be due to a different Mg composition (according to Figure 5.38, with x around 0.14) present in the II-VI surface. Migration of atoms [36] can occur along the mesa sidewall resulting in a CdMgSe layer with different Mg concentration and different thickness with respect to a similar layer deposited on the 100 crystal plane. The peak at around 1.7 eV could be attributed to a CdSe PL contribution (see Figure 5.31). It is possible that CdSe phase separation [37] occurred during the growth, again the mesa configuration could cause this problem.

Figure 5.41 is an image of the CdMgSe-passivated mesa sample taken with the SEM. Details of the mesa sidewall are shown.

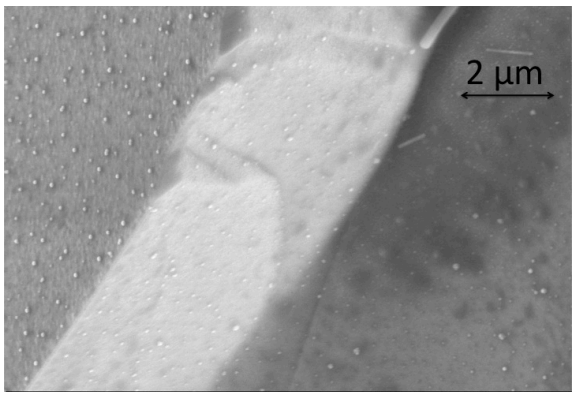

Figure 5.41 *SEM image of CdMgSe-passivated sample. The electron beam energy used was 10 kV. The picture shows the detail of a CdMgSe-passivated mesa devices sidewall. 2D growth is observed on top and sidewall of the mesa.*

In contrast with the SEM images of ZnSe and CdSe, a smooth CdMgSe surface is observed even on the mesa sidewall. Selenium clusters 50-200 nm in diameter and 20-60 nm in height are still present. These clusters occur because of the selenium background in the chamber, which is important when the samples cool after growth. At Heriot-Watt the background of the II-VI chamber is mainly Se with a little sulphur.

Dark current measurements have been taken by the University of Sheffield on these CdMgSe-passivated mesa structures showing dramatically high surface leakage currents; this could be mainly due to fabrication problems. The II-VI etching recipe could play an important role in the InAs mesa photodiode fabrication and so optimisation.

According to the predicted InAs/CdMgSe conduction band alignment, CdMgSe should be an ideal semiconductor in terms of device packaging. It has a resistivity much higher than that of the photodiode material so that any leakage current through the external bondpads should be avoided.

At the present, CdMgSe overgrowth does not successfully terminate the InAs mesa device and cannot be used as a passivation layer. Although we think that the main problem for the unexpected behaviour of the CdMgSe/InAs sample observed is due to the II-VI etching recipe used during the fabrication process, more structure analysis has

to be conducted also from the growth point of view. Multiple structural factors could contribute to an increase of dark current.

Defects, that are not visible in the PL spectra because they are not optically active, can be present in the structure causing the increase in dark current. Impurity surface states have been observed, for example, in AlGaAs/GaAs structures at the interface between the two materials [38]. A similar problem could be present also in our CdMgSe/InAs structure.

The CdSe buffer, used to accommodate CdMgSe on top of InAs, could also be too thick causing the problem of electron surface accumulation already explained in the CdSe/InAs structure.

Another CdMgSe/InAs mesa sample was grown to try to improve the quality of the surface underneath the CdMgSe film and eventually to eliminate defect levels. However for this sample similar PL peaks were observed and another unsuccessful passivation layer was produced.

The growth of CdMgSe on top of mesa samples is still a challenge. The complexity of a ternary compound has to be investigated in more detail to try to find the best growth parameters for the II-VI layer. The mesa structure configuration contains a variety of different crystal planes, contributing greatly to this problem. More studies and analysis have to be conducted for a better understanding of the CdMgSe/InAs heterostructure. CdMgSe could be ideal for passivation of mesa sidewalls in diode structures, due to both its almost perfect lattice match with InAs and its large bandgap.

Finally, data taken six months later have shown a shift over time of the PL peak indicating chemical instability. The shift to higher energy of the PL peak was observed for all the CdMgSe samples. An example is shown in Figure 5.42.

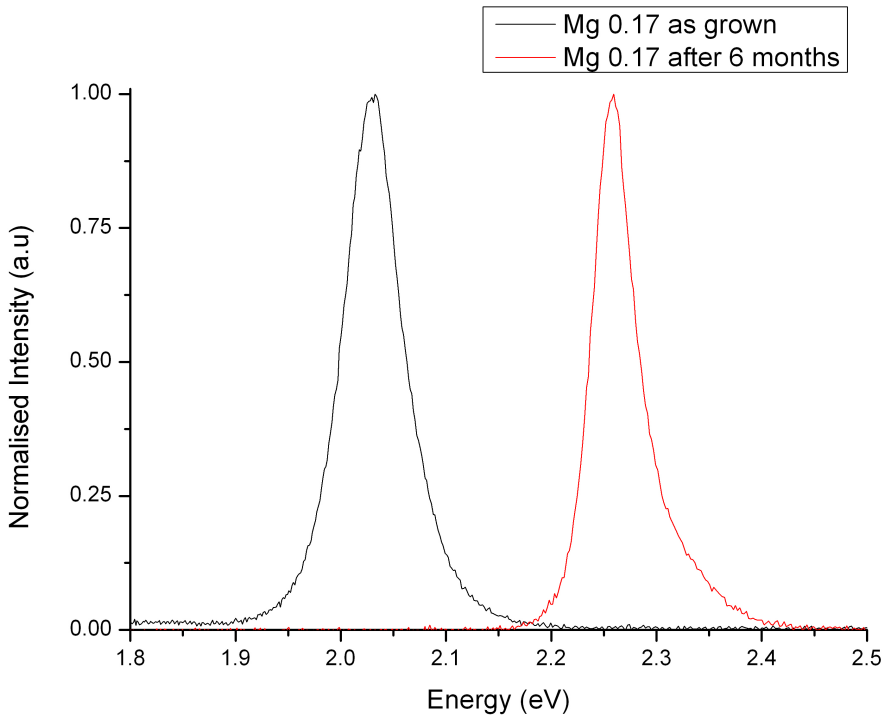

Figure 5.42 *PL spectrum from the CdMgSe sample with Mg concentration of 0.17 soon after the growth (black line) and after 6 months (red line) at room temperature.*

CdSe and MgSe have a naturally wurtzite crystal structure (hexagonal crystal system), so chemical instability problems can occur when CdMgSe has been grown in a zincblend configuration. Phase separation processes can cause the migration of Cd atoms from the ternary alloy to form CdSe leaving behind MgSe rich areas. This process should result in a shift of the CdMgSe XRD peak from its original value to a value that corresponds to higher Mg composition. In contrast with what is expected, the XRD peak is not subject to any shift indicating that the overall bulk material does not change. Moreover, PL data do not show any lower energy CdSe peaks. Another hypothesis has to be considered. The phase separation process can result in creation of CdSe quantum wells confined by MgSe barriers. These wells could be aligned along the stacking fault plane (a stacking fault is a one- or two- layer interruption in the stacking sequence). The changing from the wurtzite to the zincblend crystal structure can cause strain and build-up of an intrinsic electric field [39]. This electric field can cause band bending in the neighbourhood of the quantum well providing enough energy to the electrons to tunnel to a CdSe quantum well excited state. The luminescence from such CdSe quantum wells should be observable. Further investigations have to be conducted, and a possible experiment to prove this theory will be discuss in Chapter Seven.

5.5 Growth of II-VI compounds on InAs conducted at the City College of New York.

In order to grow Te-containing layers, it was necessary to have structures grown at the City College of New York in collaboration with their II-VI MBE group. Their MBE system had two separate III-V and II-VI growth chambers connected via an ultrahigh-vacuum transfer module; this allows the substrates to be deoxidized in the III-V chamber under As overpressure so as to ensure an As-terminated surface that is a good interface for growth of II–VI materials. The samples were then transferred under vacuum to the II-VI chamber for the II-VI growth. RIBER 2300P molecular beam epitaxial chamber with sources of 6N Zn, Se and Te content was used. In the II-VI chamber Se was evaporated using a dual zone evaporation source while the Te was evaporated via a standard Knudson source. The Se source allows the control of tip evaporation temperature and thus the Se species exiting in the source. In this experiment the source was heated to 190 ° C with the tip set at 300 °C. This is the only material parameter that differs from the samples grown at Heriot-Watt University. All the growths have been done with the help and the expertise of Dr Richard Moug and our collaborators in New York: Prof. Maria Tamargo and in particular Vasilios Deligiannakis. A schematic and photograph of the MBE system at City College is shown in Figure 5.43.

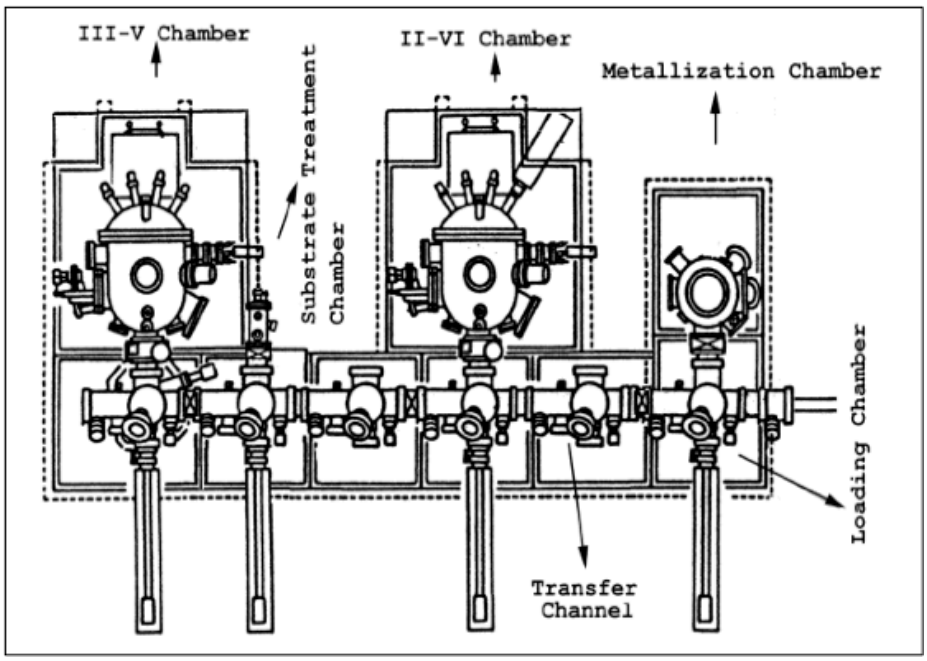

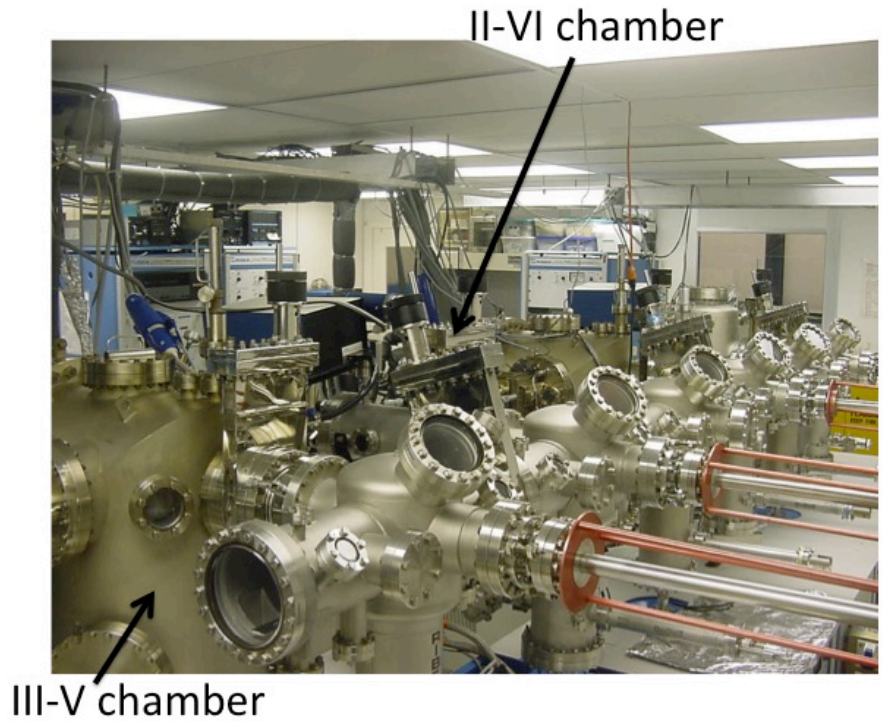

Figure 5.43 *Top, schematic representation of the City College MBE system. The main components are labelled. Bottom, picture of the system [18].*

As shown in Figure 5.43, the City College MBE system has three separate chambers: III-V, II-VI and metallization chamber. All the system is in Ultra High Vacuum conditions (around 10^{-9} torr) using a combination of cryopumps, ion pump, and liquid nitrogen shroud. The samples were inserted in the system using the loading chamber. Using the transfer channel,

the sample is moved first to the III-V chamber for the deoxidation process and then to the II-VI chamber for the growth. We studied Te compounds as possible passivation layers for InAs photodiodes. From Figure 5.1, ZnTe looks the most promising Te compound in terms of high bandgap (2.34 eV at 77 K) and lattice constant (6.103 Å). The *ex situ* chemical cleaning treatment, that was successfully developed for the samples at Heriot-Watt, could not be used for the growths at the City College. No sulphur sources are present in the New York MBE system, so an InAs sample with sulphur passivation layer could lead to chamber contamination.

P-i-n structures became available at this time, and were used in this phase of the work.

5.5.1 Growth of ZnTe on InAs

According to Anderson's rule, in the ZnTe/InAs heterostructure the conduction band offset between the two materials is significant as shown in Figure 5.44. χ^{InAs}=4.9 [6] and χ^{CdTe}=3.53 [40] (every value is subjected to at least 50 meV experimental error [23]) so $\Delta E_C{}^{InAs/ZnTe}$=1.37 eV.

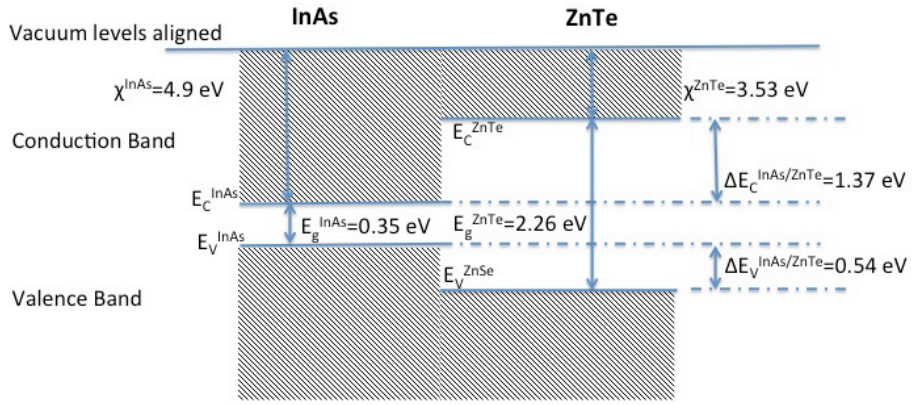

Figure 5.44 *Band structure of a heterojunction between InAs and ZnTe, based on aligning the vacuum levels.*

5.5.1.1 ZnTe growth on heat cleaned InAs samples

Initially samples were prepared by heating the InAs substrates to the deoxidation temperature of T_s=540 °C in the III-V chamber while monitoring with RHEED. Following oxide removal the substrate was moved to the II-VI chamber and then cooled to the growth temperature of T_s=240 °C for the ZnTe growth.

The growth duration was of around 1 hour to give a ZnTe layer thickness of about 400 nm. We estimated the sample thickness using RHEED oscillation measurements [21], the data taken are shown in Figure 5.45.

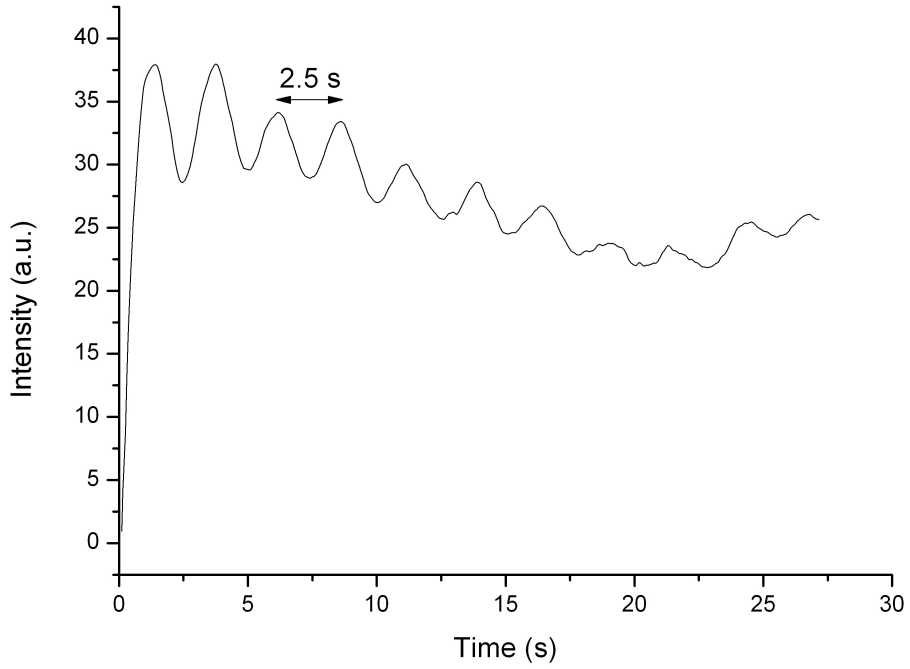

Figure 5.45 *Diffracted RHEED intensity as a function of time during the ZnTe growth.*

Figure 5.45 shows that the time needed to build up a ZnTe monolayer, estimated as the time between two consecutive diffracted beam maxima, is around 2.5 s. As the growth lasted 1 hour, the number of monolayers grown is 1440. Considering a monolayer around 3 Å in thickness, the ZnTe thickness calculated is around 430 nm.

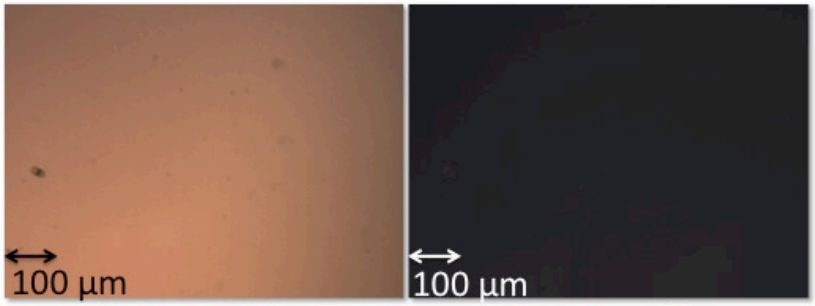

Figure 5.46 *Optical microscope images of the ZnTe heat cleaned sample. The sample area displayed is 0.5 × 0.7 mm. The sample images in bright and dark field conditions are shown on the left and on the right respectively.*

Figure 5.46 shows bright and dark optical microscope images of the samples after growth. As expected pinholes are not present: the As overpressure during the deoxidation prevents their formation. The images were both taken using the optical microscope at the City College, this allows the capture of dark field images. In dark field images the weak light that scatters off the side of small features, that are not visible in bright field microscopy, could be more apparent allowing sample details to be revealed. The dark field image shown in Figure 5.46 does not exhibit any bright spots; this means that the sample has a very good smooth surface, lacking any surface defects.

XRD results taken at room temperature using the XRD City College facilities and normalised PL spectrum at 77 K from these samples are shown in Figure 5.47.

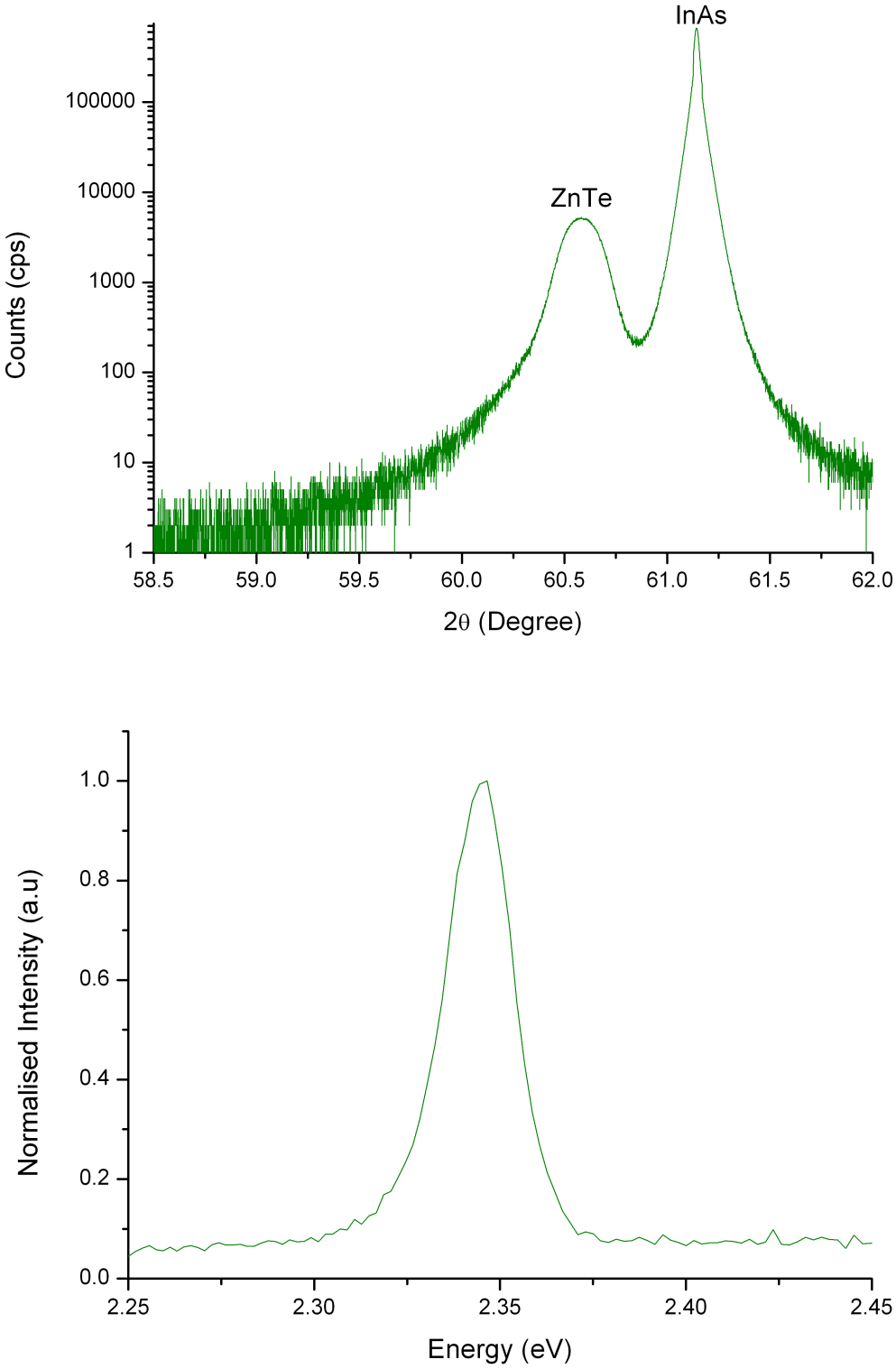

Figure 5.47 *Top, XRD from the heat cleaned ZnTe/InAs sample (room temperature). Bottom PL spectrum from the same sample (77 K).*

XRD shows two very clear diffraction peaks, for the InAs substrate and the ZnTe layer showing a very good crystalline quality. The well-defined PL peak observed at 2.34 eV with a FWHM of 22 meV demonstrates, in accordance with the XRD results, that ZnTe with

a high quality has been deposited. A deep level luminescence peak can also be detected at lower energy (not shown).

Once the growth of ZnTe on an InAs substrate was optimised, we grew ZnTe on top of an InAs mesa sample which had been heat cleaned. The samples were heated at T_s=540 °C before cooling to the growth temperature of T_s=240 °C. An optical microscope image of the ZnSe/InAs mesa sample is shown in Figure 5.48: the picture shows in detail a 200 µm, 100 µm and 50 µm diameter devices.

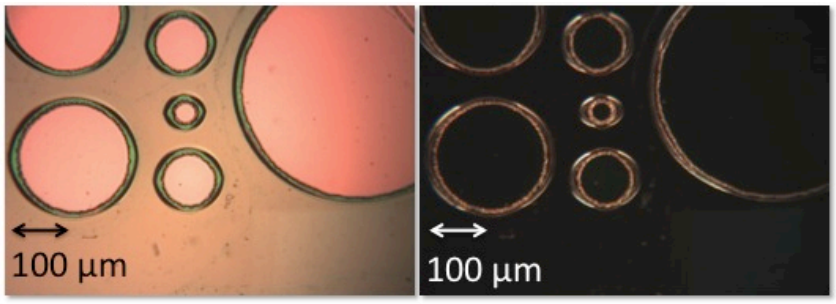

Figure 5.48 *Optical microscope images of the ZnTe heat cleaned mesa sample. The sample area displayed is 0.5 × 0.7 mm. The sample images in bright and dark field conditions are shown on the left and on the right respectively.*

Also in this case dark field images were taken so as to reveal features that could be hidden in bright field microscopy. A good quality sample was grown.

Figure 5. 49 shows images of the same sample taken with the SEM.

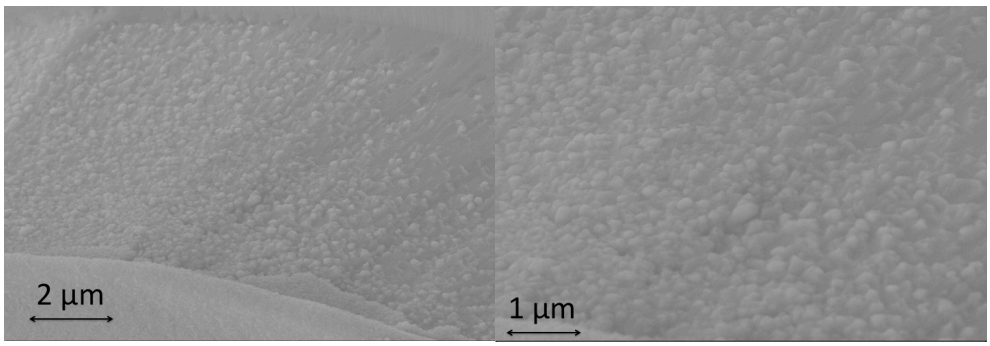

Figure 5.49 *SEM images of the sample at different magnifications. The electron beam energy was 10 kV. Left, zoom of a 200 µm diameter ZnTe-passivated mesa device sidewall. The ZnTe on the sidewall grows in 3D perpendicular to the etched surface. 2D growth is observed on top of the mesa where the ZnTe grow on a flat surface. Selenium clusters are not present on the surface due to the different background in the New York II-VI chamber with respect to the Heriot-Watt chamber. At the City College of New York the background of the II-VI chamber is mainly Te with a little of Se. Right, details of the mesa sidewall for the same device.*

X-ray scans were performed on the mesa sample, as shown in Figure 5.50.

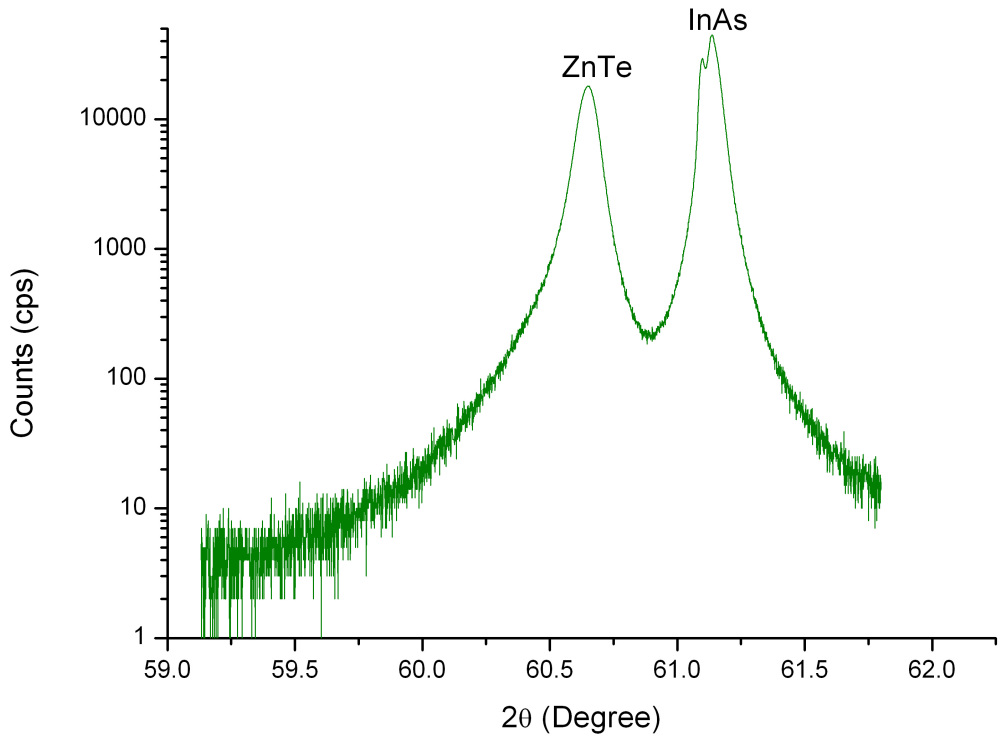

Figure 5.50 *XRD from the heat cleaned ZnTe/InAs mesa sample (room temperature).*

XRD shows three very clear diffraction peaks. Apart from the peak related to the ZnTe, two other peaks corresponding to the InAs substrate and InAs p-i-n structure that was grown on top of that layer are observed [18].

PL was performed on the ZnTe heat cleaned mesa sample, which showed a well-defined peak at 2.34 eV at 77 K. In the spectrum, a deep level peak is also present (not shown). Figure 5.51 shows the normalised PL spectrum at 77 K from the heat cleaned ZnTe mesa sample.

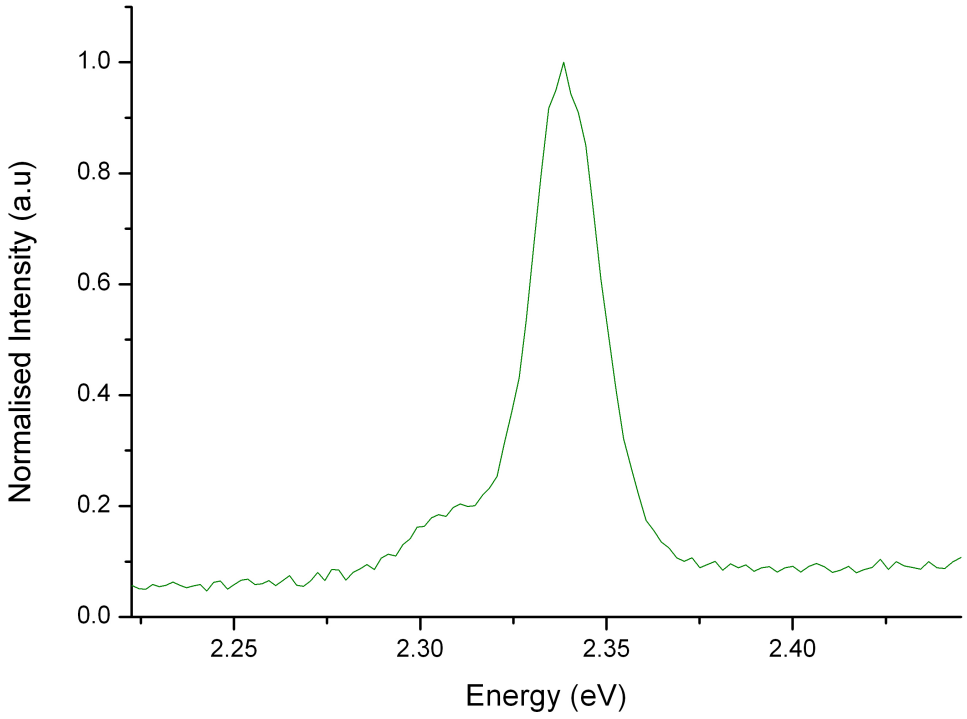

Figure 5.51 *PL spectrum from the ZnTe/InAs heat cleaned mesa sample (77 K).*

At 77 K the peak is centred at 2.34 eV with a FWHM as low as 19 meV, this demonstrates that ZnTe with a good crystalline quality has been deposited.

As already observed for ZnSe, the ZnTe overgrowth successfully terminates the InAs mesa structure preventing atmospheric oxidation of the surface layers which form traps at energy within the InAs bandgap that are the origin of the surface currents. In comparison to ZnSe, ZnTe has lower bandgap but a lattice constant much closer to

InAs. Since ZnTe has a larger bandgap than InAs it provides a high resistivity layer which prevents any additional leakage currents. This result is in agreement with the conduction band alignment between ZnTe and InAs shown in Figure 5.44. This type of structure also allows easy metallisation and packaging processes.

Dark current measurements of the ZnTe-passivated mesas at room temperature show diode dark current scales with device area indicating that surface leakage currents are negligible at these temperatures, Figure 5.52. As already observed for the ZnSe-passivated mesa sample, a bulk effect is present at room temperature and at high voltage. Further investigations at 77 K have to be conducted so as to study the electrical behaviour of the sample at low temperature.

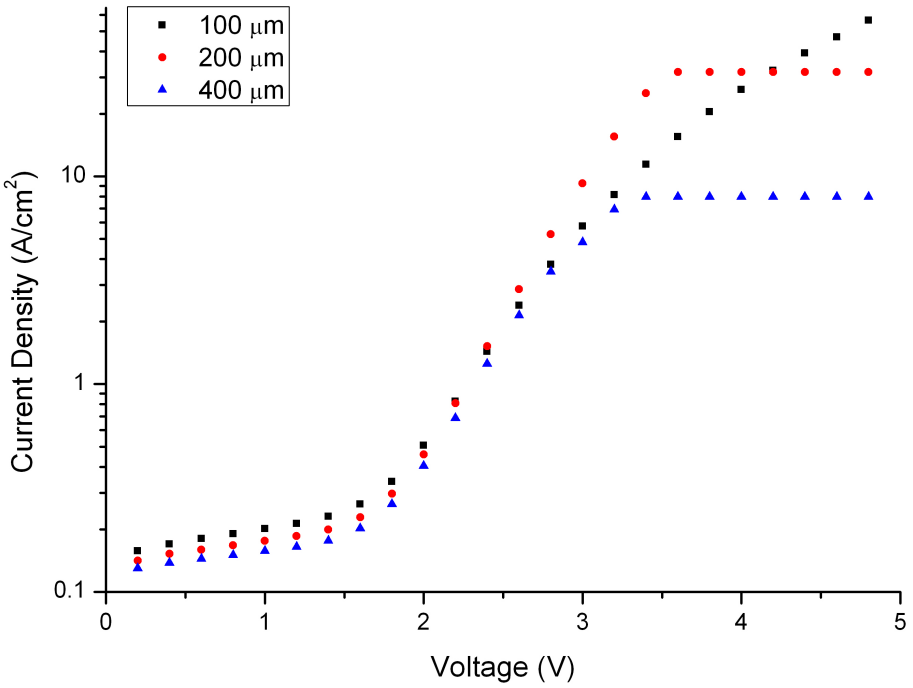

Figure 5.52 *Current density as a function of reverse bias for the ZnTe-passivated InAs mesa diodes up to 5 V reverse bias at room temperature. The diameters of the devices plotted are 100 μm (black squares), 200 μm (red dots) and 400 μm (blue triangles).*

5.5.2 Growth of ZnSe on InAs

ZnSe growth was repeated at the City College of New York so as to study the effect of the heat deoxidizing process in the III-V chamber under As overpressure.

The InAs/ZnSe heterostructure alignment is shown in Figure 5.13.

5.5.2.1 ZnSe growth on heat cleaned mesa InAs samples

Initially samples were prepared by heating the InAs mesa to the deoxidation temperature of T_s=540 °C in the III-V chamber while monitoring with RHEED. Following oxide removal the substrate was moved to the II-VI chamber and then cooled to the growth temperature of T_s=240 °C for the ZnSe growth.

An optical microscope image of the ZnSe/InAs mesa sample is shown in Figure 5.53: the picture shows in detail a 200 µm, 100 µm and 50 µm diameter devices.

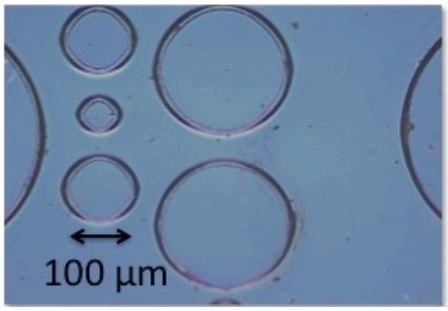

Figure 5.53 *Bright field optical microscope images of the ZnSe heat cleaned mesa sample. The sample area displayed is 0.5 × 0.7 mm.*

Figure 5. 54 shows images of the same sample taken with the SEM.

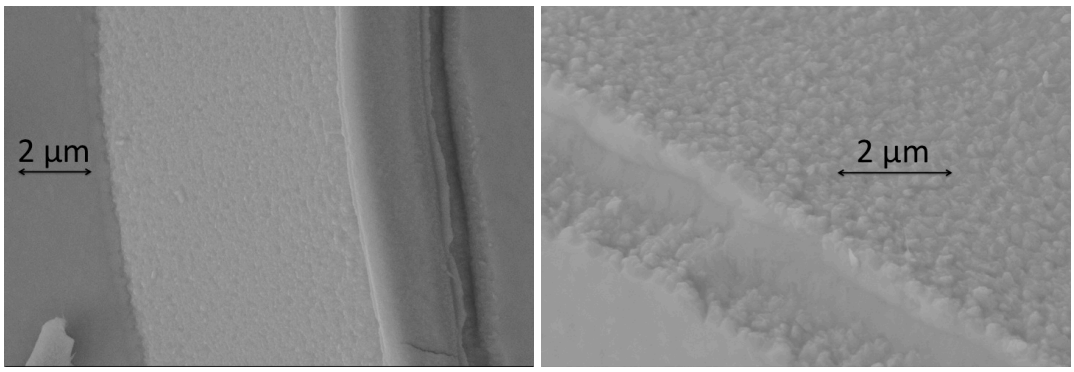

Figure 5.54 *SEM images of the sample at different magnifications. The electron beam energy used was 10 kV. Left, zoom of a 200 µm diameter ZnSe-passivated mesa device sidewall. The ZnSe on the sidewall grows in 3D perpendicular to the etched surface. 2D growth is observed on top of the mesa where the ZnSe is grown on a flat surface. Selenium clusters are not present on the surface due the different background in the II-VI chamber in New York with respect to the Heriot-Watt chamber. Right, details of the mesa sidewall for the same device.*

The X-ray scan taken at the City College XRD is shown in Figure 5.55.

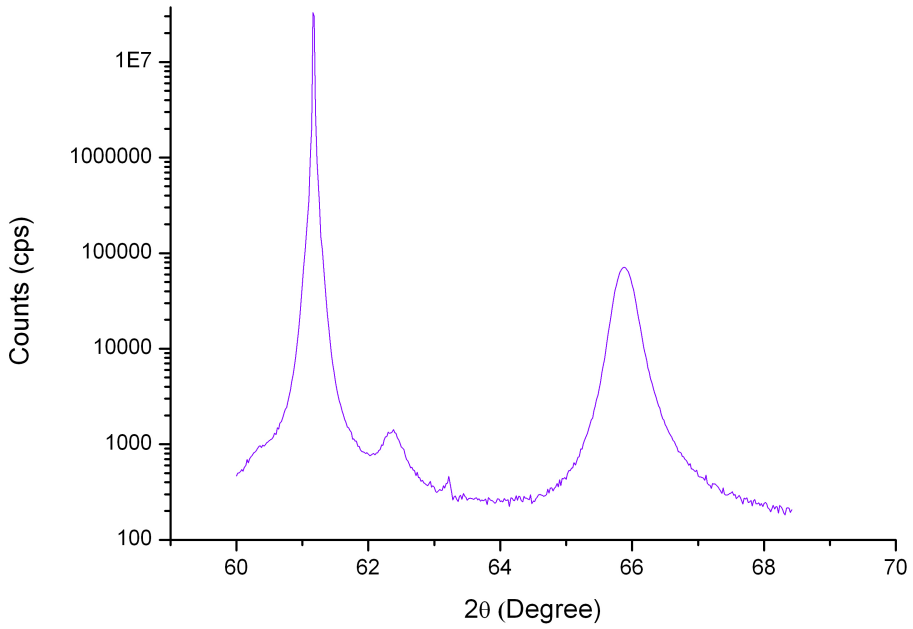

Figure 5.55 *XRD from the heat cleaned ZnSe/InAs mesa sample (room temperature).*

XRD shows two very clear diffraction peaks from the InAs mesa and the ZnSe 400 nm epitaxial layer respectively. It also shows a weak peak (around 62.5 degree) which arises from the beam interacting with the Al sample holder when the sample size is small [18].

PL was performed on a ZnSe heat cleaned mesa sample. At 77 K a well-defined peak centred at 2.78 eV is observed in the PL normalised peak shown in Figure 5.56.

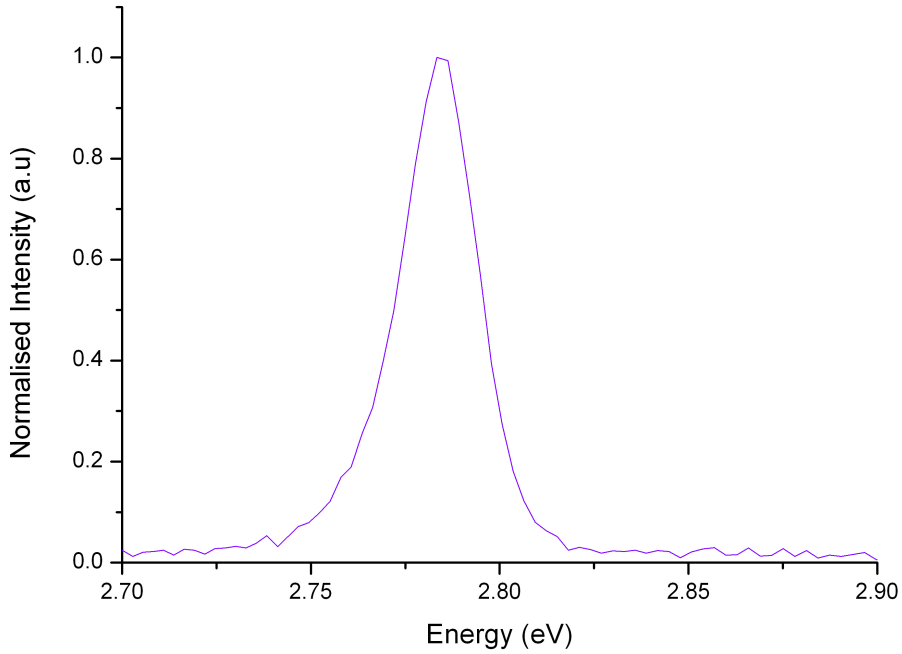

Figure 5.56 *PL from the heat cleaned ZnSe/InAs mesa sample (77 K).*

Figure 5.57 shows a comparison of the PL data taken from the ZnSe-passivated InAs mesa sample grown at the City College of New York (black line) and the ZnSe-passivated InAs mesa sample grown at Heriot-Watt (red line).

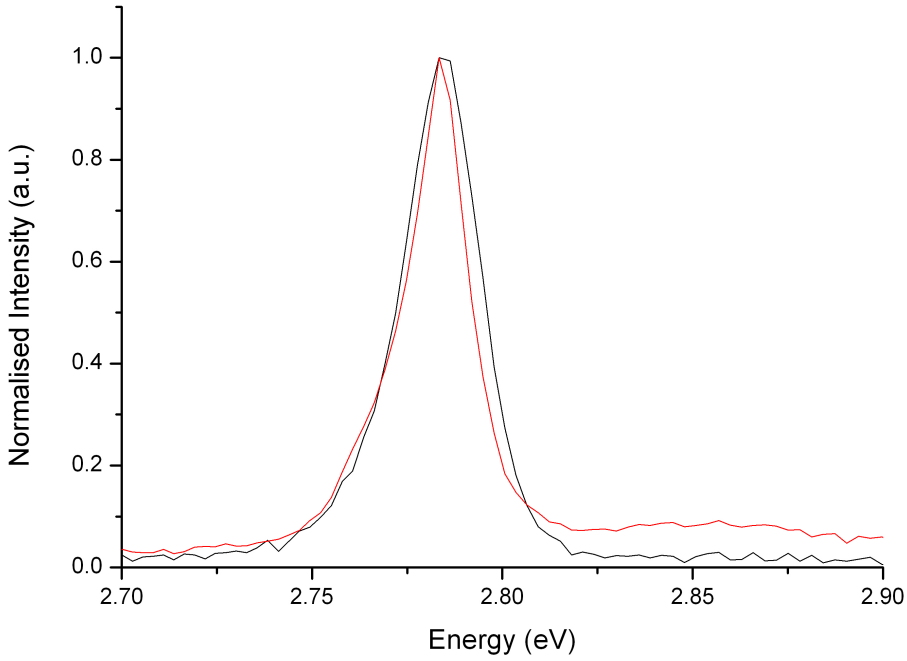

Figure 5.57 *PL data from the heat cleaned ZnSe/InAs mesa sample grown at the City College of New York (black line) and the ZnSe-passivated InAs mesa sample grown at Heriot-Watt (red line).*

The two ZnSe peaks are consistent with each other, showing good crystalline quality has been deposited in both cases. Despite the different sample preparations before the II-VI growth, both peaks present a similar FWHM: the slight increase in FWHM for the ZnSe heat cleaned sample grown in New York could be attributed to differences in growth condition.

5.5.3 Growth of ZnSeTe on InAs

The addition of Se in ZnTe allows investigation into the composition range line between ZnTe and ZnSe in Figure 5.1. A small percentage of Se in ZnTe should result in a ternary compound with slightly smaller bandgap with respect to ZnTe but a lattice constant closer to InAs. The Se should decrease the valence band barrier while little change is observed in the conduction band. The valence band states are derived predominantly from p-like atomic orbitals of the anion [31], i.e in the ZnSeTe the valence band states are derived only from the non-metal elements.

In the InAs/ZnSeTe heterostructure the valence bands of the two materials form a barrier, proportional to the Se concentration.

5.5.3.1 ZnSeTe growth on heat cleaned InAs samples

The InAs substrates were first heated to the deoxidation temperature of T_s=540 °C in the III-V chamber while monitoring with RHEED. Following oxide removal the substrate was moved to the II-VI chamber and then cooled to the growth temperature of T_s=240 °C for the ZnSeTe growth.

The growth duration was of around 1 hour to give a ZnSeTe layer thickness of about 400 nm.

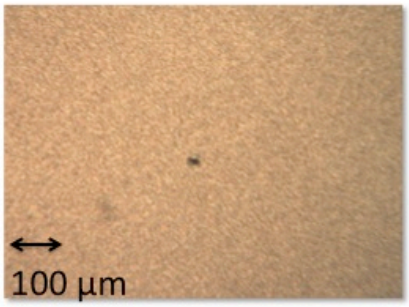

Figure 5.58 *Bright field optical microscope images of the ZnSeTe heat cleaned sample. The sample area displayed is 0.5 × 0.7 mm.*

Figure 5.58 shows bright field optical microscope images of the samples after growth. The ZnSeTe surface is very rough, possibly due to an incomplete oxide removal. The sample can also be subjected to nucleation and phase separation problems. Also in this case pinholes are not present because of the As overpressure used during the deoxidation.

XRD results taken at room temperature using the XRD City College facilities are shown in Figure 5.59.

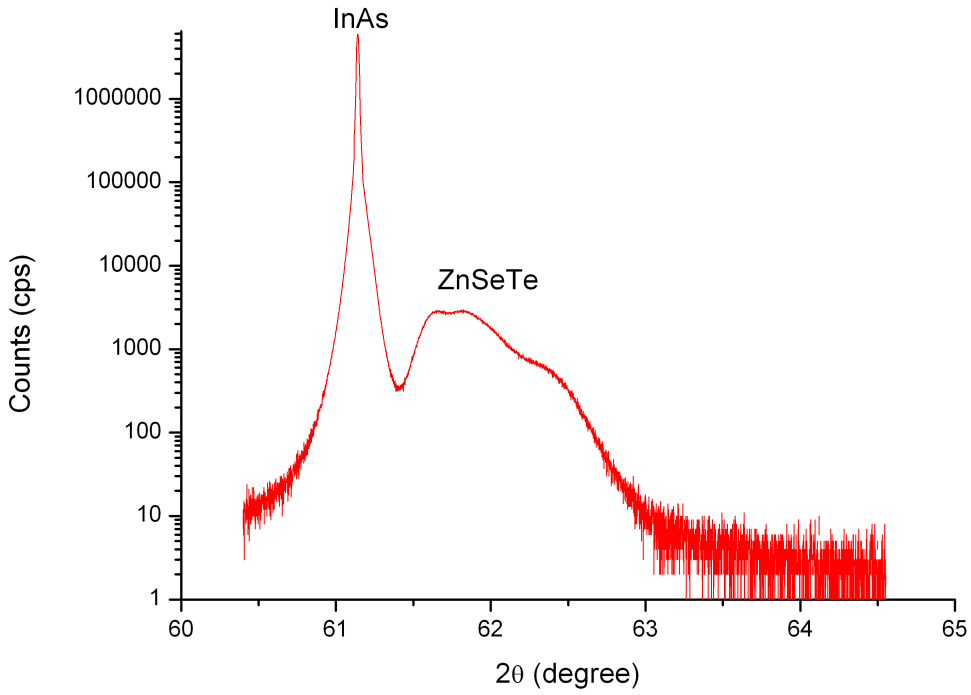

Figure 5.59 *XRD from the heat cleaned ZnSeTe/InAs sample (room temperature).*

XRD shows a narrow diffraction peak for the InAs substrate and a broad peak, which results from the sum of three smaller peaks, for the ZnSeTe. The presence of multiple peaks is in line with the idea that there has been some phase separation. Using the Bragg law, equation (5.1), it is possible to associate with each peak a Te concentration. With increasing Bragg angle these were found to be 0.827, 0.786 and 0.691.

A PL peak has not been observed. Nucleation and/or phase separation problems could occur during the growth compromising the II-VI layer properties. Further studies and further growths have to be conducted for a better understanding of the problem.

5.6 Conclusions

This Chapter presents growth of II-VI layers on InAs, and has shown effective means of passivation on mesa diode structures for the first time.

ZnSe, ZnTe, CdSe and CdMgSe compounds were grown on InAs substrates and then on InAs mesa detectors. Pre-growth surface oxide removal processes were developed to improve surface morphology of II-VI layers grown on InAs substrates. The commonly used heat cleaning oxide removal can damage an InAs mesa photodiode because of the high temperatures involved so alternative novel chemical treatment was successfully developed.

PL measurements as a function of temperature and XRD analysis at room temperature were also carried out on all the samples grown. Well-defined XRD peaks and intense PL peaks were found demonstrating very good single crystalline quality in all the II-VI layers grown on InAs.

CdSe and CdMgSe currently do not passivate InAs mesa photodiodes, the reasons behind this are not well known and further investigations are needed.

ZnSe and ZnTe successfully terminates the InAs mesa structure. They prevent atmospheric oxidation of the InAs surface layers and therefore the formation of traps inside the InAs bandgap which cause the surface currents. Experimental dark current measurements taken on the ZnSe and ZnTe-passivated mesas at room temperature, as shown in Figure 5.60, demonstrate that the surface leakage currents scale with device area from 400 μm to 100 μm at room temperature so that any surface contribution to the dark current has been suppressed. Since ZnSe and ZnTe have a much larger bandgap than InAs they provide a high resistivity layer which prevents any additional leakage currents from external bondpads. Therefore, the use of a ZnSe or ZnTe passivation layer also provides a robust and solid layer for device to chip bonding. Further passivation investigations have to be conducted at low temperatures.

It is worth to notice that ZnSe, despite having a large lattice mismatch with InAs, successfully passivates InAs mesa photodiode. From these results it is clear that lattice constant is not essential for an effective passivation layer. Thus both ZnSe and ZnTe hold great potential for the passivation of any III-V based device.

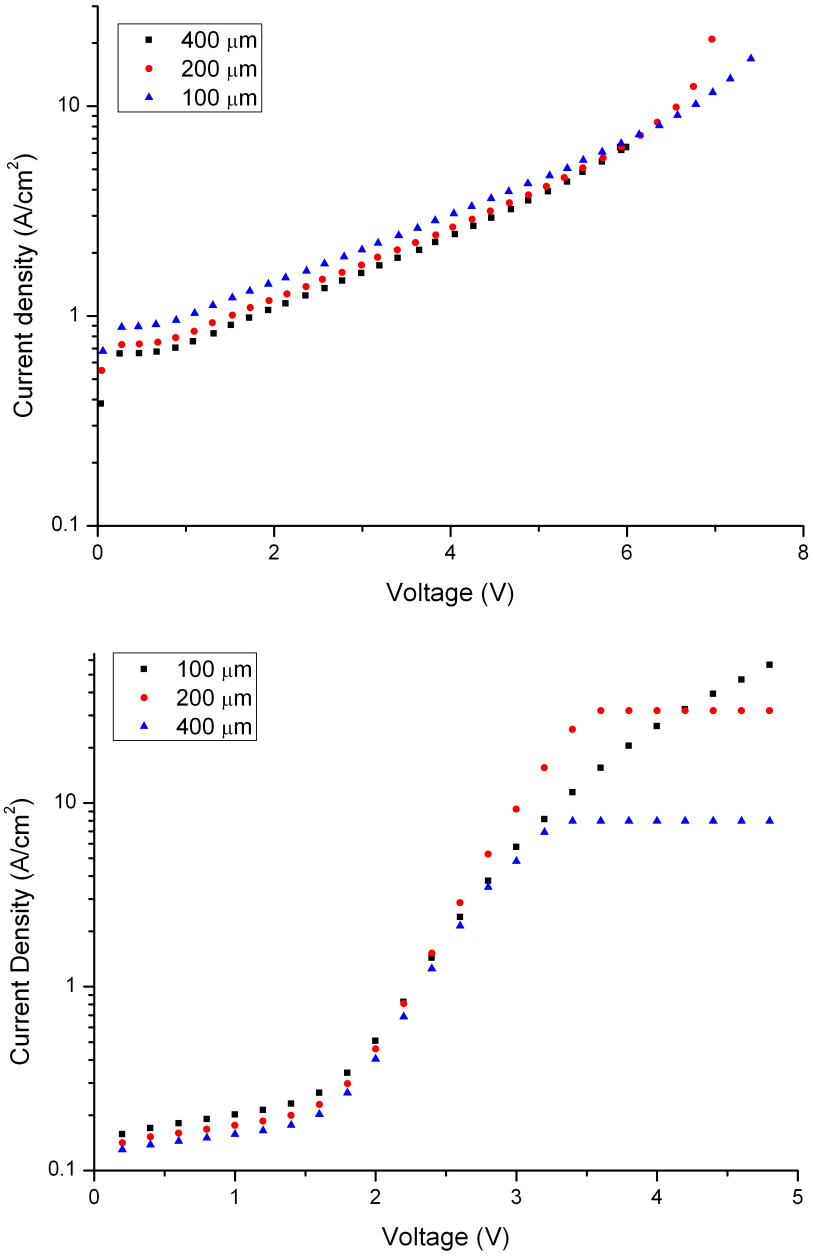

Figure 5.60 *Current density as a function of reverse bias for the ZnSe and ZnTe-passivated InAs mesa at room temperature. The diameters of the devices plotted are 100 μm (black squares), 200 μm (red dots) and 400 μm (blue triangles). The dark currents scale with device area proving that any surface contribution to the dark current has been suppressed in both cases.*

5.7 References

[1] S. Ivanov, V. Solov'ev, A. Toropov, I. Sedova, Y. V. Terent'ev, V. Kaygorodov*, et al.*, "MBE growth and luminescence properties of hybrid Al (Ga) Sb/InAs/Cd (Mg) Se heterostructures," *Journal of Crystal Growth,* vol. 227, pp. 693-698, 2001.

[2] I. Sandall, "Privite comunication, University of Sheffield," 2013.

[3] A. J. Decker, "Solid state physics," *Prentice-Hall,* 1958.

[4] Bandgap vs. Lattice Constant for III-V and II-VI Compound Semiconductors. http://woodall.ece.ucdavis.edu/resources.html.

[5] M. Tamargo, " II–VI semiconductor materials and their applications," CRC Press, 2002.

[6] IOFFE. InAs basic parameters at 300 K. http://www.ioffe.ru/SVA/NSM/Semicond/InAs/basic.html.

[7] IOFFE. GaAs basic parameters at 300 K. http://www.ioffe.ru/SVA/NSM/Semicond/GaAs/basic.html

[8] L. Ouyang, J. Fan, S. Wang, X. Lu, Y.-H. Zhang, X. Liu*, et al.*, "Microstructural characterization of thick ZnTe epilayers grown on GaSb, InAs, InP and GaAs (100) substrates," *Journal of Crystal Growth,* vol. 330, pp. 30-34, 2011.

[9] J. Fan, L. Ouyang, X. Liu, D. Ding, J. Furdyna, D. Smith*, et al.*, "Growth and material properties of ZnTe on GaAs, InP, InAs and GaSb (001) substrates for electronic and optoelectronic device applications," *Journal of Crystal Growth,* vol. 323, pp. 127-131, 2011.

[10] S. Wang, I. Hauksson, J. Simpson, H. Stewart, S. Adams, J. Wallace*, et al.*, "Blue stimulated emission from a ZnSe p-n diode at low temperature," *Applied Physics Letters,* vol. 61, pp. 506-508, 1992.

[11] T. Yao, Y. Makita, and S. Maekawa, "Molecular beam epitaxial growth of low-resistivity ZnSe films," *Applied Physics Letters,* vol. 35, pp. 97-98, 2008.

[12] C. Kittel, "Introduction to Solid State Physics", Eight Edition, John Willey & Sons," 2005.

[13] A. Rajan, "MBE growth, Processing and Stability of Zinc blende MgS based Heterostructures," *PhD Thesis,* 2013.

[14] D. K. Bowen and B. K. Tanner, "High resolution X-ray diffractometry and topography", CRC Press, 2005.

[15] R. T. Moug, "II-VI metastable sulphides: Fundamental studies of MBE growth, characterization and nanostructure formation.," *PhD Thesis,* 2009.

[16] J. Neave, B. Joyce, P. Dobson, and N. Norton, "Dynamics of film growth of GaAs by MBE from RHEED observations," *Applied Physics A,* vol. 31, pp. 1-8, 1983.

[17] T. Yao, M. Ogura, S. Matsuoka, and T. Morishita, "High-quality ZnSe thin films grown by molecular beam epitaxy," *Applied Physics Letters,* vol. 43, pp. 499-501, 1983.

[18] R. T. Moug, "Privite comunication, Heriot Watt University," 2014.

[19] LEICA DM R microscope series manual, 1995.

[20] R. T. Moug, C. Bradford, D. Thuau, A. Curran, R. J. Warburton, and K. A. Prior, "MBE Growth and Characterization of MgS-Rich Zinc-Blende $Zn_xMg_{1-x}S_{1-y}Se_y$ Alloys," *Journal of the Korean and Physical Society,* vol. 53, pp. 3004-3006, 2008.

[21] F. Turco and M. Tamargo, "Growth studies of molecular-beam epitaxial ZnSe using reflection high-energy electron diffraction oscillations," *Journal of Applied Physics,* vol. 66, pp. 1695-1698, 1989.

[22] M. Schäfer, W. Naumann, T. Finnberg, M. Hannss, A. Dutschke, and R. Anton, "UV/ozone-activated growth of oxide layers on InAs (001) surfaces and oxide desorption under arsenic pressure," *Applied Surface Science,* vol. 158, pp. 147-158, 2000.

[23] J. H. Davies, "The physics of low-dimensional semiconductors", Cambridge University press, 1998.

[24] M. Vos, F. Xu, J. Weaver, and H. Cheng, "Influence of metal interlayers on Schottky barrier formation for Au/ZnSe (100) and Al/ZnSe (100)," *Applied Physics Letters,* vol. 53, pp. 1530-1532, 1988.

[25] A. R. J. Marshall, C. H. Tan, J. P. R. David, J. S. Ng, and M. Hopkinson, "Fabrication of InAs Photodiodes with reduced surface leakage current " in *Optical Materials in Defence Systems Technology IV,* vol. 6740, pp. H7400 1-9, 2007.

[26] A. R. J. Marshall, "The InAs electron avalanche photodiode and the influence of thin avalanche photodiodes on receiver sensitivity," *PhD Thesis,* 2009.

[27] D. Petrovykh, M. Yang, and L. Whitman, "Chemical and electronic properties of sulfur-passivated InAs surfaces," *Surface Science,* vol. 523, pp. 231-240, 2003.

[28] S. Ichikawa, N. Sanada, N. Utsumi, and Y. Fukuda, "Surface structures and electronic states of clean and $(NH_4)_2$ S_x-treated InAs (111) A and (111) B," *Journal of Applied Physics,* vol. 84, pp. 3658-3663, 1998.

[29] R. Moug, C. Bradford, F. Izdebski, I. Davidson, A. Curran, R. Warburton*, et al.*, "A comparison of ZnMgSSe and MgS wide bandgap semiconductors used as barriers: Growth, structure and luminescence properties," *Journal of Crystal Growth,* vol. 311, pp. 2099-2101, 2009.

[30] M. Molnár, Y. Fu, P. Friberg, and Y. Chen, "Optical characterization of colloidal CdSe quantum dots in endothelial progenitor cells," *Journal of Nanobiotechnology,* vol. 8, pp. 1-8, 2010.

[31] H. Ehrenreich and F. Spaepen, "Solid state physics", Academic Press, 2001.

[32] V. Kaygorodov, V. Sorokin, I. Sedova, O. Nekrutkina, S. Sorokin, T. Shubina*, et al.*, "Cd (Mg) Se Single Layers and CdSe/CdMgSe Heterostructures Grown by Molecular Beam Epitaxy on InAs (001) Substrates," *Acta Physica Polonica A,* vol. 100, pp. 443-450, 2001.

[33] Y. Varshni, "Temperature dependence of the energy gap in semiconductors," *Physica,* vol. 34, pp. 149-154, 1967.

[34] E. Zielinski, H. Schweizer, K. Streubel, H. Eisele, and G. Weimann, "Excitonic transitions and exciton damping processes in InGaAs/InP," *Journal of Applied Physics,* vol. 59, pp. 2196-2204, 1986.

[35] K. O'Donnell and X. Chen, "Temperature dependence of semiconductor band gaps," *Applied Physics Letters,* vol. 58, pp. 2924-2926, 1991.

[36] D. Mui, D. Leonard, L. Coldren, and P. Petroff, "Surface migration induced self-aligned InAs islands grown by molecular beam epitaxy," *Applied Physics Letters,* vol. 66, pp. 1620-1622, 1995.

[37] P. Kevin, "Privite comunication, Heriot Watt University," 2014.

[38] N. Chand, S. Chu, and M. Geva, "Effects of substrate misorientation on incorporation of ambient oxygen and interfacial roughness in AlGaAs/GaAs heterostructures grown by molecular-beam epitaxy," *Applied Physics Letters,* vol. 59, pp. 2874-2876, 1991.

[39] Y. Yang, P. Ma, X. Wei, and Y. Zeng, "The role played by strain on phase separation in InGaN quantum wells," *Solid State Communications,* vol. 194, pp. 25-29, 2014.

[40] A. Kashyout, A. Arico, P. Antonucci, F. Mohamed, and V. Antonucci, "Influence of annealing temperature on the opto-electronic characteristics of

ZnTe electrodeposited semiconductors," *Materials Chemistry and Physics,* vol. 51, pp. 130-134, 1997.

Chapter Six

6. Time of flight ranging using InAs photodiodes

6.1 Introduction

LIDAR has become a key technique for remotely mapping terrain, as well as numerous other applications, [1] as described in Chapter One. Operating at a wavelength where the solar background is much reduced (i.e. NWIR to MWIR) is very attractive [2], and semiconductor-based detectors utilising narrow bandgap materials, such as InAs, are desirable for this purpose. In this Chapter, preliminary laboratory based LIDAR experiments were performed with our InAs avalanche photodiodes (the devices were processed with the mask set designed in Chapter Four, so they have SU8 as passivation layer and SiN underneath the gold bondpad), at ranges of around 0.5 metres stand-off distance, demonstrating time-of-flight measurements at wavelengths up to 2370 nm. Preliminary characterisation analysis was performed on n-i-p and p-i-n InAs structures; dark currents, multiplication, responsivity and detector output pulse arrival time were studied. InAs n-i-p structures were further available during the ranging experiment, and were used in linear multiplication mode. Here, the laser beam was incident on the edge of the device (rather than the top of the mesa) in order to achieve a mixed carrier injection and thus higher gain. The main source of error in the measurements is due to the position of the laser spot on the edge of the device, where a slight shift in position can alter the injection profile and hence the output pulse arrival time of the detector. For example, movement of the laser spot can cause an error in time of 40 ps, which corresponds to a 6 mm ranging error. A total system jitter of less than 50 ps has been observed in the InAs devices at room temperature and at low gain.

6.2 Samples

Unbonded p-i-n and n-i-p mesa samples were provided by the University of Sheffield. Bonding, packaging and characterization were done by us at Heriot-Watt University. The details of the p-i-n and n-i-p structures used in this Chapter are summarised in Table 6.1.

A)

	Thickness	Material	Doping type	Doping value
n	2 μm	InAs	donors	1×10^{18} cm^{-3}
i	4 μm	InAs	donors (unintentional)	1×10^{15} cm^{-3}
p	1.5 μm	InAs	acceptors	1×10^{18} cm^{-3}

B)

	Thickness	Material	Doping type	Doping value
p	0.5 μm 3.5 μm	InAs	acceptors	1×10^{18} cm^{-3} 1×10^{17} cm^{-3}
i	6 μm	InAs	donors (unintentional)	2×10^{15} cm^{-3}
n	1.5 μm	InAs	donors	5×10^{17} cm^{-3}

Table 6.1 *Detail of the n-i-p (A) and p-i-n (B) structures.*

As shown in Table 6.1, the p-i-n sample has a p-region with a doping of 1×10^{18} cm^{-3} for the first 0.5 μm and of 1×10^{17} cm^{-3} for the following 3.5 μm.

The devices were processed using an early version of the mask set presented in Chapter Four of this Thesis. To provide a high bonding yield it combines SU8 as the passivation layer with SiN under the bondpad.

Light was shone on both the structures during their characterisation. For the p-i-n structure, light was shone on top of the mesa so as to have a pure electron injection during the experiments [3], [4]. Figure 6.1 shows the p-i-n structure under illumination.

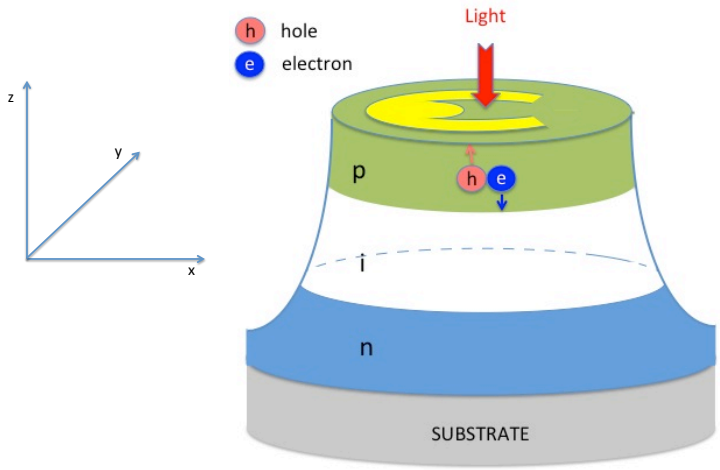

Figure 6.1 *Reverse biased InAs p-i-n structures with top gold contact under top illumination. The incident light is absorbed and electron-hole pairs are generated in the device. For clarity, only one electron-hole pair has been drawn: the blue and pink dots represent an electron and hole respectively.*

For the n-i-p mesa structure, light was incident on the edge of the mesa or on the surrounding p-region so as to study the mixed or the pure electron injection, respectively. The top of the mesa was completely covered by gold, removing the possibility of pure hole injection. This sample was processed with an early mask set in which a small number of devices were covered with gold to study different injection profiles. Due to a low bonding yield, only a device with the top of the mesa covered was available during the experiments. This mask set was not considered appropriate for our study and for this reason was re-designed as shown in Chapter Four for future work. In the ranging experiment the light was shone on the edge of the device, as shown in Figure 6.2, to give maximum responsivity.

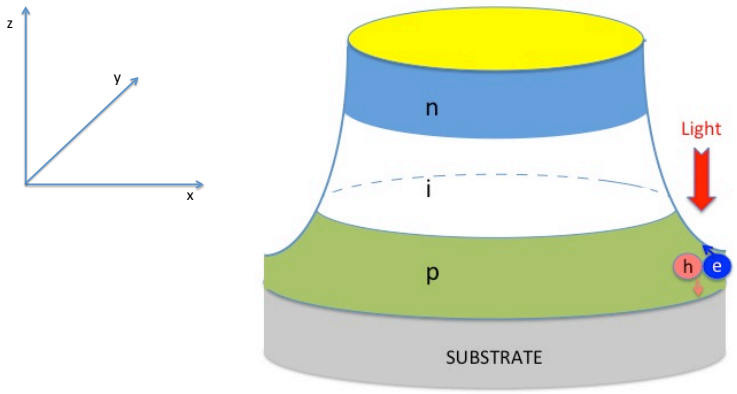

Figure 6.2 *InAs n-i-p structure covered with gold on top of the mesa under edge illumination and reverse bias. The incident light is absorbed and electron-hole pairs are generated in the device. For clarity, only one electron-hole pair has been drawn: the blue and pink dots represent an electron and hole respectively.*

The p-i-n and the n-i-p detectors analysed in the following experiments were 75 μm and 100 μm in diameter, respectively. An image using an optical microscope of both devices studied is shown in Figure 6.3.

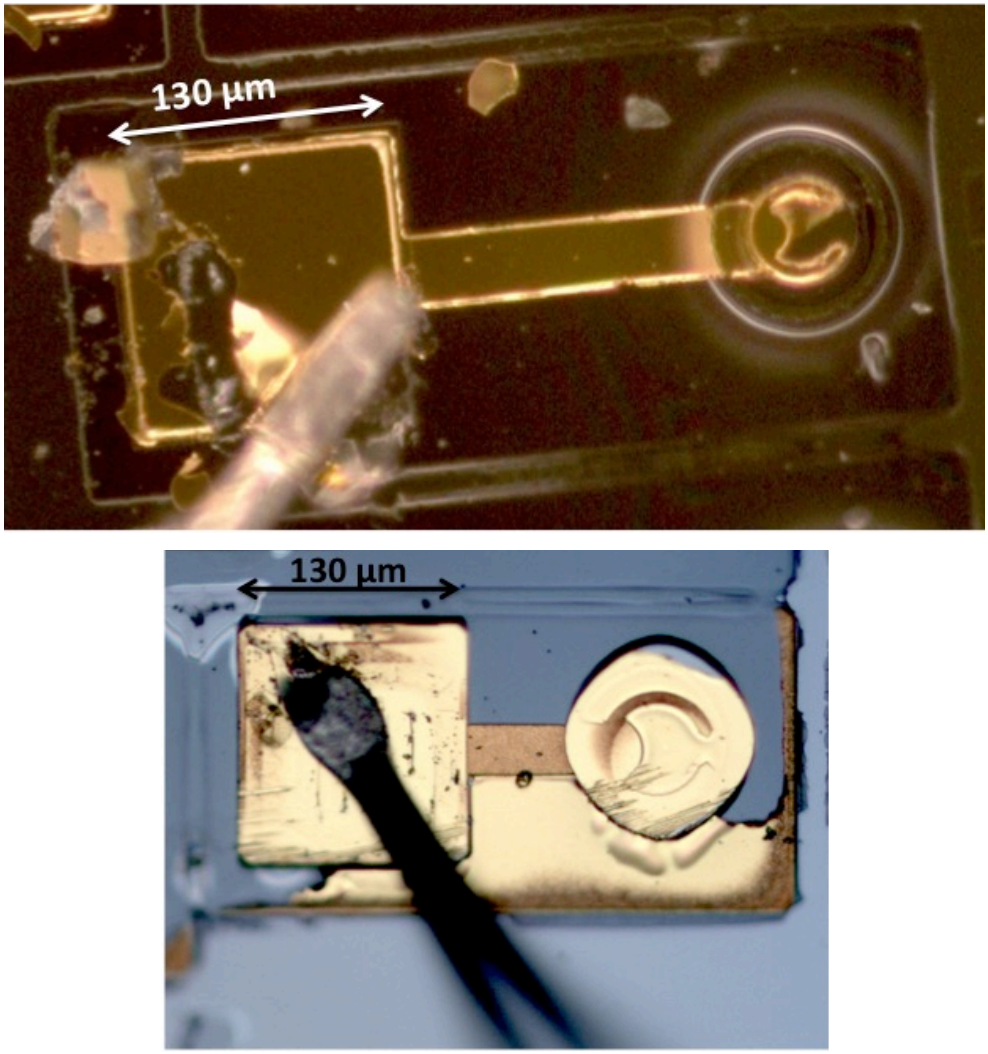

Figure 6.3 *Top, InAs p-i-n structure image under an optical microscope. The device has an annular top gold contact with some residual gold still covering part of the centre of the photodiode. The external bondpad is visible with some damage occurring during the wire bonding process. Bottom, n-i-p structure covered with gold on top of the mesa. Due to an error in processing some gold remains in a region around the device. The external bondpad and the bond are visible as well.*

For the p-i-n detector the light was incident on the top of the device. To avoid the gold in the centre of the mesa, the light was shone slightly out from the centre to the opposite side of the bondpad. The diameter of the laser spot at the device was estimated to be approximately 30 µm at every wavelength tested; this means that for the p-i-n device, part of the incident light is reflected by the gold contact. For the n-i-p structure light was shone on the edge or on the p-region next to the device. As is clear in Figure 6.3, only

part of the mesa edge and of the surrounding area were accessible because of poor sample processing.

6.3 Characterisation of p-i-n and n-i-p photodiodes

6.3.1 Dark current IV curves

6.3.1.1 Measurements at room temperature

Initially dark current measurements were taken at room temperature on both the devices under analysis. Unfortunately, due to device degradation, these dark current levels were not constant throughout our studies. Figure 6.4, for example, shows the dark current IVs for the 75 μm (diameter) p-i-n device before and after the experiments.

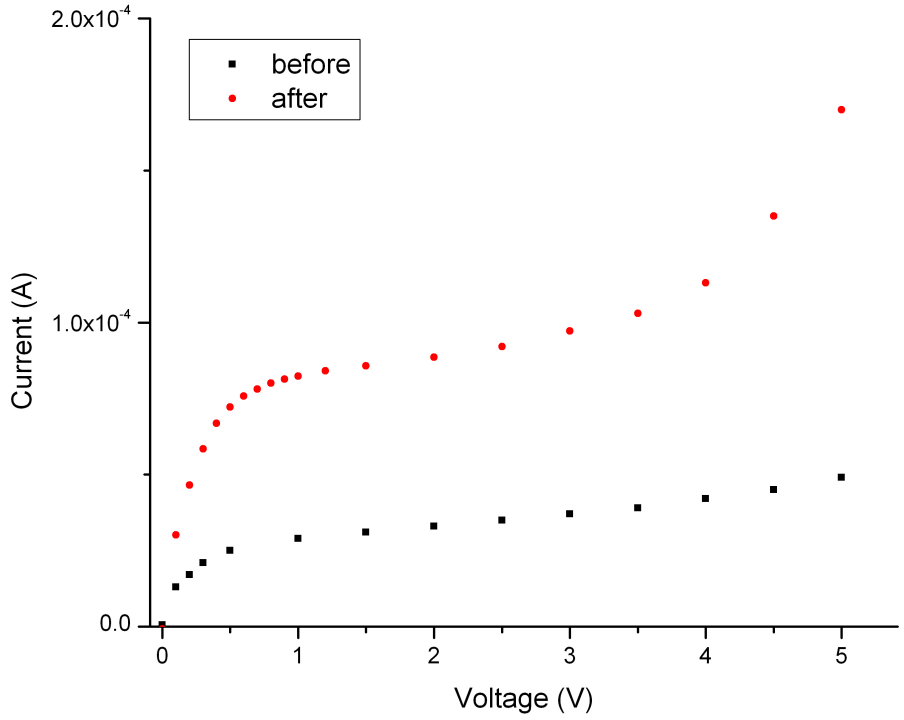

Figure 6.4 *Dark current versus reverse bias for the 75 μm diameter p-i-n device before (black squares) and after (red circles) the experiments.*

Figure 6.4 shows that, at 5 V, a dark current of 170 μA was observed at the end of all the measurements compared to the initial 50 μA.

For the 100 μm diameter n-i-p structure, higher dark current (with respect to the p-i-n structure) was observed at room temperature: 5 μA at 0 V and 4.9 mA at 5 V. Even in

this structure degradation was observed with usage: at the end of testing, the device had a dark current of 6.8 mA at 5 V.

Dark currents of the magnitudes measured here, for both structures, are possibly due to processing problems. These dark currents levels are much higher than that observed by Ker *et al.* [5].

6.3.1.2 Measurements at lower temperature

As shown by Ker *et al*. [5], the dark current of an InAs diode should decrease with device temperature down to at least 77 K, due to the expected reduction in thermal excitation of carriers. Based on the dark current measurements shown above, the p-i-n structure device was tested at a range of temperatures. The n-i-p structure device was not tested as the reduction in dark current was considered to be not significant compared to the drop in M also associated with a reduced temperature. As discussed in Section 3.4 of Chapter Three, the multiplication will reduce with decreasing temperature because in InAs the increase in bandgap has a greater effect than the decrease in phonon scattering.

Figure 6.5 shows a comparison of the dark current at room temperature, 250 K and 200 K for the p-i-n device.

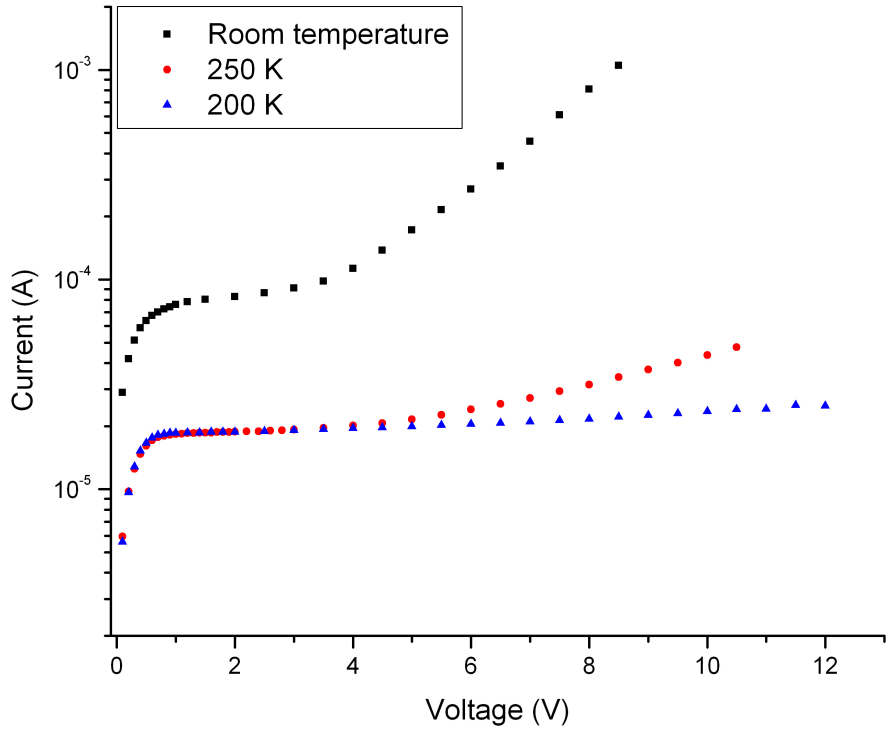

Figure 6.5 *Dark current vs reverse bias data for the 75 μm diameter p-i-n device at room temperature (black squares), 250 K (red circles) and 200 K (blue triangles).*

As can be seen, the dark current plateaus around 250 K. This could be explained by surface states in the device.

6.3.2 Photocurrent measurements with reverse biased InAs photodiodes

6.3.2.1 Experimental set up

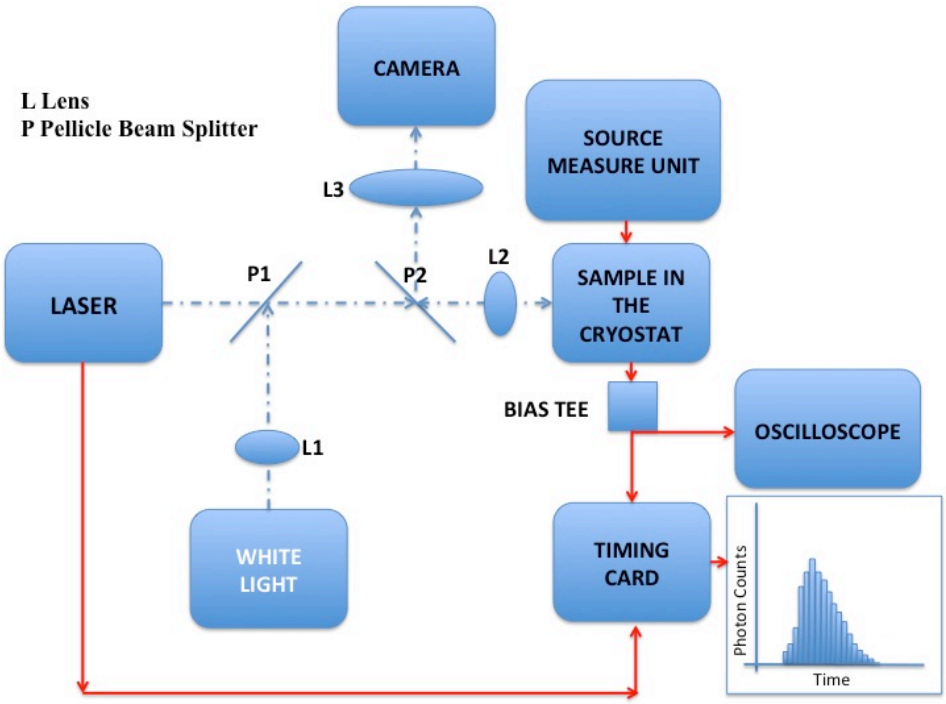

Figure 6.6 *Diagram of the experimental set up. The dashed blue line is the free space optical path while the continuous red line is the electrical connection. The main components are the SuperK continuum laser and the cryostat where the sample is placed. White light is coupled into the system (via beam splitters P1 and P2) to image the sample onto an infrared camera. The sample is reverse biased by the Source-Measure Unit (SMU) and its output pulse, after passing through a bias tee to filter the DC dark current, is analysed with a GHz oscilloscope or a timing card (see main text).*

Figure 6.6 shows a schematic of the characterisation experimental set up. The pulsed laser is directed onto the sample within the cryostat using an imaging system with an M5 objective lens (focal length 36 mm), L2. Before being incident on the sample the light beam passes through the quartz cryostat window where the measured transmission at each surface is 93 % at 1550 nm wavelength. White light imaging on the IR camera, to view both sample details and the laser focus position, is achieved via two beam splitters P1 and P2 (reflectance 8% transmittance 92%). The InAs sample is DC reverse biased by the Source-Measure Unit (SMU), Keithley 236. The SMU supplies a DC

voltage to the photodiode and at the same time allows measurement of the current that flows across the circuit. When light is detected, the detector provides an output pulse due to the photocurrent generated in the device; these pulses, after passing through a bias tee (Tektronix PSPL5550B Bias Tee, 18 GHz) to filter out the DC dark current component, are analysed with a GHz oscilloscope (Hewlett Packard 54845A Infiniium Oscilloscope). We also used a timing card in a similar manner for time-correlated single-photon counting: by histogramming the timing difference between the stop and start signals. However, it must be noted that this approach is not measuring a single-photon response from the detector and that the detector is operated in the linear multiplication mode. In this mode, the timing of the photodiode output pulse (which gives a STOP signal pulse) with respect to a reference signal (the START signal pulse) synchronised with the laser pulse output, is measured and recorded in a histogram. The timing card used in the experiment is an SPC 600 by Becker and Hickl; it has a time jitter of 13 ps, a maximum number of time channels of 4096, a minimum bin width of 813 fs, and a measurement time duration minimum of 0.1 ms. The laser used in the measurements is a SuperK Extreme supercontinuum laser system, model EXW-6, by NKT Photonics, which has an emission spectral range between 0.4 μm and 2.4 μm wavelengths. Figure 6.7 shows the spectral power density as a function of emitted wavelength [6].

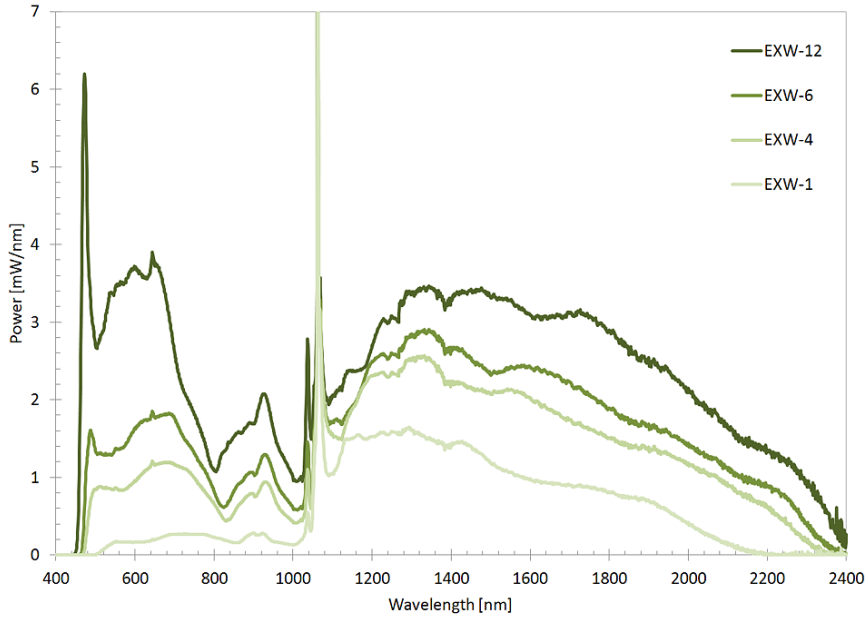

Figure 6.7 *Spectral power density as a function of emitting wavelengths for White EXW series Supercontinuum lasers by NKT Photonics [6]. The model used in the experiment is EXW-6.*

In the experiments in this Chapter, the SuperK laser has been used only to generate radiation in the infrared spectral range from 1.3 to 2.4 μm. As shown in Figure 6.7 the spectral power density emitted from the supercontinuum decreases as the operating wavelength increases from 1.3 μm to 2.4 μm.

Below 2 μm the SuperK was coupled with the Acousto-Optic Tunable Filter technology (AOTF) that allows the choice and tuning of specific wavelengths in the SuperK spectrum. The white light beam from the SuperK laser system is directed through the AOTF to one of the 2 laser apertures. Specific wavelengths can be selected with an accuracy of ~1 nm, the wavelength range covering 1.1-2 μm was used. Due to losses inside the AOTF, the spectral power density available below 2 μm is less than that of the supercontinuum output shown in Figure 6.7. The AOTF was 37% efficient at 2 μm. Above 2 μm, the AOTF was ineffective, hence we used external passive optical filters to select wavelengths from the entire supercontinuum emission. We used different narrow band pass (NB) filters, in conjunction with a long pass (LP) filter which cuts on at a wavelength of 1.85 μm. We measured the transmission of all the filters used in the

experiment. Figure 6.8 shows the transmission data taken for the long pass filter and an example of narrow band filter, centred at 1998 nm wavelength.

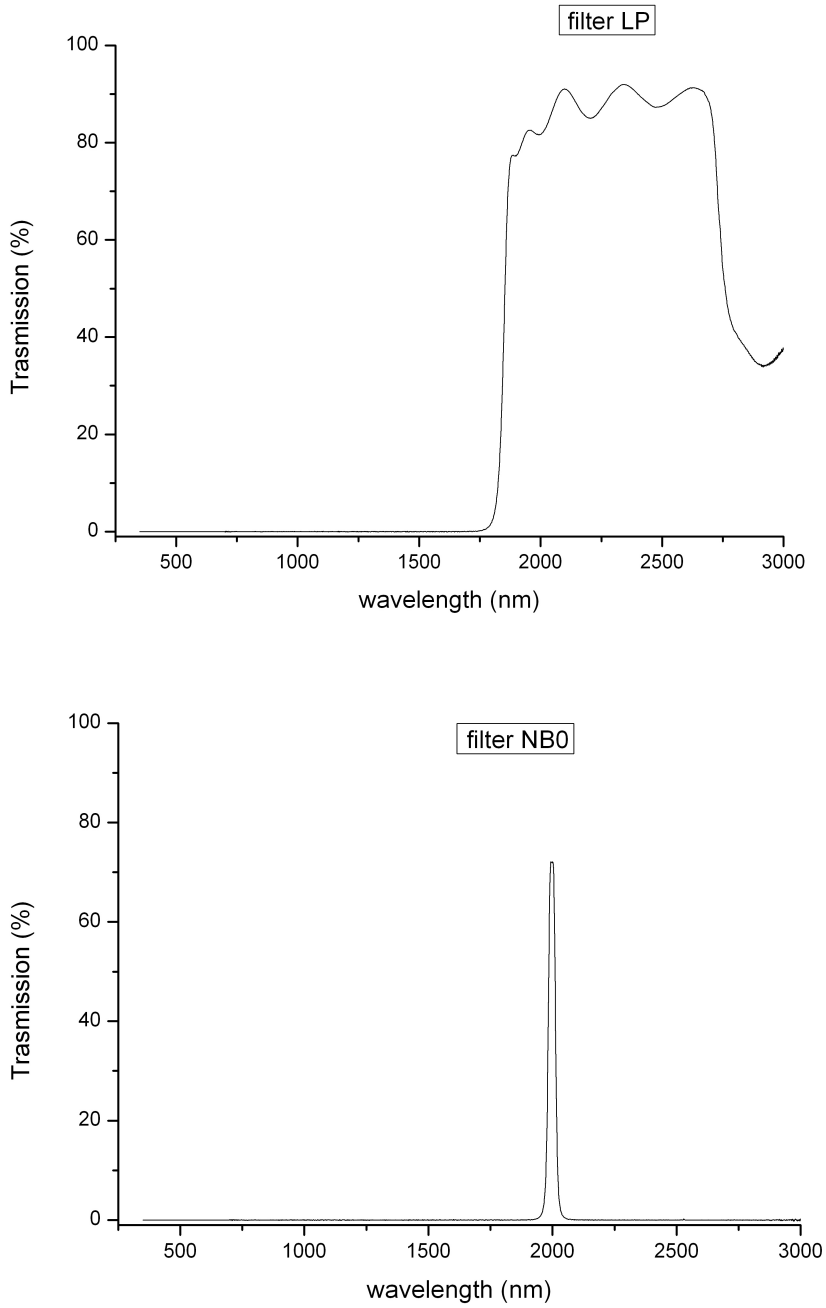

Figure 6.8 *Transmission data for the 1.85 μm long pass filter, LP, (top) and an example of a narrow band filter centred at 1998 nm wavelength, labelled NB0, (bottom). Above 2 μm wavelength, the AOTF was ineffective, hence external passive optical filters were used to select wavelengths from the entire supercontinuum output.*

Table 6.2 summarises the main properties of the five narrow band pass filters we used. The band pass filters are labelled as NB0 (peak centre at 1998 nm), NB1 (peak centre at 2100 nm), NB2 (peak centre at 2207 nm), NB3 (peak centre at 2311 nm) and NB4 (peak centre at 2370 nm). A variance in maximum and FWHM of the transmission peaks was observed for the different filters. The filter whose transmission peak is centred at 2207 nm presents the lowest maximum and FWHM. Lower FWHMs represent better selection in wavelength, though at the cost of total transmitted power.

	Peak centre (nm)	Max. Transmission (%)	FWHM (nm)
NB0	1998	72	31
NB1	2100	81	23
NB2	2207	61	12
NB3	2311	70	27
NB4	2370	75	46

***Table 6.2**. The maximum transmission and FWHM of the transmission peaks for all the band pass filters used.*

The extinction factors for all the filters analysed is around 40 dB.

6.3.2.2 Avalanche multiplication in p-i-n structure

To quantify the photocurrent generated in the device under illumination, the set up in Figure 6.6 was slightly modified so as to incorporate a Lock In Amplifier (LIA). Due to the high dark current, it was necessary to use a phase sensitive detection method to differentiate the AC photocurrent from the DC dark current. A mechanical chopper was used in front of the laser output, of frequency of around 180 Hz, to give the reference signal to the LIA. Figure 6.9 shows the electric circuit.

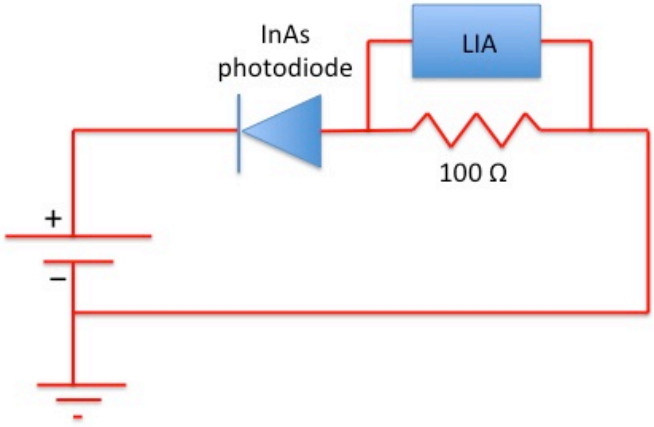

Figure 6.9 *Diagram of the reverse biased electrical circuit studied. The lock-in amplifier (LIA) measures the photo-voltage across the 100 ohm resistor in series with the InAs photodiode.*

The photo-voltage across a 100 Ω resistor was measured by the LIA. An accurate estimation of the photocurrent generated through the diode under illumination was found using the LIA. Photocurrent measurements were taken at different wavelengths and reverse biases. Wavelengths of 1150 nm, 1300 nm, 1550 nm, 1700 nm and 2000 nm were shone on the centre of the mesa. A typical photocurrent curve is shown in Figure 6.10, in this case the diode illuminated with light at wavelength of 1700 nm.

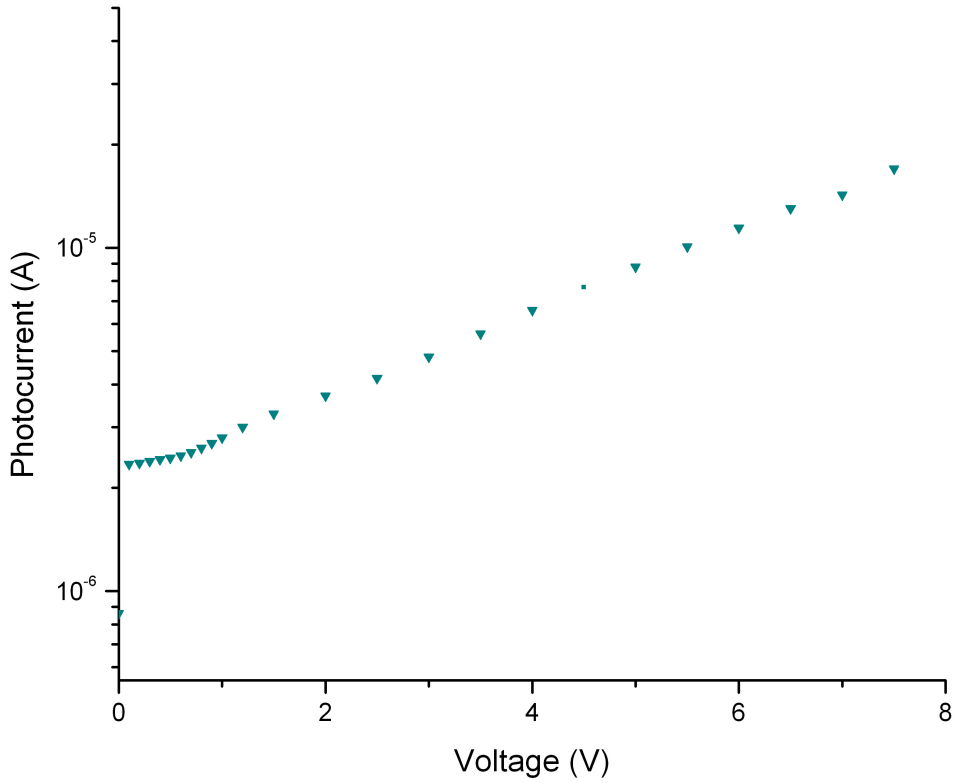

Figure 6.10 *Photocurrents measurements as a function of reverse bias voltage illuminating the p-i-n InAs photodiode with λ=1700 nm incident radiation.*

Typical results of photocurrent versus reverse bias voltage for a p-i-n InAs photodiode are shown in Figure 6.10. Increasing the voltage results in an increasing photocurrent. Two different slopes can be observed: at voltages lower than 0.5 V an almost constant un-multiplied photocurrent, referred to as the primary photocurrent, is observed, while above 0.5 V the impact ionisation process starts resulting in multiplied photocurrent that causes the different behaviour.

From these photocurrent measurements as a function of increasing reverse bias, the multiplication factor can be estimated, correcting for the primary un-multiplied photocurrent. The primary un-multiplied photocurrent is usually calculated using a linear fit at low bias. For an InAs photodiode it is very difficult to do this baseline correction because avalanche starts at very low bias and only a small range of bias can be used in the fitting. A reasonable approach to calculate the multiplication factor is to consider a fixed primary photocurrent [7]. In the data shown in Figure 6.11, the multiplication factor was calculated using the fixed primary photocurrent value at 0.3 V.

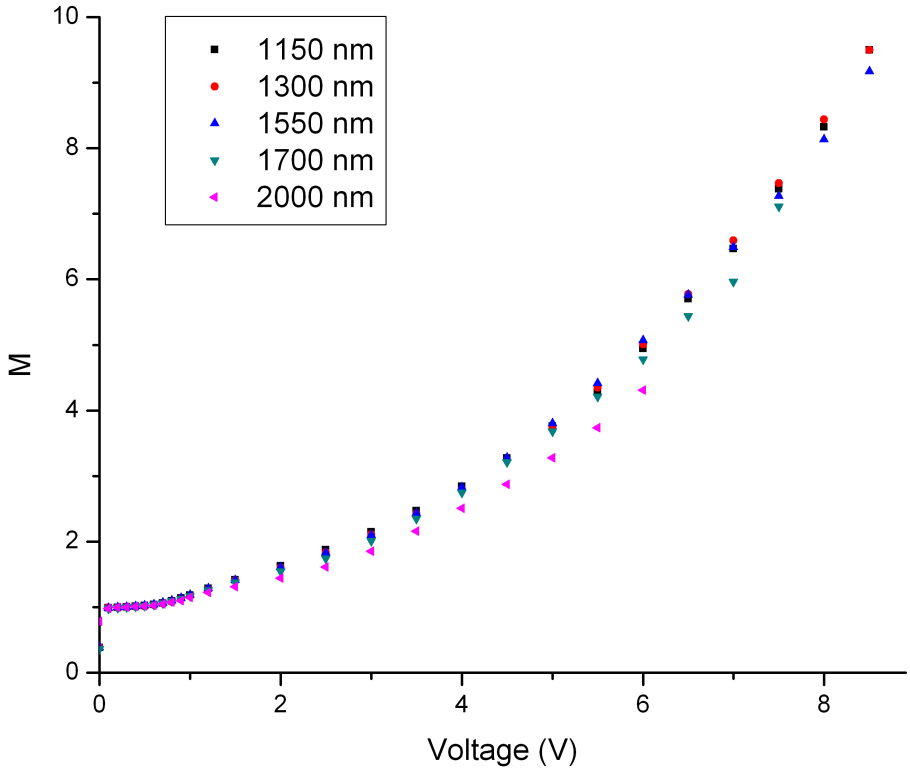

Figure 6.11 *Multiplication measurements as a function of reverse bias voltage illuminating the p-i-n InAs photodiode with wavelengths 1150 nm (black squares), 1300 nm (red circles), 1550 nm (blue triangles), 1700 nm (green triangles) and 2000 nm (pink triangles).*

Increasing the voltage, the electric field in the i-region increases leading to higher multiplication factors. Longer wavelengths penetrate deeper into the structure leading to a mixed injection profile and so to a lower multiplication factor: photons absorbed in the i-region produce electron-hole pairs that are both multiplied. As discussed in Chapter Three, due to the InAs band structure, electron impact ionisation dominates the avalanche multiplication while holes essentially play no role ($\beta << \alpha$). Shorter wavelengths instead are absorbed in the p-region causing pure electron injection and higher *M*. As shown in Figure 6.11, at wavelengths of 1150 nm, 1300 nm and 1550 nm pure electron injection is achieved where as at wavelength of 1700 nm and 2000 nm mixed injection is observed (giving a lower value of M for given voltage).

A study of the multiplication factor when the photodiode is illuminated on the edge of the p-i-n has also been conducted at 1550 nm wavelength, as shown in Figure 6.12. In this configuration the light is incident upon the sidewall of the mesa and part is absorbed in the i-region: this causes mixed injection and the injection of holes

decreases the multiplication.

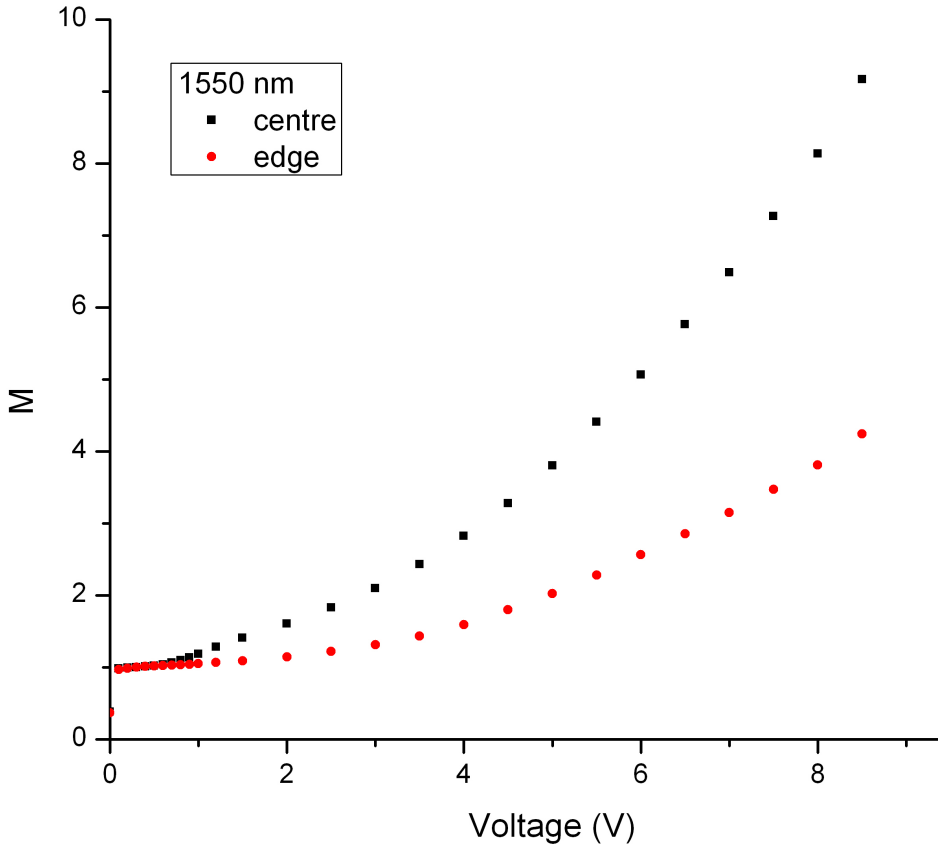

Figure 6.12 *Multiplication measurements as a function of reverse bias voltage illuminating the p-i-n InAs photodiode on the top centre of the mesa (black squares) and on the edge (red circles) with 1550 nm wavelength radiation. Pure electron injection was observed in the first case while mixed injection was observed in the second case.*

A study of multiplication as a function of temperature was conducted with pure electron injection (i.e. with the laser spot positioned on the top surface of the mesa). As expected, the multiplication decreases with temperature decrease because of the increasing bandgap and negligible phonon scattering reduction, as discussed in Chapter Three. Figure 6.13 shows this behaviour for three temperatures.

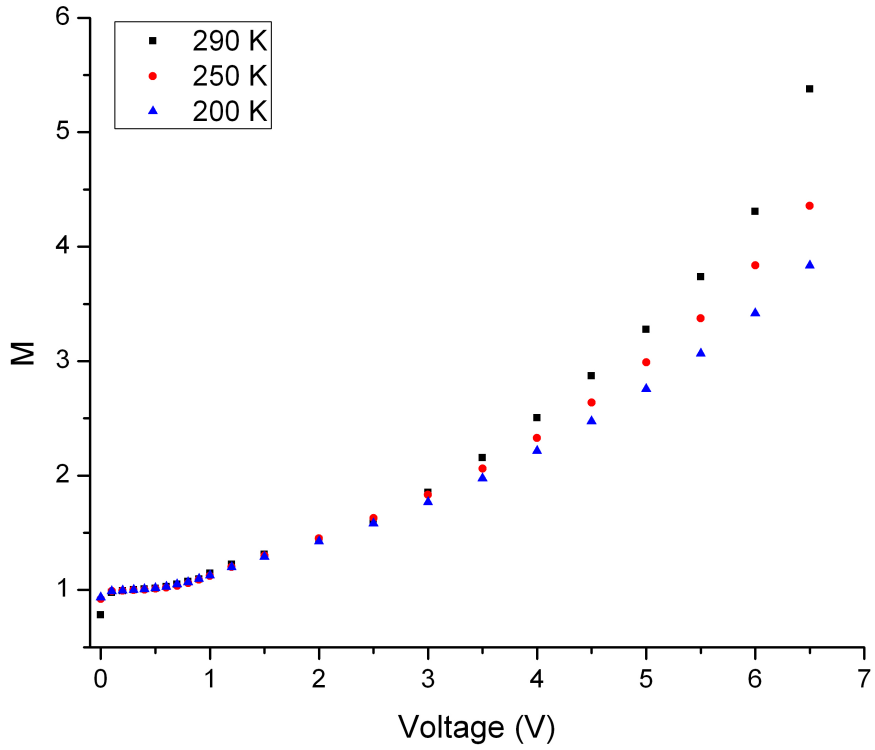

Figure 6.13 *Multiplication factor M versus reverse bias, illuminating the p-i-n InAs photodiode on the top centre of the mesa with 2000 nm wavelength radiation. Three different temperatures were analysed: 290 K (black squares), 250 K (red circles), and 200 K (blue triangles).*

Figure 6.14 shows a comparison of multiplication for 1700 and 2000 nm wavelength incident light. Again, the 2000 nm wavelength penetrates deeper into the mesa reaching the i-region, resulting in mixed injection.

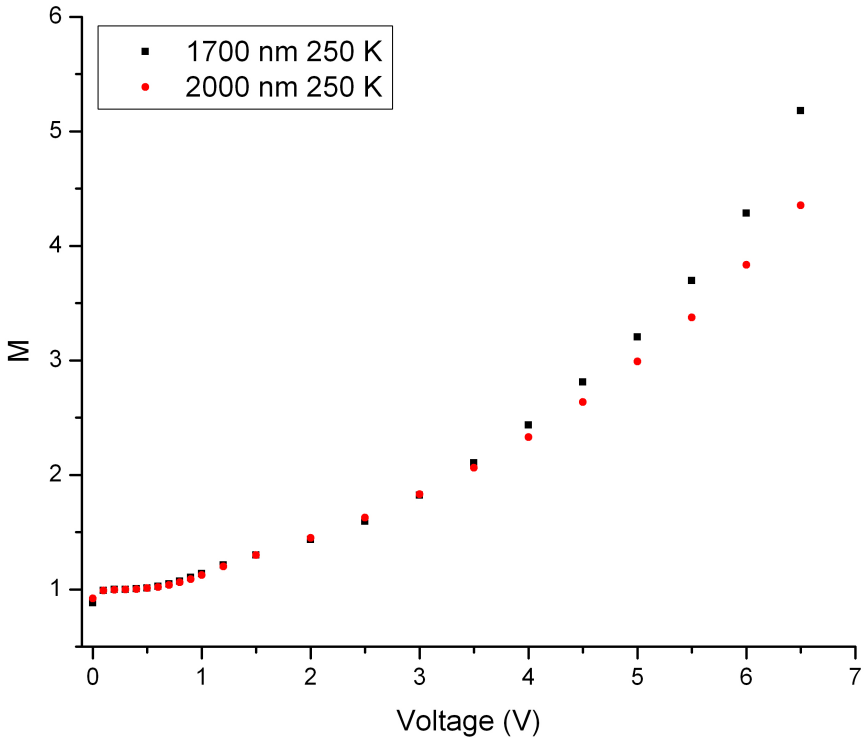

Figure 6.14 *Multiplication measurements as a function of reverse bias voltage illuminating the p-i-n InAs photodiode on the top centre of the mesa, with 1700 nm (black squares) and 2000 nm (red circles) wavelength radiation. Measurements were taken at 250 K.*

The detector responsivity as a function of voltage at a particular wavelength was also estimated for every wavelength tested when the centre of the mesa is illuminated. It was calculated by dividing the experimental photocurrent with the corresponding laser power measured at the cryostat window. Figure 6.15 shows the responsivity observed at wavelengths of 1150 nm (black squares), 1300 nm (red circles), 1550 nm (blue triangles) and 1700 nm (green triangles).

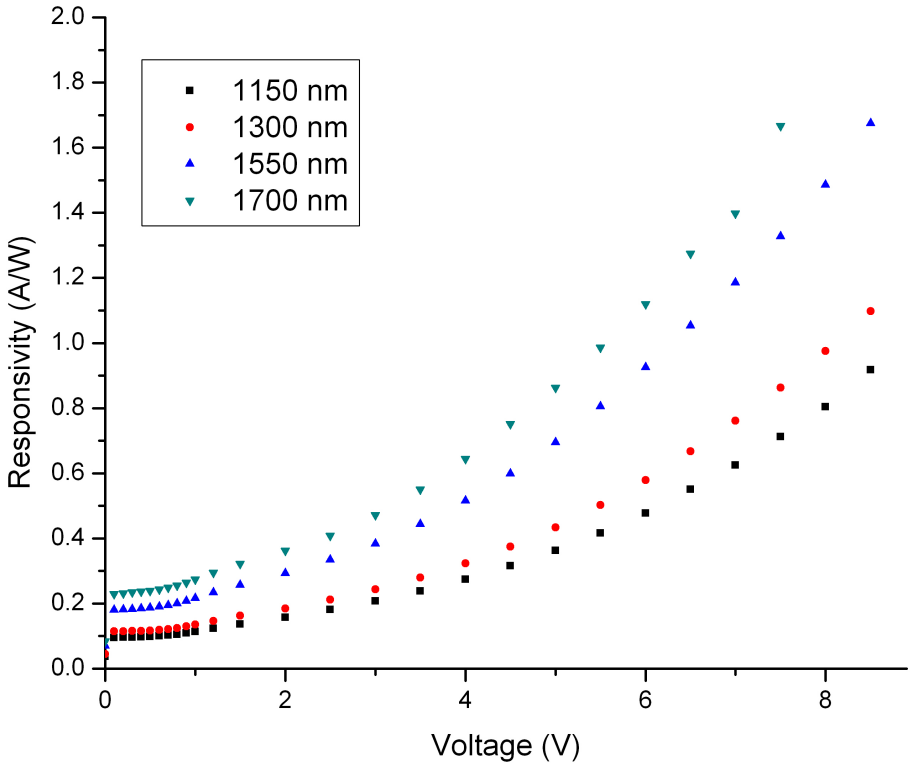

Figure 6.15 *Responsivity measurements as a function of reverse bias voltage illuminating the p-i-n InAs photodiode with wavelengths of 1150 nm (black squares), 1300 nm (red circles), 1550 nm (blue triangles) and 1700 nm (green triangles).*

Figure 6.15 demonstrates that the deeper penetration of longer wavelengths into the structure (close to the i-region) result in higher responsivity. This is because at 1700 nm wavelength the generated electrons are subjected to less recombination processes in the p-region and a high percentage of them diffuse into the multiplication region. Because part of the beam is reflected by the gold top contact (as mentioned above) and there is a loss in the laser power due to absorption by the two quartz cryostat windows, the responsivity values obtained are underestimated.

The changes in responsivity at 1550 nm wavelength when the centre and the edge of the mesa are illuminated are also shown in Figure 6.16.

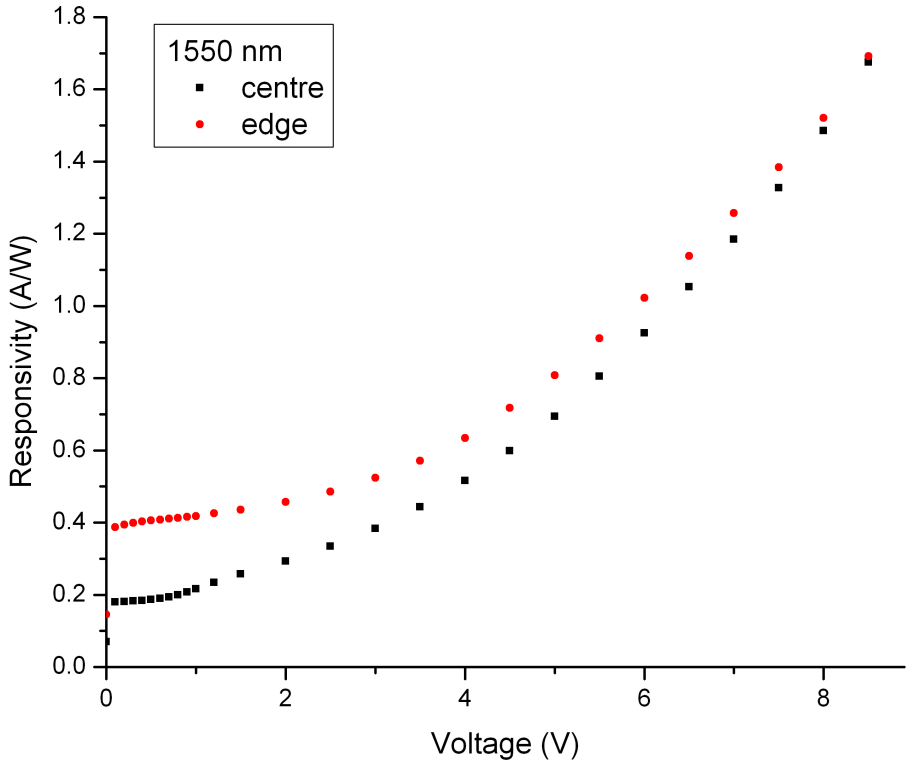

Figure 6.16 *Responsivity measurements as a function of reverse bias voltage illuminating the p-i-n InAs photodiode with wavelength of 1550 nm when the photodiode is illuminated on the centre (black squares) and on the edge (red circles) of the mesa.*

A higher responsivity is observed at low voltage when light is incident on the edge of the mesa, due to electrons generated directly in the intrinsic region. When light is shone on the centre of the mesa, the photons are absorbed in the p-region so that the electrons need to diffuse through this region to reach the multiplication region. Due to recombination processes the percentage of electrons that reach the multiplication region is lower resulting in a lower photocurrent. As the voltage is increased, the multiplication increases and, because higher multiplication has been observed when the laser spot is positioned on the centre of the mesa due to the resulting pure electron injection, the photodiode shows similar values of photocurrents and responsivity.

6.3.2.3 Avalanche multiplication in n-i-p structure

With the same set up as described in section 6.3.2.2, multiplication data were taken using the n-i-p structure. The laser spot was positioned on the edge of the mesa to give mixed injection and subsequently on the p layer that surrounds the device under analysis to give pure electron injection. Directing light on top of the mesa to study the pure hole injection was not possible because the gold contact covers this area and prevents access. Figure 6.17 shows typical photocurrent curves for the n-i-p structure; in this case the diode is illuminated with 2000 nm wavelength radiation on the edge (black squares) and on the p-region next to the mesa device (red circles).

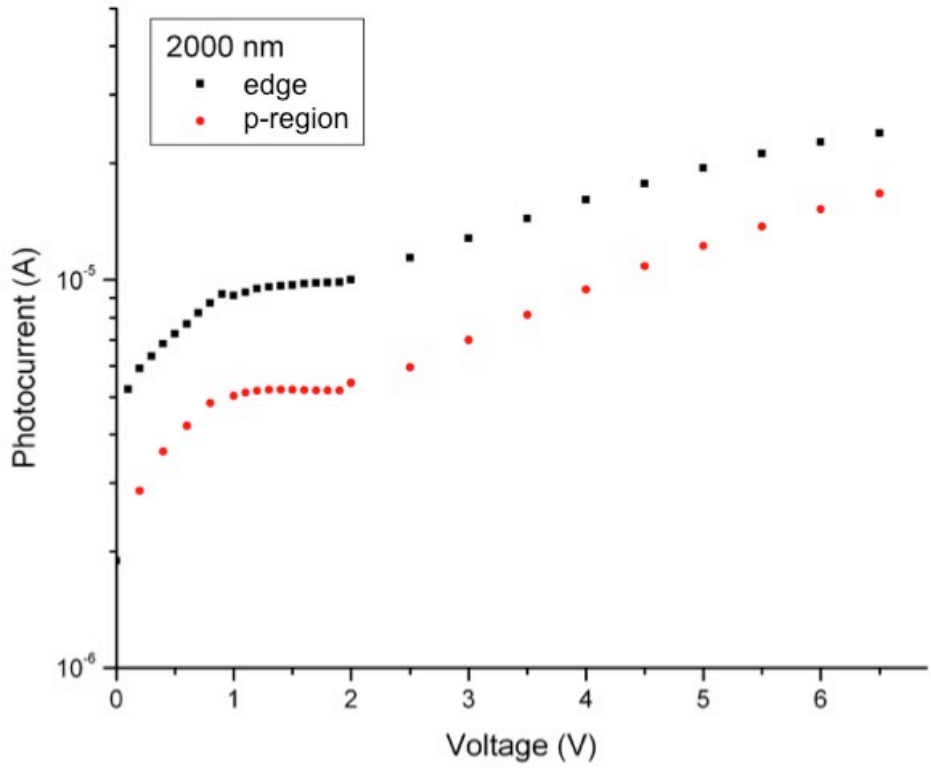

Figure 6.17 *Photocurrent measurements as a function of reverse bias voltage when the edge (black squares) of the n-i-p device and the p-region next to the device (red circles) are illuminated with 2000 nm wavelength radiation.*

As the voltage is increased the photocurrent increases. In Figure 6.17, three different slopes can be observed for each curve: at voltages lower than 1 V the diode is still depleting causing a steep slope, between 1 V and 2 V an almost constant un-multiplied primary photocurrent is observed, while above 2 V the impact ionisation process starts resulting in multiplied photocurrent. At the same laser power higher photocurrent is

observed when the laser is positioned on the edge of the device as the electrons are injected directly into the multiplication region and do not have to diffuse from the surrounding area.

As for the p-i-n structure, the multiplication factor was calculated using a fixed primary photocurrent value. In this case the value at 1.2 V was chosen. Figure 6.18 shows the multiplication factors calculated at wavelengths 1700 nm and 2000 nm when the laser spot is positioned on the edge of the photodiode and on the surrounding p-region.

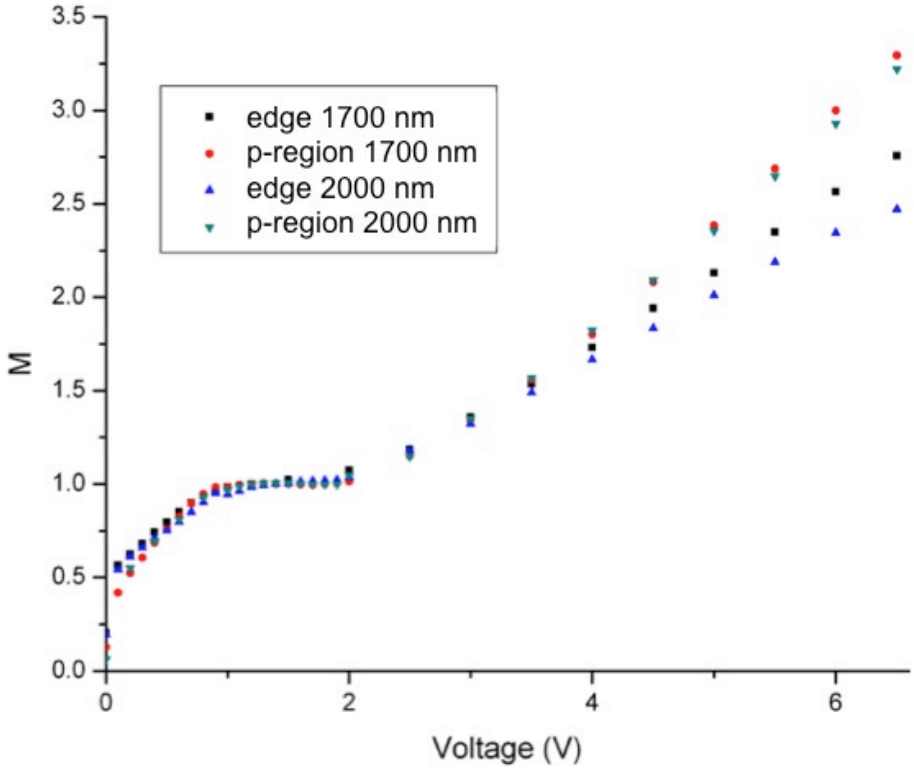

Figure 6.18 *Multiplication measurements as a function of reverse bias voltage for the n-i-p device. 1700 nm wavelength radiation is incident on the edge (black squares) and on the p-region (red circles). 2000 nm wavelength radiation is incident on the edge (blue triangles) and on the p-region (green triangles).*

For both of the analysed wavelengths, similar higher multiplications values are observed when the laser spot is positioned on the p-region: this is due to the pure electron injection. When laser spot is positioned on the edge of the mesa, mixed injection is achieved, reducing the multiplication: the differences in the *M* values observed at high voltage are possibly due to slightly different positions in the laser spot at 1700 nm wavelength with respect to 2000 nm wavelength that causes different

injection profiles. For this reason a study of the multiplication as a function of laser spot position at both 5 V and 6 V has been conducted. The results are shown in Figure 6.19.

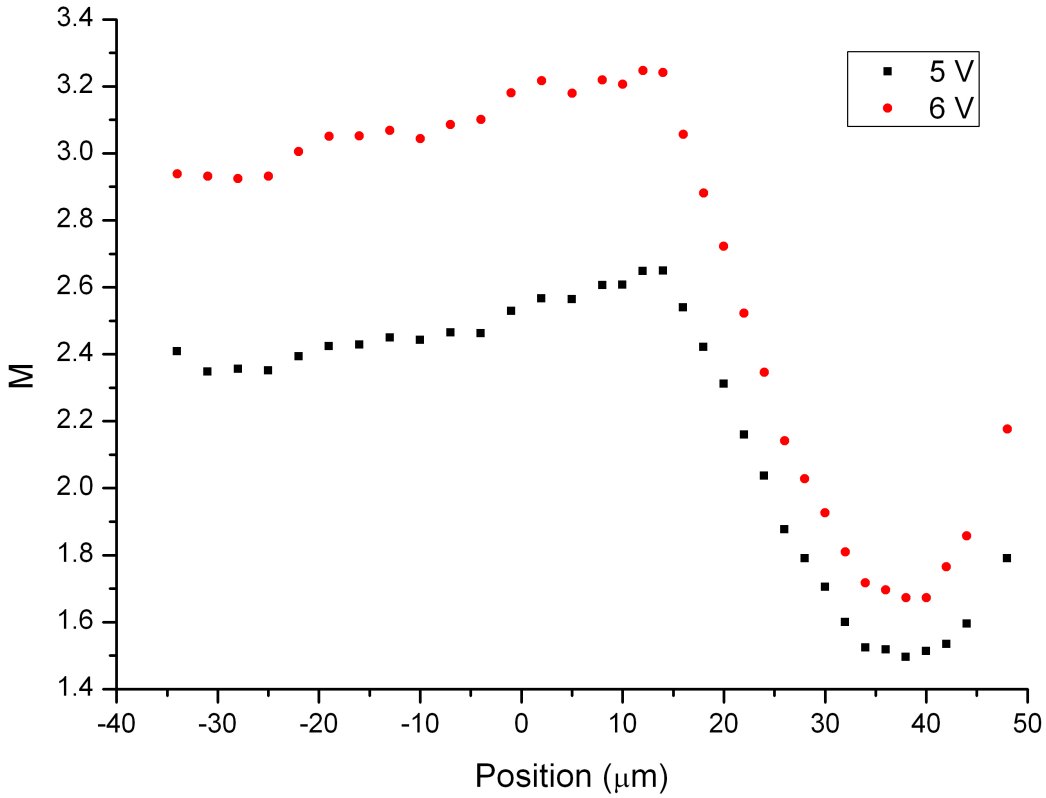

Figure 6.19 *Multiplication measurements at 5 V (black squares) and 6 V (red circles) as a function of laser spot position along y for the n-i-p device. The photodiode was illuminated with 1700 nm wavelength light. Position on the y-axis corresponds to movement across the device, the laser spot is moving over the edge of the device between 14 μm and 24 μm and over the top above 24 μm.*

The multiplication is higher when the laser spot is on the surrounding p-region (below 14 μm) due to pure electron injection. The mixed injection where holes can contribute causes a decreasing multiplication that can be seen when the laser spot illuminates the edge of the mesa (between 14 and 24 μm). Where the laser is almost illuminating the top of the device an increase in the multiplication is observed. This could be caused by a reduction in the number of injected holes due to the small diffusion coefficients for holes, while recombination processes can create further photons that will be absorbed in the i- or p-regions, generating more electrons in these regions and giving mixed injection.

A responsivity study as a function of the position and wavelength of the incident light was also conducted for the n-i-p structure. Figure 6.20 shows the responsivity observed at 1700 nm wavelength on the edge of the device and on the p-region.

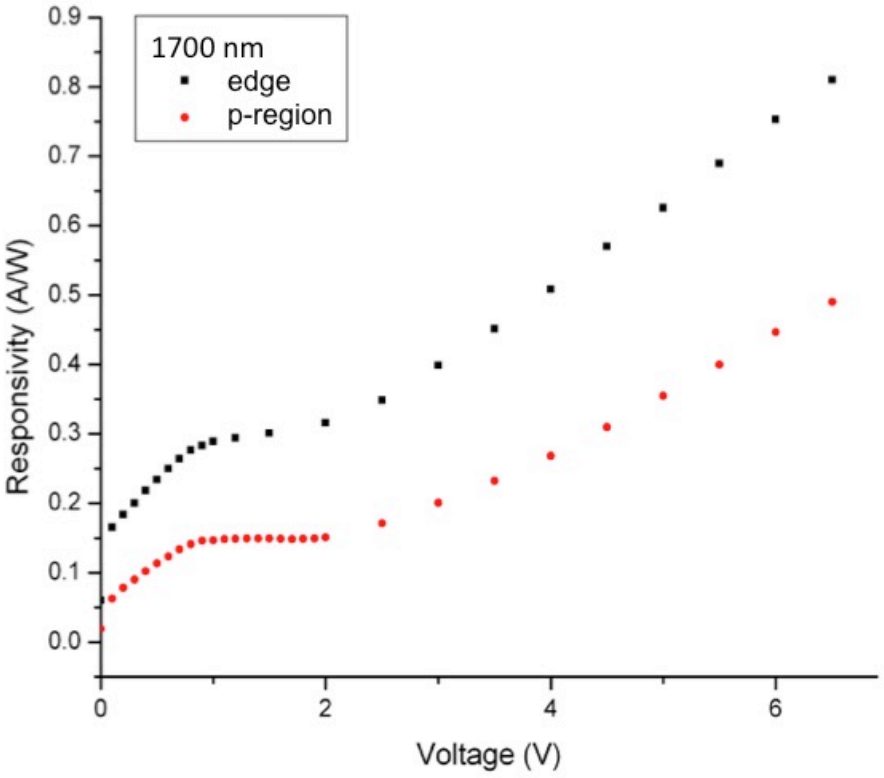

Figure 6.20 *Responsivity measurements as a function of reverse bias voltage at a wavelength of 1700 nm when the photodiode is illuminated on the edge of the device (black squares) and on the p-region (red circles).*

The higher responsivity observed in edge illumination is explained by direct photon absorption within the i-region, resulting in less recombination and thus higher responsivity.

For the ranging experiments described later in this Chapter (section 6.4) edge illumination was chosen. This decision was made to provide the higher responsivity, despite the reduction in multiplication.

6.3.2.4 Timing of the InAs device output pulse as a function of laser spot position

Using the set up shown in Figure 6.6 and the timing card, we studied the device pulse arrival time as a function of laser spot position on both p-i-n and n-i-p structures.

The device pulse arrival time was measured by recording a histogram using the timing card. The centroid of the histogram peak, $\bar{t}$, corresponds to this arrival time and is calculated as a weighted sum: each pulse arrival time t_k is weighted by the number of times n_k it occurs [8].

$$\bar{t} = \frac{\sum_k t_k n_k}{N}, \tag{6.1}$$

with $\sum_k n_k = N$

Where N is the total number of counts within the histogram.

Figure 6.21 shows this study for the p-i-n structure. The laser spot was moved from one area of the n-region to another across the top of the device.

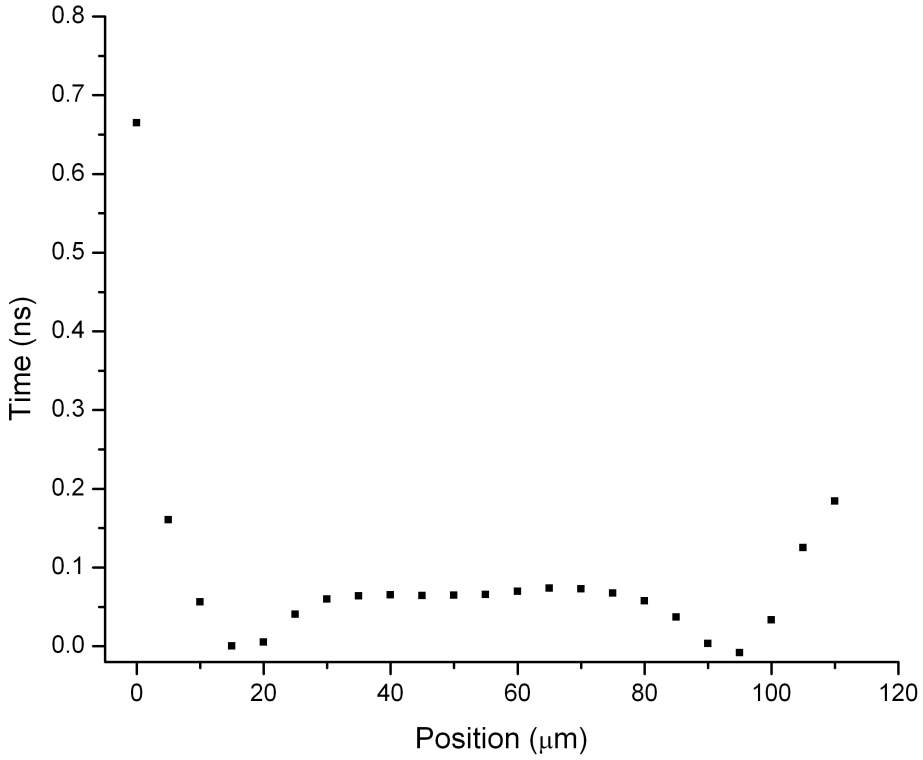

Figure 6.21 *Device pulse arrival time as a function of position along y of the 1700 nm wavelength laser spot for the p-i-n structure.*

The pulse arrival time has a minimum when the laser spot is positioned on the edge of the device, this is due to electrons being directly generated in the i-region. When the

laser spot is moved from the edge of the device to the centre, a slight delay in the pulse time arrival is observed; this is due to the time taken for electrons to diffuse across the p-region before reaching the multiplication region. Thus, when the laser spot is scanned across the top of the mesa (at positions between 30 μm and 80 μm in Figure 6.21), the pulse arrival time has a constant value of around 0.06 ns as electrons have to travel the same path through the p-region. On either side of the device, generated holes need to diffuse further (through the n-region to the multiplication region) resulting in a pulse time arrival delay: the further the laser spot is from the device; the more delayed the pulse arrival time will be.

As shown in Figure 6.3, the top of the n-i-p mesa and part of the surrounding p-region on one edge were covered by gold, so only one side of the device was accessible for this study. Figure 6.22 shows the device pulse arrival time as a function of laser spot position along *y* for the n-i-p structure.

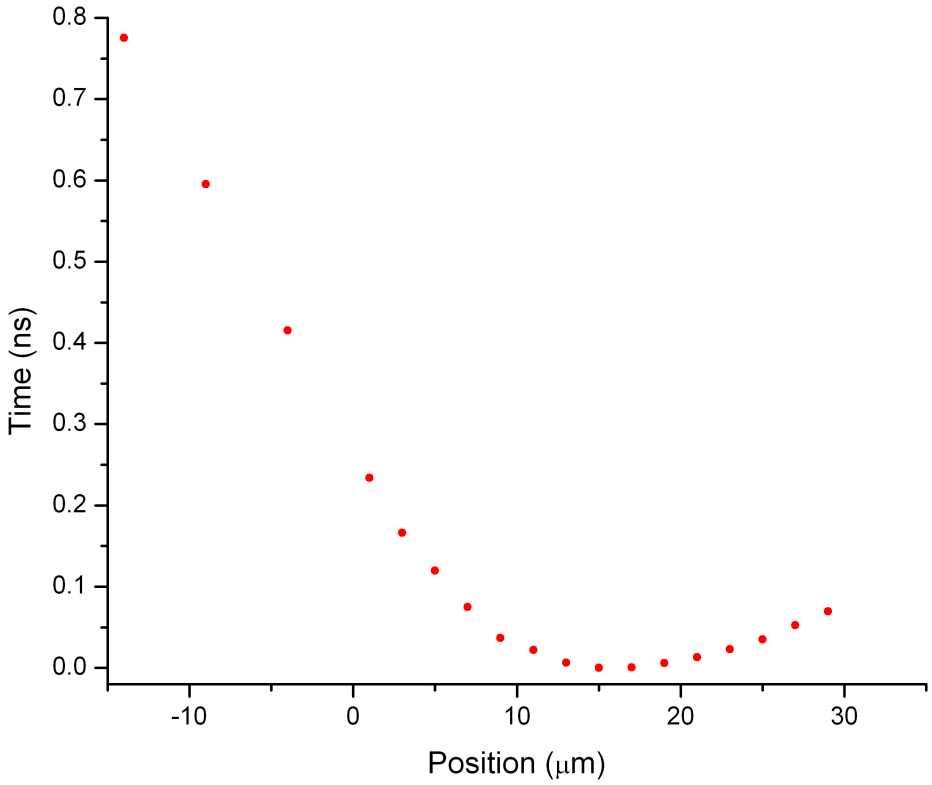

Figure 6.22 *Device pulse arrival time as a function of position along y of the 1700 nm wavelength laser spot for the n-i-p structure.*

The pulse arrival time has a minimum (position 15 μm in Figure 6.22) when the laser spot is positioned on the edge of the device, this is due to electrons being directly generated in the i-region. Moving away into the p-region, the delay in the pulse arrival time increases.

The pulse arrival time for the p-i-n and n-i-p structures are compared in Figure 6.23. It is possible to observe that the delay as a function of distance increases much faster when we moved the laser spot away from the p-i-n than n-i-p device. This is due to a much shorter diffusion length (two order of magnitude less [9]) for holes with respect to that for electrons.

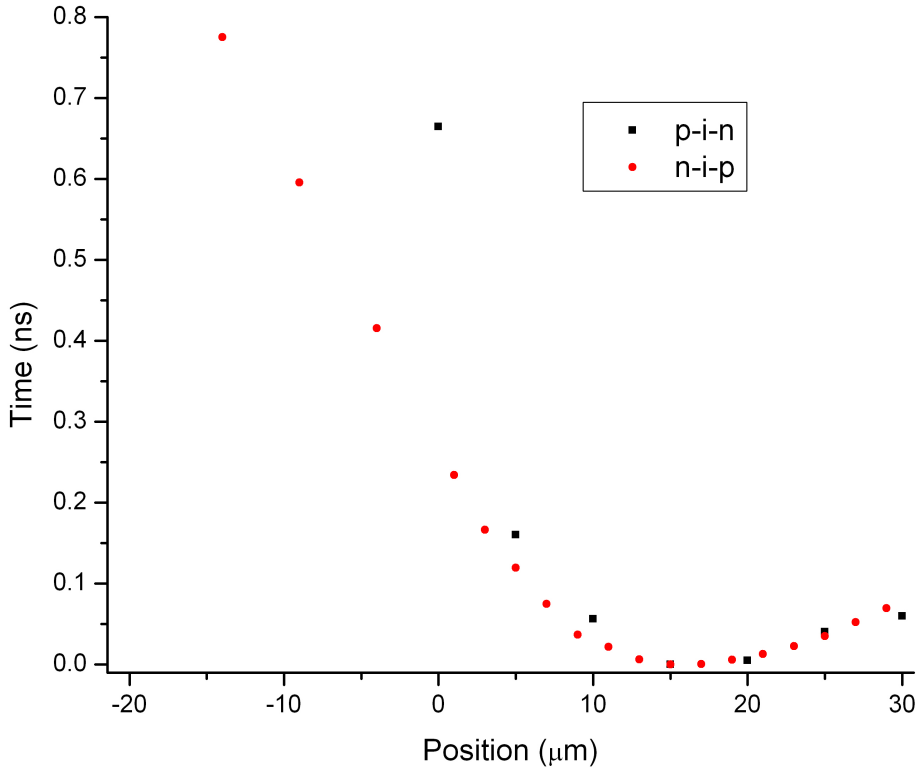

Figure 6.23 *Comparison of the device pulse arrival time as a function of laser spot position along y for p-i-n (black squares) and n-i-p (red circles) structures. 1700 nm wavelength radiation was used.*

Both devices show a minimum time for edge illumination, with a small increase in arrival time delay moving to the top of the mesa, as explained previously.

6.3.2.5 Study of the InAs device output pulse as a function of laser power and reverse bias

A study of the device output pulse height as a function of the different reverse bias voltages (and therefore different gains) was conducted to find the minimal laser power detectable by the detector. The laser power was decreased until the timing card collected 1 second histograms with only around 10 counts in total. With this total number of counts, the output pulse arrival time of the device can be estimated at each voltage with good precision. At every voltage 10 successive histograms were recorded showing a calculated arrival time standard deviation as high as 0.019 ns. Figure 6.24 shows the minimum laser power detectable by the p-i-n (illuminated at the top) structure at different voltages and at 1700 nm wavelength.

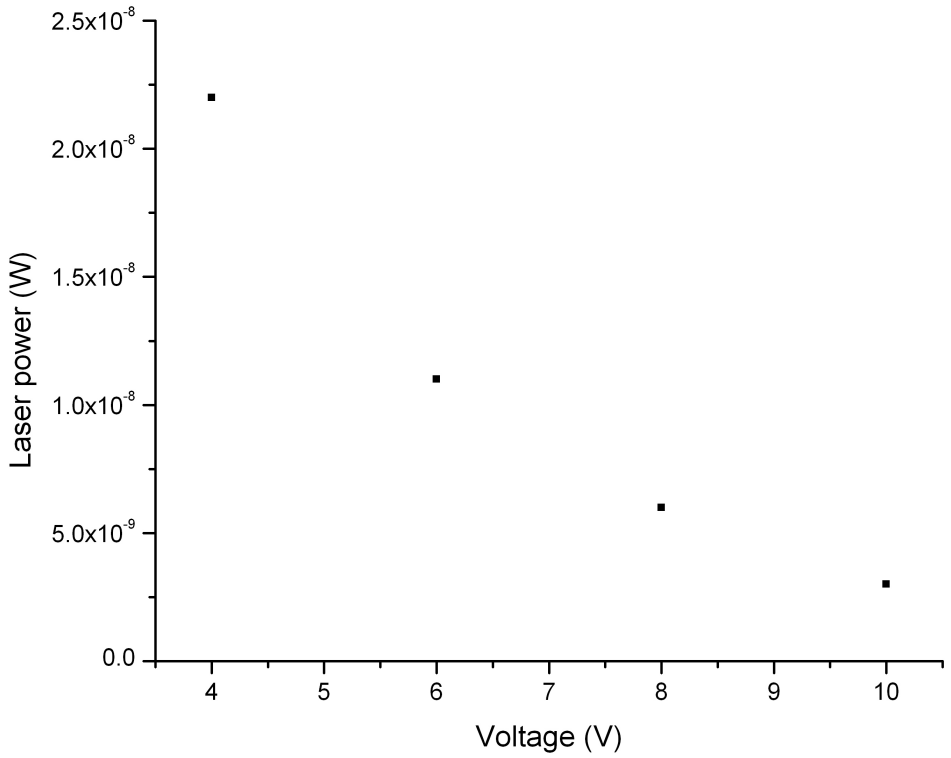

Figure 6.24 *Laser power, corresponding to around 10 counts in total in the 1 second histogram, as a function of reverse bias at 1700 nm wavelength for the p-i-n structure.*

The laser power required for around 10 counts per second in total in the histogram, decreases with an increasing reverse bias voltage, because the multiplication is higher: a multiplication bigger than 7 was estimated above 7.5 V from the previous measurements. From 4 V to 6 V a decrease in laser power of a factor of 2 is observed;

this result is in accordance with the increase in responsivity (same factor of around 2) observed in Figure 6.15 at the same voltages. At 10 V, a laser power as low as 3 nW was measured at the cryostat window so as to ensure the 10 counts per second in the histogram. This laser power corresponds to around 1×10^5 photons per pulse [N.B this is still very far from single photon regime]. Because of the loss in the laser power due to reflections from the two quartz cryostat window surfaces, the number of photons per pulse is overestimated. A higher working voltage can drastically decrease the number of photons per pulse needed. Unfortunately, random breakdown limited our measurements, so higher voltages and the higher associated gain were not available. As previously shown, a reduction in operating temperature would not solve this problem, as the high dark current would not allow for the increase in voltage required for higher gain.

A similar study was conducted for the n-i-p structure (illuminated at the edge). Because of the higher dark current and the lower gains in the photodiode, higher laser powers were needed to have the 10 counts per second in the histogram. Figure 6.25 shows the minimum laser power detectable by the n-i-p structure at different voltages and at 1700 nm wavelength.

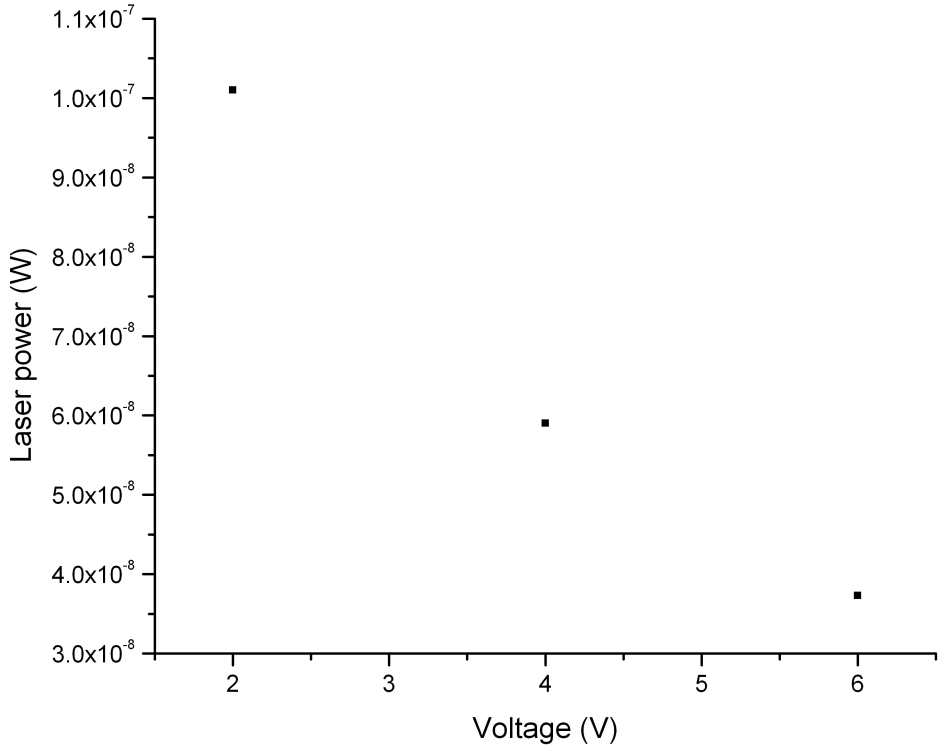

Figure 6.25 *Laser power corresponding to around 10 counts in total in the 1 second histogram, as a function of reverse bias voltage at 1700 nm wavelength for the n-i-p structure.*

The laser power required for around 10 counts in total in the 1 second histogram decreases with an increasing reverse voltage. At 6 V, a laser power as low as 37.3 nW was measured at the cryostat window so as to ensure the 10 counts per second in the histogram. The laser power needed for the n-i-p structure is much higher with respect to the p-i-n structure. This is due, firstly, to higher dark current observed in the n-i-p than the p-i-n structures: higher power is needed so that the diode output pulse was above the noise level; and secondly, because of the lower gain of the n-i-p. At 6 V a gain of 2.6 was measured for the n-i-p against 4.8 for the p-i-n. The laser power for the p-i-n and n-i-p structures are compared in Figure 6.26.

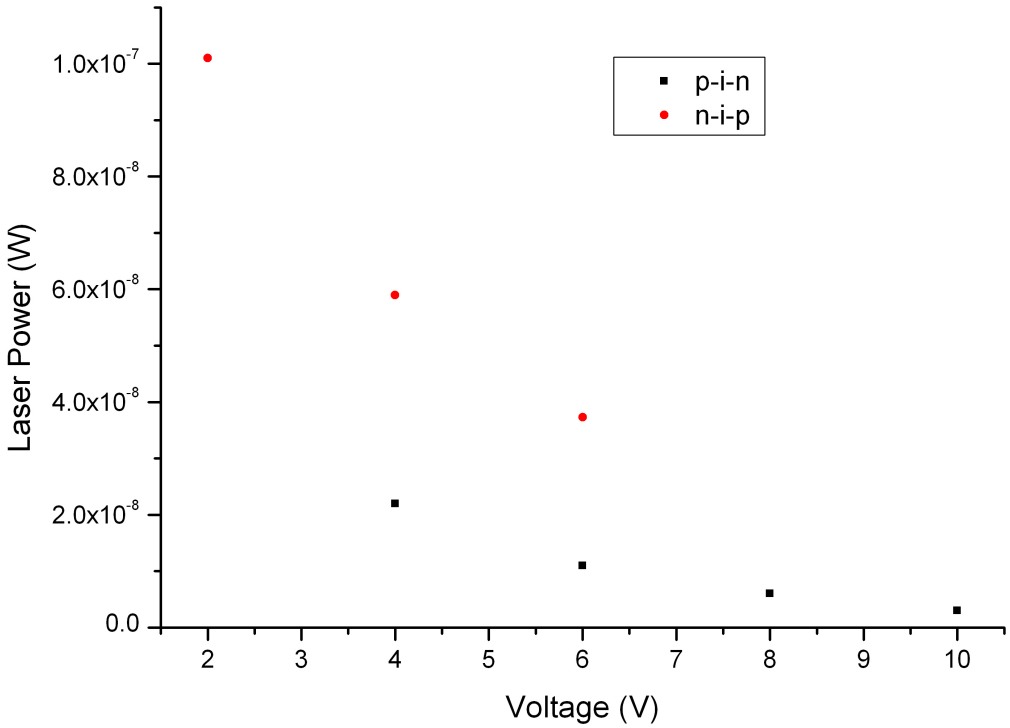

Figure 6.26 *Comparison of laser power required for p-i-n (black squares) and n-i-p (red circles) structures to have 10 counts in total in the 1 second histogram collected by the timing card. 1700 nm wavelength radiation was used in both case.*

The lower dark current and higher gain associated with the p-i-n structure make it more suitable for the ranging measurements described below. However, for these studies the p-i-n was not available, and as such a n-i-p device was used.

6.4 Ranging experiments using n-i-p photodiodes

Wavelengths where the solar background is negligible (i.e. near- to mid-infrared) are very attractive for LIDAR, and detectors based on narrow bandgap materials, such as InAs, are highly desirable for this purpose. We performed a laboratory based LIDAR experiment, with ranges of around 0.5 metres stand-off distance, with InAs n-i-p photodiodes, demonstrating time-of-flight measurements at wavelengths up to 2.37 μm.

6.4.1 Experimental set up

Figure 6.27 shows a schematic of the experimental set up along with a photograph of the optical arrangement in the lab used for these time-of-flight ranging experiments. The pulsed laser is directed through a 50:50 beam splitter and to the centre of a movable retroreflector that can be moved along the optical axis by a distance of about 0.4 m. The beam returning from the retroreflector is then reflected by the beam splitter and directed onto the sample within the cryostat using an imaging system with an M5 objective lens (focal length 36 mm), L2. White light imaging on the IR camera, to view both sample details and the laser focus position, is achieved via two beam splitters P1 and P2 (reflectance 8% transmittance 92%). In the photograph of Figure 6.29, the different arrangements of the laser output - depending on whether the supercontinuum laser is used with the AOTF (blue circle) or with the system of filters (green circle) - are shown.

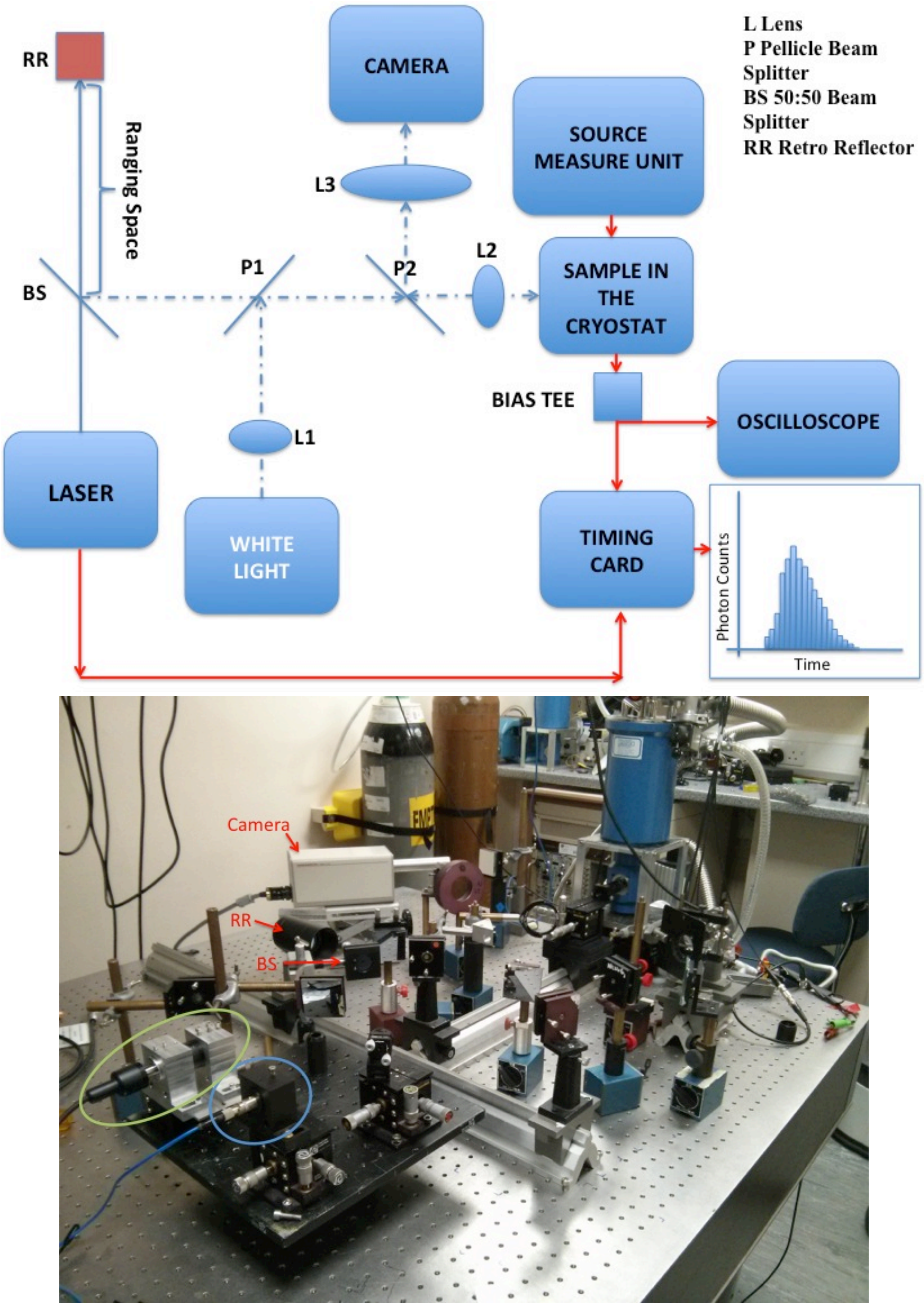

Figure 6.27 *Top, diagram of the ranging set up. The dashed blue line shows the free space optical path while the continuous red line shows the electrical connections. The main components are the supercontinuum laser, the beam splitter, the retroreflector and the cryostat where the sample is placed. White light is coupled into the system (via beam splitters P1 and P2) to image the sample onto an infrared camera. The sample is reversed bias by the SMU and its output pulse, after passing through a bias tee to filter the DC dark current, is analysed with a GHz oscilloscope or a timing card. Bottom, photograph of the lab bench where the ranging experiment was set up. The blue and green circles represent the different laser output arrangements: AOTF and filters, respectively.*

During the experiment the retroreflector is moved along the optical axis over a distance of about 0.4 m: starting from the position near the beam splitter, the retroreflector was moved at 2-5 cm steps over a distance of between 16 cm and 40 cm giving a laser path effective distance of between 32 cm and 80 cm. The different beam path lengths result in a delay of the output pulse from the diode. This delay is recorded in the timing card that builds up a histogram for each position. The retroreflector's scan was performed for different wavelengths in the infrared spectral range from 1.3 to 2.37 μm.

6.4.2 Ranging measurements

At room temperature the 100 μm diameter n-i-p device was reverse biased and illuminated using the pulsed laser with a repetition rate of 40 MHz. For each wavelength, the optical alignment of the beam path was adjusted to maximise the photocurrent through the device at 0 V reverse bias. The diode was then reverse biased to give sufficient gain without catastrophically increasing the dark current. Since at this stage photon counting was not studied, initially the optical power of the laser was chosen to give a definitive pulse above the noise level of the device; however at increasing wavelength access to higher power was limited by the supercontinuum, as shown in Table 6.3. Pulses from the n-i-p diode were sent to the timing card for collection onto a histogram to give a peak whose position related to the collective timing of the pulses. The timing card CFD threshold trigger level was selected, in relation to the output pulse peak height, to provide minimal FWHM of this histogram peak. The histogram acquisition times were kept between 5 and 20 s to achieve a clean measurement of the temporal response with approximately the same total number of counts (around 10^6).

Wavelengths (μm)	Average laser power at the cryostat window (μW)
1.3	26.4
1.55	17.3
1.7	12.8
1.8	8.4
1.9	Less than 8.4
2.0	30
2.1	30
2.2	3
2.3	3
2.37	1

Table 6.3. *Laser optical power used during the ranging experiment at each wavelength analysed. The inaccurate reading at 1900 nm is due to the low sensitivity of the InGaAs optical power-meter at this wavelength. The optical power of the laser was chosen to give a definitive pulse above the noise from the device. The timing card CFD trigger level was selected so as to provide minimal FWHM of this histogram peak.*

The increase in power observed in the Table 6.3 at 2 μm wavelength is due to the change from the AOTF wavelength selection method to the use of optical filters described above. The higher bandwidth of the filters provided higher throughput.

Histograms were collected to estimate the peak whose position is related to the collective timing of the device pulses. A typical clean histogram from the timing card is shown in Figure 6.28, corresponding to the time response of the system when it is illuminated by the laser at 2.1 μm wavelength and reverse biased at 2.5 V.

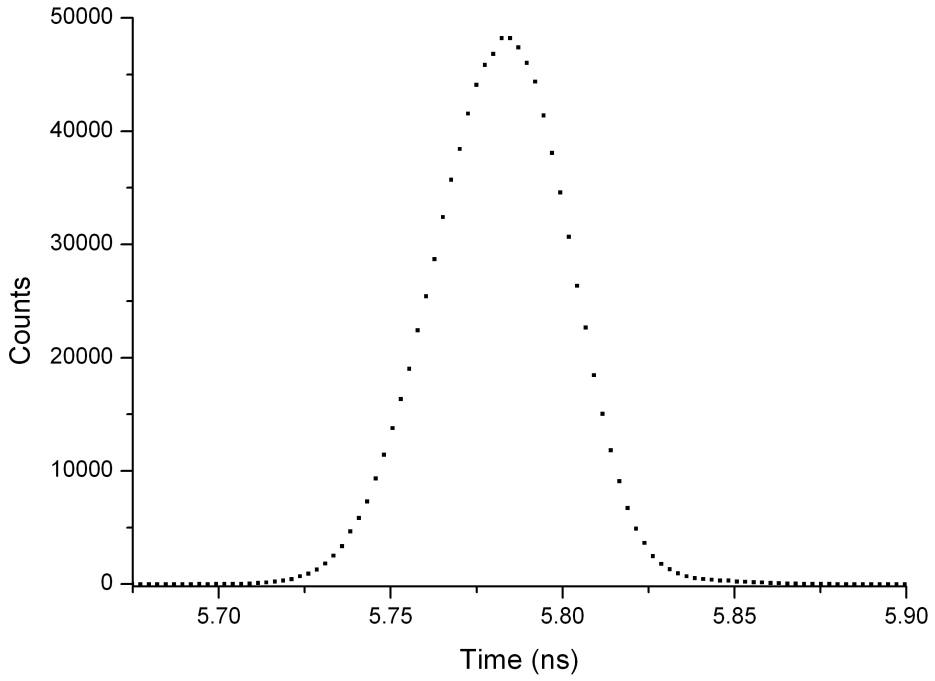

Figure 6.28 *Histogram collected by the timing card of the time response of the 100 μm diameter diode when it is illuminated by the laser at 2.1 μm wavelength and reverse biased at 2.5 V.*

A typical smooth and regular histogram recorded by the timing card with a collection time of 7 s is shown in Figure 6.28. In this case, the shape of the system temporal response is nearly Gaussian. Figure 6.29 shows the same data with a Gaussian fit.

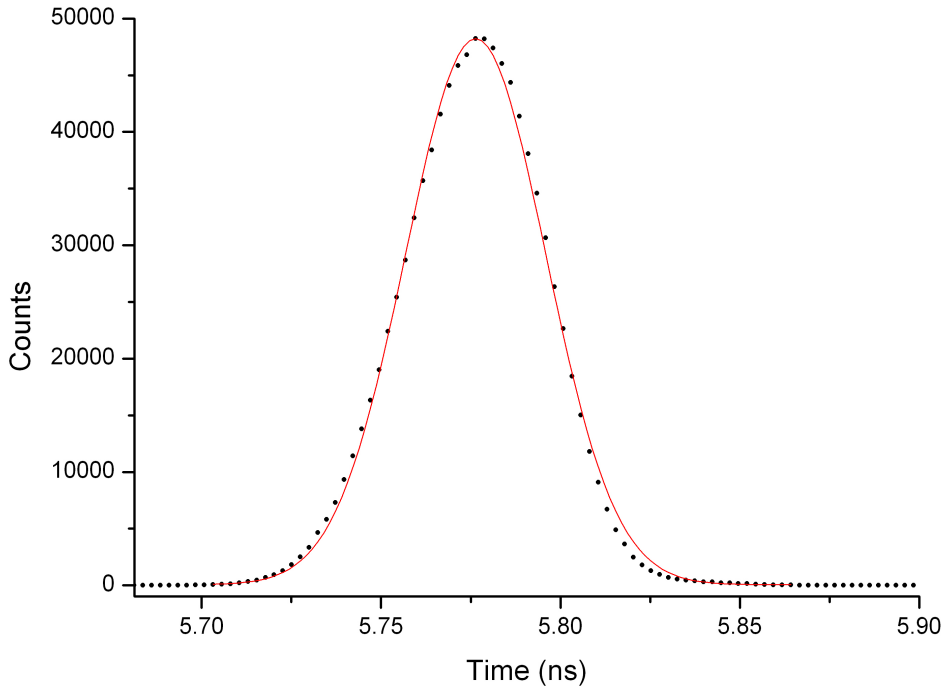

Figure 6.29 *Gaussian fit to the histogram collected by the timing card of the time response of the 100 μm diameter diode when it is illuminated by the laser at 2.1 μm wavelength and reverse biased at 2.5 V.*

The centroid of this histogram corresponds to the arrival time of the photons, this time is proportional to the light path, so by increasing the distance between the retroreflector and the beam splitter, the distribution within the histogram is shifted and a delay in time can be observed.

For the histogram presented in Figure 6.28 the peak centroid estimated is 5.78172 ns. The centroid of the peak for every distance at each wavelength, is given by equation 6.1. The standard deviation associated to the calculated arrival time is given by [8]:

$$\sigma_t = \sqrt{\frac{\sum_k n_k (t_k - \bar{t})^2}{N-1}} \tag{6.2}$$

From the standard deviation σ_t the FWHM of the distribution can be calculated:

$$\text{FWHM} = 2.35\,\sigma_t = 0.046 \text{ ns} \tag{6.3}$$

The calculated centroid and FWHM from the Gaussian fit shown in Figure 6.29 are 5.77637 ns and 0.046 ns respectively.

The FWHM, calculated using equation 6.3, corresponds to the timing jitter of the system; for high laser power and low gain it is as low as 46 ps. The jitter of the system, τ_s, takes into account the jitter of the InAs device (τ_d) as well as the jitter of the timing card (τ_{tc}) and the laser (τ_l).

$$\tau_s^2 = \tau_l^2 + \tau_{tc}^2 + \tau_d^2 \tag{6.4}$$

In order to achieve this small FWHM, a high CFD threshold voltage in the timing card was set. This ensures both the system noise floor and the noise on the detector output cannot influence the measurements and temporally spread the histogram. In the measurements shown in Figure 6.28, the threshold CFD voltage was set at around 15 mV.

Similar or even lower FWHM values are expected for a top illuminated p-i-n diode where pure electron injection is achieved and the avalanche process is more deterministic. In this type of structure, only electrons can undergo impact ionisation, and thus secondary holes cannot provide feedback to create new electrons (i.e. β=0). The avalanche, therefore, builds up in only one transit though the depletion region and so a similar timing jitter should be observed even at higher gain. Due to the high dark current of the n-i-p diode studied, it was not possible to reverse bias the diode to high voltage and so reach high gain and study any variation in the FWHM values.

Unfortunately it was not possible to keep the CFD threshold to high voltage values during all the experiments. When weak signals from the diode are observed due to the low power incident on the detector, the threshold was decreased down to a minimum of 5.02 mV, which happened in particular for the longest wavelengths analysed. The decrease in pulse height to the approximate level of the CFD threshold significantly decreases the number of pulses collected onto the histogram as shown in Figure 6.30.

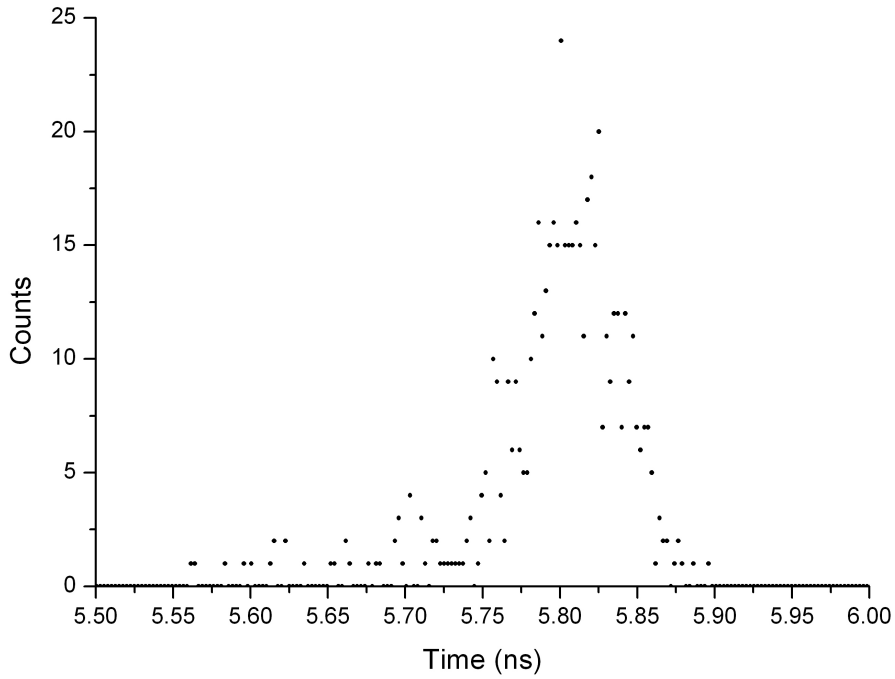

Figure 6.30 *Histogram collected by the timing card of the time response of the 100 μm diameter diode when it is illuminated by the laser at 2.37 μm wavelength and reverse biased at 6.5 V. The retroreflector position was 67 cm along the ranging track.*

A typical histogram with a low number of counts (in this case, around 500) recorded by the timing card is shown in Figure 6.30 with a collection time of 20 s. In this case, the Gaussian shape of the system temporal response is not so evident. The calculated centroid of the histogram is 5.7981 ns. Longer duration measurements are needed to collect a larger number of counts, or alternatively, a higher gain could be used to increase the number of device pulses to be above the 5 mV threshold of the timing card. Even with lower counts the time response of the detector can be calculated with precision using equation 6.1.

Another method for locating arrival time is by performing a cross correlation between the histogram and the instrumental reference signal of the system [10]. The cross correlation function measures the similarity between the two signals and can be calculated using equation 6.5.

$$C(t)=ifft\,(F_{ref}\,G^{*}) \tag{6.5}$$

where *ifft* is the inverse fast Fourier transform, F_{ref} is the Fourier transform of the instrumental reference and G^* is the complex conjugate of the Fourier transform of the histogram studied. It essentially calculates the integral of the product of the two signals.

Figure 6.31 shows the cross correlation method applied to the lowest counts histogram (retroreflector position around 16 cm away from the beam splitter) at 2370 nm wavelength. The histogram recorded at the nearest position from the retroreflector was used as reference signal. The cross correlation curve has a Gaussian shape with a well defined centroid.

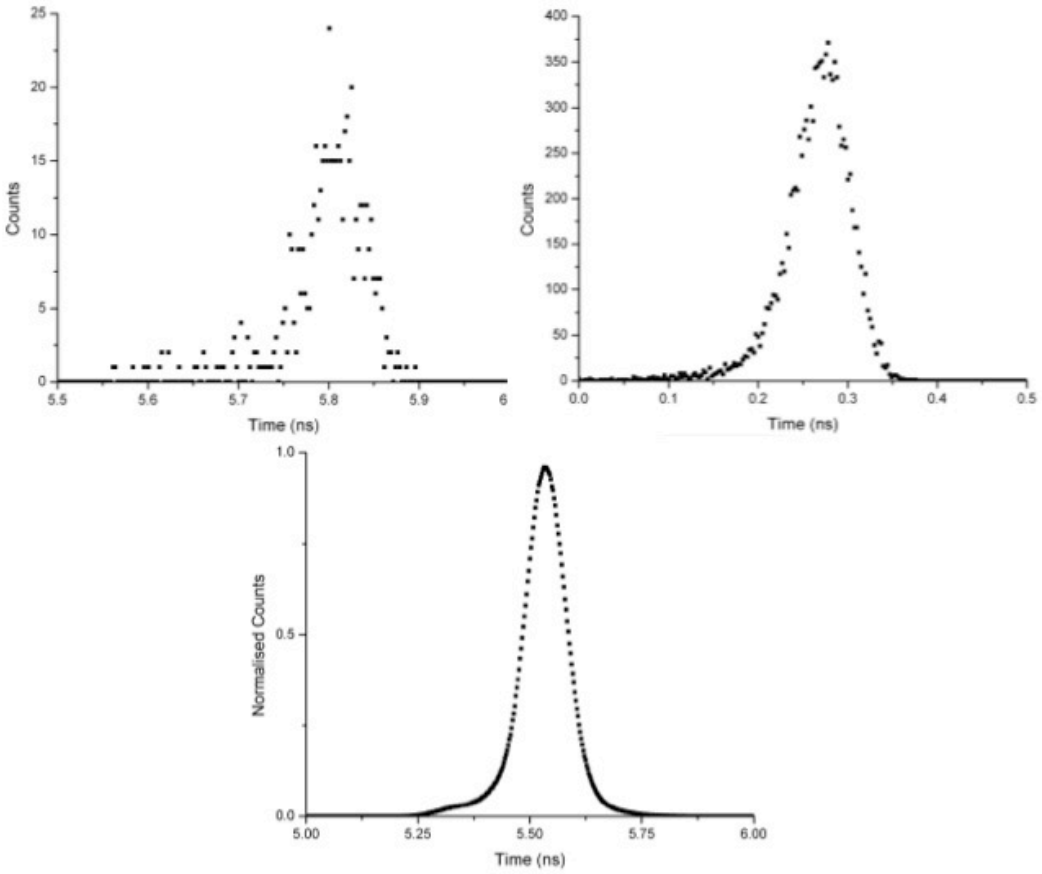

Figure 6.31 *Illustration of the cross correlation method. Top left, a low count histogram collected by the timing card when the laser at 2370 nm wavelength illuminates the diode and the retroreflector is placed 67 cm along the ranging track. Top right, reference signal used to perform the cross correlation. Bottom, histogram after the cross correlation process.*

6.4.3 Measuring the speed of light

Illuminating the n-i-p structure with light at wavelengths in the range 1.3 to 2.37 μm, a study of the output pulse arrival time as a function of the retroreflector position has been conducted. Figure 6.32 shows a typical graph related to this study; in this specific case, radiation at 2.3 μm wavelength is shone on the device.

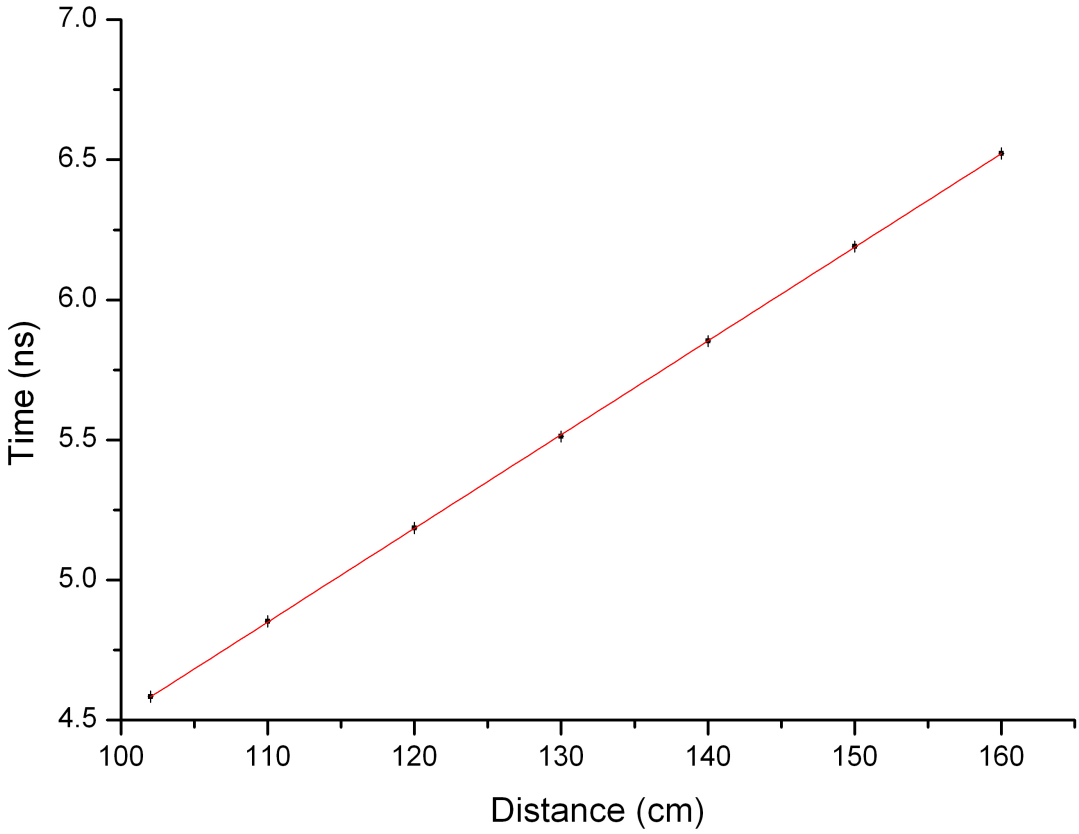

Figure 6.32 *Analysis of the variation in time of diode output pulse arrival as a function of retroreflector position. In this case, light at 2.3 μm wavelength was shone on a n-i-p structure.*

Graphs similar to Figure 6.32 have been plotted and studied for all of the wavelengths analysed.

In the graph 6.32, errors bars for distance and time have to be included for every point because different error sources are present in the system and consequently can influence the measurements. The position of the retroreflector along the metal track could affect the data: even if the track has a mm scale along its length to help positioning, a 0.5 mm (1 mm return) ranging error has to be associated at every distance. A further source of error is due to instability of the laser, which can affect the pulse arrival time: the error in

repeating measurements at fixed laser spot position on the sample was found to be around 2 ps. This value has been calculated from the standard deviation associated with 40 repeating pulse arrival time readings taken over a time of 40 minutes.

The main error in our data is related to a problem with our set up: movements in the retroreflector position result in small lateral movements of the laser spot across the edge of the n-i-p sample due to an imperfect alignment of the system. Since the laser spot is positioned on the edge of the device, slight movements in the laser spot position cause the electron–hole pairs to be created in different device regions. This results in different times for the avalanche to be built up and the output pulse be detected. This problem can be overcome by using light incident vertically on the top of the mesa: in this case, even if the laser spot is moved across the mesa, the electron-hole pairs are created in the same region, the distances the injected carriers need to diffuse to reach the multiplication region will be identical and the time the avalanche output pulses are detected will remain unchanged. However, for an n-i-p structure top mesa illumination is not convenient as only very low gain can be achieved with hole injection. Furthermore, the n-i-p structure analysed in this thesis did not allow top illumination as gold was deposited over all the top of the mesa. P-i-n structures are instead suited for top mesa illumination and are not strongly affected by the alignment error. As shown in Figure 6.21, small movements in the laser spot position on the top of the mesa do not affect the pulse arrival time in a p-i-n structure. During the ranging experiment only the n-i-p structure was available, so all the pulse arrival time values are subject to the error due to the laser spot position drifting. This error was measured to be around 40 ps.

The speed of light can be calculated by determining the time-of-flight over known distances. By using a number of retroreflector positions it was possible to determine the speed of light from the gradient of graphs like the one shown in Figure 6.32.

During the ranging experiment, the retroreflector was scanned over a distance of around 30-40 cm for wavelengths from 1.3 to 2.3 μm, however at 2.37 μm wavelength, the range was limited to only 16 cm because of limitations in source power. As mentioned above, the lateral drift of the laser spot gives a 40 ps error in time that influences our calculated speed of light. This error can cause a discrepancy in the calculation of the speed of light between $v_{min}=2.952\times10^{8}$ ms^{-1} and $v_{max}=3.042\times10^{8}$ ms^{-1} or $v_{min}=2.909\times10^{8}$ ms^{-1} and $v_{max}=3.107\times10^{8}$ ms^{-1} over a distance of 80 cm or 32 cm, respectively.

Table 6.4 summarises the different values of the speed of light obtained for the different wavelengths at which the experiment was performed. The determined speeds of light are all within the experimental errors calculated above, depending on the wavelengths analysed.

Wavelengths (μm)	Experimental Speed of Light (ms^{-1})
1.3	2.976×10^{8}
1.55	2.971×10^{8}
1.7	3.016×10^{8}
1.8	3.005×10^{8}
1.9	3.007×10^{8}
2.0	3.020×10^{8}
2.1	2.955×10^{8}
2.2	2.981×10^{8}
2.3	2.991×10^{8}
2.37	3.051×10^{8}

Table 6.4 *Speed of light values obtained at different wavelengths. All the values are within the calculated experimental errors: for wavelengths from 1.3 to 2.3 μm the determined speeds of light are all between* $v_{min}=2.952\times10^{8}\ ms^{-1}$ *and* $v_{max}=3.042\times10^{8}\ ms^{-1}$*; while for 2.37 μm wavelength the determined speed of light is between* $v_{min}=2.909\times10^{8}\ ms^{-1}$ *and* $v_{max}=3.107\times10^{8}\ ms^{-1}$.

The speed of light at 2370 nm wavelength was also calculated performing the cross correlation method for locating arrival time. This wavelength gave the smallest number of counts in the histogram. No significant improvement using the cross-correlation technique was found. This is because all the histogram counts come from the detector response to the laser pulse and no dark counts are present.

6.5 Conclusions

InAs p-i-n and n-i-p structures were mainly characterised at wavelengths 1700 nm and 2000 nm; dark currents, multiplication, responsivity and detector output pulse arrival time were studied at room temperature. The study of multiplication as a function of

laser position and wavelength for both the p-i-n and n-i-p structures shows higher gains when pure electron injection, instead of mixed injection, is achieved. The top illuminated p-i-n structure, can give gains greater than 9 at 9 V. The output pulse arrival time is approximately constant at every laser spot position on the top of the mesa. Because the electron-hole pairs are created in the same region of the device, the distances that the injected carriers need to diffuse to reach the multiplication region are similar and the avalanche output pulses can be detected at similar times. Low laser power was used to illuminate the p-i-n structure. At 10 V, a laser power as low as 3 nW was measured at the cryostat window to give 10 counts per second in the histogram collected by the timing card. This laser power corresponds to around 1×10^5 photons per pulse- still very far from the single photon regime. A higher working voltage can drastically decrease the number of photons per pulse needed. Unfortunately, random breakdown limited our measurements, so higher voltages and the higher associated gain were not available. P-i-n structures were not obtainable during the ranging experiment.

In summary, for the first time, laboratory based LIDAR experiments, with ranges of around 0.5 metres stand-off distance, were performed with InAs n-i-p edge illuminated photodiodes, demonstrating time-of-flight measurements at wavelengths up to 2.37 μm. The system alignment limits the precision of the data taken: small mis-alignments in laser spot position were observed as the retroreflector was moved. The position of the laser spot on the edge of the device can dramatically change the injection profile introducing an error; an error in pulse arrival time of around 40 ps, that corresponds to a 6 mm ranging error, was observed in our measurements. The speed of light calculated was mainly subject to this error. A total system jitter of less than 50 ps has been observed in the n-i-p InAs devices at room temperature and at low gain. The experiment can be improved using p-i-n structures under top illumination. In this case high gain can be achieved from pure electron injection and the pulse arrival times are not strongly affected by the alignment resulting in a decrease of the ranging error.

6.6 References

[1] E. Browell, S. Ismail, and W. Grant, "Differential absorption lidar (DIAL) measurements from air and space," *Applied Physics B,* vol. 67, pp. 399-410, 1998.

[2] M. Diagne, M. Greszik, E. Duerr, J. Zayhowski, M. Manfra, R. Bailey*, et al.*, "Integrated array of 2-μm antimonide-based single-photon counting devices," *Optics express,* vol. 19, pp. 4210-4216, 2011.

[3] A. R. Marshall, J. P. David, and C. H. Tan, "Impact ionization in InAs electron avalanche photodiodes," *IEEE Transactions on Electron Devices,* vol. 57, pp. 2631-2638, 2010.

[4] A. Marshall, C. Tan, M. Steer, and J. David, "Electron dominated impact ionization and avalanche gain characteristics in InAs photodiodes," *Applied Physics Letters,* vol. 93, pp. 111107 1-3, 2008.

[5] P. J. Ker, A. R. J. Marshall, A. B. Krysa, J. P. R. David, and C. H. Tan, "Temperature Dependence of Leakage Current in InAs Avalanche Photodiodes," *IEEE Journal of Quantum Electronics,* vol. 47, pp. 1123-1128, 2011.

[6] NKT Supercontinuum. Data Sheet http://www.nktphotonics.com/superk_extreme_specifications?cid=7856.

[7] A. R. J. Marshall, "The InAs electron avalanche photodiode and the influence of thin avalanche photodiodes on receiver sensitivity," *PhD Thesis,* 2009.

[8] J. Taylor, "Introduction to error analysis, the study of uncertainties in physical measurements vol. 1", 1997.

[9] IOFFE. Diffusion Coefficients http://www.ioffe.ru/SVA/NSM/Semicond/InAs/electric.html.

[10] ORIGIN Lab. Cross Correlation http://www.originlab.com/doc/Origin-Help/Corr1-Algorithm

Chapter Seven

7. Conclusions and future work

7.1 Conclusions

The ability to detect light efficiently in the near infrared is becoming increasingly important for many emerging applications. Gas sensing, defence/geoscience ranging, clinical thermography, rocket plume detection, and industrial manufacture monitoring all rely on detection in this spectral region.

In many of these applications, the optical signal on the detector is very weak due to high levels of optical loss during the transmission of light. For detection of such low level radiation, APDs or SPADs can be used to provide internal gain due to the impact ionisation phenomenon.

In the infrared range above 1.7 μm, type II semiconductor superlattices, HgCdTe and InSb photodetectors are promising technologies. Another material that allows detection up to a wavelength of 3.5 μm that has shown excellent electron multiplying behaviour is InAs.

InAs is a III-V narrow bandgap material allowing, due to its band structure, single carrier impact ionisation: electron impact ionisation dominates the avalanche multiplication so that holes effectively play no role. The behaviour of InAs can be explained by consideration of the confinement of electrons in the first conduction band Γ valley. Due to high X and L valley separation energies with respect to the Γ valley minimum and the low phonon scattering in InAs, the electrons can impact ionise within the Γ valley at moderate electric fields. While the electrons can easily acquire the required energy for impact ionisation, the holes cannot: the relatively flat heavy hole band limits the rate at which holes can gain energy. This contrast leads to preferential electron impact ionisation (the electron impact ionisation coefficient α is much greater than the hole impact ionisation coefficient β). Such single carrier type dominated multiplication leads to a low excess noise factor.

InAs detectors were provided by the University of Sheffield and characterized at Heriot-Watt University. Such a narrow bandgap detector unfortunately suffers from high dark currents mainly due to surface leakage problems.

To achieve the best InAs detector performance, a good passivation layer deposited on top of the InAs devices is essential to protect the sample surface without increasing the surface leakage current. This dielectric layer is also crucial for the deposition of the device's external bond pads to avoid stressing during device packaging.

SiN and Al_2O_3 have been studied as passivation materials. Good quality layers of hundreds of nm of SiN and Al_2O_3 have been deposited. Current-voltage characteristics for both these coated samples exhibited increased dark current that compromises device performances. Despite SiN not being ideal for passivation purposes, it can be used under external bondpads giving a high bonding yield. A new mask set was been designed to combine the excellent passivation properties of SU8 with SiN.

For the first time, II-VI semiconductors have also been studied as possible passivation layers on InAs mesa photodiodes. Pre-growth surface oxide removal processes were developed to improve surface morphology of II-VI layers grown on InAs samples. The commonly used heat cleaning oxide removal can damage an InAs mesa photodiode because of the high temperatures involved so an alternative chemical treatment was successfully developed. A combination of 1:1:1 H_3PO_4, H_2O_2, H_2O and 1:8:80 H_2SO_4, H_2O_2, H_2O solutions remove the oxide layer from InAs and produce a clean surface; a $(NH_4)_2S_x$ (ammonium polysulphide) solution has then been used so as to allow a sulphur layer to form on the sample surface preventing any re-oxide formation. During the sulphur step, the samples were left 1 hour at 21 ˚C in the $(NH_4)_2S_x$.

For the first time high quality single crystal II-VI passivation layers were grown on InAs mesa structures. ZnSe, ZnTe, CdSe and CdMgSe layers of hundreds of nm have been grown in collaboration with the II-VI group at Heriot Watt University and the City College of New York. PL, XRD, AFM and SEM analysis were succesfully carried out on the samples grown. ZnSe and ZnTe successfully terminate the InAs mesa devices preventing atmospheric oxidation. Negligible surface leakage currents are observed at low bias and at room temperature for both materials. We have shown that packaged ZnSe and ZnTe mesa photodiodes can be produced. The growth of CdMgSe on top of mesa samples is

still a challenge. The PL peak indicates chemical instability in this ternary compound over time. CdMgSe-passivated InAs mesa samples have not yet been demonstrated.

LIDAR at a wavelength where the solar background is negligible (i.e. in the NWIR and MWIR bands) is very attractive, and detectors based on narrow bandgap materials, such as InAs, are highly desirable for this purpose.

For the first time, laboratory based LIDAR experiments, with ranges of around 0.5 metre stand-off distance, were performed with InAs n-i-p edge-illuminated mesa photodiodes, used in linear multiplication mode, demonstrating time-of-flight measurements at wavelengths up to 2.37 μm. Here, the laser beam was incident on the edge of the device (rather than the top of the mesa) in order to achieve a mixed carrier injection and thus higher gain. A problem with the system alignment limits the precision of the data taken; because the laser spot is incident on the edge of the device, any slight shifts in the laser position can dramatically change the injection profile causing a 6 mm ranging error. A total system timing jitter of less than 50 ps has been observed in the n-i-p InAs devices at room temperature and at low gain.

The experiment can be improved using p-i-n structures under top illumination. In this case, high gain can be achieved from pure electron injection, and the pulse arrival time is not strongly affected by the alignment resulting in a decreasing of the ranging error. High gain allows the use of low laser power to illuminate the structure. At 10 V, a laser power as low as 3 nW was measured at the cryostat window so as to ensure the 10 counts per second in the histogram collected by the timing card. This laser power corresponds to around 1×10^5 photons per pulse [N.B. still very far from the single photon regime]. A higher working voltage can drastically decrease the number of photons per pulse needed. Unfortunately, the p-i-n structure characterised does not allow this because of its high dark current. The decreasing in the alignment error is due to an approximately constant detector output pulse arrival time for every laser spot position on the top of the mesa: because the electron-hole pairs are created in the same region, the distances that the injected carriers need to diffuse to reach the multiplication region are similar and the avalanche output pulses can be detected at similar times.

7.2 Future work

Further improvement in InAs technology must be made so as to reach the single photon regime. To achieve this goal having a dark current as low as possible is a key factor. Although significant advances in dark current suppression have been achieved after the studies in this thesis, further improvements are essential for low level radiation detection.

Due to its electron impact ionisation characteristics, InAs gives the possibility of achieving high gain at low electric fields and to work in linear mode operation with potential for photon number resolving technology. This ability to detect more than one photon could be very useful in such applications as characterization of nonclassical light sources (for example single photon [1] or *n*-photon [2]) and in quantum information studies [3]. Furthermore, since the device will not have a self-sustaining avalanche, the absence of long reset times associated with external quenching circuitry could result in potentially very high maximum count rates. High count rates are crucial for quantum imaging applications (to help reduce acquisition times) and in quantum key distribution (QKD) where high data transmission rates are dependent on fast detector systems [4]. The ability to perform QKD at wavelengths longer than 1550 nm will be of importance to the extension of communications bandwidths, and also has the potential to be used in free space communications, where atmospheric transmission is key.

Following Chapter 5, further passivation investigations have to be conducted on the ZnSe- and the ZnTe-passivated mesa samples so as to study the detector dark currents at low temperatures. Multiplication analyses can also be conducted to see if *M*, as expected, is unaffected by the passivation process. The growth of CdMgSe on InAs is still a challenge. The complexity of a ternary compound has to be investigated in more detail with particular attention to the chemical instability over time. For this reason new CdMgSe samples have to be grown, and periodic analysis has to be conducted on the samples so as to study the alloy evolution with time. The present results show that after 6 months from the growth, a shift to higher energy (2.26 eV) of the PL peak was observed for all the CdMgSe samples. The phase separation process can result in creation of CdSe quantum wells confined by MgSe barriers. These wells could be aligned along the stacking fault plane (where the stacking fault is a one- or two- layer interruption in the stacking sequence). The change from the wurtzite to the zincblend crystal structure, can cause strain and build up of an intrinsic electric field [5]. This

electric field can cause band bending in the neighbourhood of the quantum well providing enough energy for the electrons to tunnel to a CdSe quantum well excited state. The luminescence from such CdSe quantum wells can be observed. A PL experiment as a function of an external electric field has to be conducted, so as to see if the PL CdMgSe peak returns to its original value at a particular applied electric field.

This new idea to use II-VI layers for passivation techniques can be extended to every III-V semiconductor-based device.

Following on from Chapter 6, the experiment should first be repeated with a p-i-n detector, to achieve the highest possible timing accuracy by removing the error associated with edge illumination. The LIDAR experiment can then be modified by substituting the retroreflector with a non-cooperative target to simulate a more realistic scenario. Spatial information can also be obtained either by scanning mirrors to move the beam across the target [6] or by using structured illumination techniques [7] so as to build up a depth image of the target. Once single photon sensitive InAs detectors become available, this would vastly increase the ability of the LIDAR system to measure return signals from non cooperative targets. This jump in sensitivity could then be used either to lower the required laser output power, or alternatively to increase the stand off distance to the target. Such a system would then need to be tested in daylight conditions outside of the laboratory, to prove the advantages of using longer wavelength illumination. Scattering of the illumination beam by small atmospheric particulates is also reduced by moving to longer wavelengths, increasing the utility of the LIDAR approach [8]. Further testing can be performed on the differential absorption of various gases. By using the supercontinuum source to select specific wavelengths, comparative signals on the InAs detector can highlight the presence of known gases. Again single photon sensitivity here would give the system a greater working range.

7.3 References

[1] Z. Yuan, B. E. Kardynal, R. M. Stevenson, A. J. Shields, C. J. Lobo, K. Cooper, *et al.*, "Electrically driven single-photon source," *Science,* vol. 295, pp. 102-105, 2002.

[2] E. Waks, E. Diamanti, B. C. Sanders, S. D. Bartlett, and Y. Yamamoto, "Direct observation of nonclassical photon statistics in parametric down-conversion," *Physical review letters,* vol. 92, p. 113602 1-4, 2004.

[3] G. Brassard, N. Lütkenhaus, T. Mor, and B. C. Sanders, "Limitations on practical quantum cryptography," *Physical Review Letters,* vol. 85, p. 1330-1333, 2000.

[4] A. Dixon, Z. Yuan, J. Dynes, A. Sharpe, and A. Shields, "Continuous operation of high bit rate quantum key distribution," *Applied Physics Letters,* vol. 96, p. 161102 1-3, 2010.

[5] Y. Yang, P. Ma, X. Wei, and Y. Zeng, "The role played by strain on phase separation in InGaN quantum wells," *Solid State Communications,* vol. 194, pp. 25-29, 2014.

[6] A. McCarthy, R. J. Collins, N. J. Krichel, V. Fernández, A. M. Wallace, and G. S. Buller, "Long-range time-of-flight scanning sensor based on high-speed time-correlated single-photon counting," *Applied optics,* vol. 48, pp. 6241-6251, 2009.

[7] G. A. Howland, D. J. Lum, M. R. Ware, and J. C. Howell, "Photon counting compressive depth mapping," *Optics express,* vol. 21, pp. 23822-23837, 2013.

[8] N. Kopeika, S. Solomon, and Y. Gencay, "Wavelength variation of visible and near-infrared resolution through the atmosphere: dependence on aerosol and meteorological conditions," *JOSA,* vol. 71, pp. 892-900, 1981.